OCS Study
BOEM 2021-049

Hydrodynamic Modeling, Particle Tracking and Agent-Based Modeling of Larvae in the U.S. Mid-Atlantic Bight

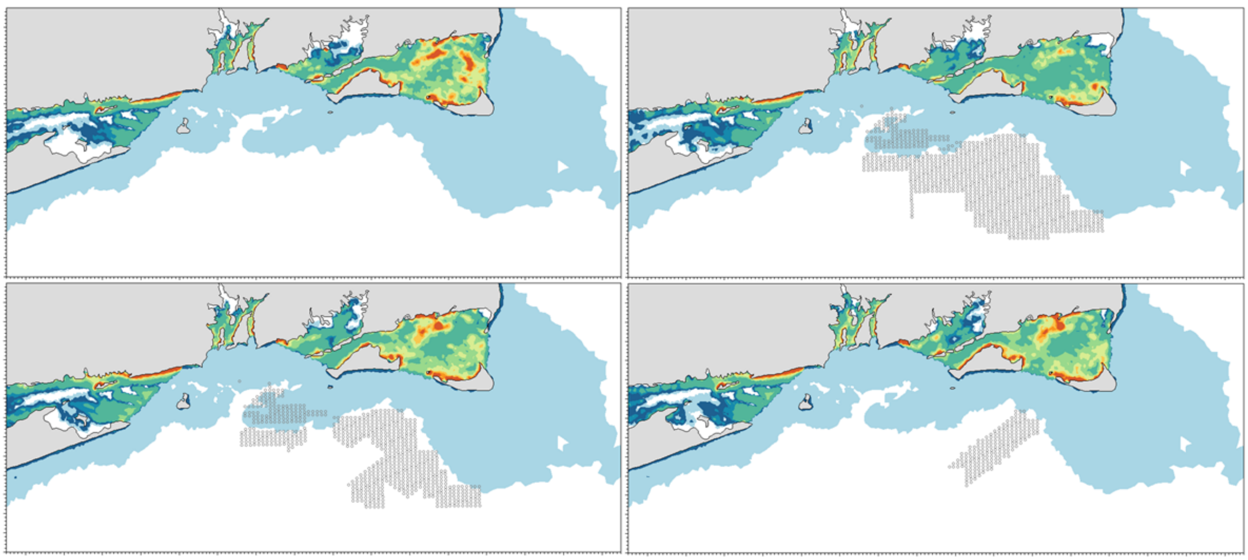

US Department of the Interior
Bureau of Ocean Energy Management
Atlantic Region

BOEM
Bureau of Ocean Energy Management

OCS Study
BOEM 2021-049

Hydrodynamic Modeling, Particle Tracking and Agent-Based Modeling of Larvae in the U.S. Mid-Atlantic Bight

June 2021

Authors:
Thomas L. Johnson, Joshua Jon van Berkel, Lars O. Mortensen, Michael A. Bell, Iris Tiong, Benjamin Hernandez, David B. Snyder, Frank Thomsen, Ole Svenstrup Petersen

Prepared under 140M120C0004
By
DHI Water & Environment, Inc.
141 Union Boulevard, Suite 320
Lakewood, Colorado 80235 USA

US Department of the Interior
Bureau of Ocean Energy Management
Atlantic Region

BOEM
Bureau of Ocean Energy Management

DISCLAIMER

Study concept, oversight, and funding were provided by the US Department of the Interior, Bureau of Ocean Energy Management (BOEM), Environmental Studies Program, Washington, DC, under Contract Number 0140M0120C0004. This report has been reviewed by the BOEM and approved for publication. Approval does not signify that the contents necessarily reflect the views and policies of the Bureau, nor does mention of the trade names or commercial products constitute endorsement or recommendation for use.

REPORT AVAILABILITY

To download a PDF file of this report, go to the US Department of the Interior, Bureau of Ocean Energy Management [Data and Information Systems webpage](http://www.boem.gov/Environmental-Studies-EnvData/) (http://www.boem.gov/Environmental-Studies-EnvData/), click on the link for the Environmental Studies Program Information System (ESPIS), and search on 2021-049. The report is also available at the National Technical Reports Library at https://ntrl.ntis.gov/NTRL/.

CITATION

Johnson TL, van Berkel JJ, Mortensen LO, Bell MA, Tiong I, Hernandez, B, Snyder, DB, Thomsen, F, Svenstrup Petersen, O: 2021. Hydrodynamic modeling, particle tracking and agent-based modeling of larvae in the U.S. mid-Atlantic bight. Lakewood (CO): US Department of the Interior, Bureau of Ocean Energy Management. OCS Study BOEM 2021-049. 232 p.

ABOUT THE COVER

Cover image (Image of summer flounder settlement patterns (starting at upper left and moving clockwise): baseline, scenarios 2, 3 and 5 with possible locations of wind turbines). Used with permission.

ACKNOWLEDGMENTS

This project was supported by the Bureau of Safety and Environmental Enforcement (BSEE), the United State Department of the Interior (DOI); on behalf of the Bureau of Ocean Energy Management (BOEM) under contract number 140M120C0004. We would like to thank the BOEM supervisors for this project: Ms. Jennifer Draher (Oceanographer and Contracting Officer Representative), Mr. Brian Hooker (Marine Biologist) and Dr. Ursula Howson (Fish Biologist) all of whom provided us valuable advice and suggestions for this study.

Table of Contents

List of Figures

List of Tables

List of Abbreviations and Acronyms

ADCP	Acoustic Doppler Current Profiler
AWAC	Acoustic Wave and Current profiler
ABM	Agent-Based Model
BCO-DMO	Biological & Chemical Oceanography Data Management Office
BOEM	Bureau of Ocean Energy Management
BSEE	Bureau of Safety and Environmental Enforcement

CFSR	Climate Forecast System Reanalysis
CFSv2	Climate Forecast System version 2
CFD	Computational Fluid Dynamic
CODAR	Coastal Ocean Dynamics Applications Radar
COP	Construction and Operation Plan
CONMAP	Continental Margin Mapping Program
CSA	Continental Shelf Associates
CSE	Council of Science Editors
DHI	DHI Water & Environment, Inc.
DOI	US Department of the Interior
EcoMon	Ecological Monitoring of Zooplankton
EFH	Essential Fish Habitat
EIS	Environmental Impact Statement
ESP	Environmental Studies Program
ESPIS	Environmental Studies Program Information System
FEHY	FEhmarnbelt HYdrography
FYCOM	Finite Volume Community Ocean Model
GEBCO	General Bathymetric Chart of the Oceans
GHRSST	Group for High Resolution Sea Surface Temperature
GIS	Geographic Information System
GODAE	Global Ocean Data Assimilation Experiment
HD	Hydrodynamic
HDM	Hydrodynamic Model
HF	High Frequency
HFRO	High Frequency Radar Observation
HYCOM	HYbrid Coordinate Ocean Model
IWFBL	Infinite Wind-Farm Boundary Layer
MAB	Mid-Atlantic Bight
MA-RI	Massachusetts – Rhode Island
MBBDB	Multibeam Bathymetry Database
MVCO	Martha's Vineyard Coastal Observatory
MW	Megawatt
MAMFC	Mid-Atlantic Fishery Management Council
MARACOOS	Mid-Atlantic Regional Association Coastal Ocean Observation System
MARMAP	Marine Resources Monitoring, Assessment and Prediction Program
MIKE	“MIKE” is a tradename for DHI software systems
MIKE ABM Lab	MIKE Agent-Based Model
MIKE ECO Lab	MIKE Ecological Model
MIKE 3 FM HD	MIKE 3 Flexible Mesh Hydrodynamic model
MIKE 21 SW	MIKE 21 Spectral Wave model
MOST	Monin-Obukhov Similarity Theory
NCEI	National Centers for Environmental Information (NOAA)
NCEP	National Centers for Environmental Prediction (NOAA)
NDBC	National Data Buoy Center (NOAA)
NEFMC	New England Fisheries Management Council
NEFSC	Northeast Fisheries Science Center
NEPA	National Environmental Policy Act
NOAA	National Oceanic and Atmospheric Administration
NROC	Northeast Ocean Data Portal
NSF	National Science Foundation
OSTIA	Operational Sea Surface Temperature and Sea Ice Analysis
OSW	Offshore Wind Farms
POM	Pattern Oriented Modeling

psu	Practical Salinity Unit
SL	Standard Length
SMAST	School of Marine Science and Technology
SST	Sea Surface Temperature
SW	Spectral Wave
SWUS-EC	US East Coast Spectral Wave Model
3D	Three dimensional
2D	Two dimensional
TL	Total Length
Ct	Thrust coefficient (turbine wind-wake parameter)
USGS	US Geological Survey
WAM	Wave Modeling Consortium
WHOI	Woods Hole Oceanographic Institution

Executive Summary

Offshore wind construction projects have the potential to alter local and regional physical oceanic processes, via their influence on currents from turbine foundations and by extracting energy from the wind. Hydrodynamic modeling (HDM), particle tracking modeling and Agent-Based Models (ABMs) were used to assess how the introduction of commercial scale offshore wind energy facilities in the Massachusetts-Rhode Island (MA-RI) marine areas may affect local and regional oceanic responses (e.g. currents, temperature stratification) and related larval transport under typical seasonal conditions. The HDM and ABM were developed, calibrated, and verified against a range of observed oceanographic and survey data to demonstrate that related conditions prior to offshore wind construction were well represented by the integrated model. Four post-installation scenarios of a single facility (OCS-A 0501) (Scenario 3), two full build-out scenarios using representative 12 Megawatt (MW) (Scenario 2) and 15 MW turbines (Scenario4) and a mid-level build-out scenario (Scenario 5) were selected for investigation. The results of the HDM study show that the introduction of these structures into the MA-RI offshore area do modify oceanic responses by reducing the current magnitude through added flow resistance, influencing the temperature stratification by introducing additional mixing and reducing the current magnitude and wave height by the extraction of energy from the wind by the OSW turbines. For the key oceanic determinant response for the ABM – current – the HDM showed changes in depth averaged currents varying from Baseline on the order of +11% to -8% in the 75th percentile differences depending on the OSW scenario investigated. These changes in currents, lead to varying degrees of discernable increases and decreases in larval settlement density across the three focal species and four OSW build-out scenarios. Here, depending on the release characteristics of the particular larvae, altered current direction and speeds either act independently and/or collectively to cause the observed shifts. At a regional fisheries management level, these shifts are not considered overly relevant with regards to larval settlement

The background of the study is the Bureau of Ocean Energy Management's (BOEM) concerns regarding the potential cumulative impacts on oceanographic transport patterns in the Mid-Atlantic Bight due to the sixteen offshore commercial wind energy leases in southern New England and the Mid-Atlantic. In response, BOEM commissioned this modeling study to assess the changes in hydrodynamic conditions and, among other aspects, fisheries pertinent larval transport impacts resulting from the build-out of one or several OSW energy facilities in the MA-RI lease area.

As suggested above, the key objective of this study was to determine the 'mesoscale' effects of offshore wind energy facilities on coastal and oceanic environmental conditions and habitat by examining how oceanic responses will change after turbines are installed, particularly with regards to turbulent mixing, bed shear stress and larval transport.

The project was divided into six major tasks: *1. Data Management, 2. Desktop Review and Statistical Analysis, 3. Model Development, 4. Model Calibration, 5. Modeling Scenarios and Analysis and 6. Report and Technical Summary*. The initial stages of the project aimed at further refining modeling approaches and collecting the background studies and survey datasets necessary to establish them. Several critical decisions were also made, the most important of which were the above-mentioned OSW build-out scenarios and the target fish and invertebrate larvae that would undergo ABM. Namely:

- Atlantic sea scallops (*Placopecten magellanicus*)
- Silver hake (*Merluccius bilinearis*)
- Summer flounder (*Paralichthys dentatus*)

Among other notable decisions, one decision was to apply typical seasonal conditions by selecting two years for modeling with few tropical storms or hurricanes passing through or nearby the study area.

The subsequent project tasks focused on establishing the necessary models, which ultimately entailed various levels of integration of selected MIKE Powered by DHI models. The HDM, developed with MIKE 3 FM HD, MIKE 21 SW and other nearfield models, was established as a 3D regional model ranging from Cape Hatteras to offshore Cape Cod. A finer model mesh was embedded in the specific MA-RI study area. Localized turbulence effects of individual wind turbines were addressed through nearfield Computational Fluid Dynamics (CFD) modeling of water flow near turbine foundations. The CFD results were then parameterized and included in the regional HDM. Localized wind wake effects were included by using an embedded wake loss model in the regional HDM. The overall model therefore fully implemented near and far field oceanic processes including surface wind, ocean currents (both lateral and vertical), air pressure, precipitation/ evaporation, surface heat flux, water temperature and salinity.

The applied ABM, carried out in MIKE ABM Lab/MIKE ECO Lab, allowed for bottom-up ecological modeling via coupling of the ABM template to an HDM. ABM Lab offers an open and flexible coding environment for defining and customizing simple to advanced biological traits and processes using a series of user-defined arithmetic expressions and state variables, which allows simulated agents (e.g. larvae) to react and interact with a dynamically changing virtual environment. This generally involved customizing ABM templates with key transportation traits of the selected species (i.e. associated with the zygote and larval development stages) and subsequent stages of testing, calibration and validation.

The oceanic responses analyzed in relation to the OSW build-out scenarios mainly entailed currents, waves, bed shear stress and temperature stratification. Limited inert particle tracking modeling was also included. The results of the HDM study clearly reveal that introduction of the OSW structures into the Massachusetts-Rhode Island offshore area modifies the oceanic responses of current magnitude, temperature, and wave heights by 1) reducing the current magnitude through added flow resistance, 2) influencing the temperature stratification by introducing additional mixing, 3) reducing current magnitude and wave height by extracting of energy from the wind by the OSW turbines.

The results of the HDM with regards to oceanic responses were:

- The depth averaged currents vary from Baseline on the order of +11% to -8% in the 75th percentile differences depending on the OSW scenario investigated.
- Particle tracking which "integrates" the overall effect of the current on objects subject to them showed variations on the order of +10% between the baseline and the 12 MW full build-out scenario. This is in line with the observed order of magnitude change in the depth averaged currents.
- The effect on the waves due to the introduction of the 12 MW full build-out scenario was a reduction on the H_{m0} (significant wave height) inside and around the OSW. The 95th percentile statistics showed H_{m0} reductions that were on the order of 0.5 to 0.55 m inside the OSW. Outside the OSW the reduction was 0.15 to 0.2 m or less. At the coast the reduction was shown to be on the order of 0.05 to 0.10 m or less. The 99th percentile statistics showed reduction in H_{m0} were on the order of 0.75 m or less inside the OSW. Just outside the OSW the reduction was on the order of 0.4 to 0.45 m. At the coast the reduction was shown to be on the order of 0.10 to 0.15 m or less.
- The changes in bed shear stress between 12 MW full build-out (Scenario 2) versus the baseline (Scenario 1) were seen mainly in the OSW area and immediate vicinity. It was found that the difference in grain size that can be moved after installation of the 12 MW full build-out scenario was on the order of +/- 0.3 mm.

- A review of the 12 MW full build-out (Scenario 2) versus the baseline HDM temperature stratification results showed a relative deepening in the thermocline of approximately 1 to 2m and a retention of colder water inside the OSW farm area through the summer months compared to the situation where OSW structures were not present. The modeled effects on the temperature stratification due to the introduction of OSW build-out area appeared to be different than field measurements in two OSW's in the German North Sea (see Floeter et al. 2017). Further study of these effects is thus warranted. However, for the present study the small differences in the effects of temperature stratification did not alter the larval transport modeling results or conclusions.

The ABM templates, which include the parameterization of larval release, transport and settlement characteristics (or larval transport characteristics), for each target species were coupled with the HDM baseline results and subjected to Pattern Oriented validation modeling (POM). Here, progressively targeted spatial distribution comparison showed an overall good (and partly excellent) agreement between model and survey results (e.g. against datasets such as EcoMon, SMAST). Vertical and temporal model results were also shown to have a good match with cited literature values for all three species.

OSW scenarios modeling that included this proper coverage of relevant larval transport characteristics showed are outlined in the subsequent paragraphs. For sea scallop transport, particularly for Scenario 2, 4 and 5, a shift in settlement to the southwest of the OSW buildup areas is evident with discernable and notable increases in settled larval density in an area south of Block Island and south to the east of Long Island. Distinct areas of decreases in sea scallop larval settlement density are predicted south of Martha's Vineyard in all build-out scenarios and, to some degree, in the Nantucket Shoals. The oceanic response attributed to these changes is an increase in current speeds north of the OSW build-out areas that shift Georges Bank sea scallop larval transport from the area north of the OSW area, and for several scenarios the Nantucket Shoals, in a southwesterly direction where they either simply settle in normal current speeds or encounter areas of reduced current speeds and settle in greater densities.

When reviewing the overall build-out modeling results for silver hake larval settlement, it is evident that reduced current speeds are the prominent OSW related oceanic response behind a general shift in settled larvae to the south of the Nantucket Shoals and into the general Georges Bank area. While increases in current speed are generally apparent to the west and north of all OSW build-out scenario areas, a broad pattern of reduced current speeds is apparent within the OSW build-out scenarios and/or to their southwest, south, and east. This suggests that observed silver hake larval density shifts in each OSW build-out scenario are primarily caused by suspended larvae that encounter slightly lower current speeds and settle in higher densities.

An analysis of the cumulative summer flounder OSW development scenario modeling results illustrates the combined influence of parameterized swimming speed and direction and altered currents; where it is again evident that a reduction in current speeds is a determinant OSW related oceanic response. The main discernable change in summer flounder density across all analyzed OSW build-out scenarios is a general decrease in larval settlement density in the Nantucket Sound. The postulated reason for this is that predominant summer flounder larval transport from the south enters into, at varying degrees but generally evident, areas of lower current speeds to the southwest of each OSW build-out scenario area. In these waters, summer flounder's horizontal swimming and directional attributes cannot overcome the reduction in current speed, thereby preventing some larvae from entering the Nantucket Sound.

Relevance of the change in larval dispersal pathways is largely associated with possible disruption in processes of connectivity, settlement, and recruitment. OSW effects to oceanographic conditions such as those described in this report may potentially create "sinks" or subpopulations that no longer contribute propagules to the overall regional population network. Alternatively, the loss of viable and productive subpopulations ("sources") is also a possible consequence of these effects. Depending on the species and spatial scale of the population network, changes in larval distribution and settlement density can affect regional or local abundances. In this regard, it is noted that dispersal pathways, settlement habitat, spawning, and recruitment vary greatly in time across the MAB and Georges Bank region (e.g. Steves et al, 1999; Carey and Stokesbury, 2011; Perretti and Thorson, 2019).

In relation to the above, it is noted that sea scallop populations are not closed at small scales throughout the region. Therefore, changes in modeled settlement near the OSW are not likely to affect larger Georges Bank or MAB stocks as managed by NEFMC. Modeled changes in larval distributions may, however, affect distribution and survival of settlers adjacent to the OSW areas. In relation to silver hake, their wide distribution of settlement over the adjacent continental shelf (Steves et al. 1999), suggest that shifts in settlement density are not likely to affect regionally managed fishery stocks or changes in subpopulations near the OSW. For summer flounder, evidence indicates that although there is a subpopulation structure, a high proportion of larval settling in the project area can be from as far away as Cape Hatteras, North Carolina (Hoey et al. 2020). Thus, regionally managed fishery stocks are also not likely to be affected by changes caused by the OSW build-out scenarios.

The results generated by this study can be considered to be a highly advanced and reliable interpretation of the oceanic responses to OSW developments and the related impacts to target species larval transport and settlement. In terms of oceanic responses, the related results lead to the conclusion that the introduction of the OSW structures does modify the oceanic responses of current magnitude, temperature, and wave heights. These responses, particularly changes in currents, lead to discernable increases and decreases in larval settlement density across the three target species and four OSW build-out scenarios. Here, depending on the release characteristics of the particular larvae, altered current directions and speeds either act independently and/or collectively to cause the observed shifts. At a regional fisheries management level, these shifts in larval settlement density are not considered overly relevant. However, analysis does suggest that there could be a risk of impact to certain subpopulations, thereby warranting future localized investigations.

The main area for potential further work on Hydrodynamic and Agent-Based modeling of larval transport and settlement modeling is to simulate additional years. From an HDM perspective, this is recommended as it is not possible to assess the year-to-year variability in the residual currents with a single year of model simulations. For the larvae ABM, modeling more than the requested single spawning season would allow experts to better understand the long-term structural shift in larval settlement patterns and the possible corresponding secondary impacts. Other areas for possible future related work include adding additional species, OSW development scenarios and locations in the MAB, and/or target species life cycle stages.

1 Introduction

The Bureau of Ocean Energy Management (BOEM) engaged DHI Water & Environment, Inc. (DHI) to undertake the project 'Hydrodynamic Modeling, Particle Tracking and Agent-Based Modeling of Larvae in the U.S. Mid-Atlantic Bight'. This involved the use of a suite of integrated modeling components capable of assessing the influence that Offshore Wind Farms (OSW) have on small-scale coastal and regional offshore physical environmental processes and the corresponding impacts to the distribution of the larvae of key fisheries species.

To provide further context to the study, a brief overview of relevant background information, general approach/objectives, OSW build-out analysis scenarios, and key project execution decisions are provided in the following subsections. This is followed by report sections that comprehensively describe the applied modeling methodologies and the associated results.

1.1 Project Background, General Approach and Objectives

1.1.1 Project Background

Stakeholders have expressed concerns with regards to the alteration of oceanographic transport patterns as a result of offshore wind construction projects in the Mid-Atlantic Bight between Cape Hatteras and Cape Cod. A previous BOEM-funded study (Chen 2016) examined the potential impacts of a representative wind energy facility offshore southern New England on particle transport during two storm conditions (August 1991 Hurricane Bob and February 1978 Nor'easter storm) using the Finite Volume Community Ocean Model (FVCOM). Since the conclusion of this study, more precise facility layouts have been proposed and interest has been expressed with regards to potential impacts due to seasonal conditions and the cumulative impacts of multiple offshore facilities.

1.1.2 General Approach

In order to address these concerns, the present project was charged with developing a detailed hydrodynamic model (HDM) capable of accurately assessing potential changes in hydrodynamic flows resulting from several representative OSW build-out scenarios. The chosen HDM approach included a regional Mid-Atlantic Bight (MAB) regional model that incorporated localized turbulence and wind wake effects of individual wind turbines. It was therefore capable of more accurately simulating pertinent OSW-induced oceanographic changes and their corresponding impacts on affected environments (as mandated by the National Environmental Policy Act (NEPA)). The localized turbulence effects were addressed via nearfield computational fluid dynamic (CFD) modeling of water flow near turbine foundations, while localized wind wake effects were analyzed with a wake loss model. These were integrated in the three-dimensional (3D) regional model that covers a broad area from Cape Hatteras to offshore Cape Cod, with a finer mesh embedded in the specific study area offshore Massachusetts – Rhode Island (MA-RI) area. The model therefore fully implemented near and far field oceanic processes including surface wind, ocean currents (both lateral and vertical), air pressure, precipitation/evaporation, surface heat flux, water temperature and salinity.

The project was also mandated with carrying out larval dispersion modeling of three representative Mid-Atlantic fisheries relevant species with the abovementioned HDM. While some particle tracking was carried out, the decision was made to primarily apply an agent-based modeling (ABM) approach. The applied DHI ABM methodology allowed for bottom-up ecological modeling via coupling of the ABM to a HDM, and the sensory sphere (Eulerian grid cells) it enabled around each agent (a Lagrangian particle). Agents reacted to generated HDM variables (e.g. water temperature) or external variables within the radius of its sensory sphere. The ABM approach was deemed to better include the influence of pertinent larval behavior characteristics, thereby providing more refined results for assessing the effect that offshore turbines may have on larval transport.

It should be noted that no new modeling software was developed as a part of the study.

1.1.3 Project Objective and Sub-objectives

The main objective of the project was to determine the mesoscale effects of offshore wind energy facilities on coastal and oceanic environmental conditions and habitat by examining how oceanic responses will change after turbines are installed, particularly with regards to turbulent mixing, bed shear stress and larval transport. In attaining these primary objectives, the following sub-objectives were also applicable:

1. Researching available datasets and information pertinent to:
    a. establishing an initial inventory of data and information for use in the model set-up, calibration, and validation of an initial long list of fisheries species larvae options
    b. choosing the larvae of three fisheries species based, in part, on the availability of required data and information
    c. obtaining and managing the data for establishing the aforementioned numerical models
2. The set-up of the baseline HDM and ABMs for the selected fisheries species that included:
    a. MIKE 3 FM HD, MIKE 21 SW (wave) and the nearfield CFD turbulence / localized wind wake loss models as the base for subsequence agent-based modeling
    b. set-up and integration (i.e. with the hydrodynamic models) of the ABM Lab models in a manner that assured biologically realistic dispersion modeling of selected larvae species
3. Assuring acceptable modeling via the execution of necessary calibration, validation and sensitivity of the baseline models noted under item, above
4. Set-up of the aforementioned baseline (integrated) HDM and ABMs to include specified OSW development scenarios to enable simulation of the dispersion effect of the OSW structures to the 3 chosen larvae
5. Carrying out expert analysis of the modeling results.

1.2 Project Scenarios and Decisions

As already suggested, there were several moments during project execution where significant decisions were made with BOEM representatives that influenced the ultimate analysis, scope, and associated deliverables. In general, these included:

- The selection of three larvae from representative fisheries species,
- Defining key model parameters such as model structure and years of analysis,
- Establishing the four OSW build-out scenarios to undergo HDM and ABM impact modeling,
- Other scope alterations or analysis specifications.

1.2.1 Selection of Fisheries Species Larvae

The selection of three fisheries species larvae from a BOEM specified long-list of possible options constituted one of the initial project tasks and key analysis scope decisions. This was aided by an initial inventory of project area datasets and peer reviewed papers, established by fisheries expert colleagues from Continental Shelf Associates (CSA) with pertinent project area and subject matter knowledge. Joint deliberation on data availability for the long-list species and their representative characteristics eventually led to the selection of the following three species:

- Atlantic sea scallop (*Placopecten magellanicus*)
- Silver hake (*Merluccius bilinearis*)
- Summer flounder (*Paralichthys dentatus*).

1.2.2 Key Model Parameters

With the arrival of new insights associated with HDM progression and review of empirical larval distribution datasets, several occasions arose where it was necessary to either define or alter originally conceived modeling parameters. This primarily entailed moving away from a local nested model (i.e. within the HDM) and making decisions regarding which past years would provide the most representative HDM hindcasts runs.

At the onset of the project, it was expected that two HDMs would be required, a regional model from Cape Hatteras to Cape Cod and a local nested model that focused on the study area. In practice, however, the spawning areas, connectivity and distribution of chosen larvae was quite extensive. It was thus found that a better solution was to maintain the full regional model domain but include a finer mesh embedded in the specific study area offshore Massachusetts – Rhode Island (MA-RI) area. It was agreed by all parties that this allowed tracking of the larvae to their eventual settlement areas that were at first, perhaps, not expected.

As mentioned, an original rational for this study was to review the cumulative impacts on the hydrodynamics in the MA-RI OSW lease area. While previous studies looked at specific storm impacts (Chen 2016), the present study focused on "normal" conditions. It was thus necessary to select a study period with fewer passing storms and one that was contemporaneous to present time but still had sufficient measurement data available to allow for calibration and verification of the HDM. Thus, after a historic review of extreme metocean events and deliberation with BOEM representatives, the two-year period from February 2017 to January 2018 and February 2018 to January 2019 was selected.

1.2.3 OSW Build-out Scenarios

Project requirements identified five analysis scenarios, where one involved the obligatory baseline scenario[1], referred to as Scenario 1 (scenarios without any OSW structures {0 tower foundations in the model}). While some preliminary input was provided, the characteristics of the remaining 4 OSW build-out scenarios were provided by BOEM representatives. They were:

- Scenario 2: Fully built-out OSW lease offshore MA-RI area, 12 MW turbines (1,063 towers)
- Scenario 3: OCS-A 0501, 12 MW turbines (197 towers)
- Scenario 4: Fully built-out OSW lease offshore MA-RI area, 15 MW turbines (1,063 towers)

[1] The baseline scenario is obligatory as it must be modeled to model calibration and validation purposes, and to enable an analysis of impacts associated with the build-out scenarios.

- Scenario 5: Mid-level, 12 MW turbines (766 towers). This scenario was selected based on the known projects at time of award of this contract.

Additional details of these scenarios are provided in **Section 4.1.1**. It is noted that the contract called for a maximum of fifteen (15) modeled scenarios. With three (3) species and five (5) scenarios the maximum number of scenarios was completed.

1.2.4 Other Analysis Scope Alterations or Specifications

There were two other, minor but notable, analysis scope alterations or specifications that were made during execution of the project. Briefly, these were:

- The decision, made at the start of the project, not to address the tracking of loss of containment spills related to ship allisions,
- BOEM specifications regarding the characteristics of turbine foundations or overall turbine size to be included in the modeling.

2 Hydrodynamic Baseline Model Input Data

The following subsections provide a comprehensive overview of the various input data that were used to set-up the HDM.

2.1 Overview of Geographic Coverage

The geographic extent of the regional HDM was approximately from offshore Massachusetts (Cape Cod) to offshore North Carolina (Cape Hatteras). The model was established in hindcast mode, using MIKE 3 FM HD. Data is included for the years 2017 and 2018, with targeted localized resolution in the project area (i.e. the OSW leases located off of Massachusetts and Rhode Island).

2.2 Bathymetric Data

The bathymetry in the HDM is based on a combination of MIKE C-Map digital navigational charts and U.S. NOAA survey archive at National Centers for Environmental Information (NCEI), which have high resolution gridded bathymetries for the project area. Data from the General Bathymetric Chart of the Oceans (GEBCO) was also used as a source for deep-water bathymetry.

2.3 Meteorological Data

Climate Forecast System Reanalysis (CFSR) wind fields were the basis for continuous wind forcing in the 3D HD model. The CFSR wind fields cover the North Atlantic from 1979 to 2020 with two model updates. The CFSR data is comprised of surface winds, pressure and relevant air-parameters as relative humidity, cloud cover and air temperature. The CFSR dataset was established by NOAA's National Center for Environmental Prediction (NCEP). CFSR is a coupled meteorological and oceanographic model system that uses synoptic data for initialization. The data are available on an hourly basis from January 1, 1979 through the present. The initial CFSR dataset covers the 31-year period from 1979 to 2010. More recently, the operational dataset, the Climate Forecast System version 2 (CFSv2), has been utilized in modeling and these data are available from 2010 through the present. The underlying model in CFSv2 is the same as for CFSR, however, the spatial resolution of the atmospheric model was increased from 0.3 degree to 0.2 degree, while the resolution of atmospheric pressure, relative humidity and precipitation was 0.5 degree for the entire period (interpolated to the same grid as the wind speed). In the analysis conducted for the project, the CFSv2 dataset was used.

CFSR was designed as a global, high-resolution, coupled atmosphere-ocean-land surface-sea ice system to provide the best estimate of the state of these coupled domains. The atmospheric model behind the CFSR modeling complex is NCEP's Global Forecast System. In coastal areas, CFSR (by default) gives priority to land surfaces. For the present model, however, the land mask was adjusted to ensure focus on the sea surface.

In addition to 10 m wind data, the CFSR parameters included in this project for estimating air-sea heat exchange were:

- Air temperature at 2 m,
- Air relative humidity,
- Cloud cover.

2.4 Oceanographic Data

The 3D ocean model required salinity and temperature as well as ocean currents prescribed on the open boundaries and for initial conditions. For this, the HYbrid Coordinate Ocean Model (HYCOM) global circulation model was used with data from the HYCOM database (Helber et al. 2013). HYCOM is a layered ocean model with generally a spatial resolution from 0.08 degree and 40 non-equidistant layers. The model is fully dynamic and applies a variational data assimilation technique for surface elevations and temperature. The HYCOM archive has daily 3D fields of elevation, current profiles, temperature, and salinity and covers the period of 1995 to 2020 from various model versions. This model is well established in the North Atlantic.

2.5 Astronomical Tide Data

Tidal boundary water levels were sourced from DHI's global tidal model DTU10 (Andersen and Knudsen 2009).

2.6 Boundary Conditions with Combined Oceanographic and Tidal Forcing

In order to consider ocean (baroclinic) forcing together with the tidal-induced (barotropic) forcing, these had to be combined in a downscaling approach. The current components and surface elevation from the daily ocean data (HYCOM) at the boundaries were linearly added to the hourly tidal components extracted from the DHI's global tidal model DTU10. This procedure was applied to the years simulated (2017 and 2018).

2.7 River Discharge

Freshwater inflow from rivers is important as it affects the stratification in coastal areas and the nearshore circulation. For the present project, the major rivers of concern are the East coast rivers Hudson, Hackensack and the Raritan that discharge into the Lower Bay, as well as Connecticut. There are data archives for river discharges from U.S. Geological Survey (USGS) that cover daily data from 2010 to 2020. In total, sixteen (16) rivers were specified in the model for freshwater inflow in the 3D model. Plots in **Figure 1** are the time series of the river discharges that were included in the model.

Table 1. Rivers included as freshwater sources in the hydrodynamic model.

Rivers		
Merrimack River, MA	Raritan River, NJ	Rappahannock River, MD
Blackstone River, RI	Hackensack River, NJ	Pocomoke River, MD
Connecticut River, CT	Delaware River, NJ	York River, VA
Hudson River, NY	Nanticoke River, DE	James River, VA
Carmans River, NY	Potomac River, MD	
Mullica River, NJ	Susquehanna River, MD	

Figure 1. Time series of river freshwater discharges used in the HDM
Sixteen (16) selected rivers were specified as freshwater inflow in the 3D model, using discharge time series from January 2017 to January 2019.

2.8 Observational Data Sources

The development of numerical marine models is dependent on the availability of ground-truth data that can provide calibration and a check on the validity of the model results. While there are considerable data for the study area, these data are held by many different entities and span many different periods with varying quality and monitoring methodology. Data collection from both public and developer sources was undertaken during the project.

2.8.1 Current Observational Data Sources

Currents are generally one of the most complicated parameters to measure and data are therefore scarce. Relevant current measurement data compiled that has a time overlap with 2017-2018 and used in this project included:

- Martha's Vineyard Coastal Observatory (MVCO) maintained by Woods Hole Oceanographic Institution (WHOI) has an Acoustic Doppler Current Profiler (ADCP) approximately 1.5 km south of Martha's Vineyard (41.33 N, 70.55 W) with observations in ~12 m water depth.
- Coastal Pioneer Array maintained by Ocean Observation Initiative has several ADCPs approximately 120 km south of Martha's Vineyard (39.6 N, 70.6 W) at the shelf edge. The locations that were used were:
    - Central Offshore Profiler Mooring (CP02PMCO) (40.10108 N, 70.88765 W) in ~148m water depth
- Wind farm developer Orsted provided data from a number of ADCP locations (Ørsted, 2020):
    - Orsted OR F190 ADCP (41.11917 N, 70.60056 W) in ~42.2 m water depth
    - Orsted OR F180 ADCP (40.92 N, 70.92972 W) in ~55.6 m water depth
    - WBU Triaxys ADCP (41.11333 N, 70.59111W) in ~42.8 m water depth
    - Orsted OR F240 ADCP (41.08806 N, 71.22194 W) in ~35.4 m water depth
    - Orsted Acoustic Wave and Current profiler (AWAC) (71.51675W, 41.10964N) in ~26.5 m water depth
    - Orsted OR F 230 ADCP (39.07028 N, 74.4472 W) in ~18.6m water depth
- High-frequency Radar of surface currents using Coastal Ocean Dynamics Applications Radar (CODAR). Roarty et al. (2020) outlined the use of CODAR in the Mid-Atlantic Bight over a ten-year period 2007-2016. The data was collected by the Mid-Atlantic Regional Association Coastal Ocean Observation System (MARACOOS). In addition, MARACOOS continued to collect CODAR data. The project used data collected for the 2017 and 2018 study period.

Figure 2 shows the ADCP measurement locations.

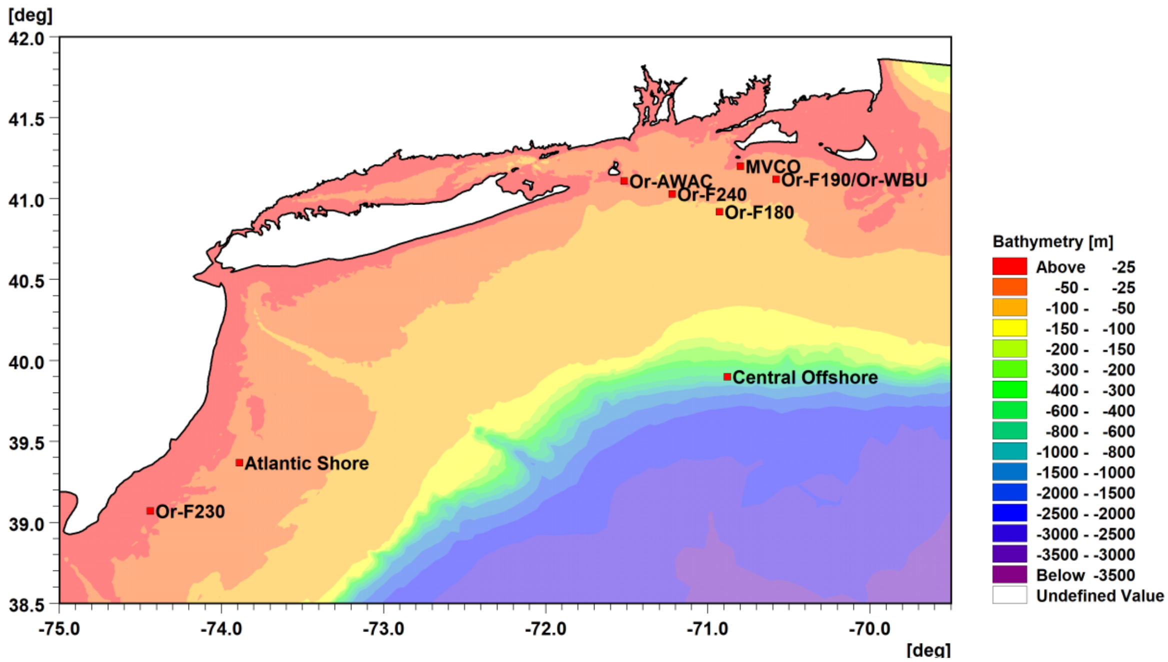

Figure 2. ADCP measurement locations
Current measurements from ADCPs deployed by MVCO, Coastal Pioneer Array and Orsted available for use.

2.8.2 Water Level Observational Data Sources

Relevant water level measurement data collected (from NOAA's Tides and Currents database) and used included:

- Station NTKM3 - 8449130 - Nantucket Island, MA (41.285 N 70.096 W)
- Station NWPR1 - 8452660 - Newport, RI (41.504 N 71.326 W)
- Station QPTR1 - 8454049 - Quonset Point, RI (41.586 N 71.407 W)
- Station ACYN4 - 8534720 - Atlantic City, NJ (39.357 N 74.418 W)
- Station BRND1 - 8555889 - Brandywine Shoal Light, DE (38.987 N 75.113 W)

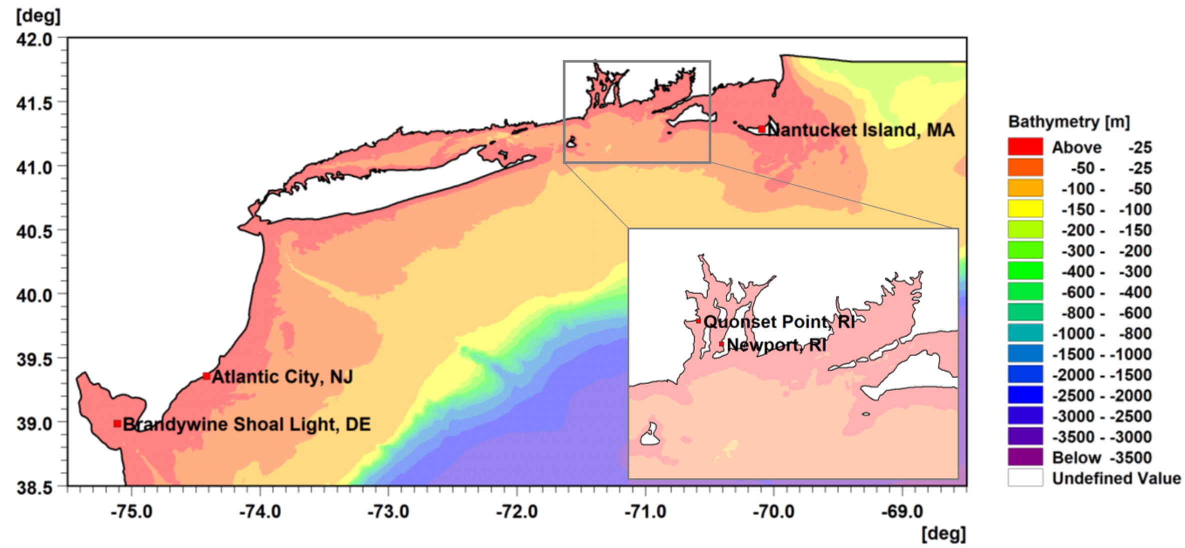

Figure 3. Water level measurement locations
Water level measurement data are available for five (5) locations, from Brandywine Shoal Light (Delaware) in the south to Nantucket Island (Massachusetts) to the north.

2.8.3 Wave Observational Data Sources

Relevant wave measurement data collected and used included:

- National Data Buoy Center (NDBC) operates several buoys in the area with various configurations. The two closest to the focus area were Block Island and Nantucket as listed below.
  - Station 44097 - Block Island, RI (40.967 N 71.126 W), Sea temp depth: 0.46 m below water line, Water depth: 51 m
  - Station 44008 (offshore) - Nantucket 54 NM Southeast of Nantucket. 40.504 N 69.248 W). Sea temp depth: 1.5 m below water line. Water depth: 74.7 m

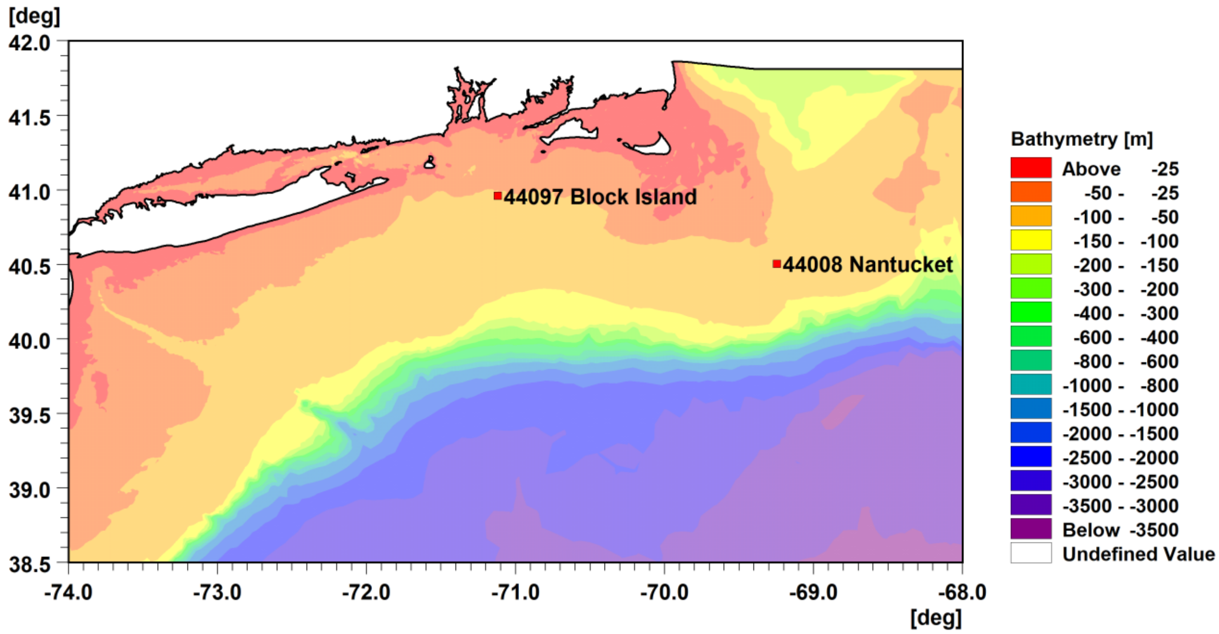

Figure 4. Location of NDBC and other wave buoys used in the wave model verification
Two (2) NDBC buoys located closest to the project area were Block Island (44097) and Nantucket (44008).

2.8.4 Sea Temperature Observational Data Sources

Relevant sea temperature measurement data collected and used from NDBC buoys included:

- Station 44008 (offshore) - Nantucket 54 NM Southeast of Nantucket. 40.504 N 69.248 W). Sea temp depth: 1.5 m below water line. Water depth: 74.7 m
- Station 44097 - Block Island, RI. (40.967 N 71.126 W). Sea temp depth: 0.46 m below water line. Water depth: 51 m
- Station 44017 - Montauk Point - 23 NM SSW of Montauk Point, NY (40.693 N 72.049 W). Sea temp depth: 1.5 m below water line. Water depth: 48 m
- Station 44025 - Long Island - 30 NM South of Islip, (NY40.251 N 73.164 W). Sea temp depth: 1.5 m below water line. Water depth: 36.3 m
- Station 44065 - New York Harbor Entrance - 15 NM SE of Breezy Point, NY (40.369 N 73.703 W). Sea temp depth: 1.5 m below water line. Water depth: 25 m

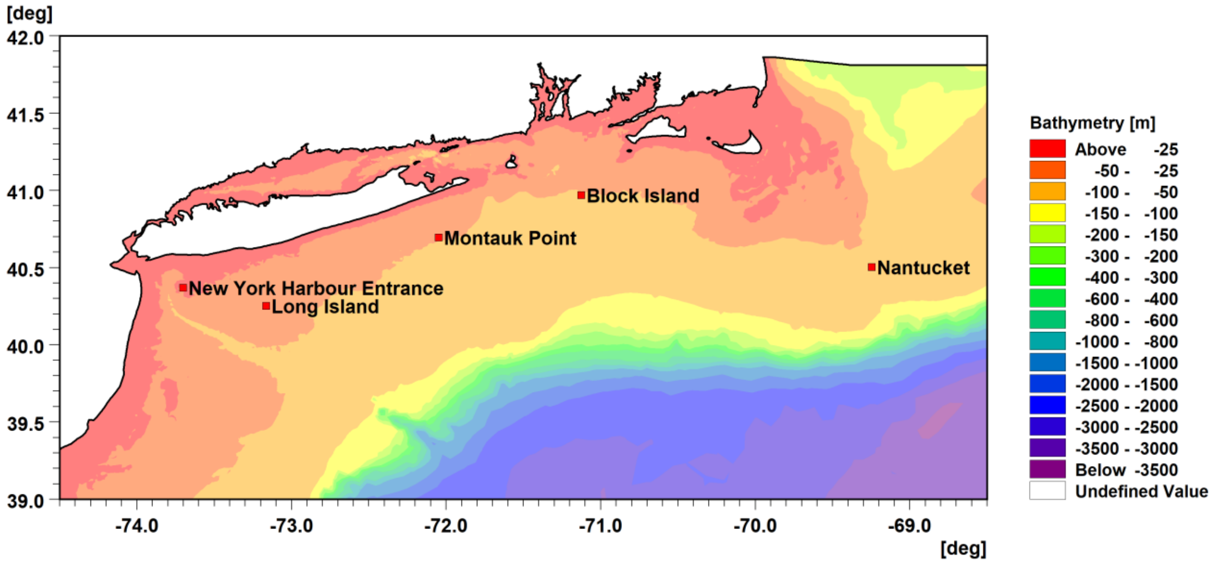

Figure 5. Sea temperature measurement locations
NDBC buoys from five (5) locations, spanning from New York Harbor Entrance in the west to Nantucket in the east, provided sea temperature data used as inputs to the HDM.

3 Hydrodynamic Baseline Model Validation

3.1 Mid-Atlantic Bight Oceanographic Process Review

The oceanographic processes of the Mid-Atlantic Bight (MAB) are well documented by numerous researchers. The following review is included to provide context to the hydrodynamic modeling that was completed for this study. In general, the MAB is characterized by the relatively wide shelf following the Bight and the Gulf Stream that veers eastward from Cape Hatteras. As a western boundary current, the Gulf Stream sheds several large eddies on its way, eddies that may travel onto the shelf and provide quite varying conditions. Also, cold water from Gulf of Maine and the banks enters the area contributing to the so-called 'cold-pool' of water resting during spring and early summer on the shelf. The coastal areas, where also the offshore wind development takes place, is generally tidal. It should be noted that general statements regarding the oceanography and the specifics of the model may sometimes not correlate in a one-to-one manner. However, it was a goal of the project to use field measurements (currents, water levels, temperature, wave height elevations, etc.) to verify the model results against baseline conditions.

The overall oceanography of the MAB is influenced by the warm Gulf Stream, that flows Northeastward along the shelf edge to Cape Hatteras, where it continues as a warm surface current in North easterly direction. The edges of the stream are unstable and from time to time sheds off large consistent eddies that may protrude across the shelf. There is also a cold current flowing from New England southwest-ward along the coast, bringing cold bottom water to the shelf areas. One significant effect of this is the formation of the so-called cold-pool, i.e. cold bottom waters arrested on the shelf during spring and early summer, forming a strong vertical stratification (Stevenson et al. 2004). Other significant forces are the tides, that are relatively strong in the sounds and shallow waters along the coast as well as fresh water sources from the main rivers Hudson-Raritan estuary, Connecticut, and Delaware.

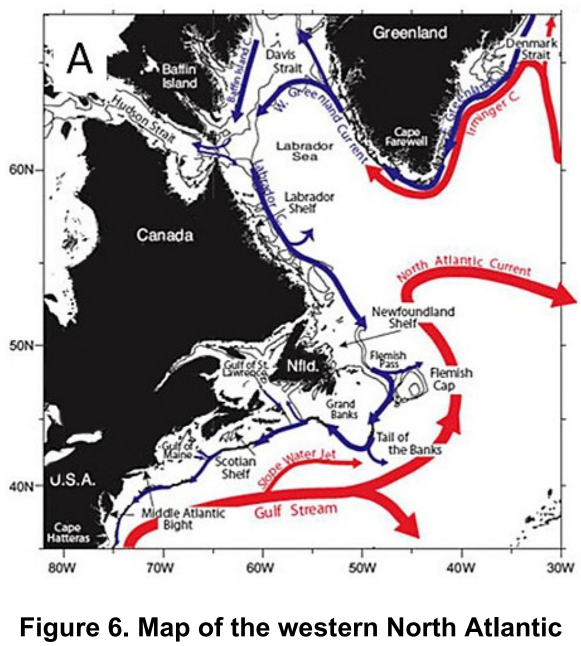

Figure 6. Map of the western North Atlantic Ocean Currents
Showing two dominant current systems affecting the Mid-Atlantic region: Gulf Stream (red) and Labrador Current (blue). (Credit: Mid-Atlantic Fishery Management Council (MAMFC))

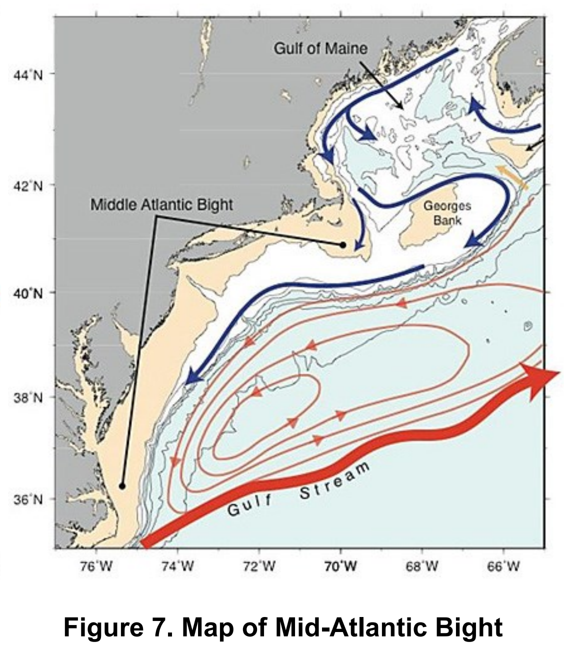

Figure 7. Map of Mid-Atlantic Bight
Influence on the Mid-Atlantic region of southward-flowing cool currents (blue) and warmer currents (red) associated with the Gulf Stream. (Credit: MAFMC)

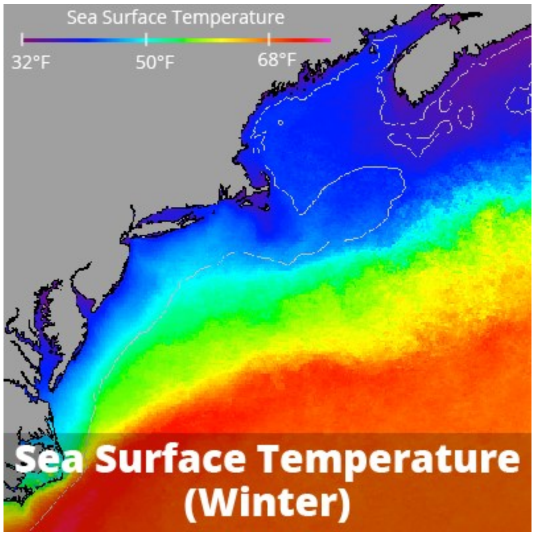

Figure 8. Sea Surface Temperature (Winter)
Wintertime satellite imagery reveals cold water (blue) near the Mid-Atlantic coast. Warmer water (red) lies offshore in the Gulf Stream. (Credit: National Oceanic and Atmospheric Administration (NOAA))

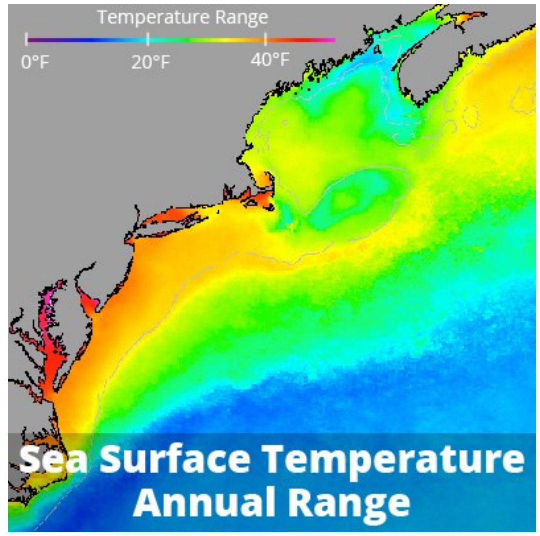

Figure 9. Sea Surface Temperature (Annual Range)
This map shows average annual range of sea surface temperature from 1985 to 2009 based on satellite imagery. The Mid-Atlantic coast experiences a wide range of temperatures, as indicated by red and orange. (Credit: NOAA)

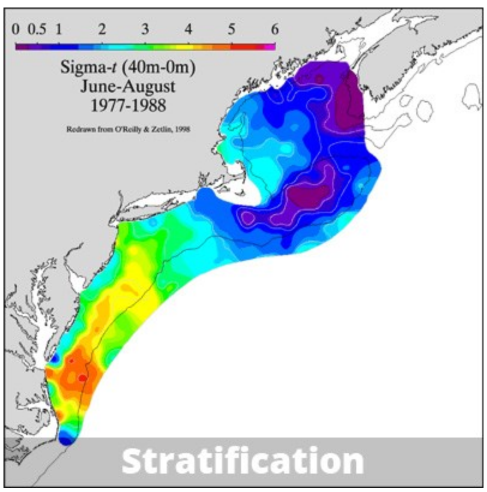

Figure 10. Stratification in the Mid-Atlantic Bight
Regional differences in summer stratification, showing strongly stratified areas (indicated by red, orange, and yellow colors) in the MAB. (Credit: NOAA)

Wave conditions in the area are generally characterized by relatively persistent south-easterly swell from North Atlantic combined with local wind-sea from various directions. Mean significant wave height is about 1m and extremes up to above 7 m. Extreme wave conditions often occur during hurricane passage or extratropical Northeasters. This study purposely tried to avoid inclusion of hurricanes in the timeframe studied.

3.2 Overview, Model Domain and Setup

As noted above, this study was commissioned to carry out the 'Hydrodynamic Modeling, Particle Tracking and Agent-Based Modeling of Larvae in the U.S. Mid-Atlantic Bight'. The project aimed at studying the effect of OSW development on oceanographic conditions. Based on this, the approach adopted for the modeling is as follows:

- Set up a regional hydrodynamic with a higher resolution mesh surrounding the Massachusetts-Rhode Island Offshore Wind Farm lease area model using DHI's Flexible Mesh Hydrodynamic modeling software (MIKE3/21 FM HD), here called the Mid Atlantic Bight HD model (HD_{MAB}), and validation using available observations. The study period was selected as noted above to be February 1, 2017 through March 1, 2018.
- Set up a wave model to cover the study area using DHI's Spectral Wave modeling software (MIKE21 SW) and ran it for the same two-year period. This model used data from the DHI's US East Coast regional model to provide boundary conditions. The wave model was driven with the validated CFSR wind datasets. The regional wave model has been validated against the measured wave data.

The details of the model setups and their calibration and validation are described in the following sub-sections.

3.2.1 Model Domain

Figure 11 below shows the local 3D bathymetry model employed by DHI for the MAB area. **Figure 12** below shows the hydrodynamic model mesh. The full regional model domain was found to be critical for simulation of the mesoscale features. The influence of the Gulf stream was required and therefore the boundary of the model was extended eastward to allow the Gulf Stream to "exit" the model perpendicular to the Eastern model boundary. The model was bounded on the south near Cape Hatteras at 35° North Latitude with the boundary angled to the Southeast to a point at 33° North and 73° East. From there the model boundary proceeds Northeast to a point 36° North and 68° degrees East. The boundary from there goes north to Cape Cod at 41.8° North Latitude.

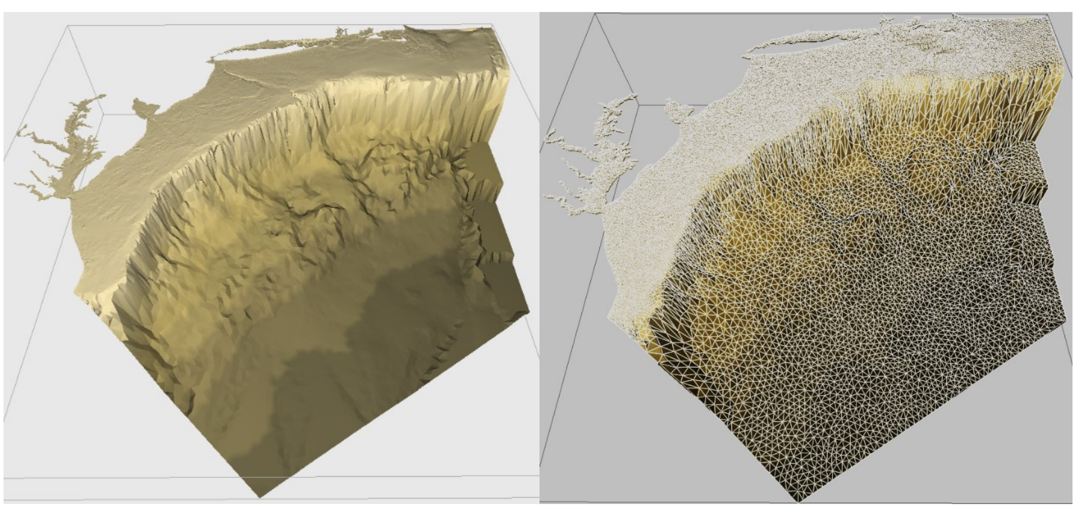

Figure 11. Hydrodynamic model bathymetry
MAB from Cape Hatteras to Cape Cod. The vertical to horizontal scale exaggeration is 2,000 to 1.

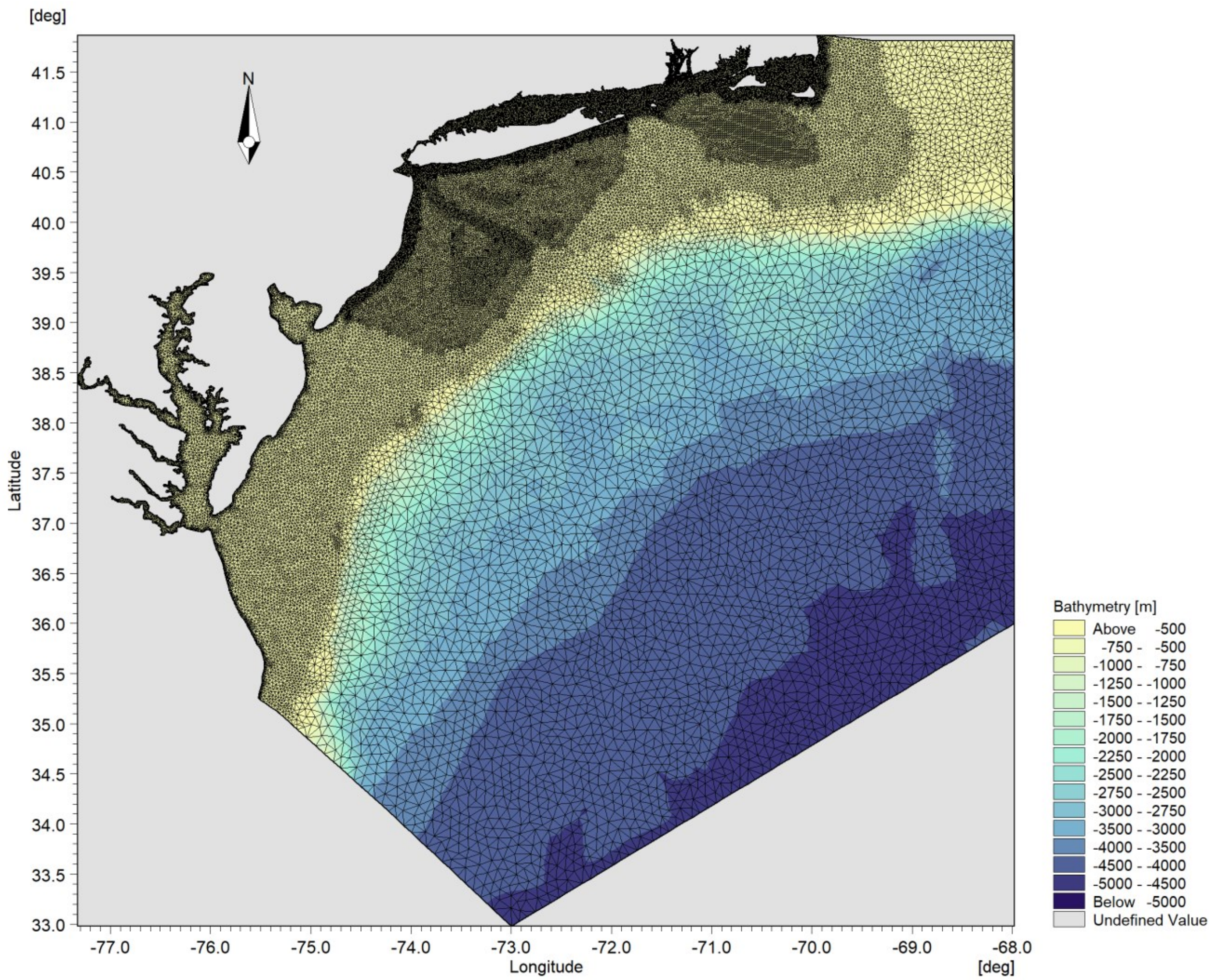

Figure 12. Hydrodynamic model mesh for the HD_{MAB}
The HDM domain covers the MAB from Cape Hatteras to Cape Cod.

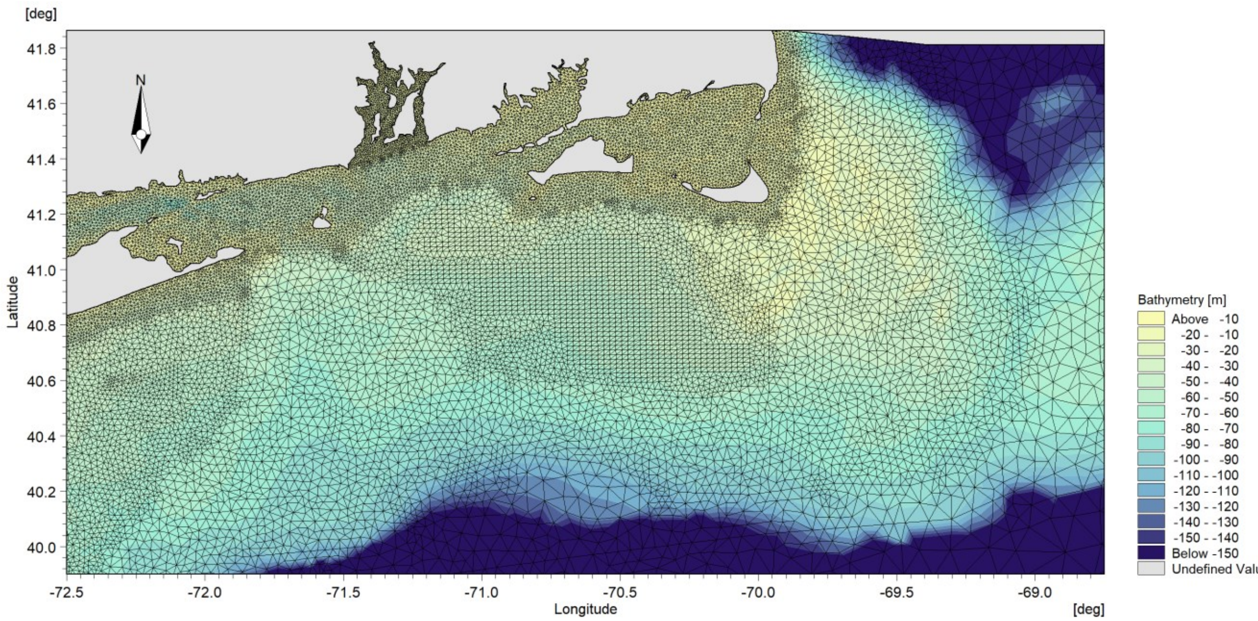

Figure 13. Hydrodynamic model mesh for HD_{MAB}
The figure shows a subarea of the model mesh, zoomed in at the MA-RI area.

The focus of the study was with regards to the impacts due to the OSW development in the MA-RI area. While a local model was not used, plots of results were extracted in the MA-RI focus area generally as shown below in **Figure 14.**

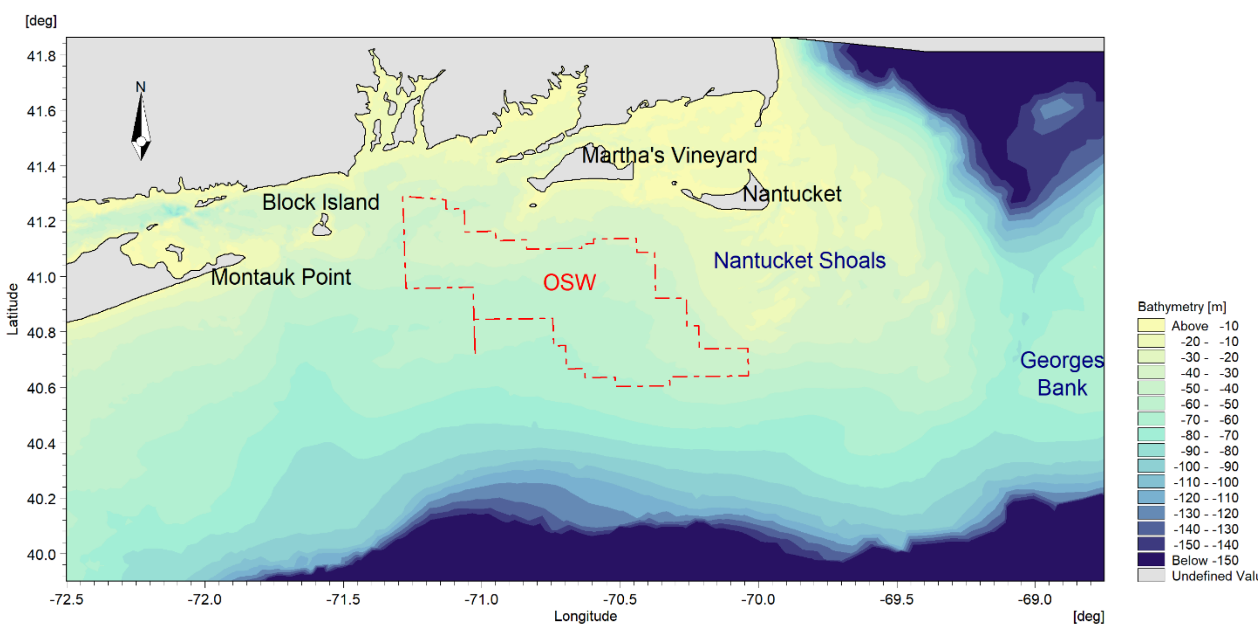

Figure 14. Massachusetts-Rhode Island Offshore Wind Farm study focus area
The extent of a fully built out OSW lease area is included for information.

3.2.2 Current Model (HD_{MAB}) Setup

In this section, some aspects of the model setup including model forcing, domain, parameterizations and their impact on model results are discussed. As mentioned, the currents were modeled using DHI's general marine 3D modeling framework, MIKE 3. MIKE 3 Flexible Mesh Hydrodynamic (MIKE 3 FM HD) model is a hydrostatic full 3D ocean model[2] that uses a semi-implicit finite-volume method with high-order spatial and temporal discretization. It also uses an unstructured flexible mesh and combined sigma-z layer vertical discretization. The flexible mesh allows for efficient focusing of computer resources around the areas of interest, while avoiding unnecessary resolution and computational demands in areas where high resolution is not essential to the problem at hand. The model solves the 3D baroclinic shallow water equations, coupled via an equation of state to heat and salt transport and statistical turbulence parameters described by a k-epsilon model. The model includes all the most relevant physical processes including but not limited to tides, atmospheric forcing (winds, temperature, solar radiation, etc.), density effects, turbulent mixing, river inflows, flooding and drying, etc. **Table 2** below shows the reference model set-up, which was used as a baseline to assess model sensitivity to variations in forcing and in some model parameters as described in the following sections. The baseline model set-up is based on DHI experience on 3D downscaling modeling.

Table 2. Main HDM set-up parameters

Variable / Parameter	Description
Sigma levels	20 levels on the top 100m
z-levels	58 levels, 10m to 500m resolution below the sigma levels, reaching 5,245m in water depth
Time/space discretization	First order
Horizontal eddy viscosity	Smagorinsky formulation, constant = 0.3
Vertical eddy viscosity	k-ϵ model
Bed roughness height	0.1m
Wind friction	Varying with wind speed
Initial condition	Surface elevation from HYCOM model Salinity and temperature from HYCOM
Boundary conditions	Salinity and temperature from HYCOM Current components and surface elevation from combining HYCOM and tidal model
Transport equation solution technique	High order discretization scheme
Number of 2D/3D elements in Regional model	45,473/2,113,751

[2] Full scientific documentation is available upon request or at: https://manuals.mikepoweredbydhi.help/2017/Coast_and_Sea/MIKE_321_FM_Scientific_Doc.pdf .

3.2.2.1 Horizontal Viscosity

The turbulent stresses are modeled using separate approaches for horizontal and vertical directions. Horizontally a Smagorinsky coefficient for eddy viscosity was applied. The factor was increased to assess the impact of a higher viscosity. The coefficient was increased from the recommended value of 0.28 to 0.3. Changes in current speed showed an improvement when compared with measurements. Therefore, the 0.3 value was used for HD model simulations.

3.2.2.2 Heat Exchange

A key to the success of this project was the ability of the 3D HDM to reproduce the annual thermal fluctuations of the region. To achieve this, DHI employed the 3D hydrodynamic heat exchange module. The heat exchange with the atmosphere is calculated in 3D hydrodynamic based on four physical processes:

- Latent heat flux (or heat loss due to vaporization)
- Sensible heat flux (or the heat flux due to convection)
- Net short wave radiation
- Net long wave radiation

Latent and sensible heat fluxes and long wave radiation are assumed to occur at the surface. The following paragraphs describe the methods used in 3D hydrodynamic for the four physical properties. Solar radiation is implemented using an astronomical solar height model, taking into account daylength variations.

3.2.2.2.1 Latent Heat Flux

The absorption profile for the short wave flux is approximated using Beer’s law. The attenuation of the light intensity is described through the modified Beer’s law. Dalton’s law (Sahlberg 1984) was used for the estimation of the evaporative heat loss (or latent flux).

3.2.2.2.2 Sensible Heat Flux

The sensible heat flux (or the heat flux due to convection) depends on the type of boundary layer between the sea surface and the atmosphere. The heat loss due to convection occurs by wind driven forced convection and free convection. The free convection was taken into account by introducing a critical wind speed.

3.2.2.2.3 Net Short Wave Radiation

Radiation from the sun consists of electromagnetic waves with wavelengths from 1,000 to 30,000 Angstroms. Most of this energy is absorbed in the ozone layer leaving only a fraction of the energy to reach the surface of the Earth. Furthermore, the spectrum changes when sunrays pass through the atmosphere. Most of the infrared and ultraviolet compound is absorbed such that solar radiation on Earth consists of light with wave lengths between 4,000 and 9,000 Angstroms. The intensity depends on the distance to the sun, declination angle and latitude, extra-terrestrial radiation and the cloudiness and amount of water vapor in the atmosphere (Iqbal 1983).

3.2.2.2.4 Net Long Wave Radiation

A body or a surface emits electromagnetic energy at all wavelengths of the spectrum. The long wave radiation consists of waves with wavelengths between 9,000 and 25,000 Angstroms. The long wave emittance from the surface to the atmosphere minus the long wave radiation from the atmosphere to the sea surface is call the net long wave radiation and is dependent on the cloudiness, the air temperature, the vapor pressure in the air and the relative humidity. The net outgoing long wave radiation is given by Brunt's equation (Lind and Falkenmark 1972).

3.2.3 Spectral Wave Model Setup

This section describes the wave model developed and used for the present assessment. The data was established through state-of-the-art numerical modeling using MIKE 21 SW Spectral Wave FM model developed by DHI, that simulates the growth, decay and transformation of wind-generated waves and swells in offshore and coastal areas.

DHI's existing database contains long-term wave dataset of US East Coast region that was used as a backbone for this project. The regional US East Coast Wave Model, SWUS-EC, covering from Florida to Nova Scotia has previously been established by DHI (2017), to describe the spatial variation of the waves in the region for the period between 1979 and 2017 at one (1) hourly time interval. The SWUS-EC model uses an unstructured mesh with progressively increasing spatial resolution towards land. For the purpose of this project the model was revised employing higher resolution in the OSW area and extending the model to years 2017 and 2018.

The modeling was performed using state-of-the-art numerical model MIKE 21 SW, which is a 3rd generation WAM model. The SWUS-EC wave model was set up with a fully spectral, in-stationary formulation that is suitable for wave studies involving time-dependent wave events and wind conditions varying rapidly in space and in time. The spectral resolution of the wave model consisted of 25 frequencies and 16 directions. The model used atmospheric forcing from CSFR and the offshore open boundaries were obtained from DHI global model, providing directional spectra.

Table 3. Wave Model set-up parameters

Variable / Parameter	Description
Mesh resolution	See Section 3.2.2
Simulation period	Between February 1, 2017 and March 1, 2018, 1 hour interval
Basic equations	Fully spectral, in-stationary
Discretization	25 frequencies, period ranging from 0.9 to 33s. 16 directions
Time step (adaptive)	0.01-3600s with a maximum time-step factor of 32
Water level	2D HDLOC (temporally and spatially varying)
Wind forcing	CFSR wind
Wave breaking	Included, Specified Gamma, $\gamma = 0.8$, $\alpha = 1$
Bottom friction	Nikuradse, equivalent roughness 0.001 m
White-capping	Cdis = 2.1, DELTAdis =0.7
Boundary conditions	2D spectra varying in time and along line from SWUS-EC
Dimensional growth	1.4

3.3 Baseline Validation

This section presents an overview of the final model set-up performance when compared with measurements. Model and measured data are compared in a one-to-one fashion as time series, scatter plots, current rose plots, and frequency of occurrence plots, as appropriate. The skill assessment and comparison between model and observations is made using statistical methods, that are described in detail in in **Appendix A.1**. It should be noted that for the present purpose the normal conditions are the most important, as this will affect migration routes etc. more than the extreme events.

3.3.1 Baseline Current Validation

In the study focus area the current validation was quite good. Farther offshore the currents did not match as well. This was expected as the north-south location of the offshore return current is difficult to locate in time and space in any HD modeling exercise. For a regional impact assessment, the current is essentially "integrated" by the larvae "particles" and therefore the effects of small differences in maxima are effectively evened out so that the comparisons with and without the OSW structures can be used with confidence.

The following current plots (time series, current rose, frequency of occurrence and scatter plot) are of the Orsted OR-F180 current profiler mooring (Orsted 2020). The results compared were at a depth of 5m below the surface. The comparison between model and measurement was quite good, as indicated in the timeseries in **Figure 15**. This current measurement location is also quite close to the OSW development area, so provides confidence in the overall model performance.

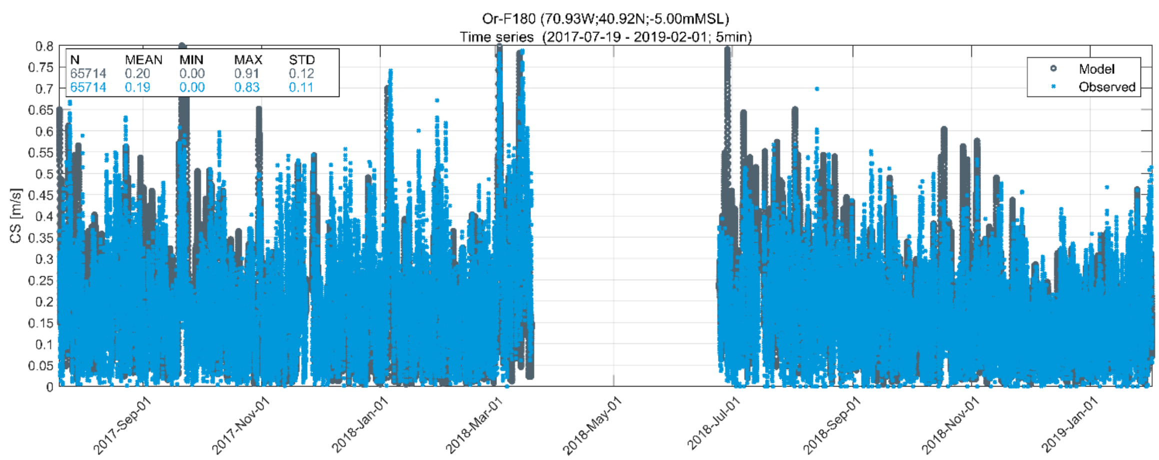

Figure 15. Validation of model results using Orsted OR-F180 ADCP current time series
Comparison of time series measurement (blue) against model results (gray), from July 2017 to February 2019.

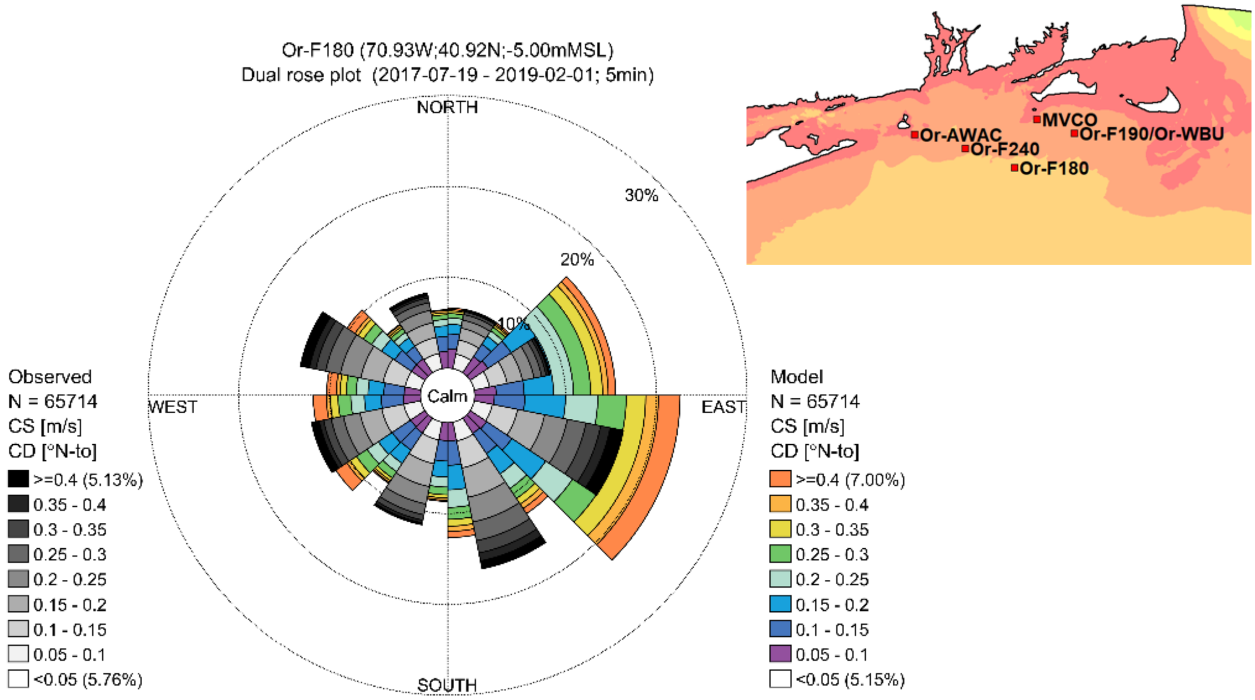

Figure 16. Validation of model results using Orsted OR-F180 ADCP rose plots
Comparison is performed between Orsted OR-F180 ADCP current rose measurement (gray) and model results (colored scale), for data from July 2017 to February 2019.

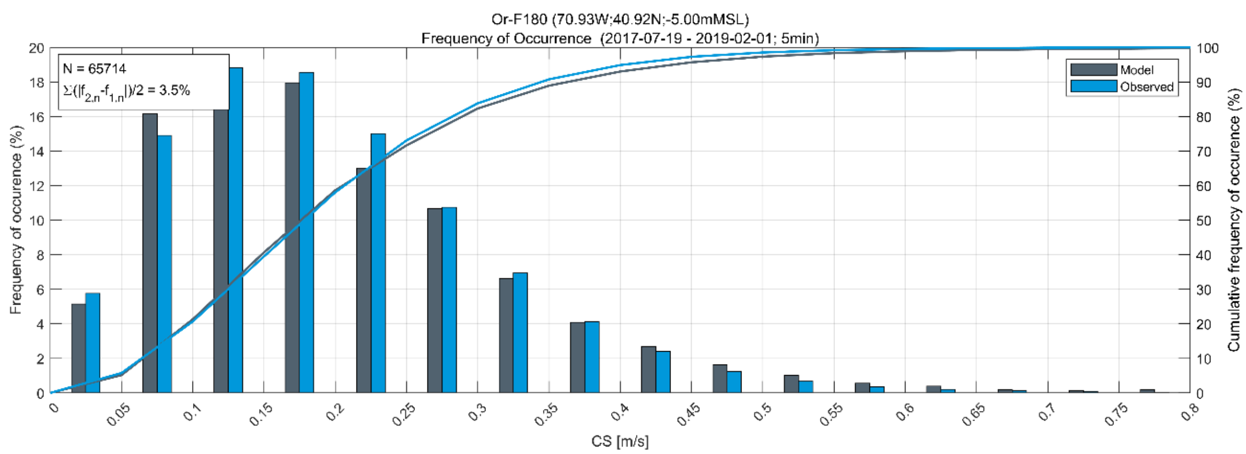

Figure 17. Validation of model results by frequency of occurrence using Orsted OR-F180 ADCP measurements
Orsted OR-F180 ADCP frequency of occurrence measurement (blue line) is compared against that of the model results (gray line) for measurements collected between July 2017 and February 2019.

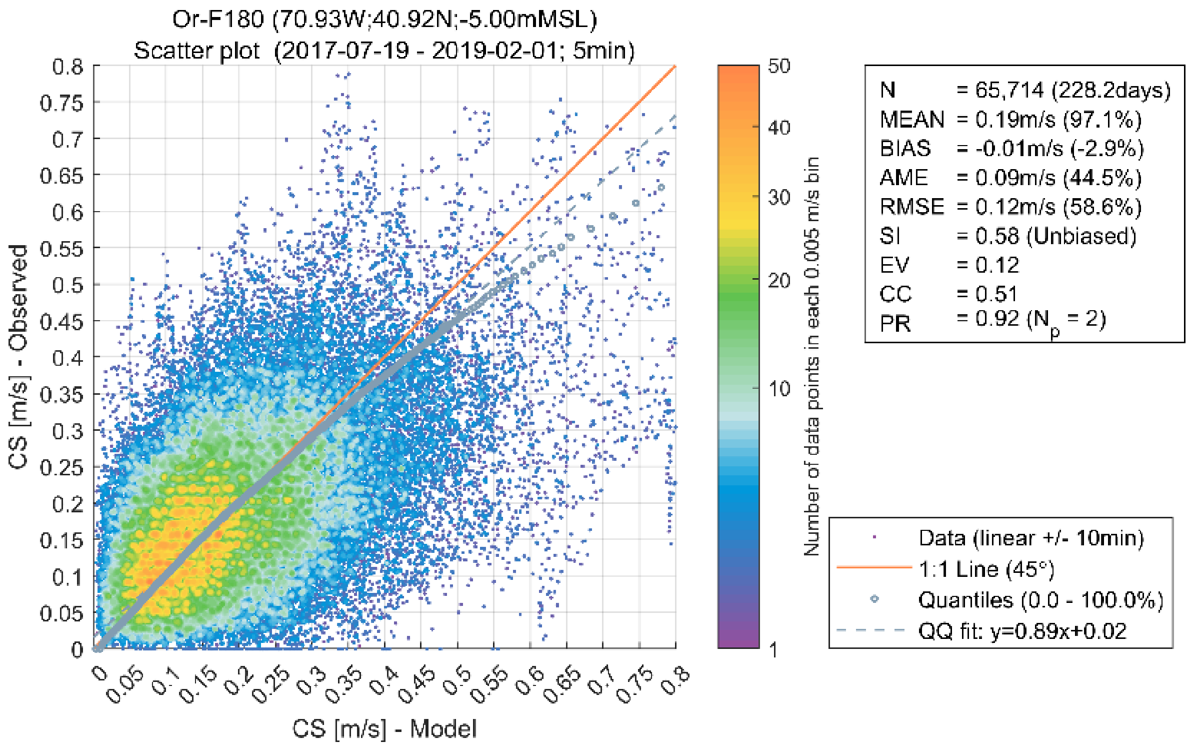

Figure 18. Comparison of Orsted OR-F180 ADCP scatter plot of measurement against model results/

The dots indicate individual datapoints, the color indicate point-density. The grey line is the quantile-quantile (QQ) line, the red line indicates perfect agreement.

The scatter plot in **Figure 18** shows the measured (horizontal axis) and modeled (vertical axis) parameter. These figures also include some statistics quantifying the accuracy of the modeled parameter such as the bias and absolute mean error. The frequency of occurrence plot in **Figure 17** shows the % frequency of occurrence (vertical scale) vs a histogram (horizontal axis) of the measured parameter. The time series and frequency of occurrence plots show both measured (grey) and modeled (blue) measured parameter. They also include some statistics such as maximum value, and standard deviation for each time series. The current rose in **Figure 16** show both measured (grey) and modeled (colored) measured parameter.

Similar ADCP current validation plots from other locations and depths of measurement vs model results are presented in **Appendix A.2.1**.

In addition to the ADCP measurements regional High-frequency radar observations (HFRO) or CODAR surface current measurements were available for the time frame modeled. The measurements made by the HFRO are truly surface current measurements as the instrument measures the doppler shift of surface ripples on the water. It should also be understood that comparing the CODAR measurements where the instrument is sensing the top few millimeters of the water surface to an HD model where the top layer has a finite thickness that is on the order of 5 meters is in some ways qualitative. Nevertheless, the ability to review the regional and within-the-study-area current patterns using the HFRO measurements was too enticing to overlook. The HFRO data was downloaded from the MARACOOS site (Roarty 2020) for the years of interest and transformed so that the scalar averages of the current speed could be directly compared to the HD model output. The figures below show the comparison of the full-time frame of the study with both the regional model and then an increased resolution plot on the study area using the same data. The results show a good comparison at both spatial scales. Take note of the higher currents over the Nantucket sill to the east and South East of Nantucket Island.

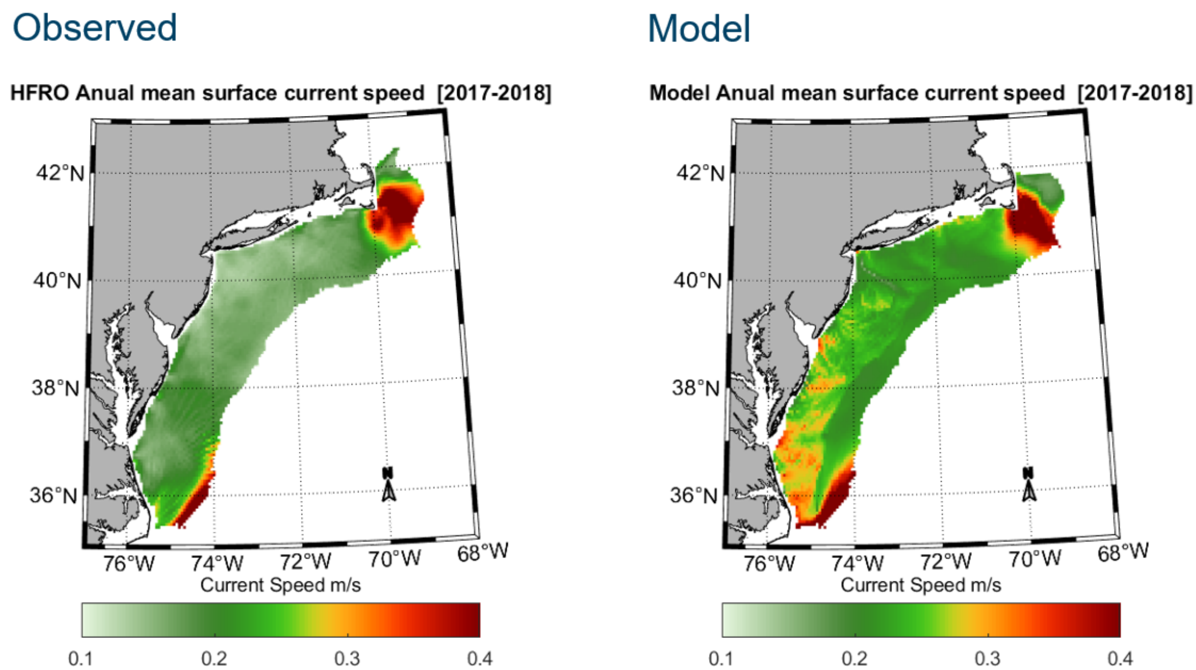

Figure 19. Average High Frequency Radar Observation (HFRO) and model results in the MAB
Observed vs. model for the full regional model where measurements exist averaged over 2017 and 2018

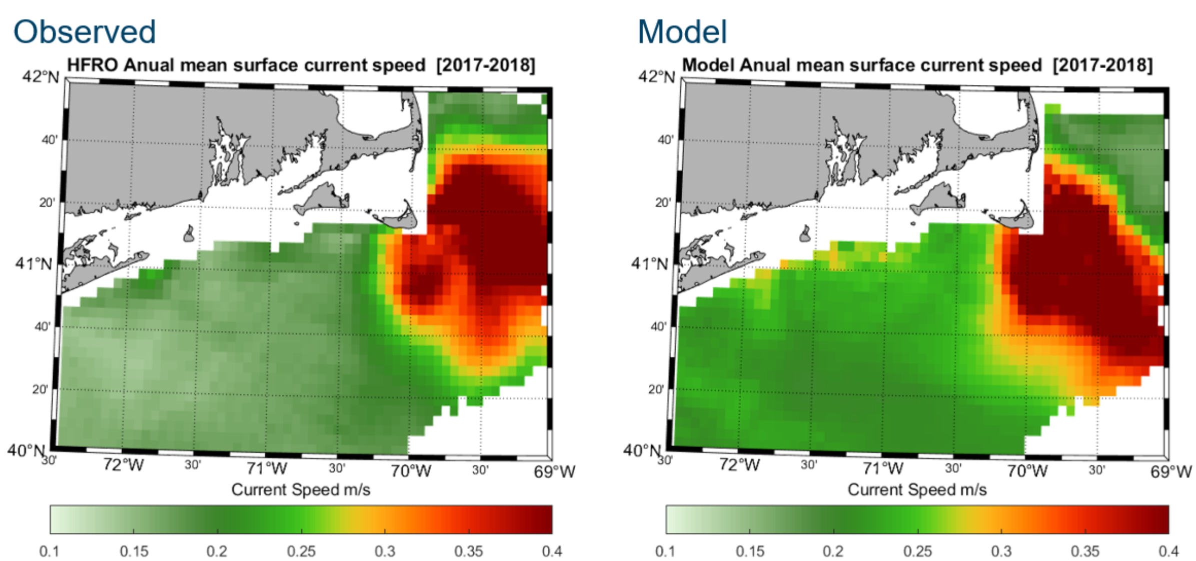

Figure 20. Average High Frequency Radar Observation (HFRO) and model results in the study area
Observed vs. model in the OSW study area averaged over 2017 and 2018. Note the broad agreement between the HFRO and model results. Also note the higher currents over the Nantucket sill to the East and South East of Nantucket Island.

3.3.2 Baseline Wave Validation

The following wave plots (time series, wave rose, frequency of occurrence and scatter plots) are taken from the Nantucket, MA station (NDBC 44008). The comparison between model and measurement were quite good. This measurement location is one of the two closest to the OSW development area, so provides confidence in the overall model performance.

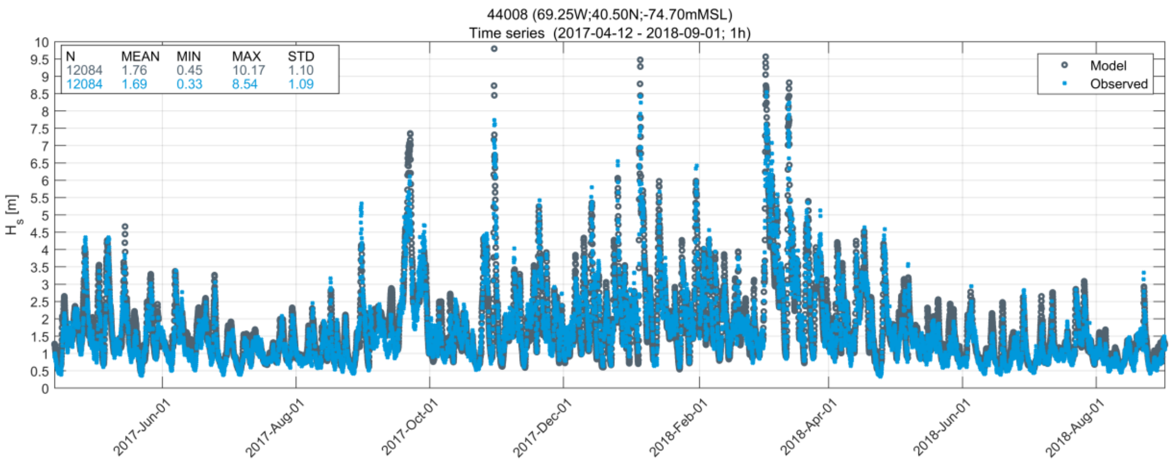

Figure 21. Validation of model results using Nantucket wave time series
Comparison of time series measurement (blue) against model results (gray), from April 2017 to September 2018.

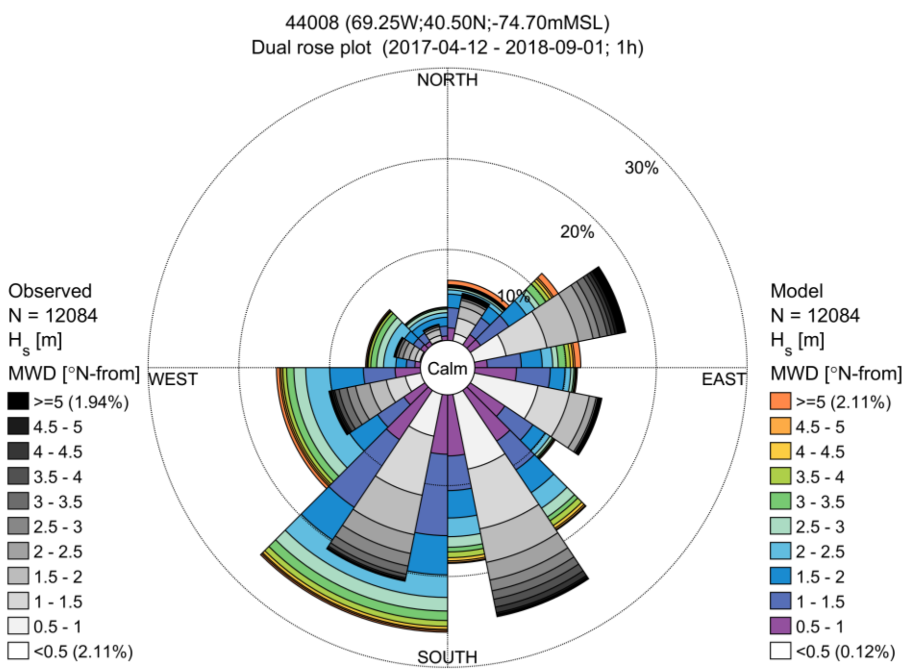

Figure 22. Validation of model results using Nantucket station rose plots
Comparison is performed between Nantucket mean wave direction rose measurement (gray) and model results (colored scale), for data from April 2017 to September 2018.

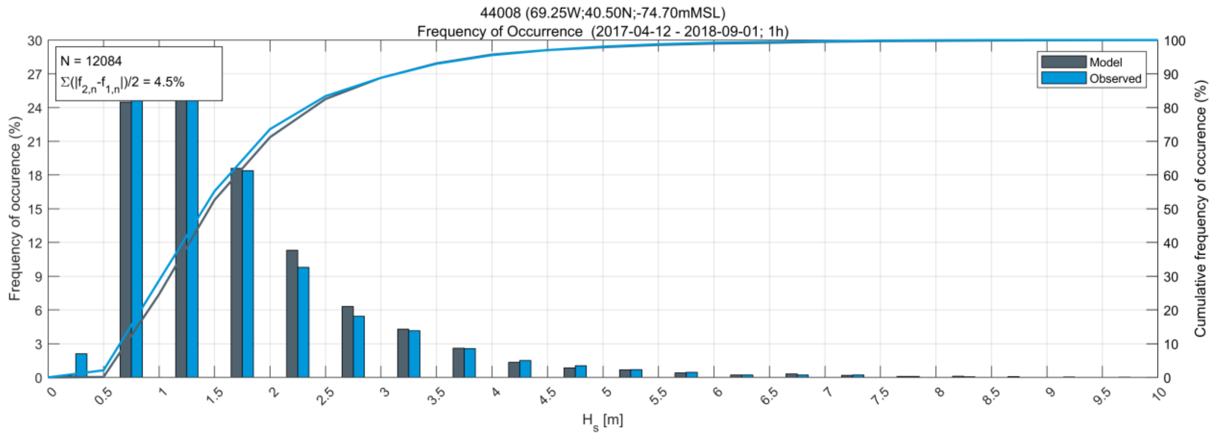

Figure 23. Validation of model results by frequency of occurrence using Nantucket station measurements
Nantucket wave H_{m0} frequency of occurrence measurement (blue line) is compared against that of the model results (gray line) for measurements collected between April 2017 and September 2018.

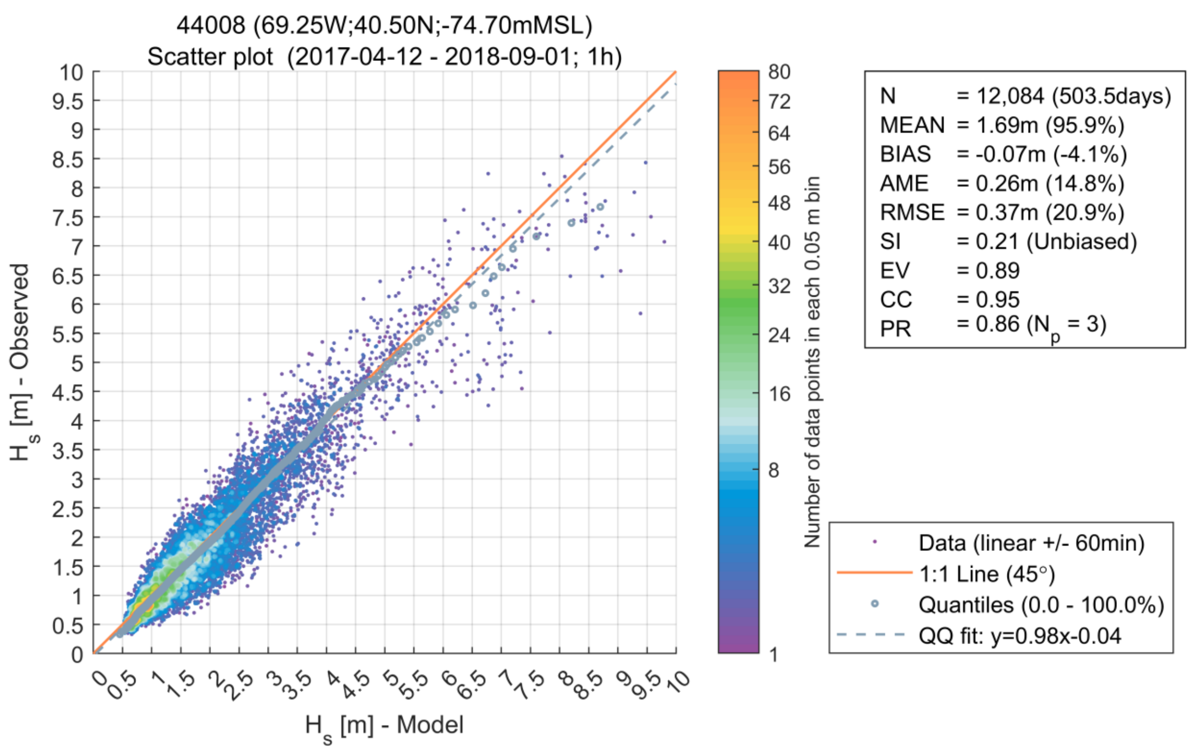

Figure 24. Comparison of Nantucket wave H_{m0} scatter plot of measurement against model results
The dots indicate individual datapoints, the color indicate point-density. The grey line is the quantile-quantile (QQ) line, the red line indicates perfect agreement.

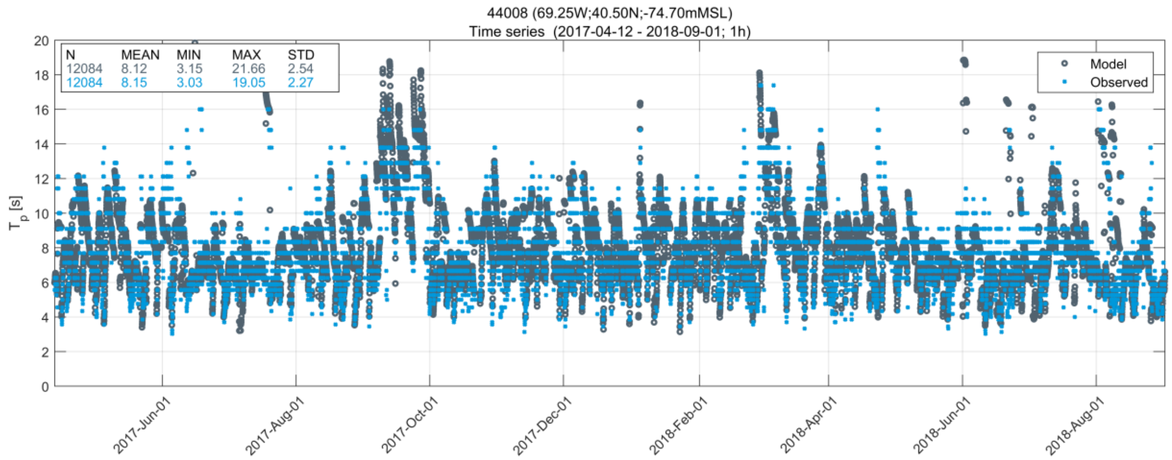

Figure 25. Validation of model results using Nantucket peak wave period time series
Comparison of peak wave period time series (blue) against model results (gray), from April 2017 to September 2018.

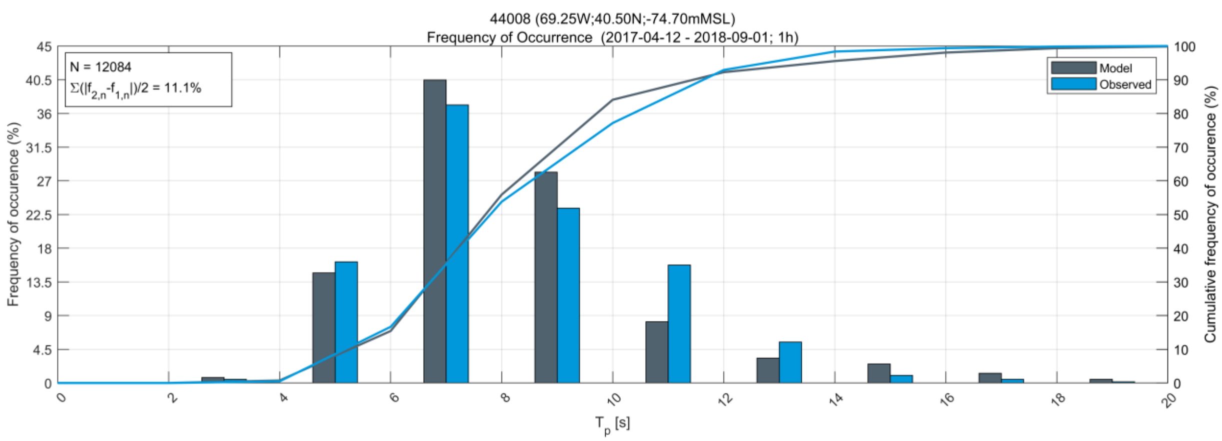

Figure 26. Validation of model results by frequency of occurrence measurement using Nantucket station peak wave period measurements
Nantucket wave peak wave period frequency of occurrence measurement (blue line) is compared against that of the model results (gray line) for measurements collected between April 2017 and September 2018.

Wave validation plots of measurements at Block Island vs model results are presented in **Appendix A.2.2**.

3.3.3 Baseline Water Level Validation

The following water level plots (time series, frequency of occurrence and scatter plot) are taken from the Nantucket Island, MA station. The comparison between model and measurement were quite good. This measurement location was the closest to the OSW development area, so provides confidence in the overall model performance.

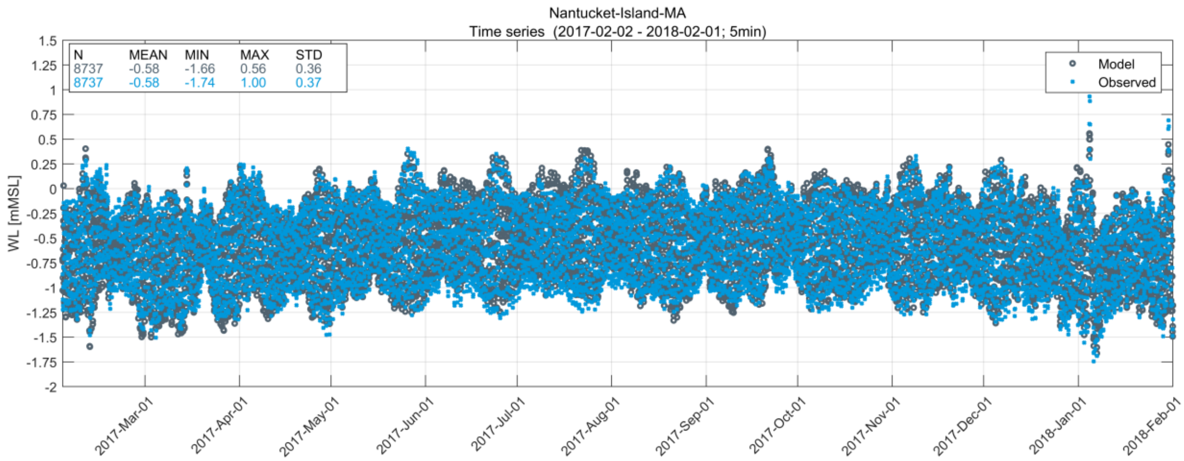

Figure 27. Validation of model results using Nantucket Island water level time series
Comparison of time series measurement (blue) against model results (gray), from February 2017 to February 2018.

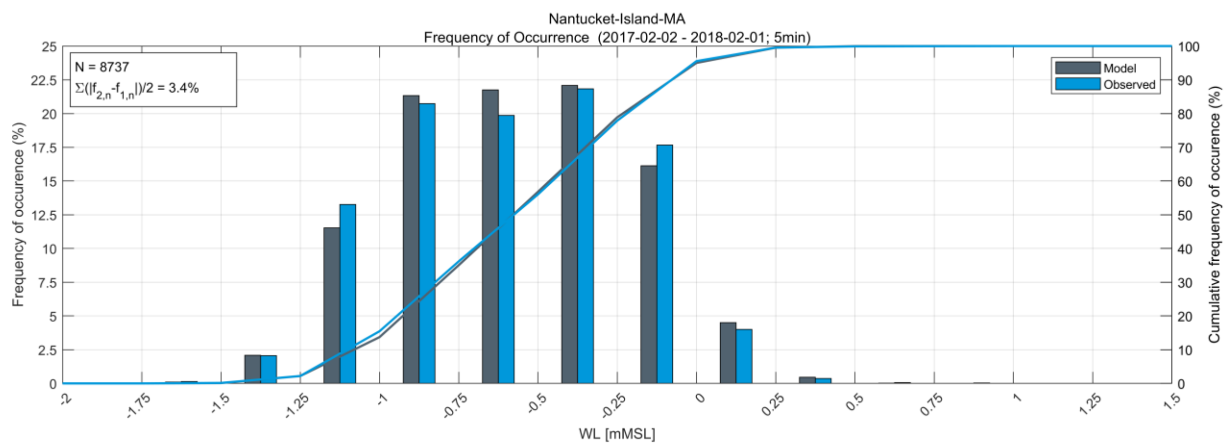

Figure 28. Validation of model results by frequency of occurrence using Nantucket Island water level measurements
Nantucket Island water level frequency of occurrence measurement (blue line) is compared against that of the model results (gray line) for measurements collected between February 2017 and February 2018.

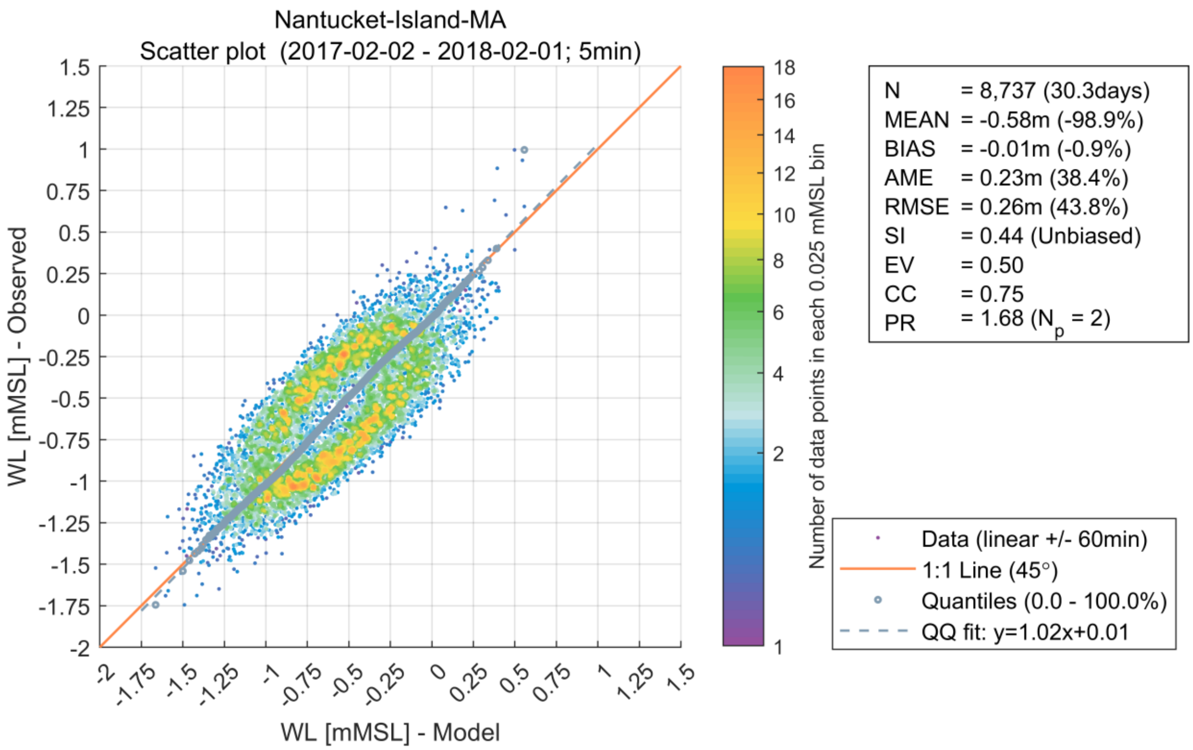

Figure 29. Comparison of Nantucket Island water level scatter plot of measurement against model results

The dots indicate individual datapoints, the color indicate point-density. The grey line is the quantile-quantile (QQ) line, the red line indicates perfect agreement.

More water level validation plots of measurement vs model results are presented in **Appendix A.2.3**.

3.3.4 Baseline Temperature Validation

The following sea temperature plots (time series, frequency of occurrence and scatter plot) are taken from the Block Island, RI station. The comparison between model and measurement were quite good. This measurement location was the closest to the OSW development area, so provides confidence in the overall model performance.

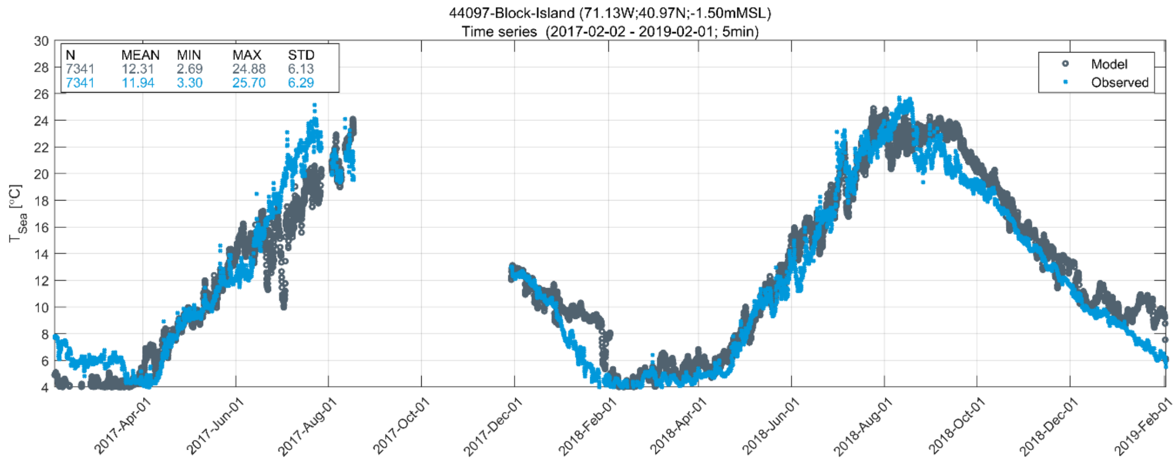

Figure 30. Validation of model results using Block Island sea temperature time series
Comparison of time series measurement (blue) against model results (gray), from February 2017 to February 2019.

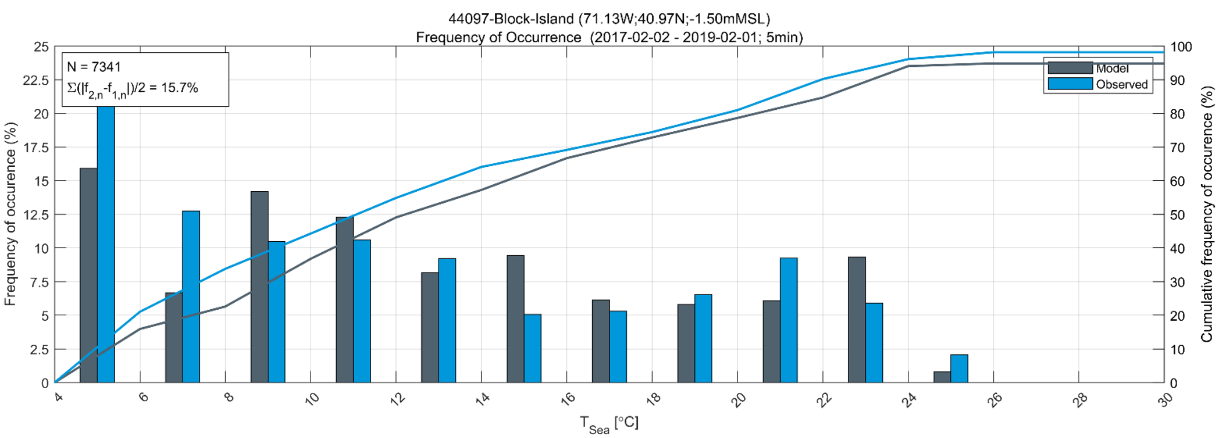

Figure 31. Validation of model results by frequency of occurrence using Block Island sea temperature measurements
Block Island sea temperature frequency of occurrence measurement (blue line) is compared against that of the model results (gray line) for measurements collected between February 2017 and February 2019.

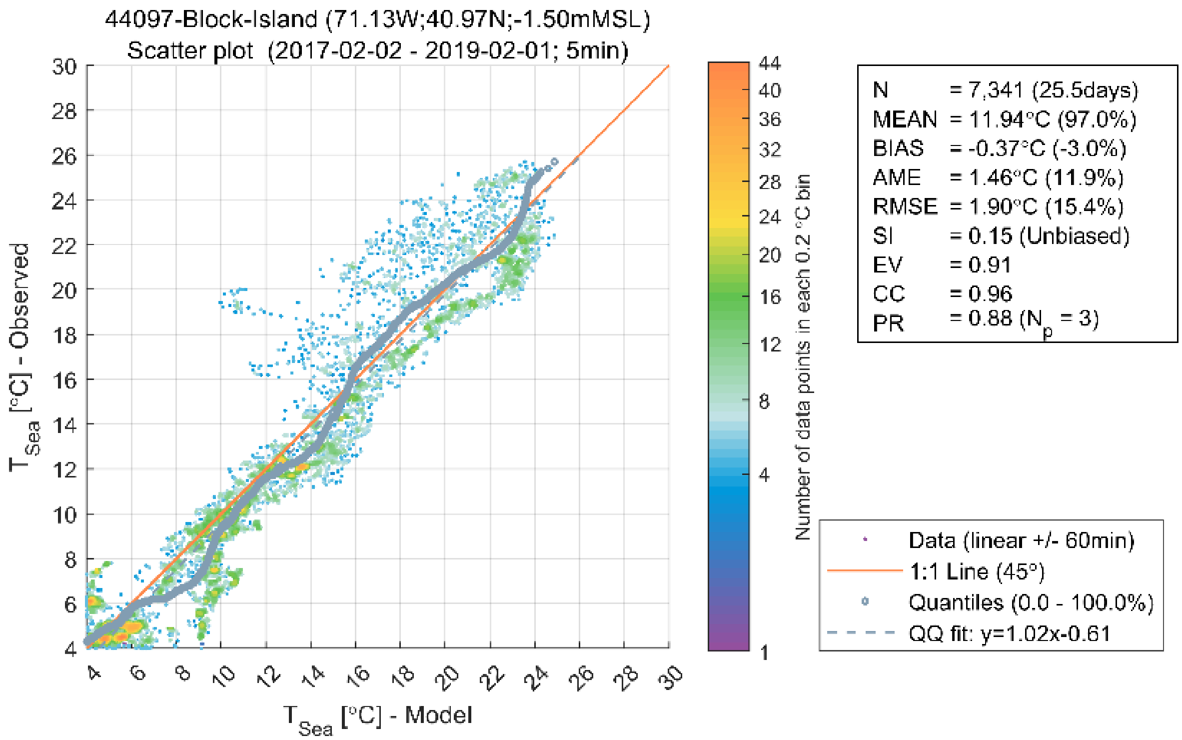

Figure 32. Comparison of Block Island sea temperature scatter measurement against model results

The dots indicate individual datapoints, the color indicate point-density. The grey line is the quantile-quantile (QQ) line, the red line indicates perfect agreement.

More temperature validation plots from measurement stations on NDBC buoys vs model results are presented in **Appendix A.2.4**.

In addition to point location validation, comparison to satellite imagery snapshots of the region was also completed. The satellite images were obtained from Physical Oceanography Distributed Active Archive Center website[3] based on the Operational Sea Surface Temperature and Sea Ice Analysis (OSTIA) analysis. OSTIA is part of the UK Met Office GHRSST (Group for High Resolution Sea Surface Temperature) Level 4 sea surface temperature analysis, which includes signals from several advanced sensors. The OSTIA analysis has a highly smoothed Sea Surface Temperature (SST) field and was specifically produced to support SST data assimilation into Numerical Weather Prediction models.

Figure 33 below is a comparison of the sea surface temperature for the full regional model domain on the 1st of October 2017 versus the OSTIA analysis of the satellite imagery. The color scale is identical on the two plots. The qualitative agreement on a regional scale is quite good. The Gulf Stream is the red thermal image on the lower left of the two plots.

---

[3] https://podaac.jpl.nasa.gov/dataset/UKMO-L4HRfnd-GLOB-OSTIA

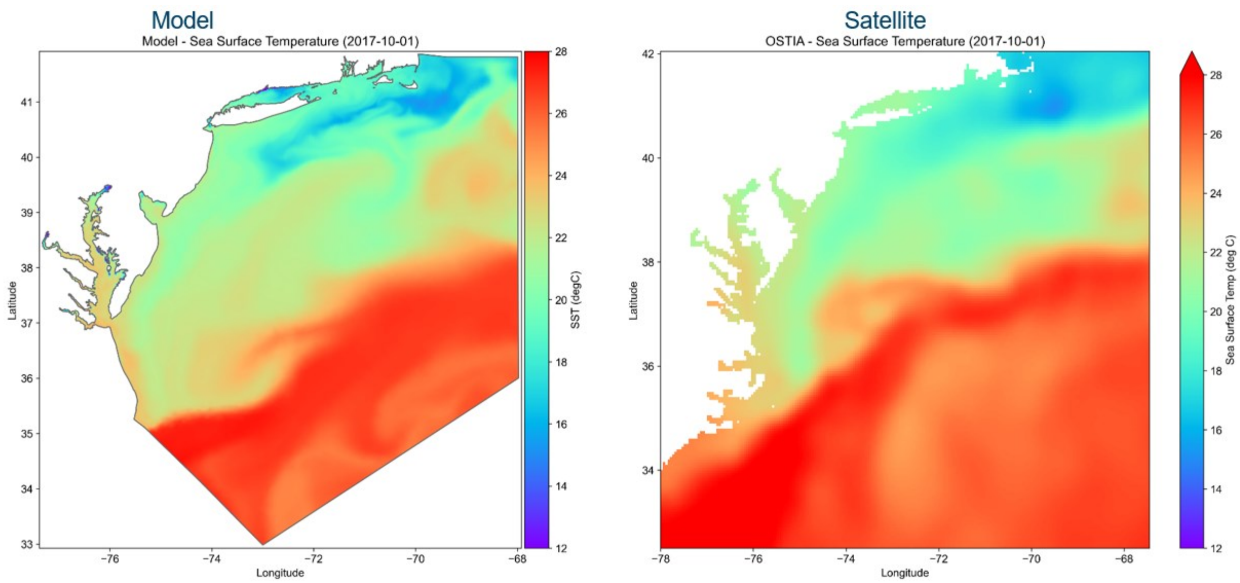

Figure 33. Sea surface temperature: model (left) and OSTIA satellite analysis (right)
Snapshots are displayed for sea surface temperature on October 01, 2017.

More temperature validation plots from the OSTIA satellite analysis vs model results are presented in **Appendix A.2.4**.

The general oceanography and ecology of the region is significantly influenced by the Cold Pool in the MAB. The Cold Pool is a thick band of cold water resting mid-shelf from George Bank to MAB in the lower 20 to 60m of the water column, that persists warming during spring to fall. This is due to the vertical stratification, effectively insulating the bottom from the surface waters, (Lenz 2017). Historical temperature profiles are used to characterize the average annual evolution and spatial structure of the Cold Pool. A comparison was made of the model results to the average historical measurements presented in Lentz (2017) as shown in the figures below. Note that the model broadly follows the monthly seasonal average measurements. However, it should be noted that the Lentz (2017) plots are composites of surveys over many years over a large geographical area between the Longitudes of 69°W and 73°W.

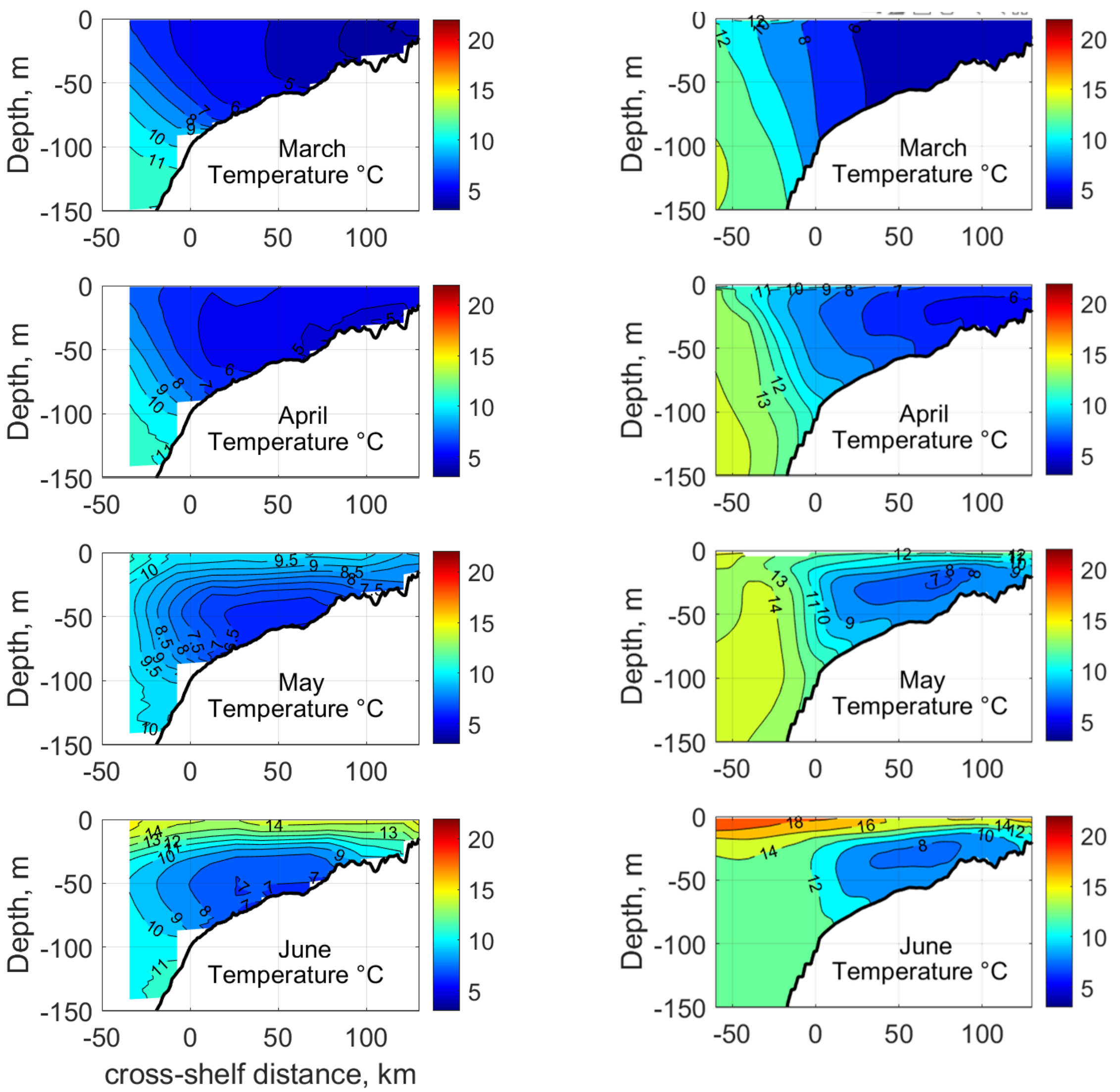

Figure 34. Average temperature transects March to June (Lentz 2017) on left / Model results on right

Average temperature sections across the New England Shelf for the months of March through June showing the Cold Pool bounded above by the seasonal thermocline and offshore by warmer slope water.

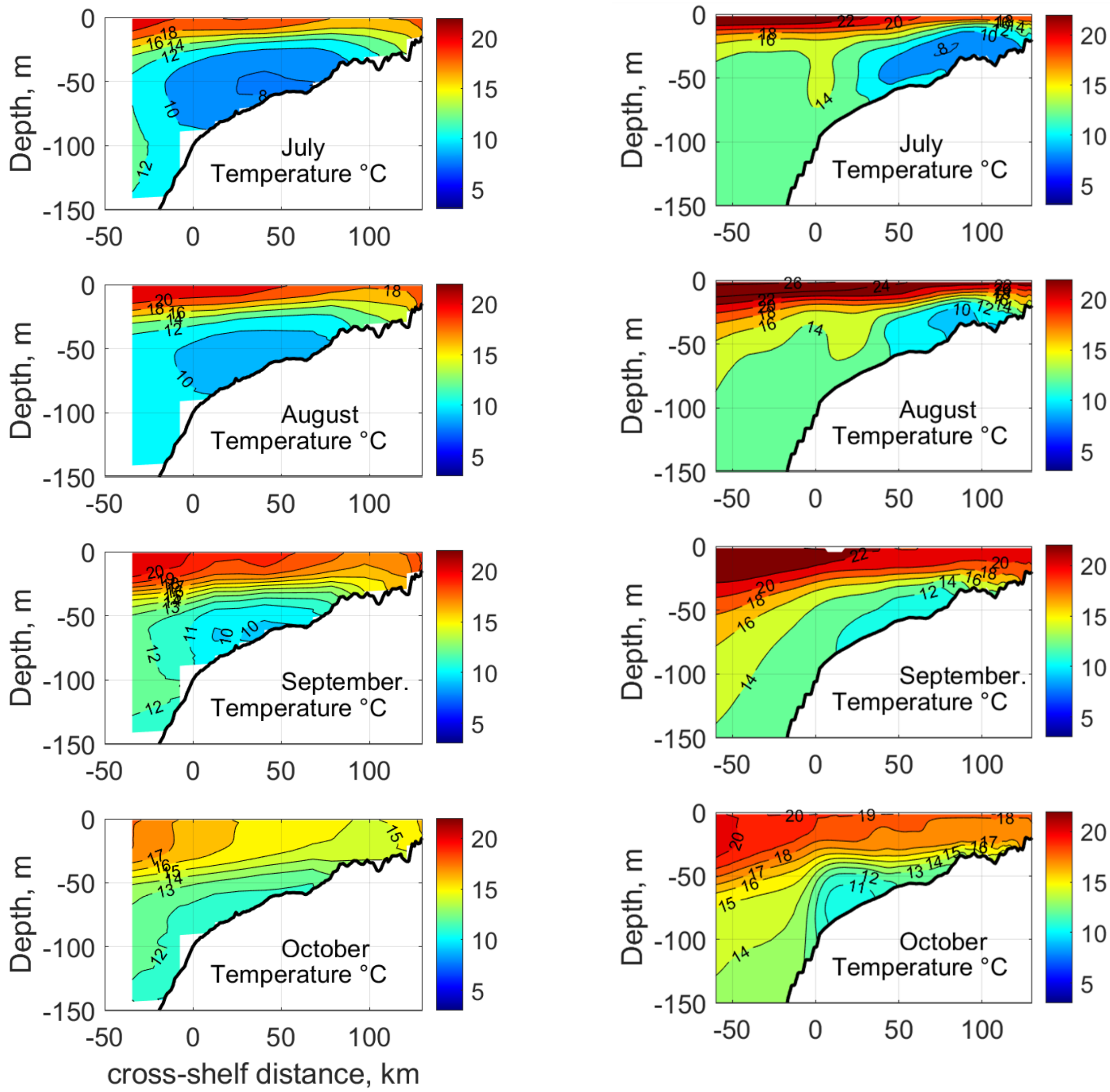

Figure 35. Average temperature transects July to October (Lentz 2017) on left / Model results on right
Average temperature sections across the New England Shelf for the months of July through October showing the Cold Pool bounded above by the seasonal thermocline and offshore by warmer slope water.

Lentz (2017) provided the authors the average temperature sections across the New England Shelf for the months of March through October showing the Cold Pool bounded above by the seasonal thermocline and offshore by warmer slope water. The Lentz plots are temperature contours taken from multiple representative profiles taken between 69°W and 73°W and consolidated using a typical bathymetric transect across the New England shelf. The data for the Lentz profiles were collected between 1955 and 2014. The plots are comprised of between 8,000 and 10,000 temperature profiles per month between March and October.

In addition to the cross-shelf transects, a series of monthly average temperatures transects for 2017 and 2018 from South West to North East connecting the physical NDBC measurement points of Barnegat, Long Island, Montauk Point, Block Island and Nantucket Sound are presented in the following figures to provide a longitudinal transect overview of the behavior of the Cold Pool from March through October as simulated in the model.

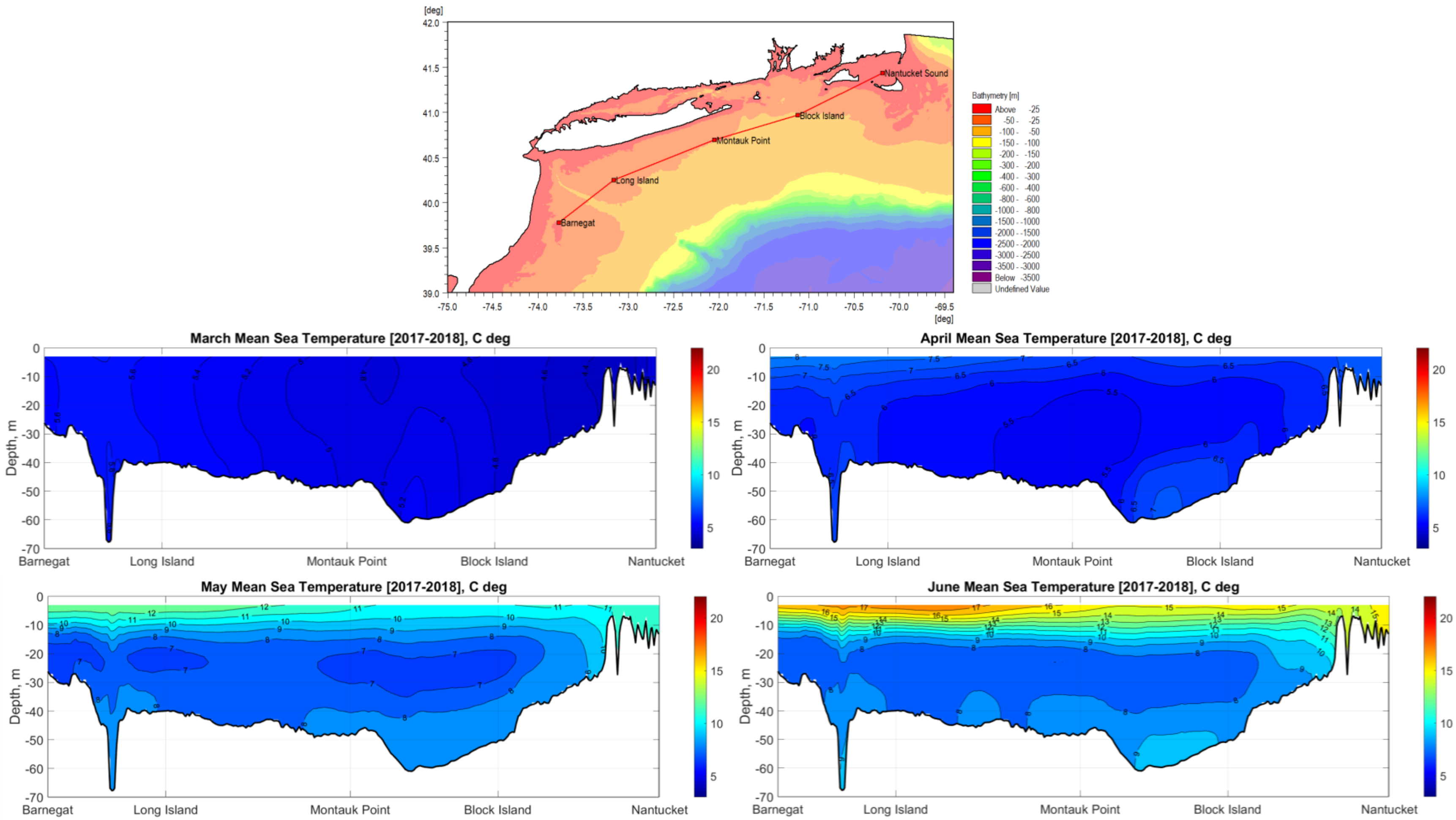

Figure 36. Average model temperature SW to NE transects from March to June
Average temperature connecting NDBC measurement points of Barnegat, Long Island, Montauk Point, Block Island and Nantucket Sound for the months of March through June showing the Cold Pool bounded above by the seasonal thermocline and offshore by warmer slope water.

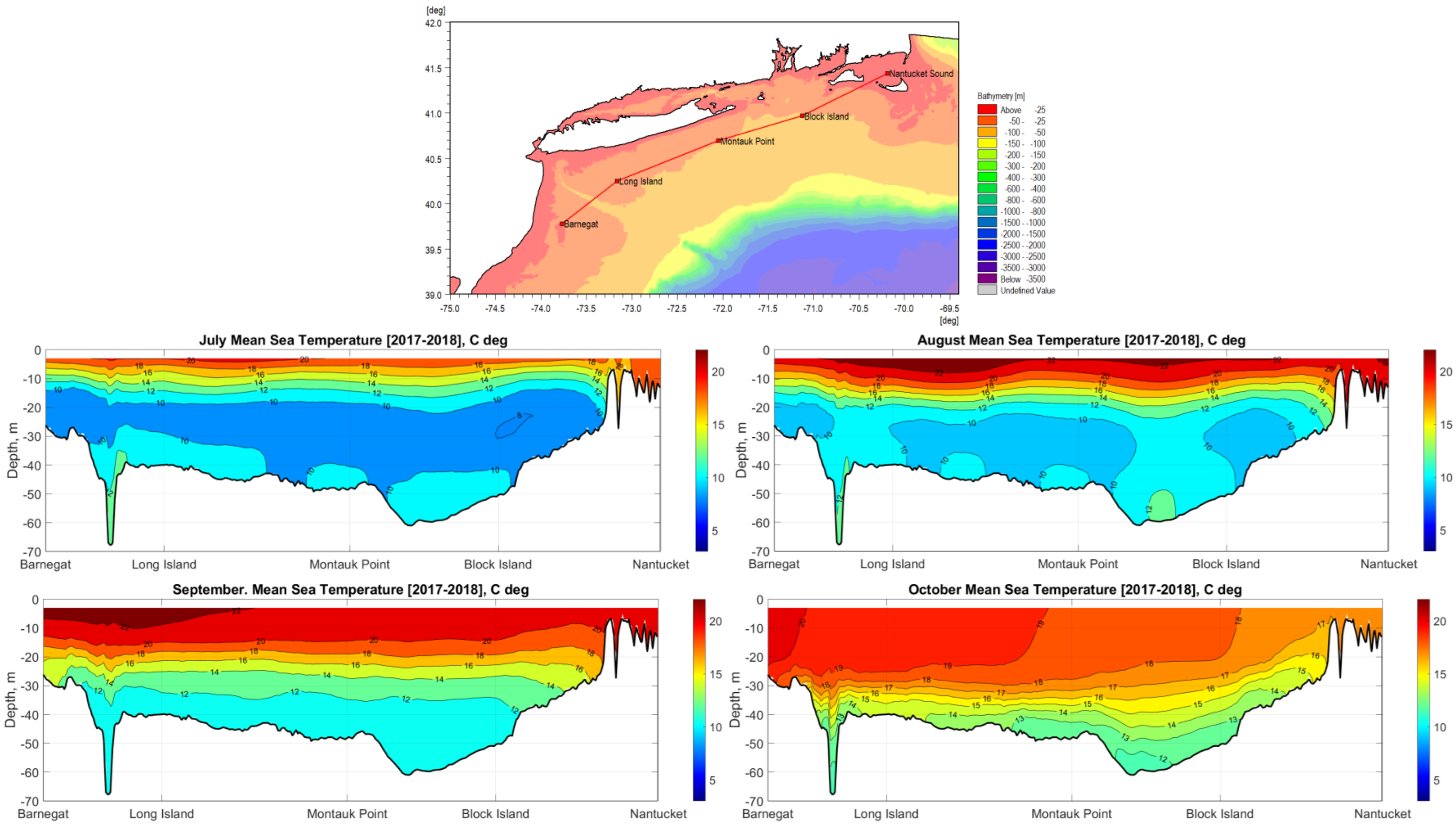

Figure 37. Average model temperature SW to NE transects from July to October
Average temperature connecting NDBC measurement points of Barnegat, Long Island, Montauk Point, Block Island and Nantucket Sound for the months of July through October showing the Cold Pool bounded above by the seasonal thermocline and offshore by warmer slope water.

One of the oceanographic characteristics of the MAB is the stratification that occurs in the Summer. This was discussed above in **Section 3.1**. The model was queried for the same salinity structure as discussed previously. The results were not as dramatic in the model for whole of the MAB, but the stratification observed in the local area of interest was slightly more stratified in the model compared to as reported by O'Reilly and Zetlin (1998) as shown in the figures below.

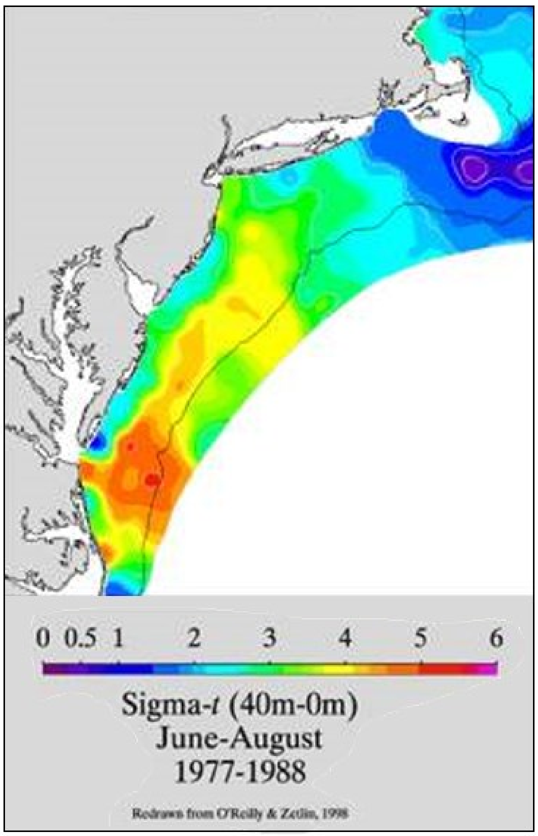

Figure 38. Stratification observations from O'Reilly & Zetlin (1998) June-August 1977-1988
Regional differences in summer stratification, showing strongly stratified areas (indicated by red, orange, and yellow colors) in the MAB. (Credit: NOAA)

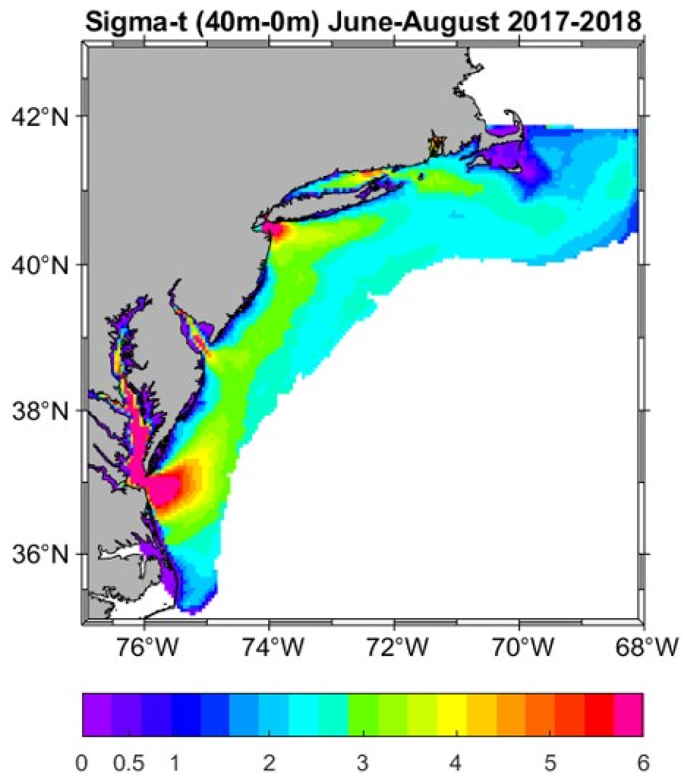

Figure 39. Model stratification structure of the MAB June-August 2017-2018
This plot shows the stratification structure in the model. Stronger stratification is noted off Chesapeake Bay than in the O'Reilly & Zetlin observations with slightly more stratification in the MA-RI study area and less offshore DE, NJ, and NY.

As reported in the above, sigma-t is a quantity used in oceanography to measure the density of seawater at a given temperature. σT is defined as ρ(S,T)-1000 kg m^{-3}, where ρ(S,T) is the density of a sample of seawater at temperature T and salinity S, measured in kg m^{-3}, at standard atmospheric pressure.

4 Hydrodynamic Model Methodology Including Wind Turbines

4.1 Overview

The following section describes the methodology employed to model the OSW in the simulations. The wind turbine locations and physical parameters for each scenario are outlined. The method of estimating the losses and mixing due to the monopile foundations is described. The wind wake loss model is also recounted and the effects on the currents and waves explained.

4.1.1 Offshore Wind Farm Scenarios

As noted in **Section 1.2** Project Scenarios and Decisions the scenarios studied included:

- Scenario 1 (Baseline): 0 towers
- Scenario 2 (12 MW, Full Build-out): 1,063 towers
- Scenario 3 (OCS-A 0501, 12 MW turbines): 197 towers
- Scenario 4 (15 MW, Full Build-out): 1,063 towers
- Scenario 5 (12 MW, Mid-level): 766 towers

The following figures show the location of the OSW turbine foundations for each of the Scenarios 2 through 5. It should be noted that Scenario 2 and Scenario 4 have the same foundation locations, just different diameter monopiles. The spacing of adjacent OSW turbine foundations was 1 nautical mile (1,852 m) by 1 nautical mile (1,852 m) in all scenarios.

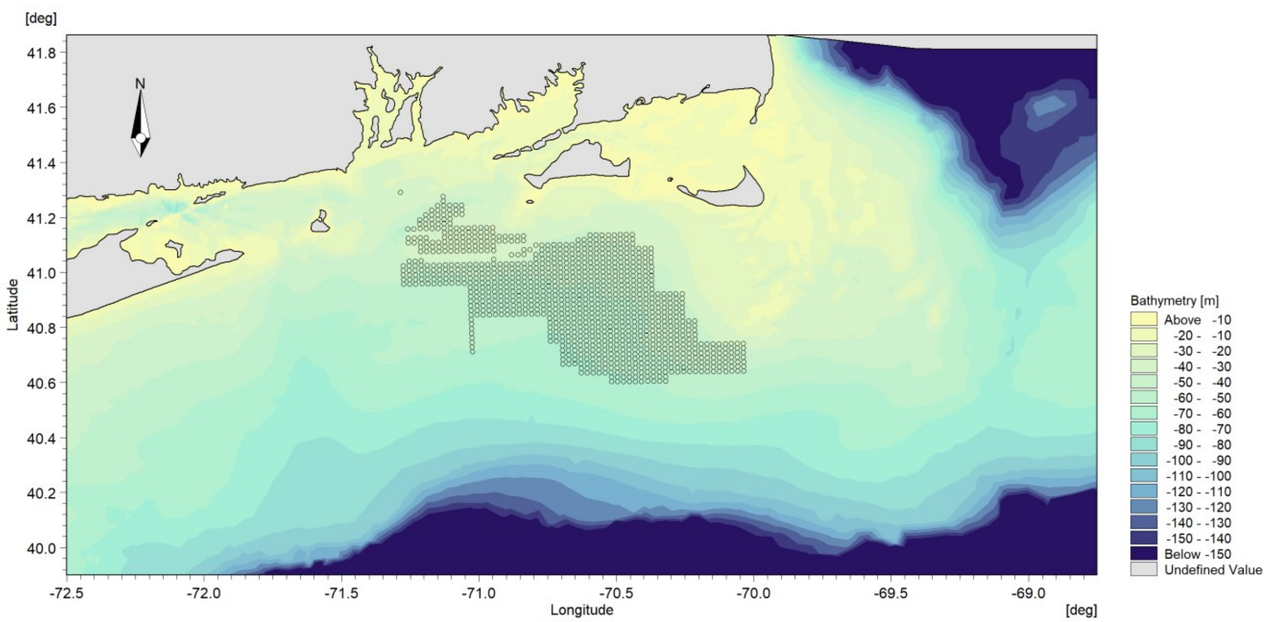

Figure 40. Foundation locations for Scenario 2 and Scenario 4: 1,063 towers
Gray circles indicate the footprint of the OSW build-out for 12 MW full build-out and 15 MW full build-out scenarios.

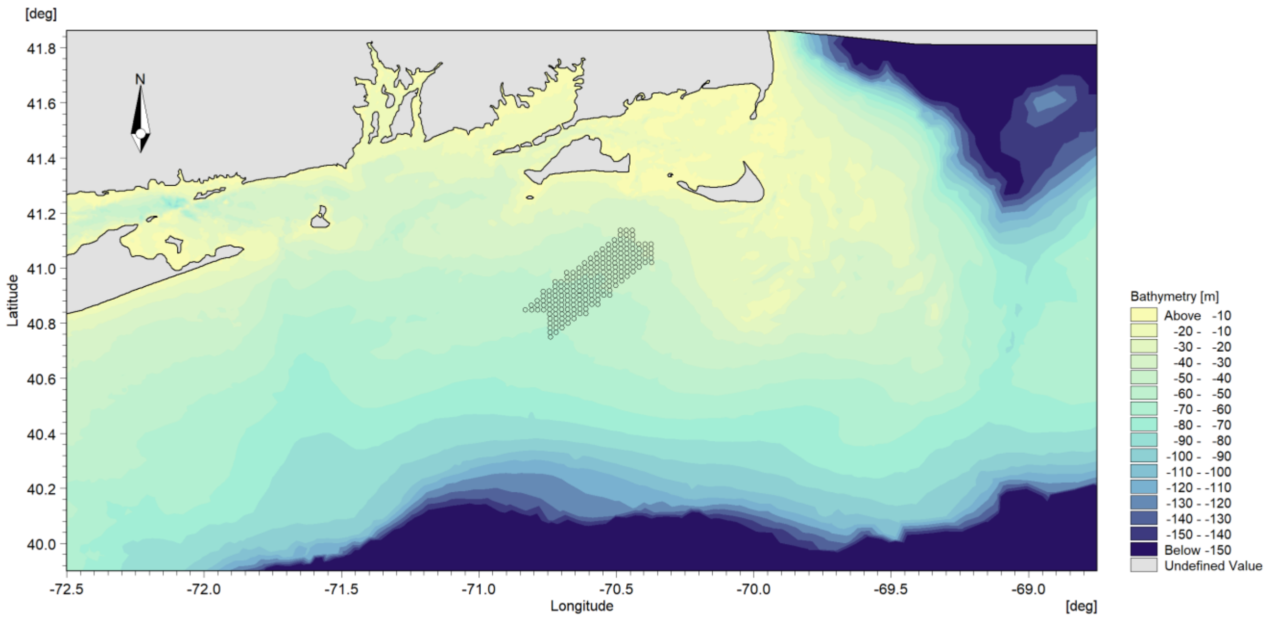

Figure 41. Foundation locations for Scenario 3: 197 towers
Gray circles indicate the footprint of the OSW build-out for OCS-A 0501, 12 MW scenario.

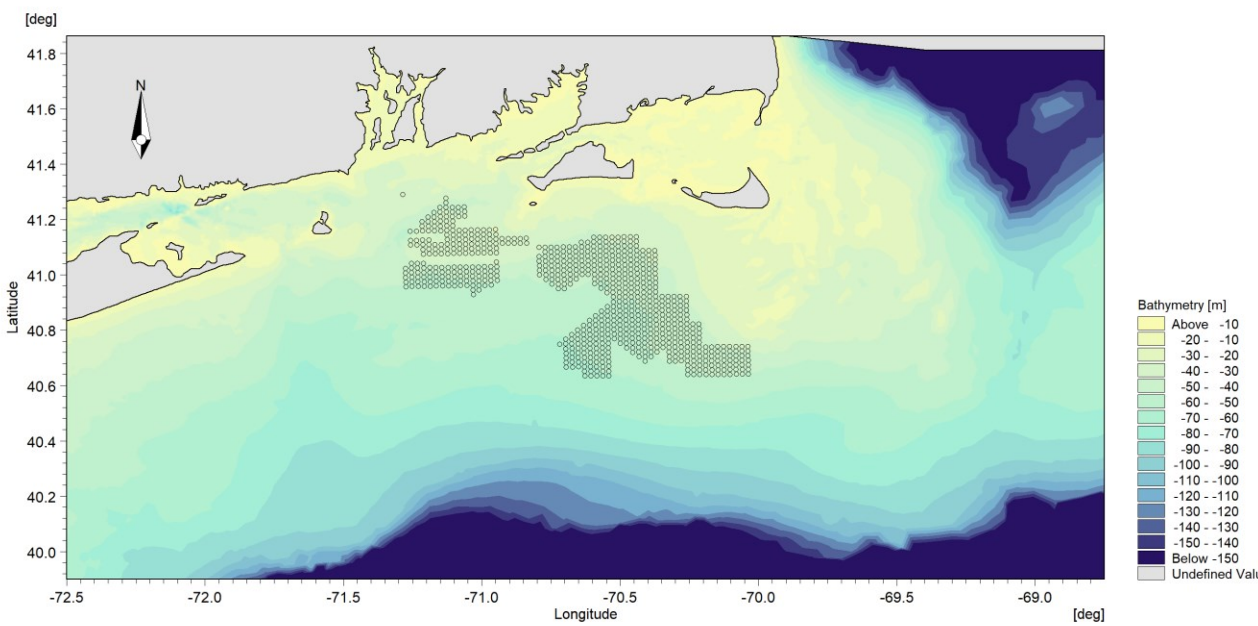

Figure 42. Foundation locations for Scenario 5: 766 towers
Gray circles indicate the footprint of the OSW build-out for 12 MW Mid-level scenario.

4.1.1.1 12 MW Turbine Configuration Modeled

The specification of the wind turbines with respect to dimensions of the foundations and turbine characteristics are generic and guided by the U.S. National Renewable Energy Laboratory reference turbines[4]. Most of the scenarios that included wind turbines used 12 Megawatt (MW) sized turbines with an estimated 12 m diameter foundation monopile. The physical dimensions of the modeled turbine and monopile are listed in the table below. The monopile was simulated as a constant diameter cylinder with biofouling added to the outside of the structure. The biofouling was included to allow for an increase in drag on the monopile. At the base a scour protection "mat" was included with a finite height and diameter. The hub height, rotor swept diameter, thrust coefficient and cu-in wind speed are values required for the wake loss model calculations.

Table 4. Generic 12 MW wind turbine physical dimensions

Item	Description	Dimension(s)
Turbine hub height	The average height of the wind turbine above water	140 m
Turbine tower diameter	The tower diameter was enhanced with marine growth to increase the diameter and increase roughness	12 m with 10 cm marine growth added
Turbine tower scour protection diameter	Scour protection was simulated around the base of the turbine tower monopile	50 m
Turbine tower scour protection height	Scour protection was simulated around the base of the turbine tower monopile and had a height above the surrounding seabed	1 m
Rotor swept diameter	Rotor diameter is used in the wind wake loss calculations.	200 m
Thrust Coefficient (C_t)	Thrust coefficient is used in the wind wake loss calculation.	0.8
Cut-in wind speed	Cut-in wind speed is used in the wind wake loss calculation	3 m/s

4.1.1.2 15 MW Turbine Configuration Modeled

As above, the specification of the wind turbines with respect to dimensions of the foundations and turbine characteristics are generic and guided by the U.S. National Renewable Energy Laboratory reference turbines[4]. One scenario included wind turbines that were 15 MW in size with their requisite 15 m diameter foundation monopile. The physical dimensions of the modeled turbine and monopile are listed in the table below. As with the 12 MW turbines, the monopile was simulated as a constant diameter cylinder with biofouling added to the outside of the structure. At the base a scour protection "mat" was included with a finite height and diameter.

[4] https://www.nrel.gov

Table 5. Generic 15 MW wind turbine physical dimensions

Item	Description	Dimension(s)
Turbine hub height	The average height of the wind turbine above water	180 m
Turbine tower diameter	The tower diameter was enhanced with marine growth to increase the diameter and increase roughness	15 m with 10 cm marine growth added
Turbine tower scour protection diameter	Scour protection was simulated around the base of the turbine tower monopile	50 m
Turbine tower scour protection height	Scour protection was simulated around the base of the turbine tower monopile and had a height above the surrounding seabed	1 m
Rotor swept diameter	Rotor diameter is used in the wind wake loss calculations.	225 m
Thrust Coefficient (C_t)	Thrust coefficient is used in the wind wake loss calculation.	0.8
Cut-in wind speed	Cut-in wind speed is used in the wind wake loss calculation	3 m/s

4.2 Calculations of Wind Turbine Foundation Drag Coefficient

Once the local 3D hydrodynamic model was calibrated and verified two different wind turbine foundations were studied to gain an understanding of the localized flow around the wind turbine foundation structures using a Computational Fluid Dynamic (CFD) model as outlined below. The goal of the CFD study was to enable modeling of their impact on the surrounding waters. The importance of accurately defining the drag coefficient is discussed below.

The CFD analysis was used to assess the amount of hydrodynamic resistance or blocking of the wind turbine foundation, the level of boundary layer turbulence, the characteristics of the surrounding vortex structure as well as the nature of the wake and vortex shedding. The CFD methodology was developed for earlier projects that studied the effect of bridge piers on flow in a stratified sea. One former study was used to determine the impact of these structures on the mixing in the highly ecologically sensitive waters of the Fehmarn Belt that control saline-fresh water exchange between the Baltic Sea and the Kattegat.

In the Fehmarn Belt study, the level of mixing induced by a range of bridge pier shapes was calculated by CFD and was validated using sophisticated physical experiments conducted and reported by Jensen et al. 2018. The CFD model provided relationships between current velocity and mixing efficiency regarding the structure shape.

The flow around a monopile is relatively complex (see **Figure 44**) and has been the subject several experimental and modeling studies. The monopile will exert a drag force on by flowing water due to the blocking effect and the resistance in the boundary layer around it. Depending on the flow conditions, the monopile will initiate a downstream wake, where eddies and turbulence may impact the vertical mixing of the waters.

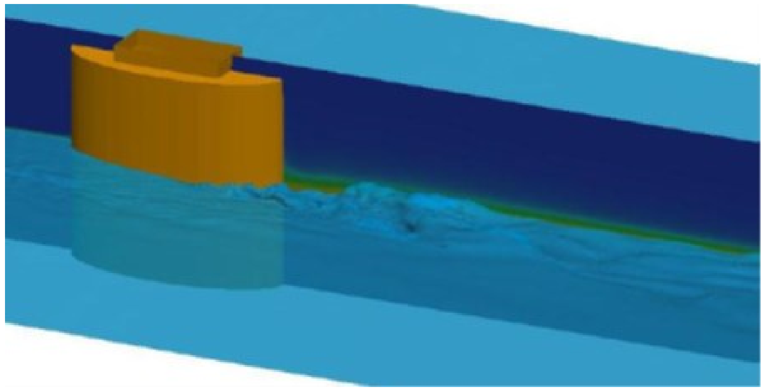

Figure 43. CFD simulation of two-phase flow around a bridge pier
The interface between the phases is shown as an iso-surface.

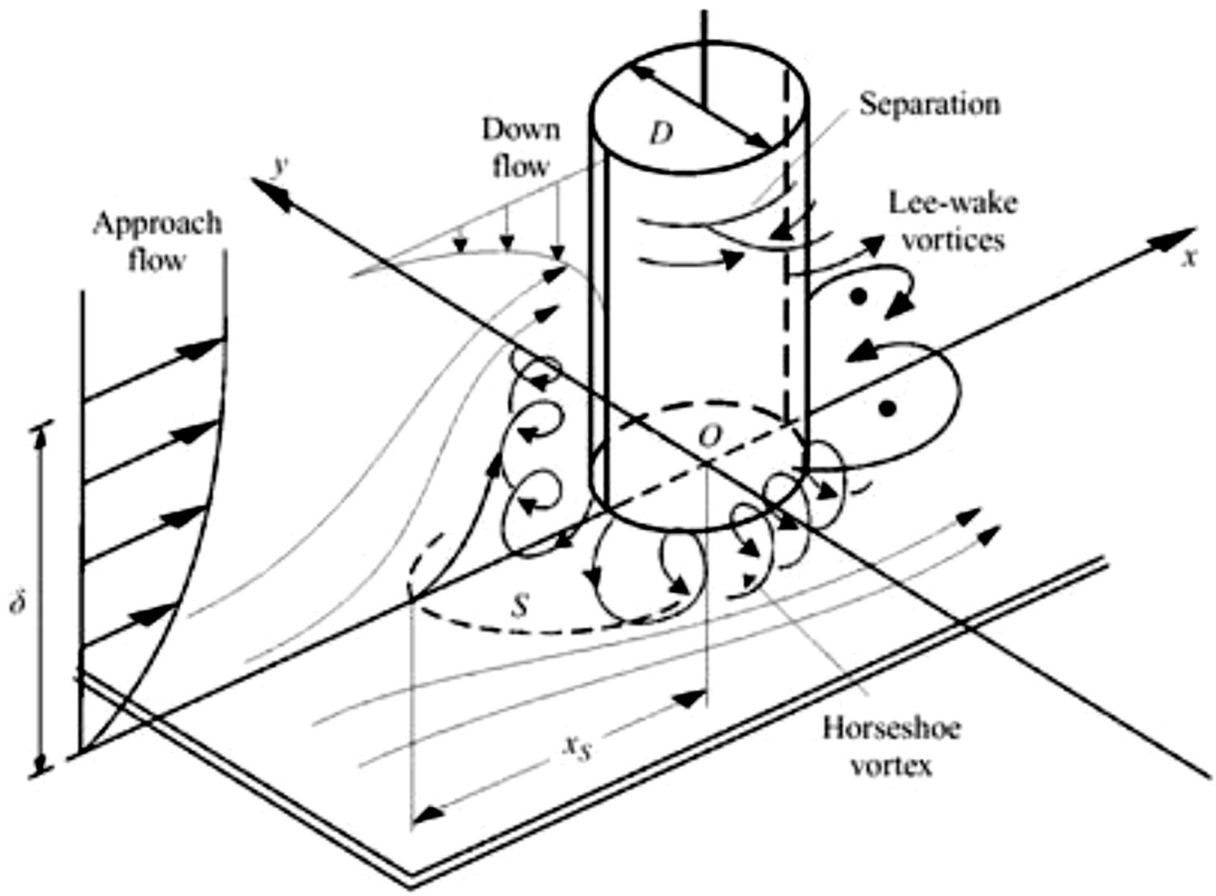

Figure 44. Computational Fluid Dynamics (CFD) processes
Sketch of large turbulent flow structures generated by the presence of a vertical pylon in a flow-field.

The methodology that was employed for the study presented in this report was based on these proven techniques that have been successfully used not only for the Fehrmarn Belt Fixed Link environmental assessment and design optimization, but also earlier for the Oresund Link project. This was another major environmentally sensitive project in Europe with similar environmental concerns as Fehrmarn.

While bridge piers due to irregular shapes are much more intrusive, the methodology remains reliable with (relatively) less intrusive, but more abundant, wind turbine foundations. The CFD model work quantified the effect in terms of the enhanced mixing, following the example enumerated in Jakobsen et al. (2010) where the added resistance due to the presence of bridge piers was investigated. Several detailed studies exist on the physical processes of natural mixing of stratified flows (e.g. Grubert 1989, Fernando 1991, Ivey and Imberger 1991, Strang and Fernando 2001, Peltier, and Caulfield 2003).

When a surface piercing wind turbine foundation is introduced into the flow, the work performed by the wind turbine foundation (reaction force) on the ambient water introduces turbulent kinetic energy from the generated vortex shedding and smaller scale turbulence. In a uniform non-stratified flow, the turbulent flow structures will undergo a turbulent cascade in which smaller and smaller eddies are being formed and finally dissipated into heat. In the stratified case, some of the energy will be used to mix the two layers, either locally or propagating away as internal waves, redistributing heavy bottom water into the lighter upper layer (e.g. Rouse and Dodu 1955, Holmboe 1962, Smyth and Winters 2003).

The term “mixing efficiency” is, for this study, related to the Richardson number (see Turner 1973). The change in potential energy by mixing the vertical layers of the density profile can be related to the kinetic energy produced by the drag forces on the wind turbine foundation. The energy produced is the turbulent kinetic energy generated when the wind turbine foundation is exposed to the steady current in the numerical simulations. The turbulent kinetic energy is approximately equal to the work performed the steady current flows around the surface piercing wind turbine foundation.

Work may be calculated as the integral of the Force on the surface piercing wind turbine foundation times the speed of the current. In steady current, the inertial term of Force trends to zero and the Drag Force remains as the key component of the Work on the fluid. Therefore, the mixing efficiency is proportional to the work done on the fluid. In steady flow, this means the mixing efficiency is proportional to the Drag Force on the surface piercing wind turbine foundation. This energy conversion is the basis of the transfer of results from the CFD model to the 3D hydrodynamic model through the introduction of localized “Drag” to the OSW region at each of the surface piercing wind turbine foundations in the model.

The 3D regional hydrodynamic solution method involves the use of a finite volume mesh with a spatially varying mesh size allowing resolution to be concentrated in key areas of interest. A typical choice of minimum mesh size of 25 m implies that foundations with a typical horizontal dimension of 12 to 15 m are not directly resolvable in the computational mesh. Therefore, the presence of wind turbine foundations was parameterized. The resistance to the flow due to the wind turbine foundations derived from the CFD study was modeled by calculating the current induced drag force on each individual pier segments and equating this force with a shear stress contribution compatible with the 3D hydrodynamic momentum formulation. The turbulence model used to represent the disturbance due to the bottom founded structures was an enhanced $\kappa-\varepsilon$ model that included an extra term for the drag derived from the CFD modeling and a work/turbulence production term that was used to balance out the energy dissipated. This was done to eliminate the shortcomings of the k-model. The length scale specification inherent in this model can be replaced by a transport equation for a turbulent quantity. The $\kappa-\varepsilon$ turbulence closure formulation implemented in 3D hydrodynamic was suggested by Rodi (1980).

In this study the specific drag coefficients and mixing efficiencies were described using a CFD model. The model is a full 3D so-called Reynolds Averaged Simulation based on the OpenFOAM[5] modeling framework. The model was used to simulate the effect of one turbine to establish a general parameterization for the energy conversion and thereby the impacts on flow resistance and mixing in the 3D regional model.

The project specific CFD modeling produced the following results. Below is shown the results of a simulation of a steady stratified flow past one monopile including scour protection. Conditions are similar to typical conditions at the OSW sites. The results show that the monopile generates a downstream unsteady wake area, as expected. The integral drag coefficient induced by the monopile and the scour protection is estimated to be $C_D = 1.034$ as shown in in **Figure 45** below. This coefficient applies to both 12MW and 15MW monopiles. The downstream mixing process, part of which can be seen as the internal waves in the density interface in **Figure 45**, is described using a Richardson number (or energy conversion efficiency) at 0.07 in agreement with earlier findings by Jensen et al. (2018).

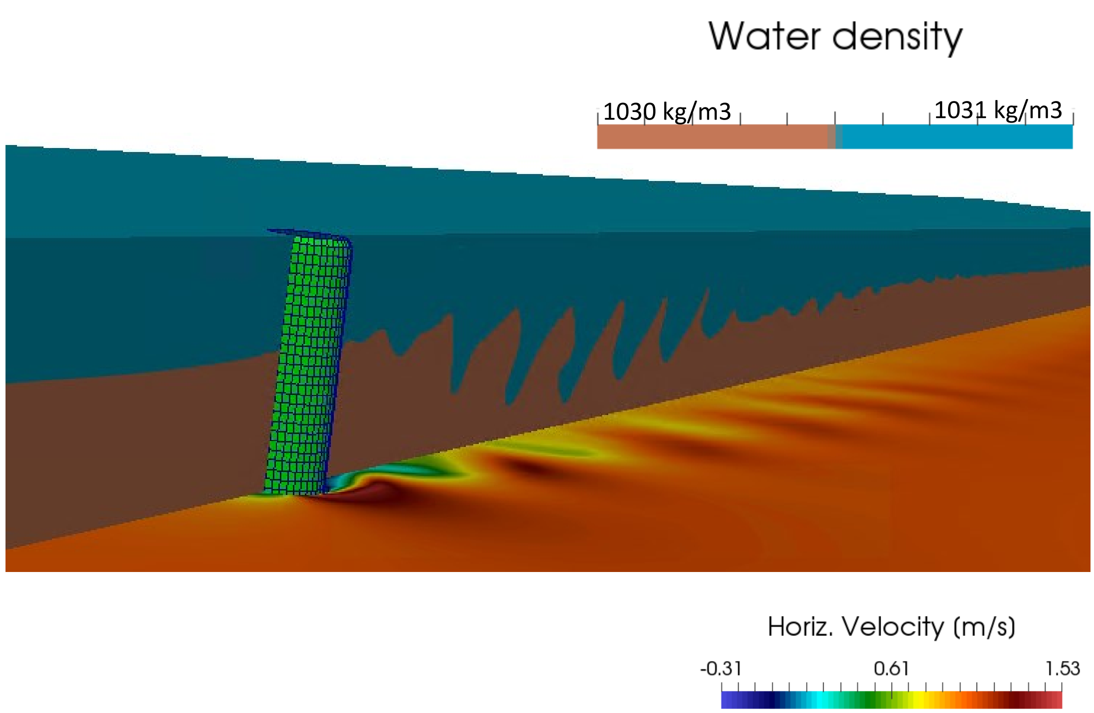

Figure 45. Illustration of the velocity and density field
Velocity and density field in a vertical and a horizontal plane in the steady flow past a 12 m diameter monopile as modeled by the CFD model.

4.3 Wind Turbine Wake Loss Model

Wind turbines extract energy from the wind and thereby also changes the wind field downstream of the turbine, the so-called wake-effect, where the wind speed is decreased a distance downstream. Typically,

[5] https://www.openfoam.com/

this distance is 5 to 10 rotor diameters but, in some conditions, may be larger. In the offshore area this effect may potentially change the surface stresses on the water surface and thereby change wave and current conditions. In the regional models used in this study we apply CFSR wind fields as atmospheric forcing. These fields are relatively coarse (about 10 km x 10 km); thus, it is not possible to describe individual turbine and their downstream wake in this resolution. The focus of the present regional model is to describe the larger patterns, i.e. changes in circulation or in sea states in the greater area. To accurately describe the impact of the OSW we use a simplified energy model, described below, to parameterize the effect of the OSW on the surface wind field, such that even with a relatively coarse resolution, we obtain an accurate description of the overall effect.

To model wind wake loss effects inside the OSW it was decided to use the Frandsen infinite wind-farm boundary-layer (IWFBL) model (Frandsen 1992) with atmospheric stratification modifications (Peña and Rathmann 2014). **Figure 46** below shows the frame of reference of the IWFBL wake model. The model is based on the following assumptions:

- The model is a two-layer model where the turbine thrust force equals the difference between the shear stress forces above and below the rotor.
- Both the layer below the rotor and the layer above are inside the atmospheric surface layer and fully described by Monin-Obukhov Similarity Theory (MOST).
- The upstream wind speed profile and the layer above the rotor is matched through a simple geostrophic drag law formulation.
- The aerodynamic roughness of the sea surface is described with a simple Charnock relationship, so that the severity of the sea states increase the drag coefficient of the surface through the turbulent transport of momentum.
- The OSW is infinitely large.
- The individual turbines are positioned with a fixed spacing inside the OSW.

Of these assumptions only the validity of MOST seems critical: with a hub height of 140 m the turbines are often above the atmospheric surface layer during nighttime and in situations where the sea surface temperature is much lower than the air temperature. In such situations physical processes dictated by the stability above the atmospheric boundary layer may also become important.

By including stability effects, the wake effect, i.e. the decrease of the wind speed behind the turbines, is enhanced when the atmospheric boundary layer is stably stratified (sea surface temperature lower than air temperature) and diminished in convective situations (sea surface temperature larger than air temperature) due to more vertical exchange.

At each CFSR reanalysis data grid point inside the OSW, the CFSR time series of wind speed at 10m, sea surface temperature, air temperature, surface pressure and relative humidity have been used to calculate a new time series of reduced wind speed at 10 m by using the wake model and associated MOST stability parameters. This time series is then assumed to represent the wind speed at the CFSR grid points inside the OSW. Cut-in and cut-out wind speeds of 3 m/s and 26 m/s, respectively, have been applied to the model, thus time stamps of wind speed outside this range are unmodified.

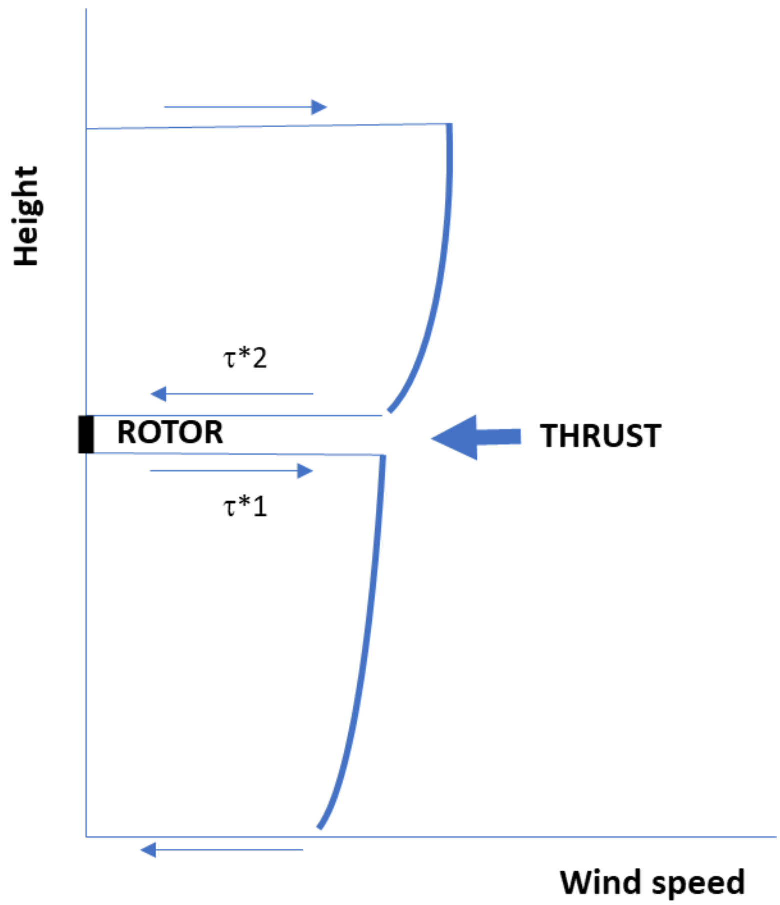

Figure 46. Conceptual framework of the wind wake loss model.
THRUST is the turbine thrust force, and τ*1 and τ*2 are the shear stress forces below and above the wind turbine rotor layer, respectively.

An example of a time series of 10 m wind speed upstream and downstream the OSW is provided in **Figure 47**. It is observed how the red curve representing wind speed inside the OSW is always below the blue curve representing upstream conditions. In the given example the average reduction in wind speed is 16%. This could seem rather low but looking at the distribution of temperature difference between the sea surface and the air in **Figure 48**, it is obvious that the atmosphere is often in a convective state and thus wake effects are diminished.

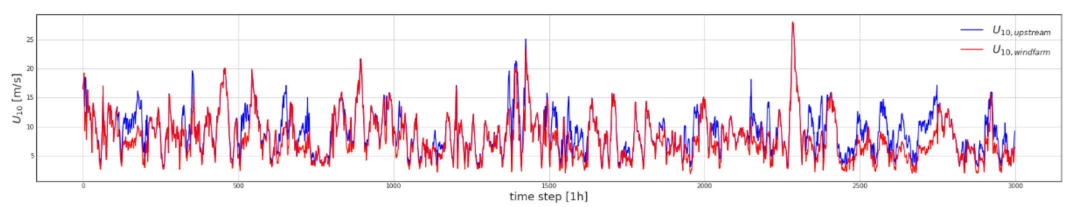

Figure 47. Time series of wind speed upstream and downstream of the OSW
The blue line is the time series of wind speed 10m upstream and the red line is the time series of wind speed inside of the OSW.

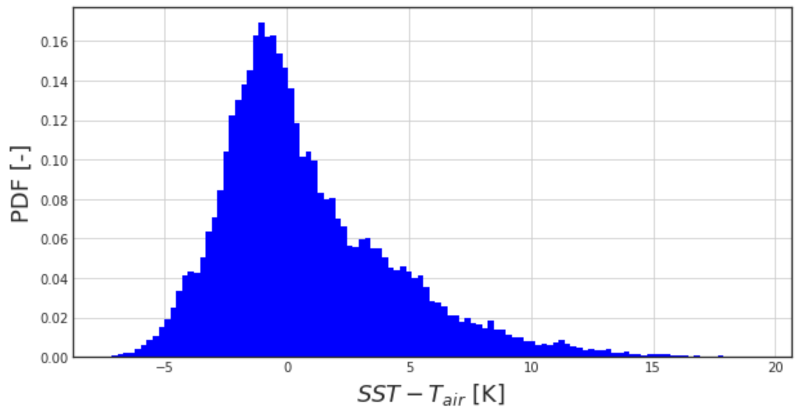

Figure 48. Probability distribution function (PDF) of temperature difference between sea surface and the air.
The PDF shows that the atmosphere is often in a convective state and thus wake effects are diminished.

4.3.1 Current Modification

By reducing the CFSR wind field over the OSW area, the HD and SW model sea surface wind shear stress was reduced, thereby reducing the overall forcing due to the wind inside the wind farm and reducing the energy transfer from wind to the sea. The model approximations of the CFSR wind speeds and sea surface wind stresses reduction was confined to the areas of the model that were inside the OSW footprint. Changes to the CFSR wind speeds and sea surface shear stress downwind and outside the confines of the OSW model area were not considered.

4.3.2 Wave Modification

The spectral wave model simulates the growth, decay and transformation of wind-generated waves and swell in offshore and coastal areas. The model is developed by DHI based on the 3rd generation WAve Modeling (WAM) standard and has been applied in numerous high-profiled projects. The model includes the following physical phenomena:

- Wave growth by action of wind
- Atlantic swell
- Wave-induced bottom shear stresses
- Dissipation due to bottom friction
- Non-linear wave-wave interaction
- Dissipation due to white-capping
- Dissipation due to depth-induced wave breaking
- Refraction and shoaling due to depth variations
- Changes in wave transmission due to turbine towers

The discretization of the governing equation in geographical and spectral space was performed using cell-centered finite volume method. In the geographical domain, an unstructured mesh technique was used. The time integration was performed using a fractional step approach where a multi-sequence explicit method is applied for the propagation of wave action.

Again, the model approximations of the CFSR wind speeds and sea surface wind stresses reduction were confined to the areas of the model that were inside the OSW footprint. Changes to the CFSR wind speeds and sea surface shear stress downwind and outside the confines of the OSW model area were not considered.

The effect of the submerged foundations is described as a simplified point source of wave energy, describing the energy changes due to reflection or transmission from the structure.

5 Hydrodynamic Model Baseline vs. Scenario Results

5.1 Overview

In **Section 3.3**, the baseline hydrodynamic model output parameters were shown to compare well with empirical observations in the OSW location. The following sections are a compilation of the effects of the OSW scenarios on the:

- Current fields
- Particle tracking
- Waves
- Bed shear stress
- Temperature Stratification

Please note that this report highlights oceanic modelling results with respect to altered currents for all scenarios. Results regarding the effects of OSW development on waves, temperature and bed shear stress are also reported. However, these results are only presented for the baseline and Scenario 2 conditions. It was a project decision to more fully present altered current results due their predominant influence on observed larvae settlement shifts. It should further be noted that water temperature and stratification are included in all results as they are integral to the ABM modeling with respect to parameterization of larvae behavior and mortality.

5.2 Difference in Depth Averaged Current Fields

The HDM employed was, as described in previous sections, a three-dimensional model. To allow for easy comparison, the depth averaged current magnitude was calculated at each grid point and each time step in the Baseline and in all the Scenarios. This allows the differences in the current patterns to be easily calculated and illustrated. The following sub-sections show the difference in the current speed magnitude: baseline vs. each of the scenarios. It is noted that in documenting typical effects as single values (e.g. percentage increase in current speed) spatial scales, considered in the model, are lost. For example, an 8.5% increase in current speed and 7.1% decrease in current speed should not be taken as a lack of continuity of mass, rather it is a simplification of the complex change in currents that best portrays the relative changes observed between scenario and baseline.

5.2.1 Baseline

The following plot is of the 50th percentile of the depth averaged current magnitude in the study area over the February 2, 2017 to February 2, 2018 timeframe. Half the time the currents were above the values shown in the plot and half the time they were below the values shown in the plot.

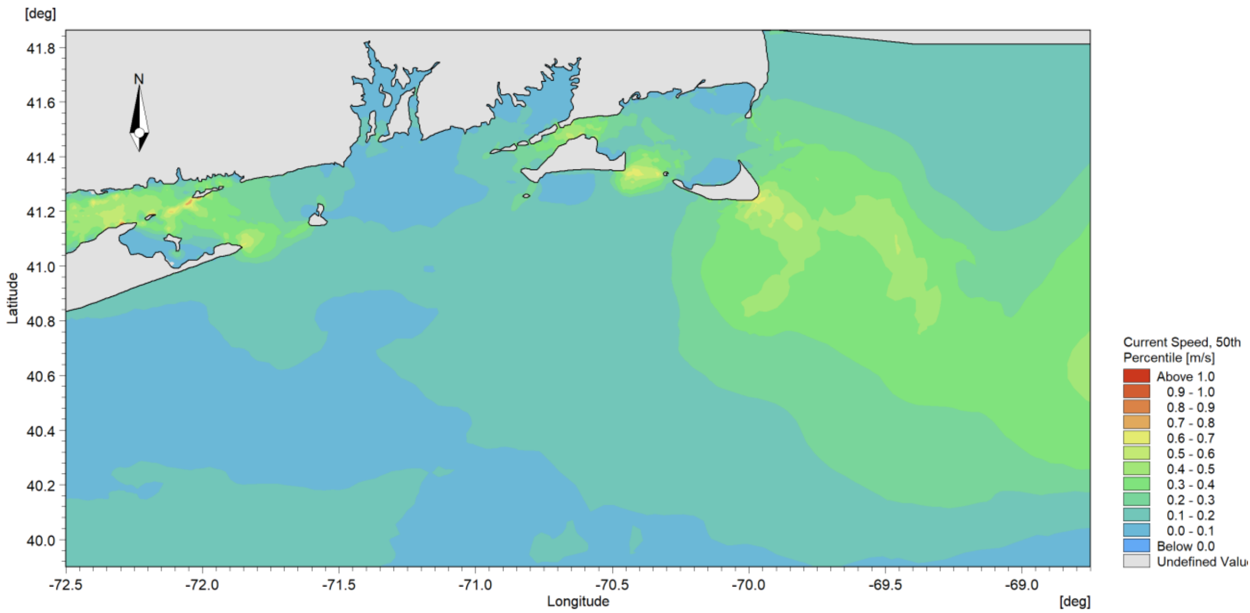

Figure 49. 50th percentile Baseline depth averaged currents in study area

The following plot is of the 75th percentile of the depth averaged current scalar in the study area over the February 2, 2017 to February 2, 2018 timeframe. Seventy five percent of the time the currents were at this level or below.

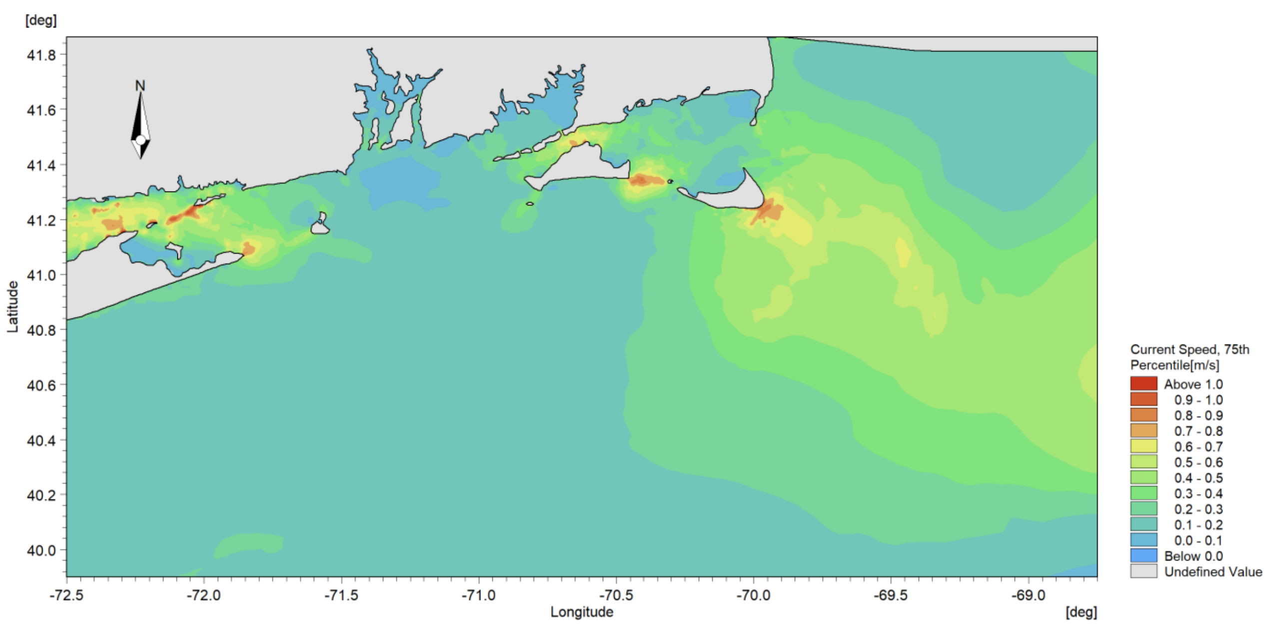

Figure 50. 75th percentile Baseline depth averaged currents in study area

The above plots are the baseline from which the differences are extracted in the following sections of the report. It is well to note that the highest average currents speeds in the 50th percentile plot were on the order of 0.65 m/s and for the 75th percentile plot on the order of 0.85 m/s. In the area of the OSW the depth averaged currents are on the order of 0.125 m/s in the 50th percentile plot and on the order of 0.175 m/s in the 75th percentile plot.

5.2.2 Baseline vs Scenario 2

The following plots are the 50th and 75th percentile difference of (Scenario 2 – Baseline) of the depth averaged currents in the study area. Scenario 2 was the 12 MW full build-out condition. The timeframe is the same as the baseline plots, February 2, 2017 to February 2, 2018.

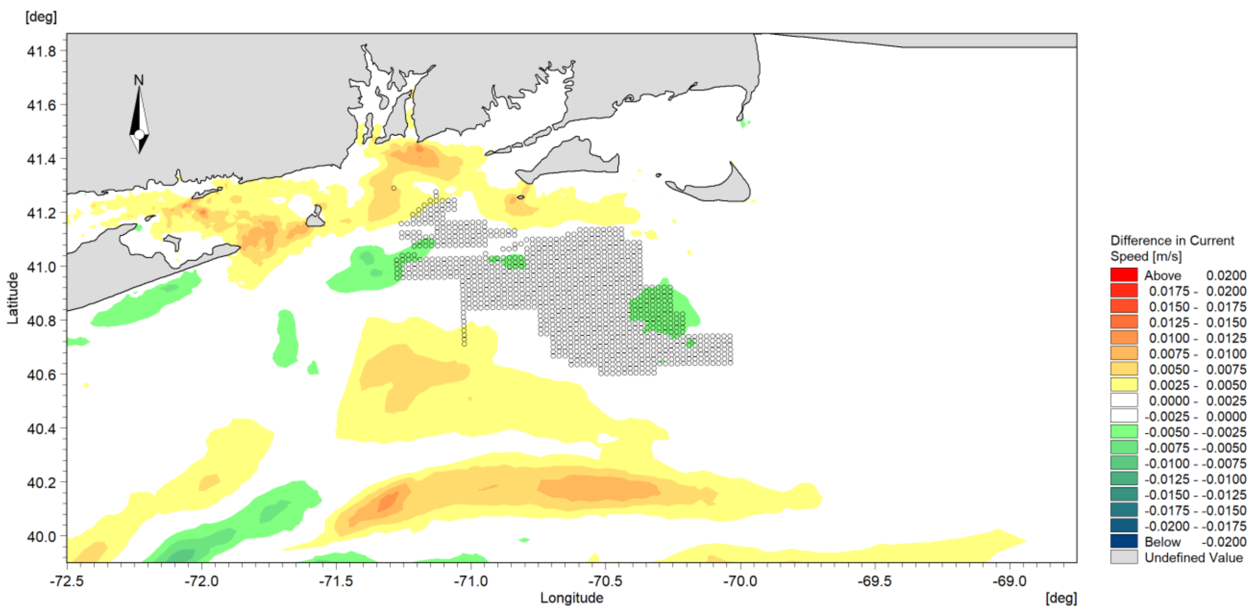

Figure 51. 50th percentile (Scenario 2 – Baseline) depth averaged current differences in study area

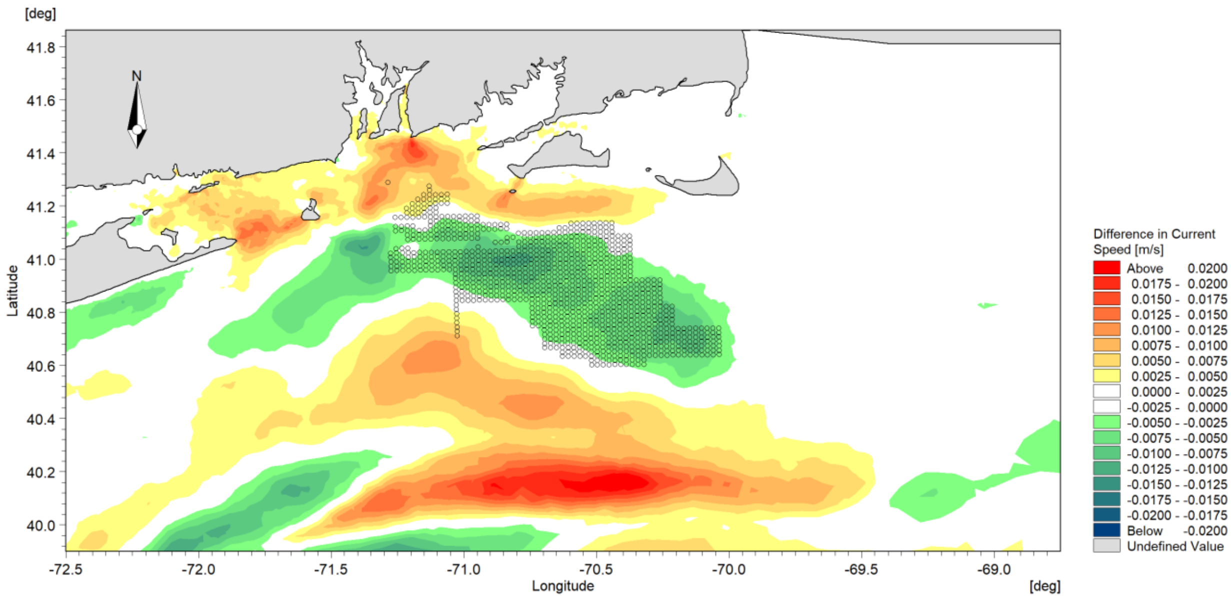

Figure 52. 75th percentile (Scenario 2 – Baseline) depth averaged current differences in study area

From inspection of the two plots, the depth averaged current speeds are accelerated North and South of the OSW area and slowed inside and East and West of the OSW.

- The impact on the current speeds in the 50th percentile plot on the observed maximum differences were +0.00625 m/s North and South of the OSW and -0.005 m/s West of the OSW. These differences when compared to the observed depth averaged currents in the baseline (0.125 m/s) are respectively +5% increase and a -4% decrease in depth averaged current speed.
- The impact on the current speeds in the 75th percentile plot on the observed maximum differences were +0.015 m/s North and South of the OSW and -0.0125 m/s inside as well as East and West of the OSW. These differences when compared to the observed depth averaged currents in the baseline (0.175 m/s) are respectively +8.5% increase and -7.1% decrease in depth averaged current speed.

5.2.3 Baseline vs Scenario 3

The following plots are the 50th and 75th percentile difference of (Scenario 3 – Baseline) of the depth averaged currents in the study area. Scenario 3 was the OCS-A 0501 with 12 MW wind turbines condition.

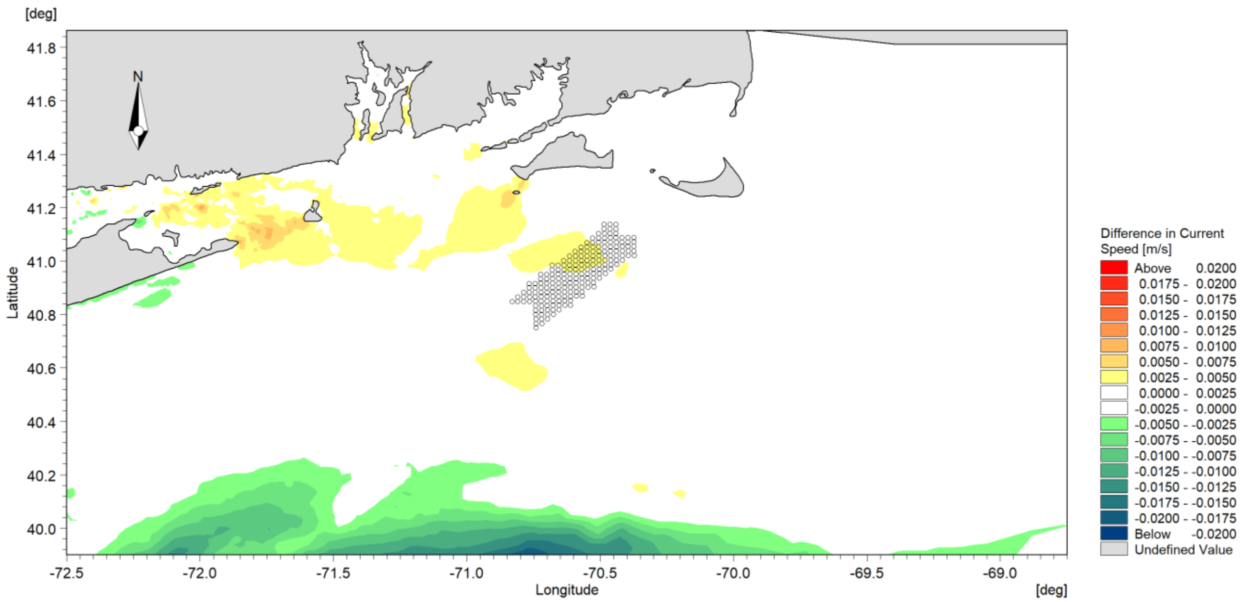

Figure 53. 50th percentile (Scenario 3 – Baseline) depth averaged current differences in study area

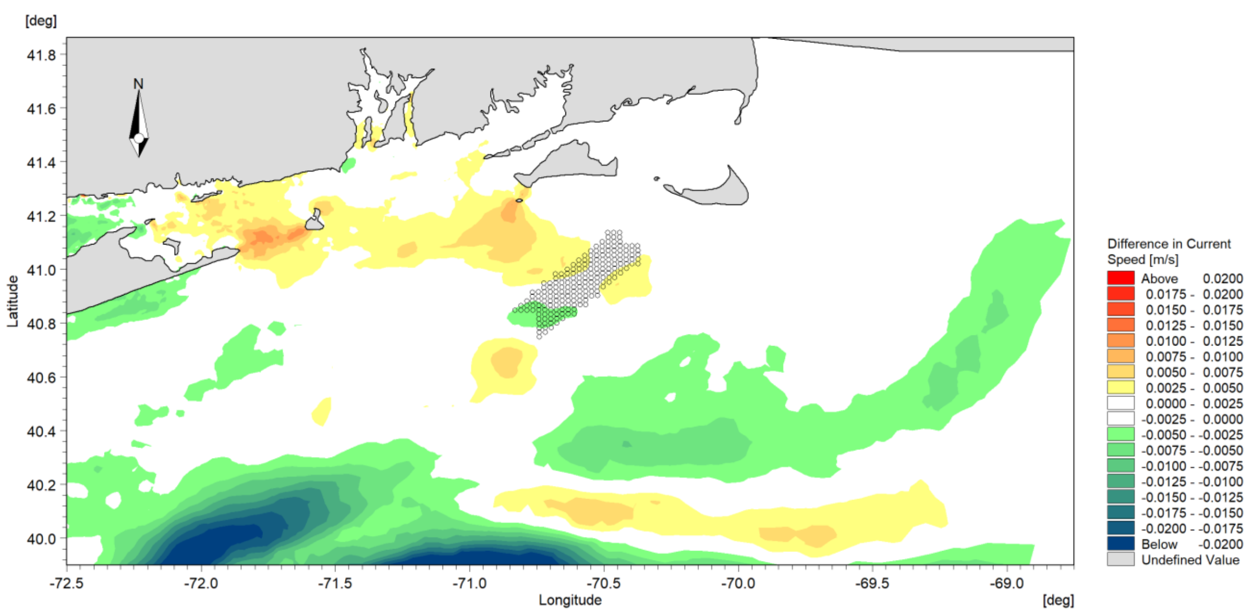

Figure 54. 75th percentile (Scenario 3 – Baseline) depth averaged current differences in study area

From inspection of the two plots, the depth averaged current speeds are slightly accelerated North, South and East of the OSW area and only slowed inside the Southwest corner of the OSW in the 75th percentile plot.

- The impact on the current speeds in the 50th percentile plot on the observed maximum differences were +0.00375 m/s North, South and East of the OSW. There were no indications of a decrease in depth averaged current speed near the OSW at the limit scale of the plot. This difference when compared to the observed depth averaged currents in the baseline (0.125 m/s) is +3% increase in depth averaged current speed and at the limit of the scale of the plot.

- The impact on the current speeds in the 75th percentile plot on the observed maximum differences +0.00625 m/s North and South of the OSW and -0.005 m/s West of the OSW. These differences, when compared to the observed depth averaged currents in the baseline (0.175 m/s), are respectively +3.5% increase and a -2.9% decrease in depth averaged current speed. The differences are very small and slight changes may be amplified in the model. Note the reduction in current speed on the southern boundary. The reduction is quite small in comparison to the current speeds extant in the baseline model results.

5.2.4 Baseline vs Scenario 4

The following plots are the 50th and 75th percentile difference of (Scenario 4 – Baseline) of the depth averaged currents in the study area. Scenario 4 is the 15 MW full build-out condition.

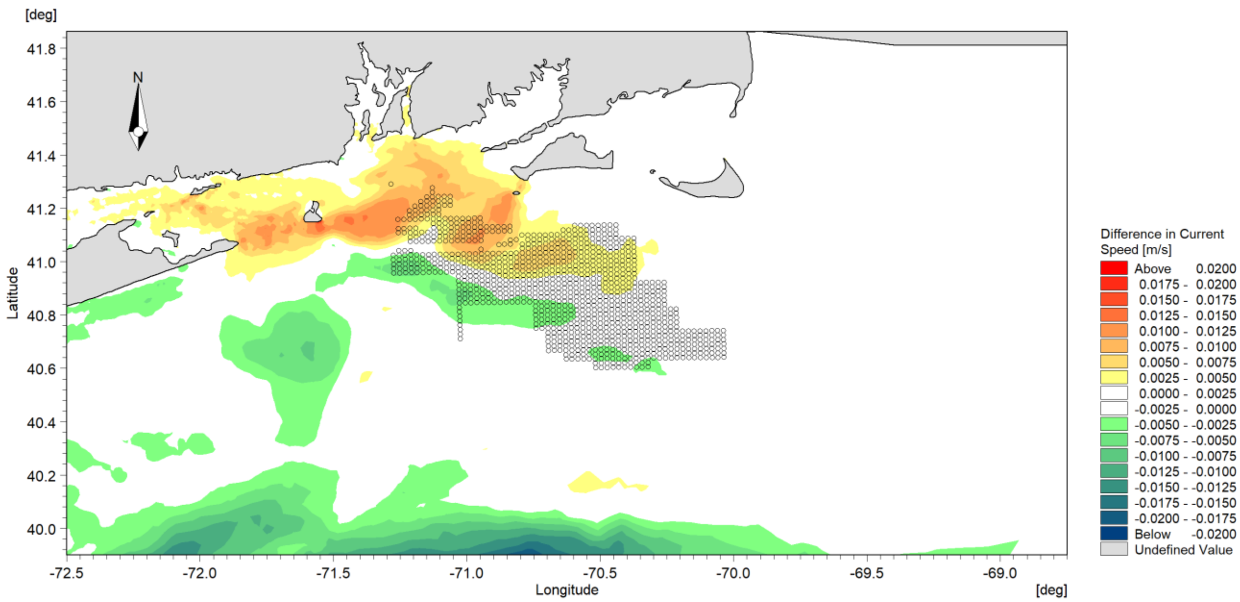

Figure 55. 50th percentile (Scenario 4 – Baseline) depth averaged current differences in study area

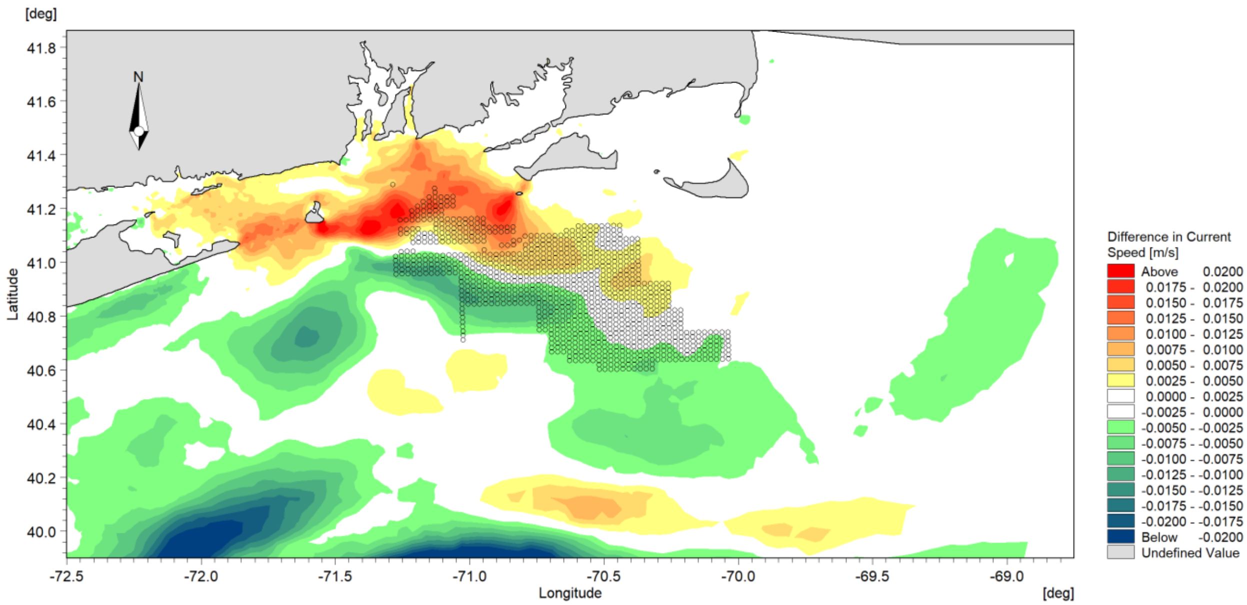

Figure 56. 75th percentile (Scenario 4 – Baseline) depth averaged current differences in study area

From inspection of the two plots, the depth averaged current speeds are accelerated North of the OSW area and slowed inside the Southwest side and South of the OSW. Compared to Scenario 2 12 MW full build-out condition, the depth averaged current speeds are affected more, as would be expected since the 15 MW turbine towers are larger in diameter creating more blockage slowing the current more and the rotors are larger and would extract more energy from the wind and hence less wind shear stress on the surface of the sea.

- The impact on the current speeds in the 50th percentile plot on the observed maximum differences were +0.01125 m/s North of the OSW and -0.00625 m/s Southwest side of the OSW. These differences, when compared to the observed depth averaged currents in the baseline (0.125 m/s), are respectively +9% increase and a -5% decrease in depth averaged current speed.
- The impact on the current speeds in the 75th percentile plot on the observed maximum differences were +0.02m/s North of the OSW and -0.01375 m/s inside as well as West of the OSW. These differences, when compared to the observed depth averaged currents in the baseline (0.175 m/s), are respectively +11.4 increase and a -7.9% decrease in depth averaged current speed.

5.2.5 Baseline vs Scenario 5

The following plots are the 50th and 75th percentile difference of (Scenario 5 – Baseline) of the depth averaged currents in the study area. Scenario 5 was the Mid-level with 12 MW wind turbines condition.

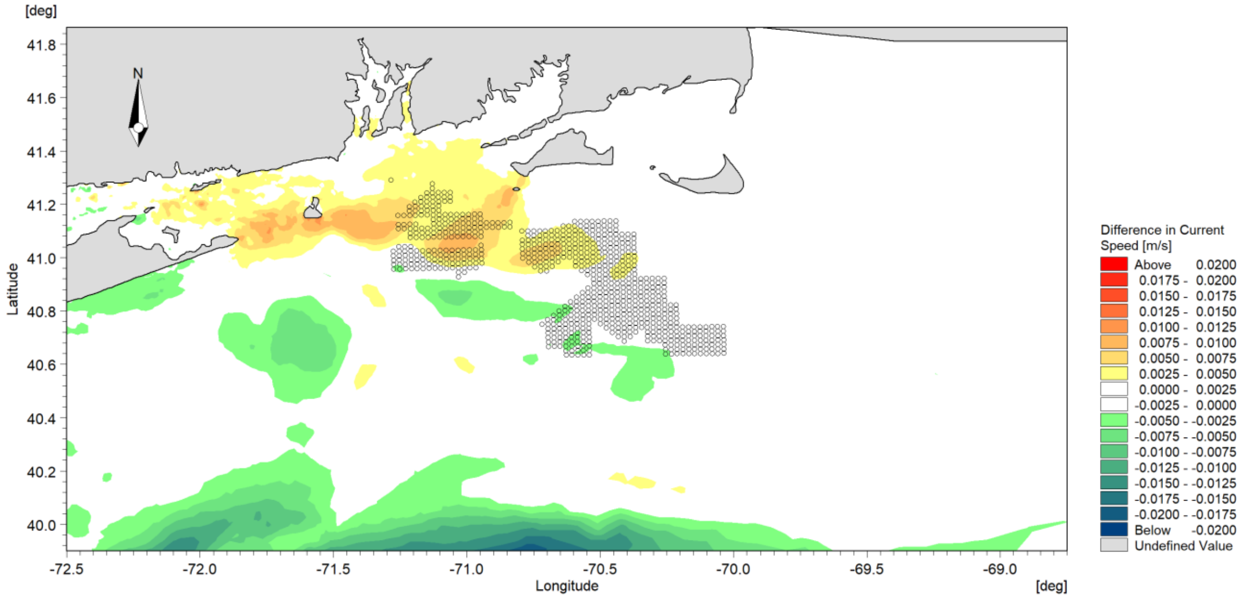

Figure 57. 50th percentile (Scenario 5 – Baseline) depth averaged current differences in study area

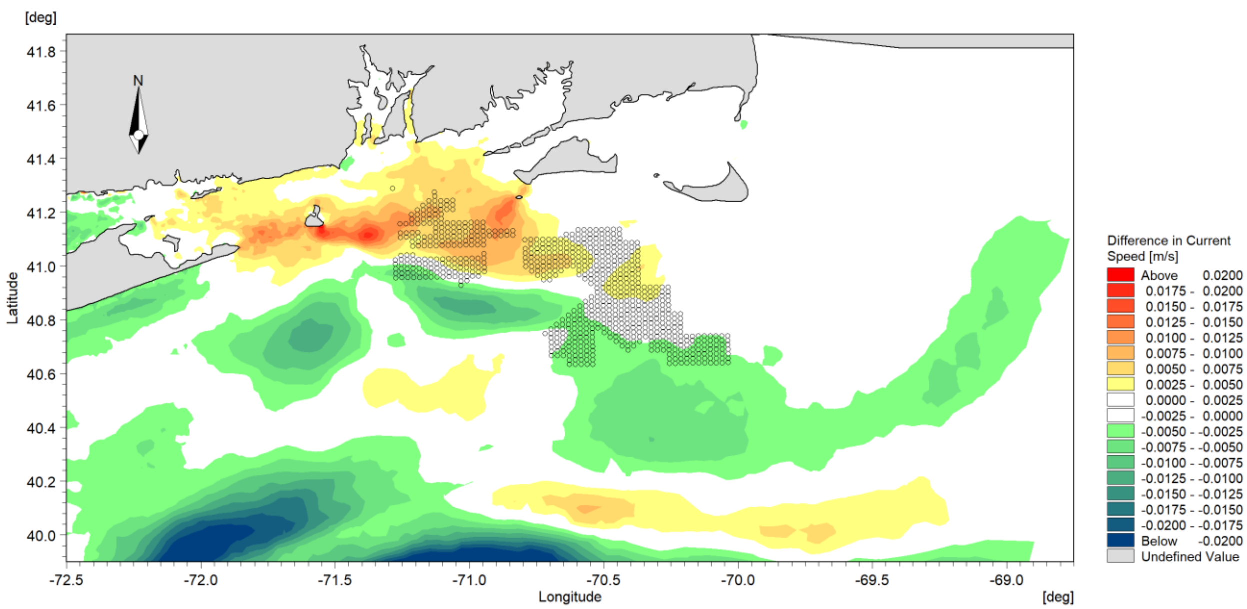

Figure 58. 75th percentile (Scenario 5 – Baseline) depth averaged current differences in study area

From inspection of the two plots, the depth averaged current speeds are slightly accelerated North, South, West and inside the Northern section of the OSW area and slowed South and close into the South side of the Northern section of the OSW.

- The impact on the current speeds in the 50th percentile plot on the observed maximum differences were +0.00625 m/s North and inside the Northern portion of the OSW and -0.00625 m/s South of the Northern portion of the OSW. These differences, when compared to the observed depth averaged currents in the baseline (0.125 m/s), are respectively +5% increase and -5% decrease in depth averaged current speed.

- The impact on the current speeds in the 75th percentile plot on the observed maximum differences were +0.01875 m/s North and South of the OSW and -0.00875 m/s West and just South of the Northern portion of the OSW. These differences, when compared to the observed depth averaged currents in the baseline (0.175 m/s), are respectively +10.7% increase and -5% decrease in depth averaged current speed.

5.2.6 Summary: Baseline vs All Scenarios

In summary, the percent differences are collated in the following table for all the Scenarios versus the Baseline. The 75th percentile results show the trends that one would expect. Scenarios 2 and 4 have the largest impact as these are the full build-out scenarios with Scenario 4 having the larger effect since the turbines are larger than in Scenario 2. Scenario 3 with the smallest number of wind turbines has the smallest impact on the depth averaged current speed.

Table 6. Summary of percent differences for the 50th & 75th percentile depth average current speeds

Scenario - Baseline	50th percentile increase	50th percentile decrease	75th percentile increase	75th percentile decrease
2 - Baseline	+5%	-4%	+8.5%	-7.1%
3 – Baseline	+3%	Null	+3.5%	-2.9%
4 – Baseline	+9%	-5%	+11.4%	-7.9%
5 - Baseline	+5%	-5%	+10.7%	-5%

The 50th percentile results are at the low end of the range and the results show similar small differences except for the Scenario 4 results that show a greater increase in current speed compared to the Baseline. It should be noted that the depth averaged current results discussed here are the larger +/- values seen in the study area and have been observed over a relatively large area and over a relatively long time.

5.3 Particle Tracking

Particle tracking was an original objective of the BOEM call. However, the offer made to and accepted by BOEM was rather to simulate three species of larvae as agents in Agent-Based Models (ABM). In order to provide further context to the full ABM simulations, two particle tracking simulations (Scenario 1: Baseline and Scenario 2: 12 MW full build-out) were run to examine at the overall effect of the 12 MW Scenario 2, in relation to the Baseline transport of inert particles. The release locations and the release timing were selected to mimic the same locations and spawning timing of Silver Hake.

Table 7 below lists the parameters used to describe the particle model. All particles settled within the regional model domain by the end of the simulation.

Table 7. Particle model parameters

Parameter	Value
Number of particles released	347,328
Location of release points in Latitude and Longitude	-71.8W 40.85S -70.2W 41.10S -71.6W 41.05S -69.8W 41.10S -72.2W 40.70S -71.1W 41.20S
Release timing	May 8, 2017 to October 31, 2017
Release quantities at each of the 6 sites	From May 15 to June 16: 288 particles per day From June 17 to June 21: 576 particles per day From June 22 to June 23: 864 particles per day From June 24 to June 29: 576 particles per day From June 30 to July 18: 288 particles per day From July 19 to July 26: 576 particles per day From July 27 to August 17: 288 particles per day From August 18 to August 25: 576 particles per day From August 26 to October 31: 288 particles per day
Release point depth below the water surface	5 m
Fall velocity of the particles	6 m/day or 6.94×10^{-5} m/s
Mass of each particle	1.5 grams
Number of particles retained within the regional model boundaries at the end of the simulation	347,328

The following plot shows the release points of the particles.

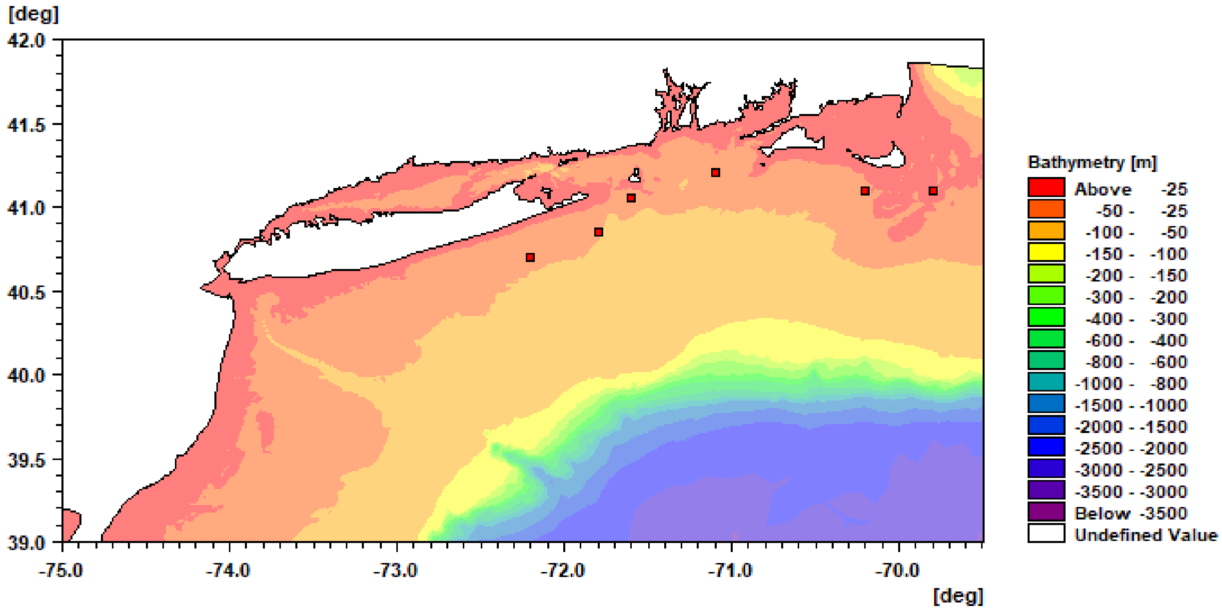

Figure 59. Particle tracking model particle release points

The following two plots generated by the particle tracking model show the final timestep settled particle results for Scenario 1 and Scenario 2. The third plot is the difference between the two scenarios.

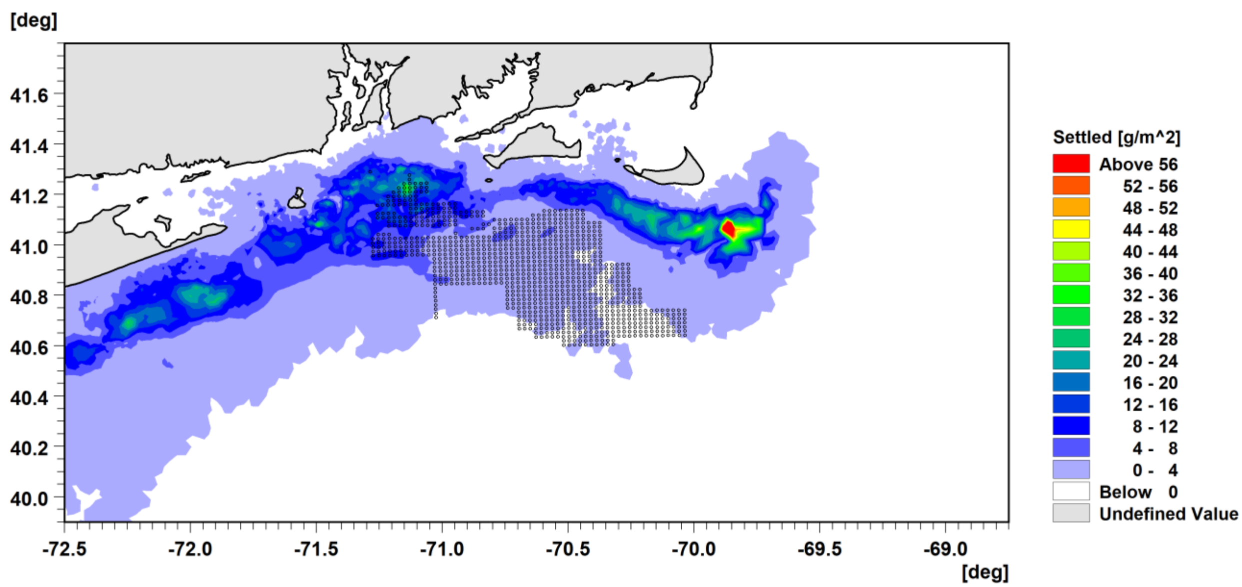

Figure 60. Scenario 1: Baseline settled particle tracking results
Outline of the full build-out OSW included for spatial reference.

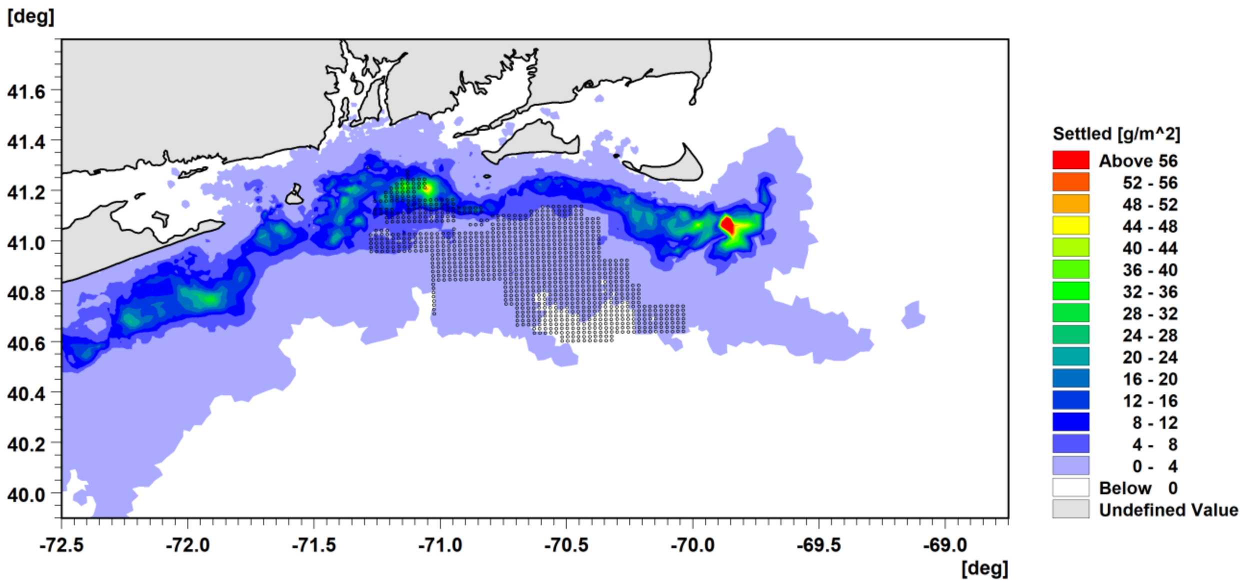

Figure 61. Scenario 2: 12 MW full build-out settled particle tracking results

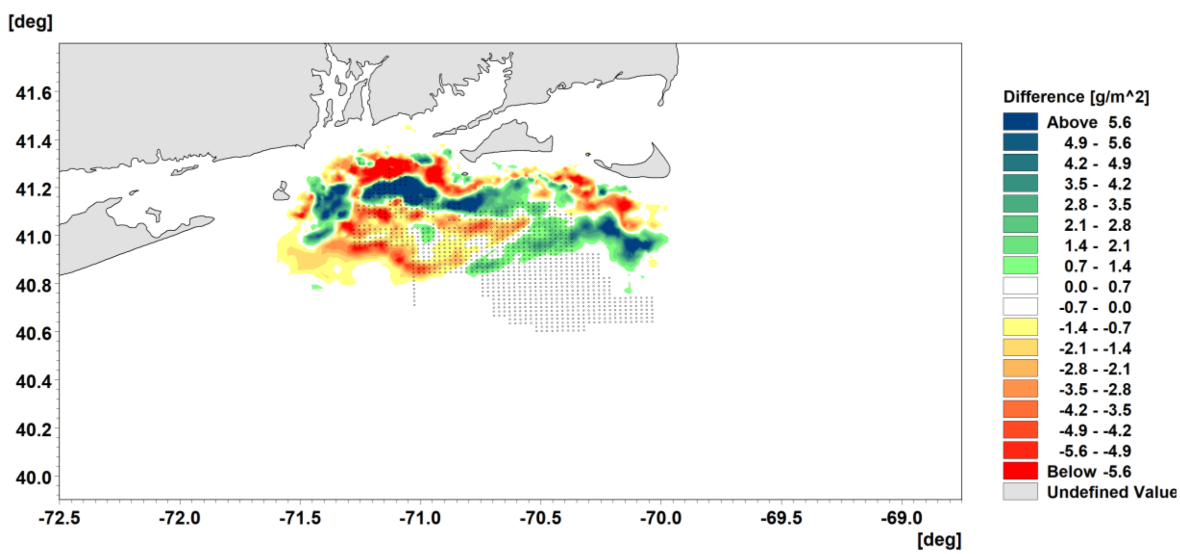

Figure 62. Difference (Scenario 2 – Baseline) settled particle tracking results

The pattern shows that more particles settle north of the OSW and fewer particles settle just inside the West side of the OSW. The east side of the OSW seems to attract a few more settled particles. Where there are mixed results of low-density differences it is likely a result of the randomness of the particle tracking model release and the random walk of the particle Lagrangian model. The difference plot, in the cases of the largest differences, shows variations that were at most on the order of +10% (dark blue) on the northwest side of the OSW and perhaps -10% (dark red) to the South east of Nantucket Island. The majority of the area shows much less than a 10% change.

5.4 Effects on Waves

The application of the wake loss model modified sea surface wind shear stress thereby affecting the local wave field inside and outside the OSW. The objective of this portion of the study was to calculate hourly sea-state in the study area for Baseline (Scenario 1) conditions and compare that to Scenario 2: 12 MW full build-out with wind-field wake loss reductions included. Since the wave climate in average conditions has no significant effect on the larval transport, it was decided that a single build-out scenario was sufficient for this study to demonstrate the effect. It is recognized that Scenario 4: 15 MW would have produced a larger decrease in the wind and therefore wave climate. However, 15 MW turbines were not commonly being deployed at the time of this study, so Scenario 2: 12 MW full build-out was selected for study.

The following two plots show the Significant wave height (H_{m0}) for 95th percentile and 99th percentile exceedance percentiles at each grid location for the Scenario 1: Baseline condition. This means 95% or 99% of the time H_{m0} is equal to or less than the value shown.

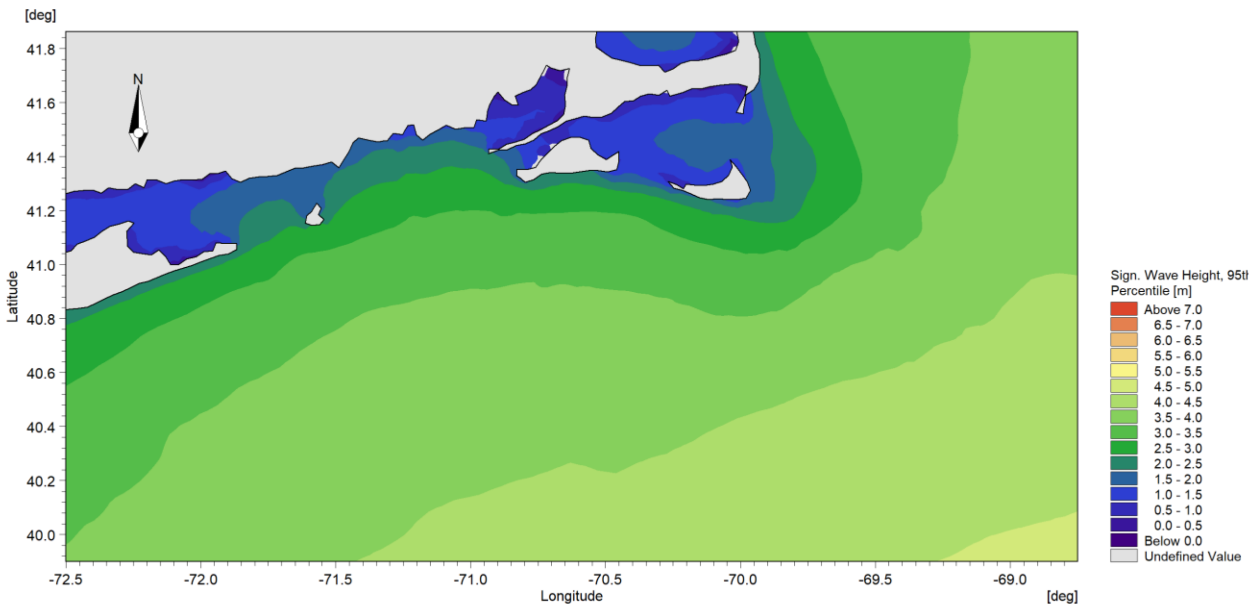

Figure 63. Significant wave height, H_{m0} 95th percentile Exceedance plot for Scenario 1: Baseline

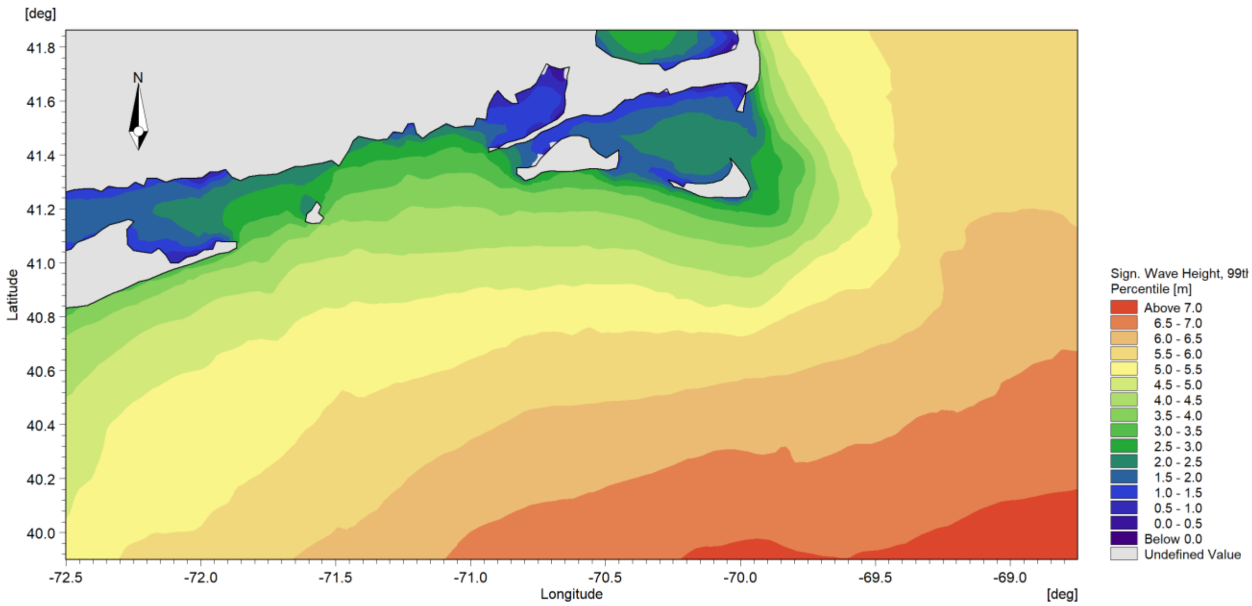

Figure 64. Significant wave height, H_{m0} 99th percentile Exceedance plot for Scenario 1: Baseline

The plots below show the exceedance difference in the Significant wave height (H_{m0}) for 95th and 99th percentiles at each grid location between the Scenario 2: 12 MW full build-out condition and the Scenario 1: Baseline condition. Upon inspection of the plots, they show:

- Ninety-five percent (95%) of the time the reduction in H_{m0} was less than 0.5 to 0.55 m inside the OSW. Outside the OSW the reduction was 0.15 to 0.2 m or less. At the coast the reduction was shown to be 0.05 to 0.10 m or less. The 95th percentile significant wave height in the area of the OSW farm structures was on the order of 2.5 to 3.5 meters.
- Ninety-nine percent (99%) of the time the reduction in H_{m0} was 0.6 to 0.75 m inside the OSW. Just outside the OSW the reduction was 0.4 to 0.45 m. At the coast the reduction was shown to be 0.10 to 0.15 m or less. The 99th percentile significant wave height in the area of the OSW farm structures was on the order of 4 to 5.5 meters.

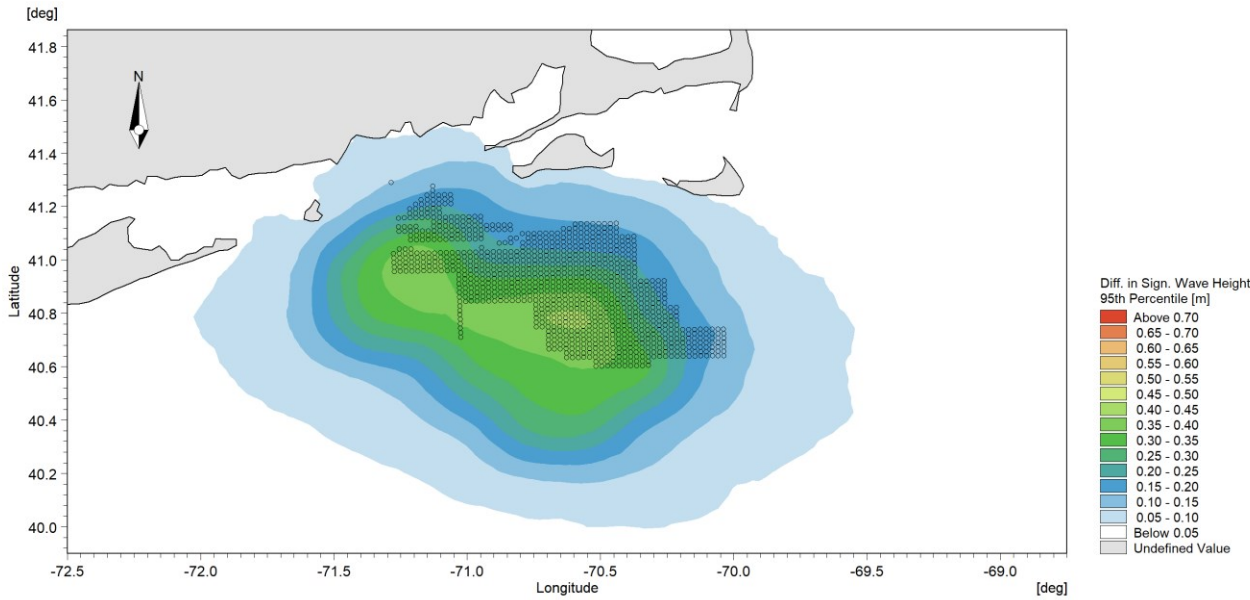

Figure 65. Exceedance difference in H_{m0} for 95th percentile
Wave Height Change for Scenario 1: Baseline minus Scenario 2: 12 MW Full build-out

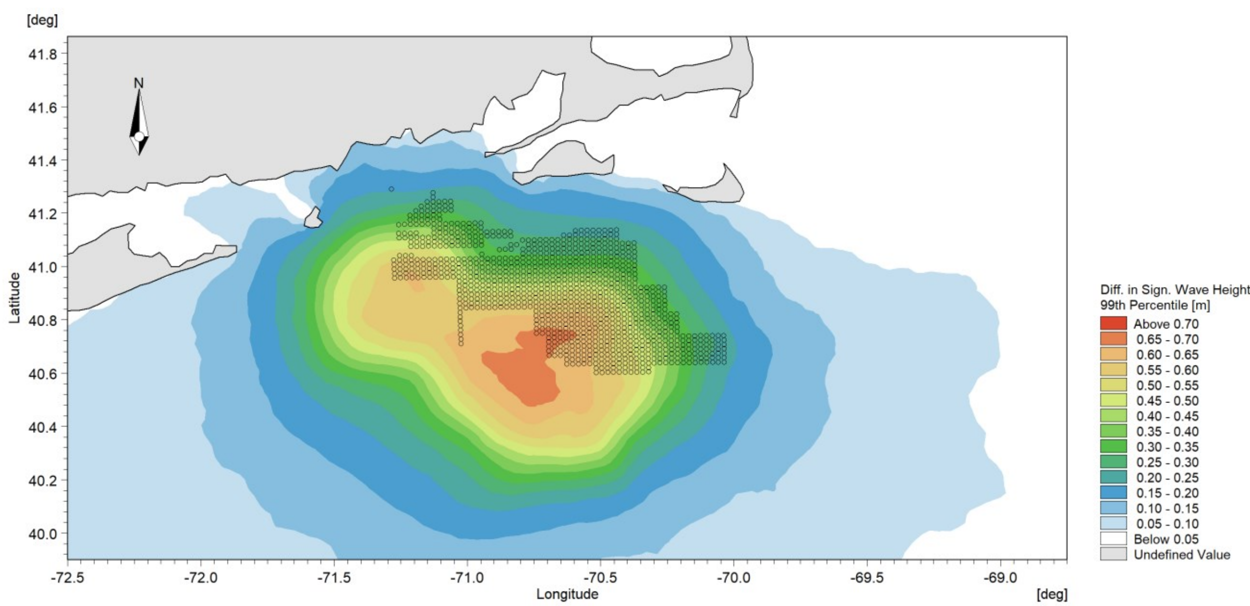

Figure 66. Exceedance difference in H_{m0} for 99th percentile
Wave Height Change for Scenario 1: Baseline minus Scenario 2: 12 MW Full build-out

It was noted in Chen (2016) that the wave heights might increase inside the OSW during storm conditions. It was postulated that this may be due to wave-current interaction. This study focused on long term regional effects and specifically tried to select a two-year period without large storms transiting the area. In addition, effects due to wave-current interaction were not included in this study. Finally, Chen (2016) correctly did not include the effect of wind wake loss during the two storms that were investigated since it is likely that the wind turbines would not be in operation during such extreme wind events. This study did include the selective shut-down of wind turbines in very low and high wind events to provide an accurate estimate of the overall reduction in wave energy.

5.5 Combined Effects of Current and Waves on Bed Shear Stress and Sediment Mobility

Another of the mesoscale effects of offshore wind energy facilities on coastal and oceanic environmental conditions and habitat that may change after turbines are installed is the bottom shear stress and thereby the potential for sediment transport. The drivers for changes in bottom stress due to the introduction of multiple structures into the offshore area are expected to be:

1. Changes in the current speeds which could include:
    a. Local acceleration of the currents around the structures
    b. Decrease in overall current due to the introduction of increased energy loss due to the drag losses
2. Changes in the wave field in and around the OSW farm changing radiation stress and hence bottom shear stresses

These effects were studied using the HD model and the wave model separately and then combined via superposition of the effects on a time-step-by-time-step basis for the baseline and Scenario 2 12 MW full build-out cases. Wave-current interaction was not considered in this study. The combination methodology followed Soulsby and Clarke (2005). The following plots show the 95th percentile non-exceedance bed shear stress results for currents and waves separately and for combined currents and waves.

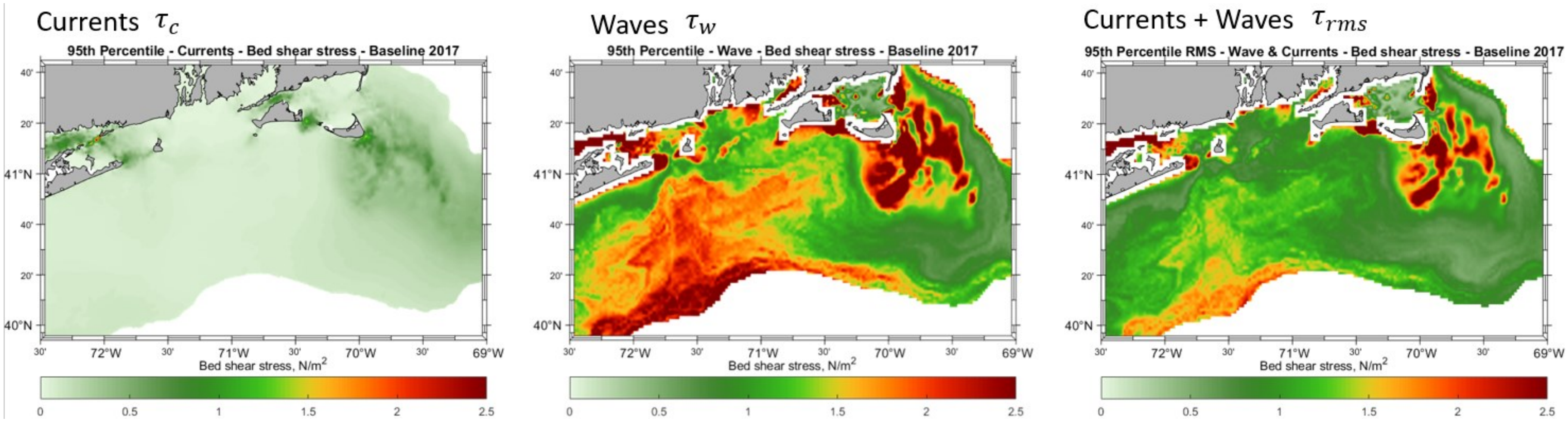

Figure 67. 95th percentile bed shear stresses in local study area Scenario 1: Baseline
LEFT: Current only, MIDDLE: RMS Wave only, RIGHT Current + RMS Wave for time period February 1, 2017 to February 1, 2018

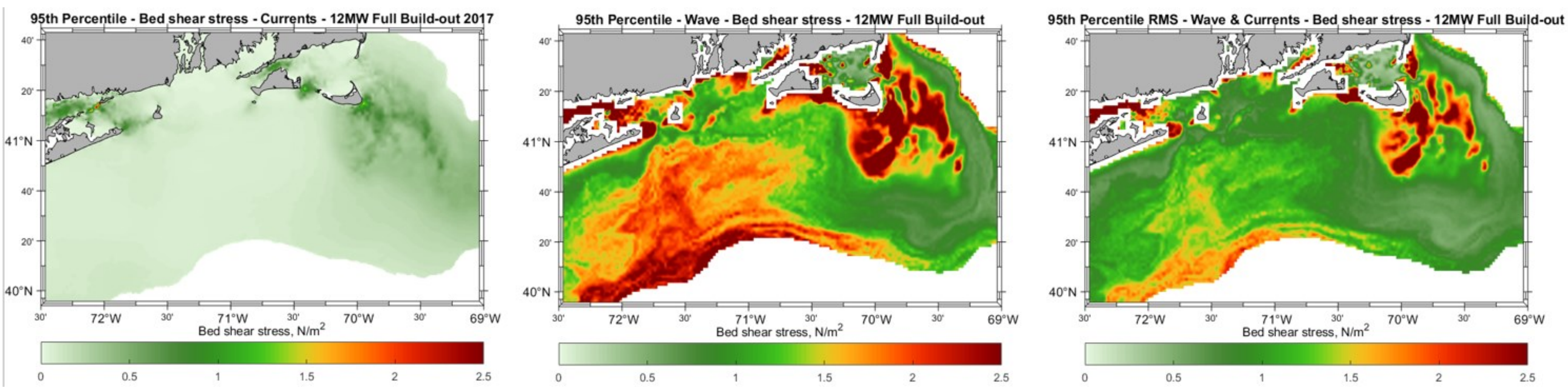

Figure 68. 95th percentile bed shear stresses in local study area Scenario 2: 12 MW full build-out
LEFT: Current only, MIDDLE: RMS Wave only, RIGHT Current + RMS Wave for time period February 1, 2017 to February 1, 2018

The following figure is a difference plot: Scenario 2 - Scenario 1 bed shear stress results. The order of the maximum Current + RMS wave bed shear stress in **Figure 67** and **Figure 68** is on the order of 2.5 N/m^2. In the difference plot below the maximum of the difference is of order of magnitude +/-0.25 N/m^2.

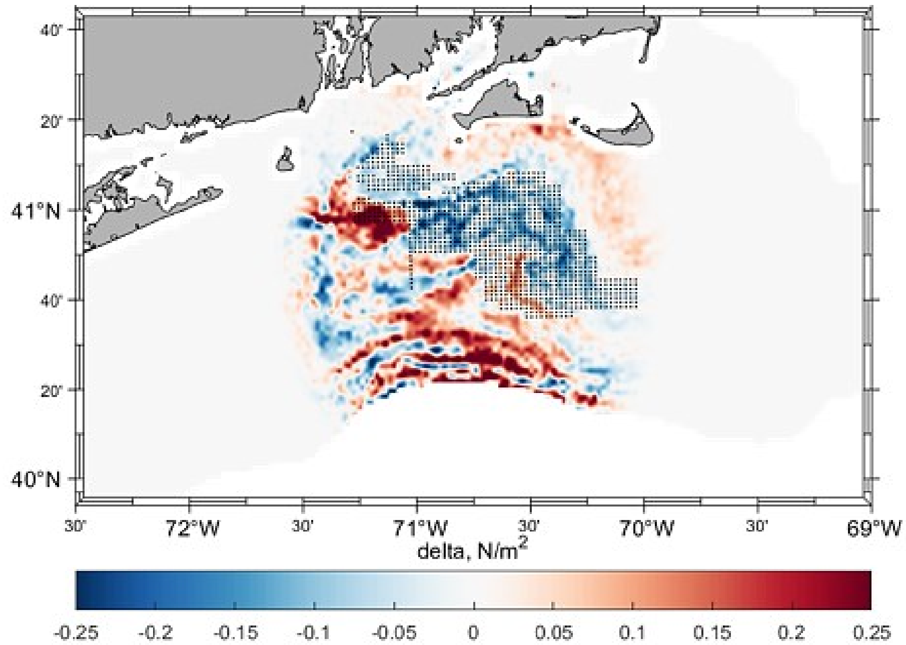

Figure 69. 95th percentile rms bed shear stress under combined waves and current difference
Local study area. Scenario 2: 12 MW full build-out – Scenario 1: Baseline. For time period February 1, 2017 through February 1, 2018

To put the bed shear stress results into context, we have estimated the largest sediment grainsize that will be moved, using a standard Shields relation for the critical bed shear stress. Below are maps of the sediment grain size that can be moved by the 95th percentile combined current and RMS wave bed shear stress. **Figure 70** shows the bed material grain sizes that can be moved under the combined 95th percentile current and rms wave forcing in the baseline (Scenario 1) and 12 MW full build-out (Scenario 2) conditions. By inspection the differences appear to be small.

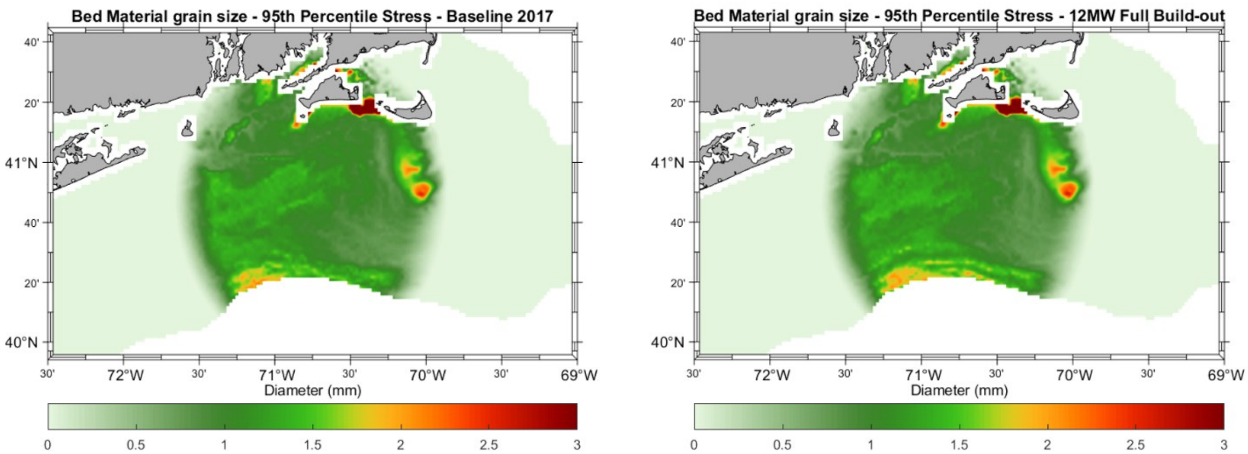

Figure 70. Bed material grain size that can be moved by the 95th percentile combined current and rms wave conditions.
On the LEFT is the map of the baseline (Scenario 1) results and on the RIGHT is the map of the 12 MW full build-out (Scenario 2) results.

Figure 71 below shows the difference in grain size that can be moved by the 95th percentile combined current and rms wave conditions. By inspection, the grain size that can be moved in the area of the OSW structures is on the order of 1 to 1.5 mm. The difference plus and minus in grain size that can be moved after the 12 MW full build-out scenario is installed can be seen to be +/- 0.3 mm or +/- 20 to 30%. However, the bed material found in this area is described in **Section 6.2.2.4** and in the habitat maps as coarse substrate, i.e. pebbles, shells, gravel, etc. It can therefore be inferred that the predominant seabed sediments in the area will likely not be affected by the changes in the bed shear stress in "average conditions" due to the introduction of the OSW structures.

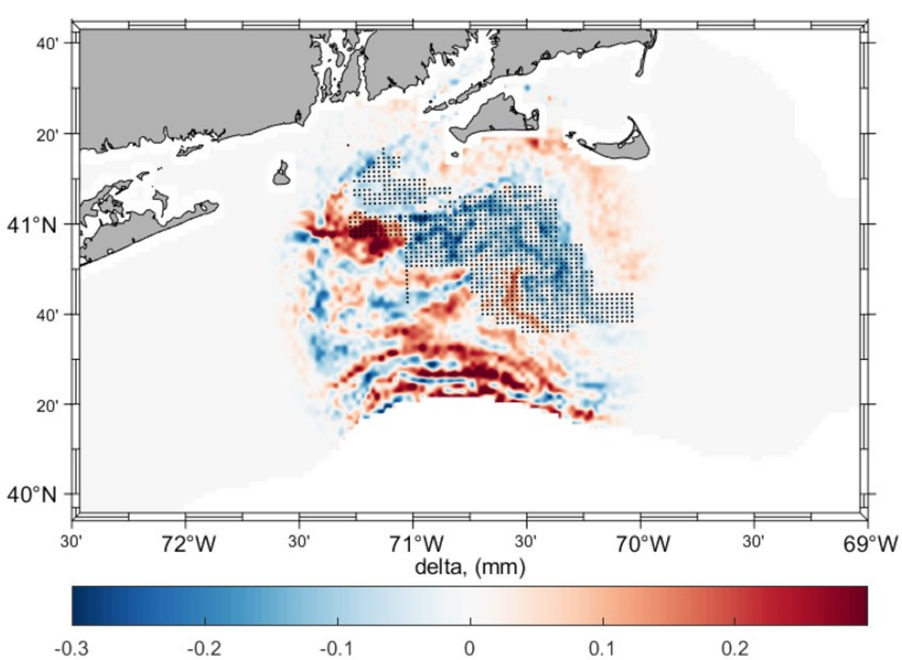

Figure 71. Difference between Baseline and Scenario 2 in critical grain size diameter (mm)
Local study area. Scenario 2: 12 MW full build-out – Scenario 1: Baseline. For time period February 1, 2017 through February 1, 2018

5.6 Effects on Temperature Stratification

Field measurements taken during a cruise over the time period of July 19–24, 2014 by Floeter et al. (2017) of temperature stratification inside a non-operational OSW in the German North Sea appeared to show "doming" of the thermocline and enhanced mixing (more uniform temperature) in the layers below the thermocline. This is illustrated in the paper where it shows two transects (W-E and S-N) through the BARD OSW in the German North Sea. It should be noted that the current in the area of the OSW is tidally dominated and predominantly in the East-West (reversing) direction. The water depth was fairly constant and on the order of 40 m with a range of 39.5 to 40.5 m) at the OSW site.

A similar modeling experiment was completed for the OSW area, reproducing the same sort of transects through the Scenario 1: Baseline and Scenario 2: 12 MW full build-out, to see if the temperature structure followed the same sort of patterns as observed by Floeter et al. (2017). The following figures show both the Scenario 1 and Scenario 2 results. The OSW is located between the two red vertical lines in each figure. Recall that the current in the OSW area is tidally dominated with mostly an East-West direction.

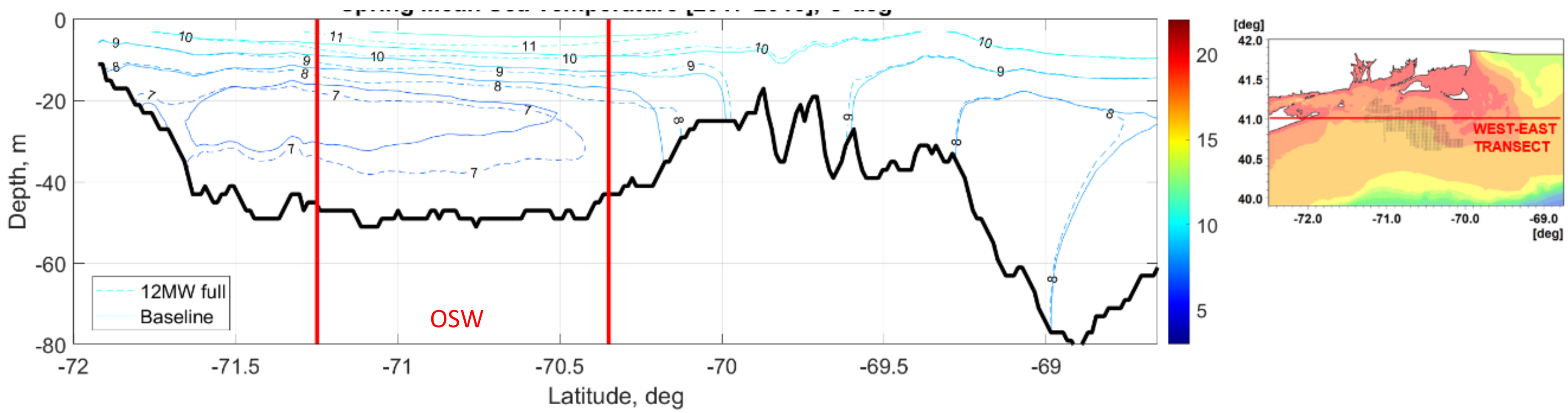

Figure 72. Average Spring vertical temperature structure of a West-East transect
The figure shows the 2017-2018 Spring average temperature contours from a transect for Scenario 2: 12 MW full build-out OSW and the same transect for Scenario 1: Baseline.

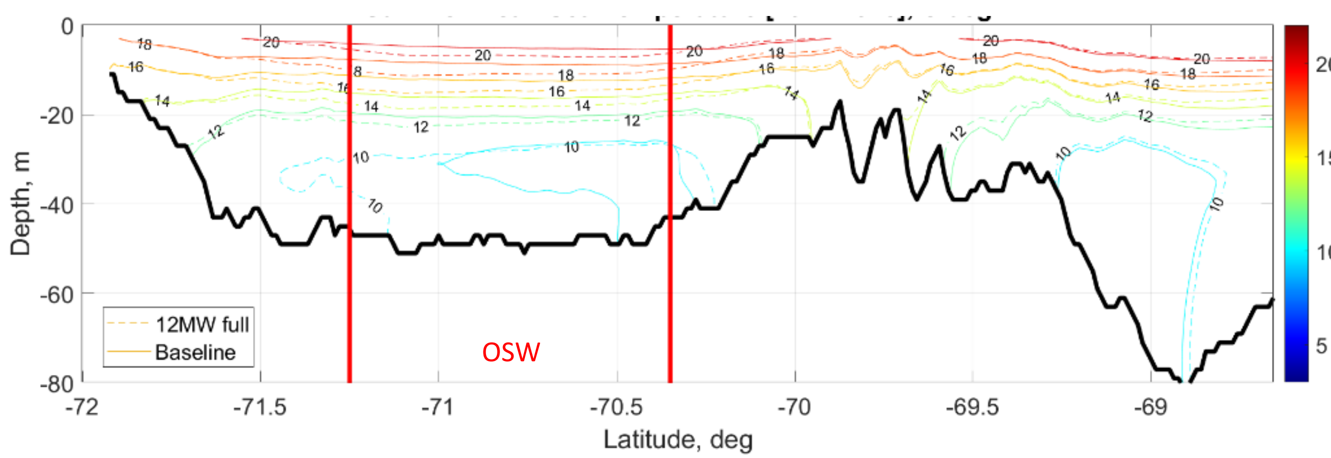

Figure 73. Average Summer vertical temperature structure of a West-East transect
The figure shows the 2017-2018 Summer average temperature contours from a transect for Scenario 2: 12 MW full build-out OSW and the same transect for Scenario 1: Baseline.

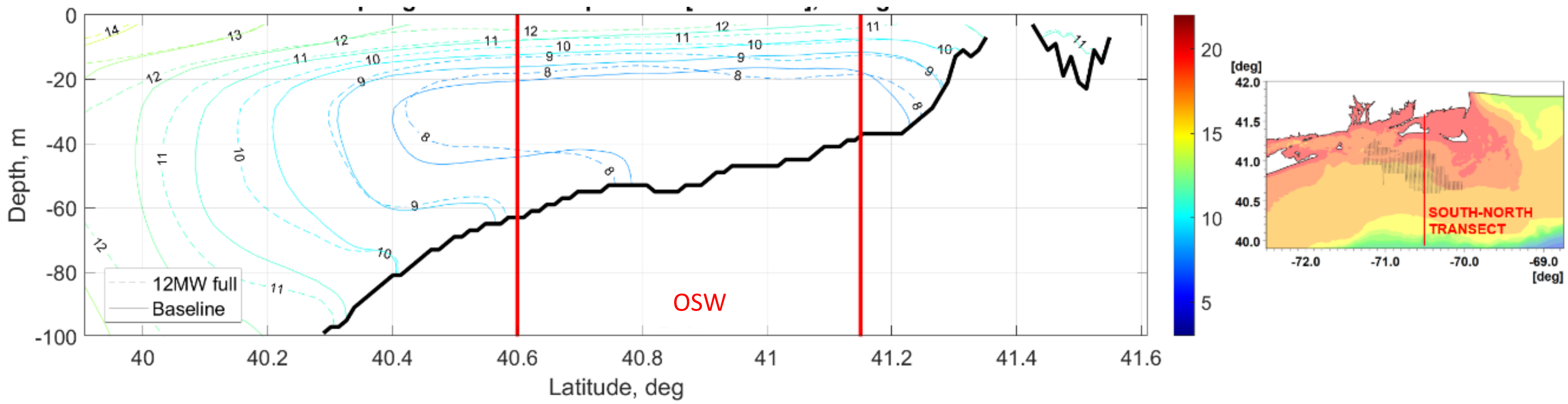

Figure 74. Average Spring vertical temperature structure of a South-North transect
The figure shows the 2017-2018 Spring average temperature contours from a transect for Scenario 2: 12 MW full build-out OSW and the same transect for Scenario 1: Baseline.

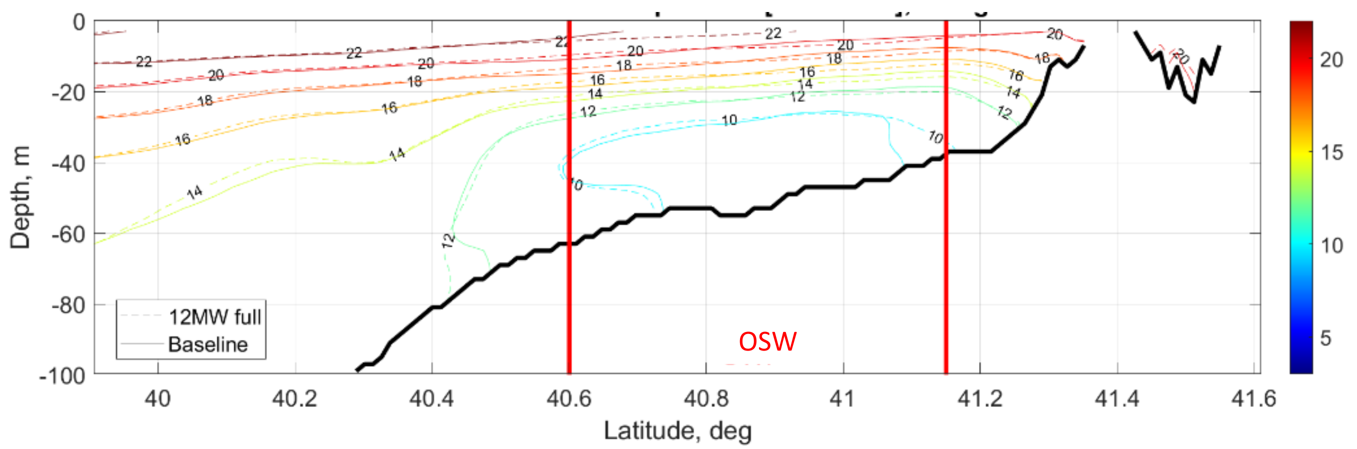

Figure 75. Average Summer vertical temperature structure of a South-North transect
The figure shows the 2017-2018 Summer average temperature contours from a transect for Scenario 2: 12 MW full build-out OSW and the same transect for Scenario 1: Baseline.

The thermocline on average moves down rather than "doming" in both the Spring and Summer model results. This is contrary to what was indicated by the field measurements collected by Floeter et al. (2017). In addition, it appears that more cold water is retained within the OSW (Scenario 2) in the Spring and Summer than without any structures (Scenario 1). Again, this may be contrary to the field measurements collected by Floeter et al. (2017), although natural variability in the field data does make the assessment uncertain. This may indicate:

- There are significant differences between the two sites in terms of location relative to the shelf and the general circulation around the OSW, the temperature and stratification regime and depth
- That the model does not yet include enough turbulent mixing or has a different vertical structure of the stratification
- That the solar radiation and therefore heat transfer at the surface is greater in the MAB than it is in the North Sea location that was investigated by Floeter et al. (2017).
- That the current speed is on average sufficiently diminished inside the OSW in the model so that in the lower water depths the cold water is retained longer.
- The BARD OSW was not operating during the Floeter et al. (2017) site surveys, so there was no current speed reduction due to wind wake loss.
- Or other site-specific effects.

Further study is warranted regarding this topic. However, for the present study of the impacts on larval transport with and without the OSW structures, the results of the ABM are largely unaffected by these relatively small differences in the water temperature stratification.

5.7 Conclusions Drawn from Hydrodynamic Modeling

Regional hydrodynamic models have been applied that describe the currents, temperature, and salinity variations as well as wave conditions. The models have been validated with available observations and applied for a hindcast covering the period 2017-2018. The validation shows that the model provides a realistic representation of the conditions in the MAB, both qualitatively and quantitatively. The models have been applied to the Baseline, with no OSW and to 4 scenarios comprising full build-out with generic 15 MW turbines and full or partial build-out with generic 12 MW turbines.

The results of the modeling study clearly reveal that the introduction of the OSW structures into the Massachusetts-Rhode Island offshore area modifies the oceanic responses of current magnitude, temperature, and wave heights by:

- Reducing the current magnitude through added flow resistance as described in **Section 4.2**,
- Influencing the temperature stratification by introducing additional mixing as described in **Section 4.2**,
- Reducing current magnitude and wave height by extracting of energy from the wind by the OSW turbines as described in **Section 4.3.1** (current) and **Section 4.3.2** (wind).

These oceanic response changes in current magnitude and wave height have the follow-on effect of influencing the bed shear stresses and thereby sediment transport potential, larval transport, and settlement. In summary the HD model results show:

- The depth averaged currents vary from Baseline on the order of +11% to -8% in the 75th percentile differences depending on the OSW scenario investigated.
- Particle tracking which "integrates" the overall effect of the current on objects subject to them showed variations on the order of $\pm$10% between the baseline and the 12 MW full build-out

scenario. This is in line with the observed order of magnitude change in the depth averaged currents.

- The effect on the waves due to the introduction of the 12 MW full build-out scenario was a reduction on the significant wave height inside and around the OSW. The 95th percentile statistics showed H_{m0} (significant wave height) reductions that were on the order of 0.5 to 0.55 m inside the OSW. Outside the OSW the reduction was 0.15 to 0.2 m or less. At the coast the reduction was shown to be on the order of 0.05 to 0.10 m or less. The 99th percentile statistics showed reduction in significant wave heights were on the order of 0.75 m or less inside the OSW. Just outside the OSW the reduction was on the order of 0.4 to 0.45 m. At the coast the reduction was shown to be on the order of 0.10 to 0.15 m or less.
- The changes in bed shear stress between 12 MW full build-out (Scenario 2) versus the baseline (Scenario 1) were seen mainly in the OSW area and immediate vicinity. It was found that the difference plus and minus in grain size that can be moved after installation of the 12 MW full build-out scenario was on the order of +/- 0.3 mm.
- A review of the 12 MW full build-out (Scenario 2) versus the baseline (Scenario 1) HDM temperature stratification results showed a relative deepening in the thermocline of approximately 1 to 2 m and a retention of colder water inside the OSW farm area through the summer months compared to the situation where OSW structures were not present. The modeled effects on the temperature stratification due to the introduction of inside the OSW farm area appeared to be different than field measurements in two OSW's in the German North Sea (see Floeter et al. 2017). Further study of these effects is thus warranted. However, for the present study the small differences in the effects of temperature stratification did not alter the larval transport modeling results or conclusions.

The hydrodynamic model developed for this study meets normal standards of calibration and validation for regional impact assessment tools and thereby provides sufficiently robust descriptions of the current and wave variations throughout the area for use in the assessment changes in oceanic responses as a result of the OSW's. Please refer to **Section 8.1.1** for a complete explanation.

6 Agent-Based Model Setup and Validation

6.1 Overview

The content of the following two subsections provides a description of the overall content in this Section.

6.1.1 Model Set-up

An initial overview of the concept of ABM and general description of the methodology taken for the present study is provided before dedicated target species subsections that provide fuller explanations of ABM set-up parameters. This description focuses on the applied modeling input for each larval species as it relates to spawning, life cycle, movement and settlement suitability. The content is further defined by a protocol for describing ABMs (ODD; Grimm et al. 2020).

6.1.2 Validation Approach

The validation of the baseline scenario (Scenario 1) consists of a quantitative validation using Pattern Oriented Modeling (POM), an approach that involves deeper spatial, temporal, and vertical levels of validation analysis. As the POM validation approach is quite extensive, additional explanation of the general methodologies, and the significance of related results is provided in **Section 6.2.4**. The baseline validation subsection ultimately provides a conclusion as to the adequacy of baseline ABM results for determining the transport and settlement impacts on the three chosen species from the chosen OSW build-out scenarios.

6.2 Agent-Based Model Methodology

ABMs can assess population changes in time and space because of external stimuli. The subsection offers a general explanation of the principles behind ABM, followed by a description of the methodologies used to carry out the agent-based modeling.

6.2.1 The Concept of Integrated Agent-Based Modeling

The assessment of the state of ecosystems, degrees of anthropogenic stress, and population dynamics has long been conducted using top-down modeling, such as population growth models, species distribution models or population survival analysis. It is common for these models to perceive populations as being composed of units of identical individuals (De Roos and Persson 2005). While this approach is acceptable when dealing with general ecological theory, it neglects the large variation between individuals when predicting the effect of ecosystem perturbations on populations (see **Figure 76**).

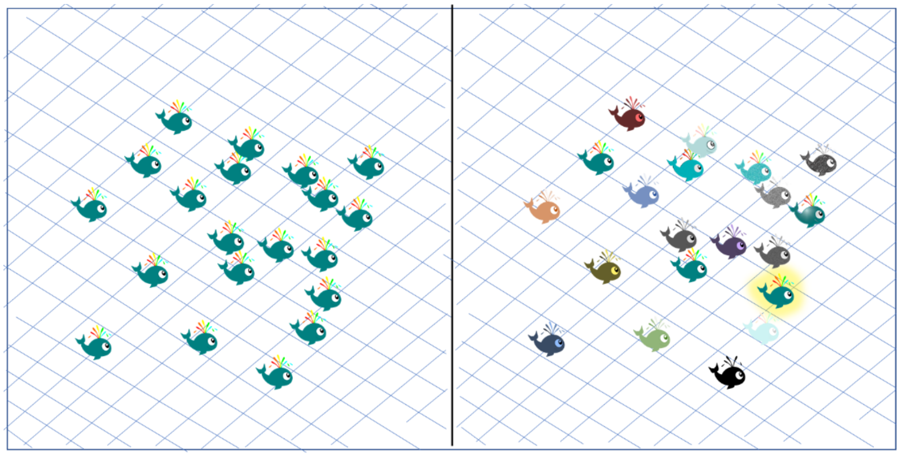

Figure 76. Illustration of difference in top-down and bottom-up population impact models
LEFT: Top-down population models assume all individuals in the population, or its sub-units are identical; RIGHT: Bottom-up models estimate the population effect by summing up the effect of the individuals.

The ABM is an alternative bottom-up population model, where focus is on the traits and variation between the individuals. A core function of the model is to allow fundamental traits of the individual to be modeled stochastically, therefore making room for trait variance between individuals. Individuals, onwards called agents, are subsequently released into a simulated domain, with a predetermined range of forcings, such as temperature, wind speed, water depth, noise, etc. In terms of their traits, the agents then interact with the simulated environment and other agents.

The sum of the behaviors expressed by the agents is the model output which in turn, as summed by the dynamics of the individuals, provides an indication of population dynamics (Thomsen et al. 2019; Mortensen et al. in press). A general ABM consists of a series of steps, wherein each agent makes a series of “decisions”. A 2 or 3D domain is supplied, to make the ABM spatially explicit.

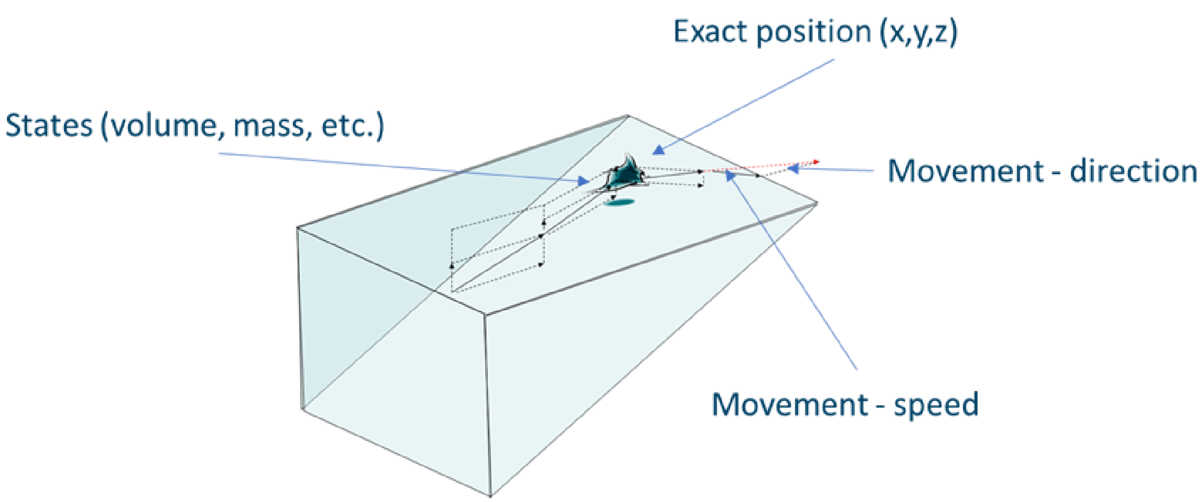

Figure 77. Example of traits possessed by individuals in ABM
In ABM, every agent possesses individual and unique traits, simulating the variation in real world populations.

Initially, agents are released into the model domain and each agent attains the traits and states defined by the model. While the value of each trait will be different between the agents due to the stochastic selection processes defined in the ABM, they remain the same throughout the life of the agent. States, such as weight of the agent, distance traveled, etc., will change over the course of the agent's life. Ultimately, decisions made by the agents are based on their traits, combined with external forcings and internal states, which will result in a range of behaviors. This decision process of the agent takes place in form of a decision tree (**Figure 78**), where the yes/no answer leads to a new decision and when the end of the decision tree is reached, behaviors are executed, state variables are updated, and the process cycles to the next timestep.

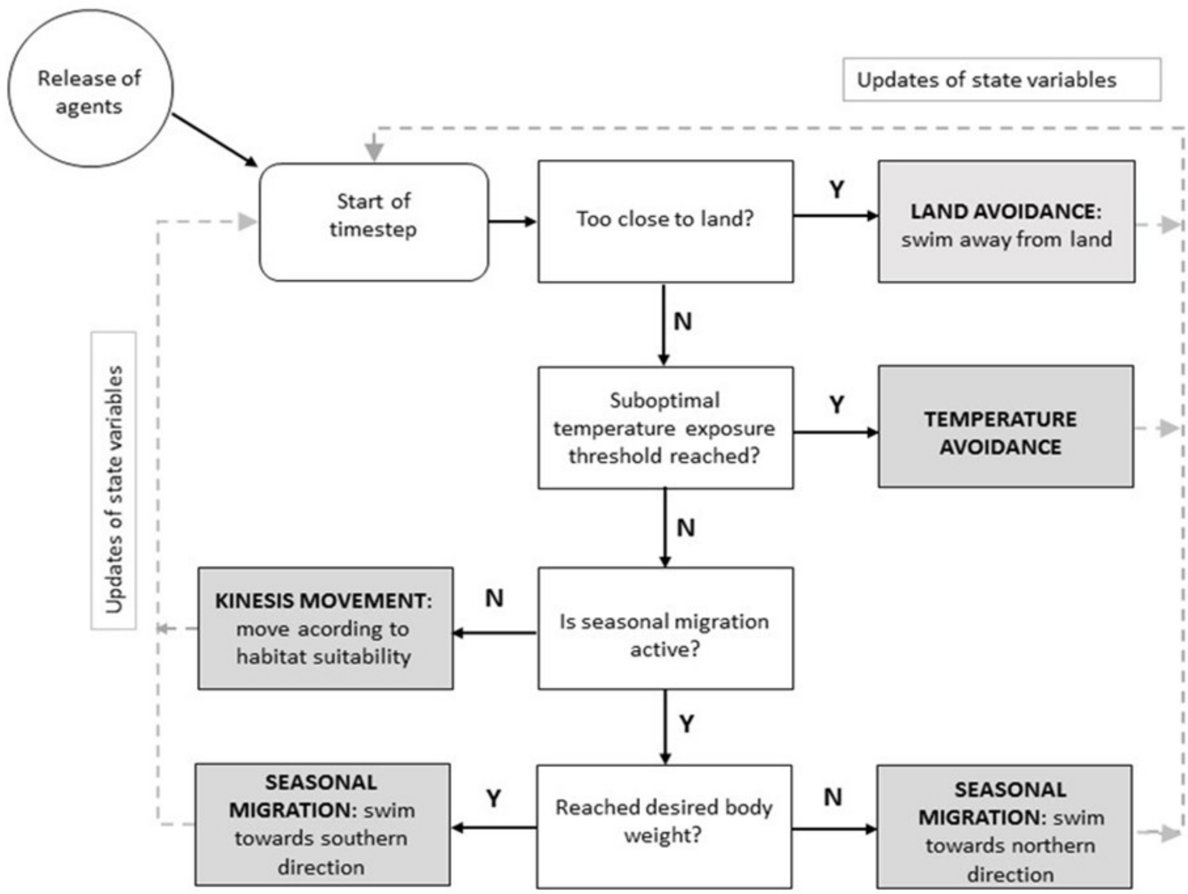

Figure 78. Example of a decision tree in an ABM, taken from Heinänen et al. (2018).
Agent-based modeling using the ABM Lab module in MIKE ECO Lab.

The ABM in this study was developed using ABM Lab, which is part of DHI's commercially available software suite, MIKE Powered by DHI. The MIKE Zero suite allows for seamless integration of agent-based models with state-of-the-art 2D and 3D hydrodynamic models using a coupled Eulerian-Lagrangian model framework. ABM Lab offers an open and flexible coding environment for defining and customizing simple to advanced biological traits and processes using a series of user-defined arithmetic expressions and state variables, which allows simulated agents (e.g. larvae) to react and interact with a dynamically changing virtual environment. Model agents are, however, not constrained by the resolution from other model output and can move independently over the grid resolution of other applied models (e.g. the HDM). The agents can, however, gather information from the grid cells that they currently occupy as well as the surrounding cells, which drives the decision-making process of each individual agent.

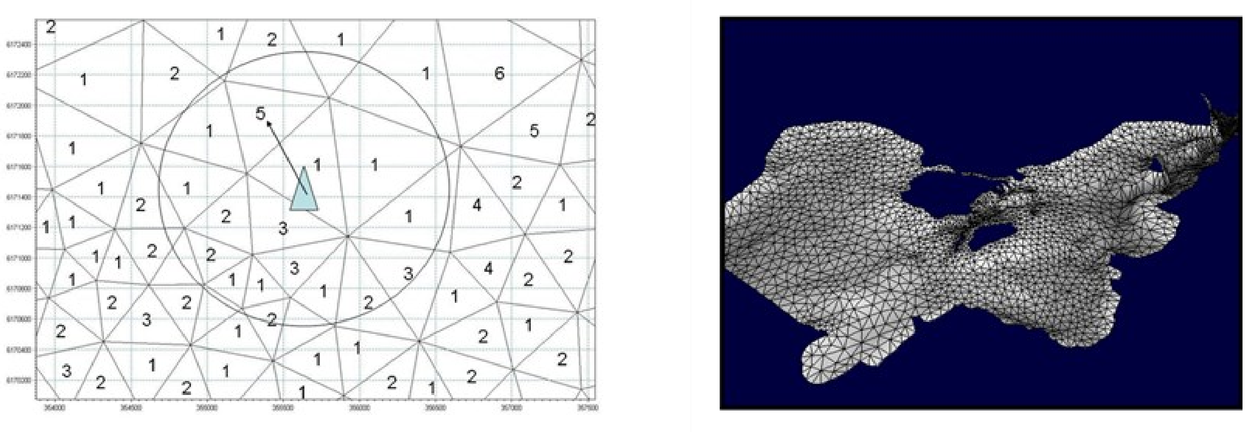

Figure 79. Example of an agent navigating grid cells
Right: full HDM for an ocean basin right: details of the HD mesh. Agents in ABM lab can navigate in the same domain as the HDM, gathering information from the grid cell that the agent occupies and the surrounding cells, however the agent's movements are not confined by the resolution of the grid cells.

Furthermore, external model forcings varying in time can be introduced into the ABM as being either vary or constant across the whole domain. This means that certain forcings can be in effect everywhere in the domain at specific timesteps, such as the GPS position of a survey vessel traveling in the domain across time. For spatially varying forcings, this is used to define specific properties of specific points in time and space. An example of a spatio-temporally varying forcing is 2D wind fields derived from outputs of meteorological models.

6.2.2 Approach for Larvae Agent-Based Modeling

In line with the overall objective of the study, the purpose of ABM was to simulate the larval transport of selected species, namely the sea scallop (*Placopecten magellanicus*), silver hake (*Merluccius bilinearis*), and summer flounder (*Paralichthys dentatus*), and changes in their transport patterns, if any, arising from the alteration of oceanographic transport patterns induced by chosen OSW build-out scenarios. The ABM approach was chosen due to its ability to better encapsulate relevant larval transport characteristics such as:

- Settlement rate and population abundance as a function of mortality and growth parameters (Allain et al. 2007).
- Settlement probability as a function of life stage, substrate material, and environmental variables including temperature, water depth, and salinity.
- Dispersal patterns, and hence recruitment rates at different sink areas, as a result of larval swimming speeds (Faillettaz et al. 2018).
- Vertical migration patterns of larvae as a function of daylight and tidal conditions (Jenkins et al. 1998, Benson et al. 2021).

Inclusion of these variables allowed experts to simulate dispersal and settlement patterns more accurately than what can be achieved with standard passive drift particle-tracking algorithms and/or with 2nd order advection-dispersion transport models.

The general Agent-Based Modeling steps included:

- Identifying relevant behavioral responses and associated state variables needed for each species to specify the ABM templates
- Customizing an existing larvae template with identified variables to match selected species
- Coupling the ABM templates to the hydrodynamic model to allow larval agents to sense (and react to) the physical environment (including current direction and speed, temperature, salinity, etc.) in time and space
- Setting-up validated baseline ABMs for the larval agents that were suitable for subsequent OSW build-out Scenario modeling analyses.

The larvae ABM templates consist of a range of behavioral decision rules and state variables, fitted to match the selected species larvae. In order to customize the templates to fit the selected species, key traits of the selected species were identified. After this, behaviors were parameterized with literature values related to the specific behavior. In the cases where literature values did not exist for the species, values for related species were used or based on expert knowledge. The templates were also adjusted based on testing and validation processes before the larvae build-out runs were executed.

The ABM templates are documented in detail in **Appendix B** following the *Overview, Design concepts and Details Protocol for Describing Agent-Based and Other Simulation Models* (ODD; Grimm et al. 2020).

6.2.2.1 Super-Agent Methodology

The concept of a *super-agent* was used in the present study's models due to the high fecundity rates of mature of the target fish and scallop species, each of which typically produces in the range of millions of eggs per spawning season. This allowed for the aggregation of numerous individual agents into a single entity, and is a common approach employed in ecological modeling (Scheffer et al. 1995). Aggregation of this form compacts similar pieces of information and reduces computational load for the simulation, preventing run-time from increasing beyond practical limits. Within the super-agent, the proportion and attributes of zygotes and larvae are varied and monitored over time, such that they undergo growth and mortality processes over the simulation period and are extracted and removed from the super-agent when they die or settle successfully. An illustration of this concept is shown in **Figure 80** below.

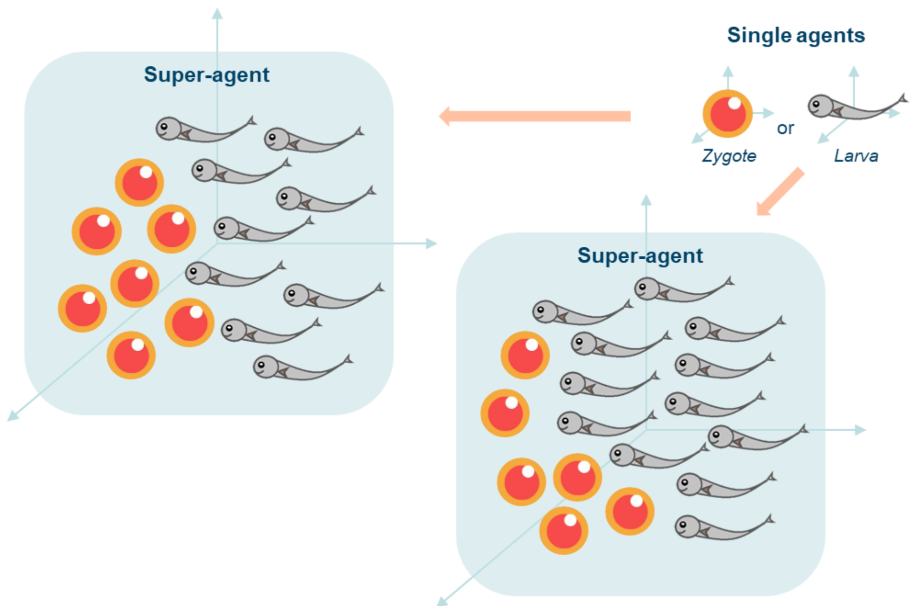

Figure 80. Implementation of the super-agent concept
Individual zygotes and larvae are aggregated as super-agents, and progress spatially through the model domain as a single unit. Each super-agent comprises either zygotes or larvae or both zygotes and larvae, with the ratio of agent types determined by arithmetic equations governing the growth and mortality processes of the super-agent.

While relatively simple to implement, there are drawbacks to this approach, one being that it is challenging to relate super-agents to individual agents in time and space (Parry and Evans 2008). In cases where the movement of super-agents is governed by the same set of rules as those of individuals, spatial clustering of individual agents may emerge i.e. super-agents may occupy fewer cells and show more limited dispersion patterns than individually modeled agents would. For spatially explicit ABMs it is therefore important to consider tests to compare the results of applying different super-agent scaling factors in the model (Parry and Bithell 2012).

Additionally, **Figure 81** shows the parameterized life stages as modeled by a typical super-agent. Each of the arrows is a decision point in the model affected by the probability of mortality, effects of the surrounding environmental stimuli, age-dependent sigmoidal gain probability curves and in the end, the suitability of the substrate habitat in which the agent settles. The parameterized movement behavior of the super-agents differ across species and are illustrated separately in **Figure 87** for sea scallop, **Figure 92** for silver hake, and **Figure 98** for summer flounder in the subsequent sections.

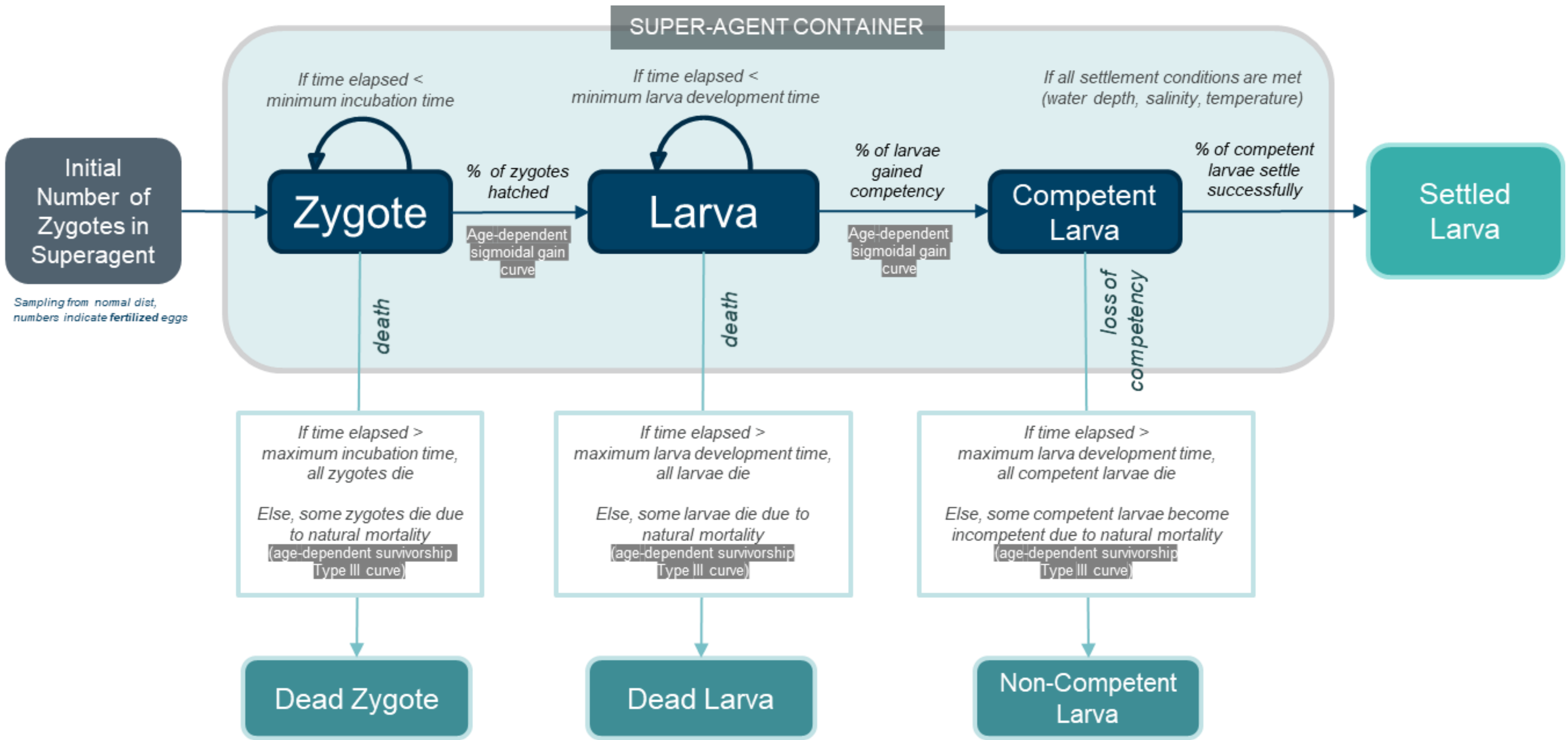

Figure 81. Parameterized life stages of a super-agent in the ABM templates
A super-agent container carries zygotes and larvae, which eventually die, become incompetent, or settle successfully.

6.2.2.2 Stochasticity

It is important to emphasize that stochasticity was applied in the model to varying degrees. The following processes are either semi- or fully dependent on stochastic processes:

- Upon the release of each super-agent, a random number is sampled from a normal distribution to determine the number of zygotes to be contained within the super-agent, in order to account for the varying levels of fecundity of each individual mature reproducing adult.
- Upon the release of each super-agent, random numbers are sampled from a normal distribution to determine the following growth parameters: minimum and maximum zygote incubation time and minimum and maximum larval development time, to account for varying pelagic larval duration for each individual super-agent.
- Mortality rates from time-step to time-step are controlled by an age-dependent survivorship Type III curve (Houde 2002), with curve parameters input by the user.
- Zygote incubation and larval development rates from time-step to time-step are controlled by an age-dependent sigmoidal gain/loss curve (Tian et al. 2007), with curve parameters input by the user.
- Horizontal and vertical dispersion of super-agents in order to account for the effects of unresolved turbulence in the hydrodynamic model. The magnitude of dispersion is scaled to the magnitude of the predicted currents.
- Release points of super-agents are randomly determined by the model (within the user-determined release areas) to account for indeterministic nature of mature adult migration.

6.2.3 Applied Datasets

Relevant sources information on benthic habitat and larval life history, spawning habitats, distribution and abundance were gathered from organizations, published literature, bibliographic and library sources, and geographic information system (GIS) datasets. **Table 8** below provides a list of general datasets used for the ABM. Detailed lists of data and references for specific species are provided in **Section 9.3** to **Section 9.5**.

Table 8. Datasets employed for the ABM

No.	Data Source	Descriptor	Citation
1	USGS CONMAP Sediments Grainsize Distribution	Maps of sediment classifications based on grain size distributions. GIS polygon layer.	USGS 2005
2	NOAA NCEI Multibeam Bathymetry Database (MBBDB)	Comprehensive database of multibeam bathymetric data on a global scale.	NOAA 2004
3	GEBCO Gridded Bathymetry Data	Global terrain model for ocean and land at 15 arc-second intervals.	GEBCO 2020
4	NOAA Essential Fish Habitat Data (EFH) Inventory	Geospatial habitat information of the species currently mapped in the NOAA Essential Fish Habitat Mapper	NOAA 2018

No.	Data Source	Descriptor	Citation
5	School for Marine Science and Technology (SMAST) Scallop Biomass Data	Scallop catches from NOAA Northeast Fisheries Science Center (NEFSC) scallop dredge surveys during the years 1966 to 2014. Accessed from Northeast Ocean Data Portal.	SMAST 2016
6	Northeast US Ichthyoplankton Dataset – EcoMon and MARMAP	Compilation of multi-species ichthyoplankton collection programs including the Marine Resources Monitoring, Assessment, and Prediction program (MARMAP, 1977 - 1987) and Ecosystem Monitoring (EcoMon, 1999 - present) program. Both datasets cover the Northeast U.S. Shelf from Cape Hatteras, North Carolina, to Cape Sable, Nova Scotia.	Hare 2015
7	Northeast Fisheries Science Center (NEFSC) Sea Scallop Survey	Distribution and abundance of scallops and associated fauna obtained via standardized sea scallop dredge and the stereo-optic towed camera array (HabCam).	NEFSC 2021

6.2.3.1 United States Geological Survey Continental Margin Mapping (CONMAP)

The Continental Margin Mapping Program (CONMAP) sediments grainsize distribution for the United States East Coast Continental Margin dataset is the result of a joint program conducted by the USGS and WHOI which commenced in 1962. The sediment map is a compilation of grain-size data classified using the Wentworth (1929) grain-size scale and the Shepard (1954) scheme of sediment classification (USGS 2000).

The sediments grainsize distribution data layer serves as the basis of formulation of the Atlantic Benthic Habitat map (**Figure 82**, left) and its corresponding GIS shapefile. For sea scallop and summer flounder ABM, 2D benthic substrate suitability maps were generated using the ABM mesh as the underlying template. Indices were thereafter derived for each substrate type based on substrate preferences of pre-transformation larvae. A grid cell located at an area of a preferred substrate type has a higher substrate suitability index value than a grid cell located at an area of a less preferred substrate type.

The substrate suitability maps were inputs in the ABM and directly influence the probability of settlement of a competent larva at any given geographical location within the model domain. An example of a substrate suitability map is presented in **Figure 82** (right).

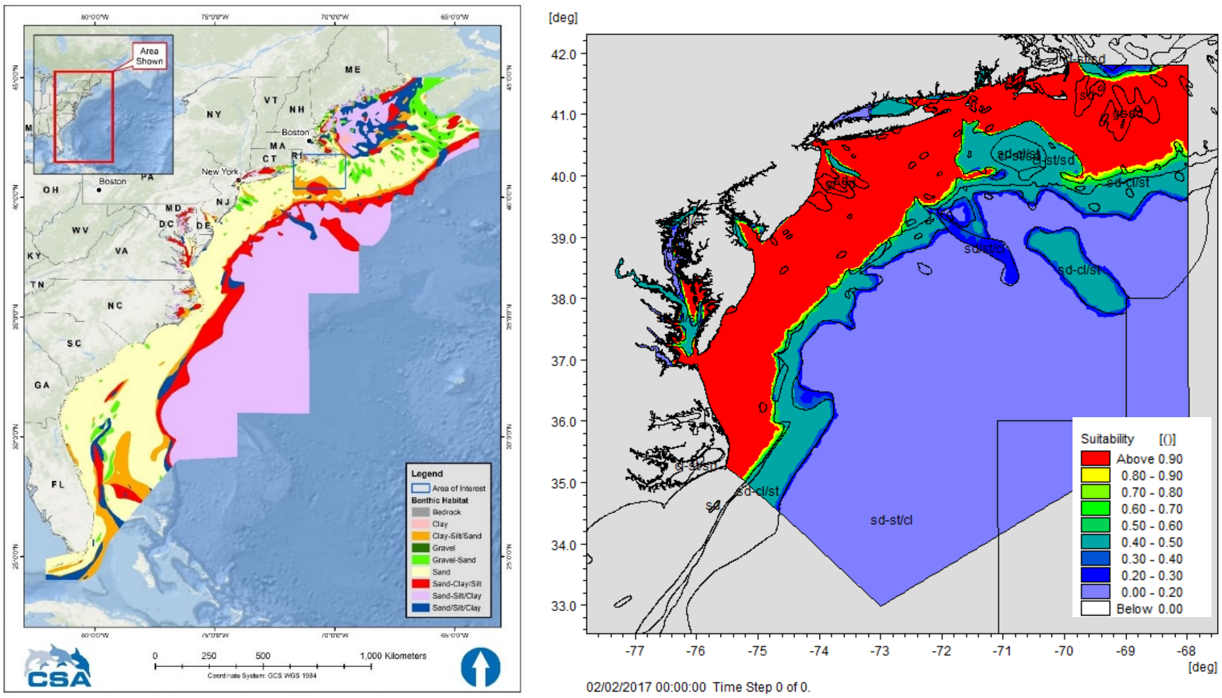

Figure 82. Benthic substrate maps
LEFT: Atlantic benthic habitat data provided by USGS Continental Margin Maps (CONMAP) program (Source: CSA 2020); RIGHT: Substrate suitability map for sea scallop, derived from substrate preference of pre-transformation larvae and benthic habitat map.

6.2.3.2 GEBCO and NOAA NCEI: Bathymetric Data

The bathymetric data used in the present study is described in **Section 2.2**. For the purpose of the ABM, the bathymetric data serves as a guideline for determining the spatial extent of spawning grounds for each modeled species, based on published research data on spawning water depths. The U.S. NOAA survey archive at NCEI provides high resolution gridded bathymetries for the project area, which is crucial for determining the settlement locations of modeled species, especially species for which settlement is only viable within set water depth thresholds (e.g. summer flounder larvae which are only observed to settle in shallow estuarine areas). Data from the GEBCO was used as a source for deep-water bathymetry.

6.2.3.3 NOAA Essential Fish Habitat (EFH) Data Inventory

Essential Fish Habitat (EFH) was officially defined by the U.S. Congress as "those waters and substrate necessary to fish for spawning, breeding, feeding or growth to maturity." in the 1996 amendments to the Magnuson-Stevens Fishery Conservation and Management Act (NOAA 2007).

NOAA Fisheries and the regional fishery management councils provide spatial data for designated EFHs that are vital for American fisheries, covering approximately 1,000 federal managed species. Pertaining to the present study, data was accessed for the Mid-Atlantic EFH, which is designated and described by the MAFMC for 12 managed species in NOAA Fisheries' Greater Atlantic region, as well as the New England EFH, which is designated for 28 managed species by the New England Fishery Management Council (NEFMC) in NOAA Fisheries' Greater Atlantic region (NOAA 2018).

Spatial information was accessed from the EFH data inventory for the purpose of establishing adult spawning areas and for calibration and validation of the ABM. The available data relevant for the study are as follows:

- Distribution and abundance of sea scallop in the Greater Atlantic region for:
  - All life stages
- Distribution and abundance of silver hake in the Greater Atlantic region for:
  - Eggs and larvae
  - Juveniles
  - Adults
- Distribution and abundance of summer flounder in the Greater Atlantic region for:
  - Eggs
  - Larvae
  - Juveniles
  - Adults

Sea scallops are capable of swimming freely throughout the water column but do not swim far or fast and are hermaphrodites with the ability of spawning whenever in proximity to other sea scallops. At broad scales, settlement occurs in areas inhabited by adults (Stokesbury et al. 2016) Therefore, the distribution of all life stages was utilized to identify areas where egg release and the eventual larval settlement would occur.

Silver hake and summer flounder distribution data was used to identify where eggs are found and were used as guidance on where the agents would be released, larval distributions were used for model calibration purposes and juveniles/adult distributions were used for model validation purposes.

6.2.3.4 SMAST and NEFSC: Sea Scallop Abundance Data

The University of Massachusetts Dartmouth's School for Marine Science & Technology (SMAST) has performed extensive drop camera surveys aimed at providing fishery resource managers, marine scientists, and fishing communities with an independent assessment of the U.S. sea scallop resource and its associated habitat (Bethoney and Stokesbury 2018). This dataset contains survey points for scallop catches from NOAA Northeast Fisheries Science Center (NEFSC) over scallop dredge surveys conducted over the years of 1966 to 2014, with estimates of total scallop biomass empirically derived from the drop camera survey image data.

The NEFSC Sea Scallop Survey began in 1980 and is an annual quantitative cruise to determine the distribution and abundance of scallops and Icelandic scallops, covering the three main areas of: MAB/Southern New England, Southern New England/Georges Bank, and Georges Bank with earlier surveys spanning as far south as Cape Hatteras (NEFSC 2021).

Both survey datasets were used for the validation of the sea scallop model via the POM methodology as detailed in **Section 6.3**, where the temporal and spatial patterns of observed sea scallop data were compared against the ABM outputs.

6.2.3.5 NOAA Ecosystem Monitoring (EcoMon) Data

The EcoMon data set was provided by the Biological & Chemical Oceanography Data management Office (BCO-DMO) and it contains the abundance and proportion of ichthyoplankton of the Northeast U.S. Shelf. The ichthyoplankton data was collected from surveys including the Marine Resources

Monitoring, Assessment, and Prediction (MARMAP) from 1977 to 1987 and the subsequent Ecosystem Monitoring (EcoMon) programs.

This dataset contains zooplankton biomass data sampled by bongo nets during the aforementioned surveys conducted at 120 randomly selected stations and 35 fixed stations throughout the continental shelf and slope of the northeastern U.S., from Cape Hatteras, N.C., to Cape Sable, Nova Scotia, and cover all of Georges Bank and the Gulf of Maine (NOAA 2018). The EcoMon data was used for the validation of the silver hake and summer flounder models via the POM methodology as detailed in **Section 6.3**, where the temporal and spatial patterns of observed silver hake and summer flounder data are compared against the ABM outputs.

6.2.3.6 Northeast Regional Ocean Council (NROC) Northeast Ocean Data Portal

The North East Ocean Data Portal was established in 2009 and is currently maintained by the Northeast Region Ocean Council (NROC). The portal provides curated theme maps covering key topics including marine life and habitat, commercial fishing, aquaculture, bathymetry, and habitat classification. Of importance to the present study are the data maps detailing abundance data of the three species of concern, as well as those detailing the physical characteristics of northeastern U.S. ocean, which serve as reliable references for the study of habitat distribution. **Figure 83** shows a screenshot of the portal displaying two data layers, namely the SMAST scallop abundance data (**Section 6.2.3.4**) and the bottom water temperature along northeast U.S. coast.

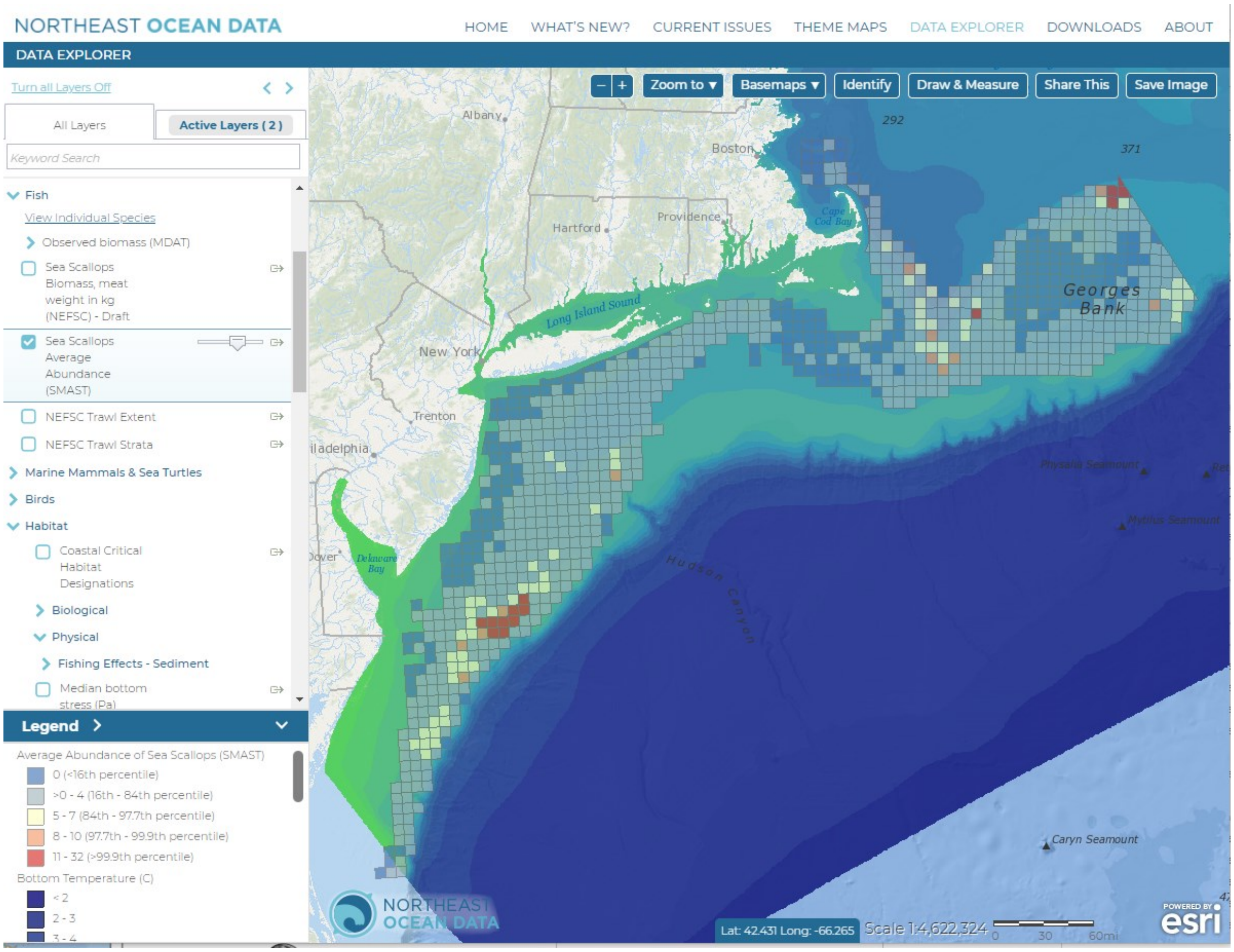

Figure 83. Screenshot from Northeast Ocean Data Portal (NROC 2009)
SMAST dataset of average sea scallop abundance in the Northeast Ocean Data Portal, displayed over a data layer showing bottom water temperature.

6.2.4 Agent-Based Model Setup

6.2.4.1 Sea Scallop

6.2.4.1.1 General Overview

Atlantic sea scallops (*Placopecten magellanicus*), hereafter referred to as 'sea scallops', are a bivalve mollusk that occur in continental shelf waters of the northwest Atlantic from the Gulf of St. Lawrence to North Carolina. Sea scallops are an important commercial fishery species in the northwest Atlantic region and are managed by the NEFMC. Two major stocks are recognized relative to the project area: a Georges Bank stock and a MAB stock (Stokesbury 2012; Stokesbury et al. 2016). In U.S. waters, the sea scallop fishery is managed by rotating fishing access among: 1) areas open to sea scallop fishing, 2) areas permanently closed to all fishing to protect seafloor habitats from destruction, 3) areas temporarily closed to sea scallop fishing, and 4) areas open to limited sea scallop fishing (NEFMC 2014). Sea scallops can live to 18 years, but most are less than 9 years old.

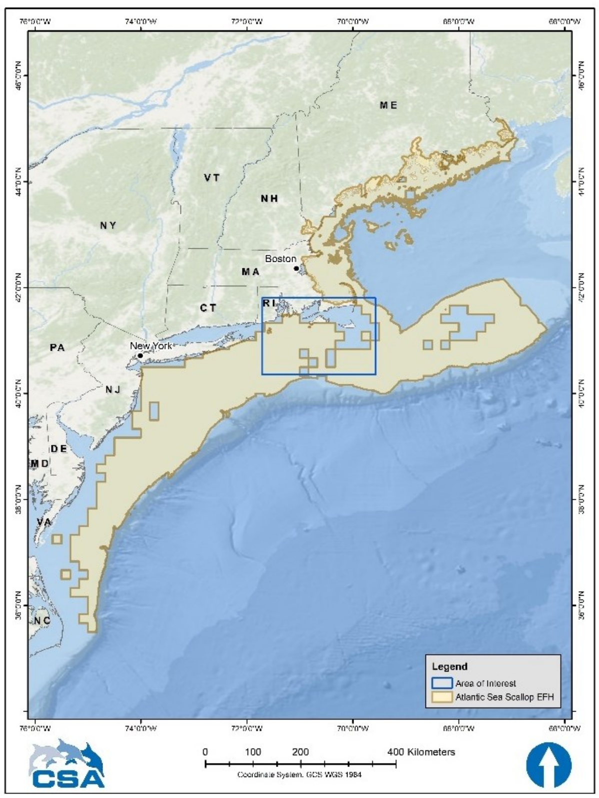

Figure 84. Sea Scallop habitat map
Sea scallops EFH in the Northwest Atlantic Ocean, extending from the Gulf of St. Lawrence to Cape Hatteras, North Carolina (NOAA 2018).

Sea scallops occur within relatively narrow ranges of temperature, salinity, and water depth. They prefer water temperatures between 10°C and 15°C, with 21°C being lethal, and are only found where salinity is greater than 26 Practical Salinity Units (psu). Salinities of 16.5 psu or lower can be lethal (Stewart and Arnold 1994). Sea scallops are found in water depths ranging from 15 to 110 m but are uncommon in water depths greater than 60 m (Hart and Chute 2004).

Sea scallops prefer areas with high current flow (Hart and Chute 2004). Habitat-specific flow rates are difficult to measure in the field but estimated values ranging from 0.03 to 0.13 m/sec have been used in habitat suitability models (Torre et al. 2018).

6.2.4.1.2 Super-Agent Class Parameterization

The simulation period for the sea scallop model (August 1, 2017 to November 30, 2017.) was selected to capture zygotes and larval activity during critical spawning seasons and larval migration periods. The parameterization of sea scallop spawning, life cycle, mortality, movement, and settlement suitability characteristics are detailed in the subsections below.

6.2.4.1.3 Spawning

Sea scallops spawn primarily during fall (August to October), but spring events occasionally occur (Stokesbury et al. 2016). Spawning occurs in shallower waters along the MAB, off of Long Island and in the Georges Bank, at temperatures from 6.5 to 16°C (Hart and Chute 2004). Mature adults do not migrate during spawning seasons; sea scallop super-agent release areas (**Figure 85, right**) were directly derived from observed distribution and abundance data of sea scallops collected from NEFSC sea scallop surveys (NEFSC 2021).

A total of 82,021 sea scallop super-agents were released over the entire simulation period in the model domain, with each super-agent initialized to contain a number of zygotes that is sampled from a normal distribution (mean = 50,000,000, standard deviation = 200,000) in order to account for the varying levels of fecundity of each individual mature reproducing adult. The normal distribution is roughly based on the Langton et al. (1987) estimation of fecundity of sea scallops from the Gulf of Maine. Egg production by adult sea scallops was related exponentially to size (shell height). For example, an individual with a shell height of 50 mm was estimated to produce one million eggs in one season whereas a 100 mm individual produced an estimated 29 million eggs in one season (Langton et al. 1987). Fecundity estimates reported by Langton et al. (1987) ranged from 1 to 270 million eggs per individual.

An analysis from NEFSC surveys on the densities associated with each spawning area in the model revealed that 20,568 (25%) agents would originate from MAB, 8,185 (10%) agents from Long Island and 53,268 (65%) agents from Georges Bank. Thus, the release patterns from each model spawning area were assimilated from the NEFSC survey data and the Stokesbury et al. (2016). A summary of parameters related to sea scallop spawning is presented in **Table 9** and **Table 10**.

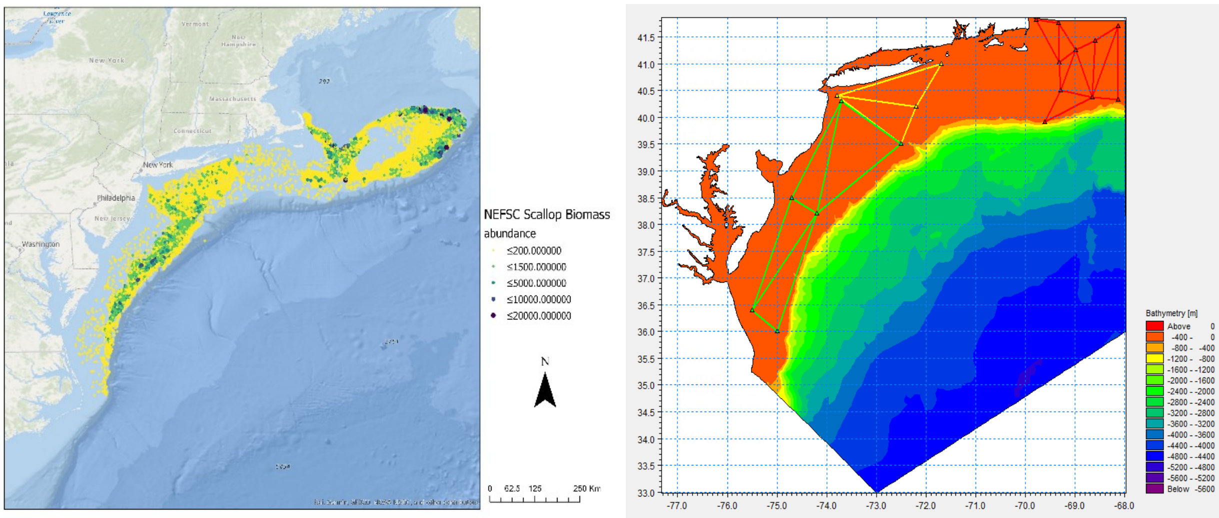

Figure 85. Sea scallop abundance map and model spawning areas
LEFT: Distribution and abundance of sea scallops collected during NEFSC sea scallop surveys during 1966-2014; RIGHT: Release areas in the sea scallop model, derived based on observed abundance data (NEFSC 2021).

Table 9. Sea scallop release period and volume

Area(s)	Release Period	Time Series
Green polygons in **Figure 85**	August 8, 2017 to October 13, 2017 Peak from August 18, 2017 to August 31 2017	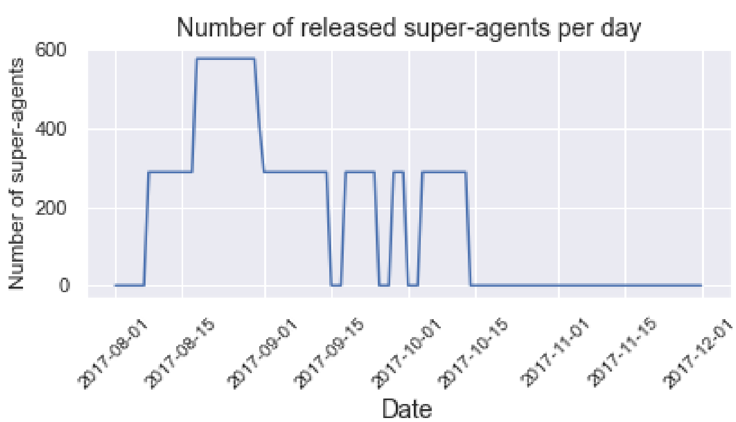

Area(s)	Release Period	Time Series
Yellow polygons in **Figure 85**	August 17, 2017 to September 1, 2017	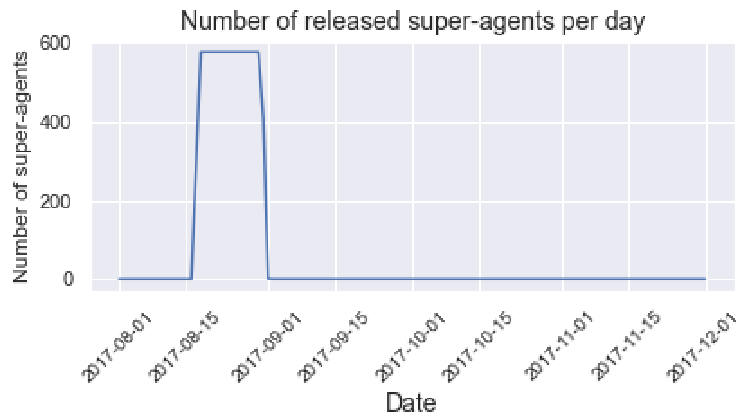
Red polygons in **Figure 85**	August 8, 2017 to October 13, 2017 Peak from August 22, 2017 to September 1, 2017	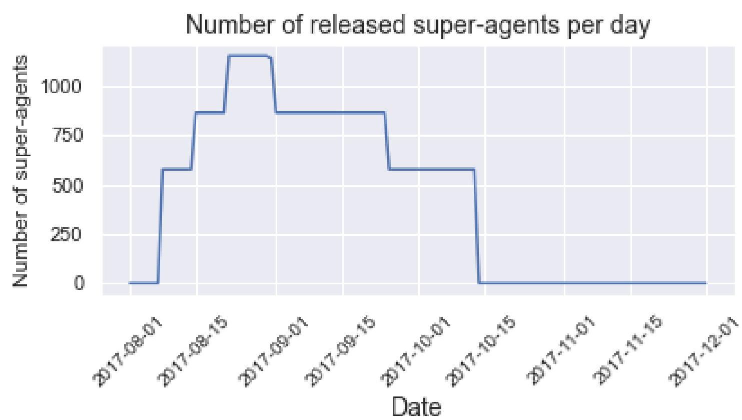

Table 10. Sea scallop spawning model parameters

Parameter	Literature Information/Value	Parameterized Value
Timing *Time of year when spawning is initiated*	Fall (Major); Spring (Minor) (Thompson et al., 2014)	Only fall spawning was modeled in the present study. Release of super-agents occurs from mid August (August 8, 2017) to mid October (October 13, 2017), peaking at end August 2017.
Duration *Spawning period*	Fall spawning periods range from Aug to Oct, depending on spawning areas (Hart and Chute, 2004)	Release of super-agents occurs from mid August (August 8, 2017) to mid October (October 13, 2017).
Quantities *Particle release during spawning*	Overall range of 1-342.8 million eggs per female across two studies:	Initial number of zygotes sampled from a normal distribution: • Mean: 50,000,000 zygotes

Parameter	Literature Information/Value	Parameterized Value
	• 2.5-342.8 million (McGarvey et al., 1992) • 1-270 million (Langton et al., 1987)	• Standard deviation: 200,000

6.2.4.1.4 Life Cycle

Eggs hatch in about 2 days and transform into pelagic larvae which after about 35-50 days in the water column, settle to the seafloor as juveniles (Hart and Chute 2004). Duration of pelagic stages are as follows:

- Buoyant eggs (~0.66 mm diameter, 1.0 specific gravity) released near-bottom, transform into trochophore larvae after two days; (Tremblay et al. 1994)
- Trochophore larvae transform into veliger larvae in 2 to 5 days (Tremblay et al. 1994)
- Veliger larvae persist for up to 35 days before becoming pediveligers which settle to the seafloor as juveniles in 5- 15 days. (Tremblay et al. 1994)

An overview of the early life stages of the sea scallop that are simulated in the model is presented in **Figure 86** and a summary of parameters related to sea scallop life cycle (growth and mortality) is presented in **Table 11**.

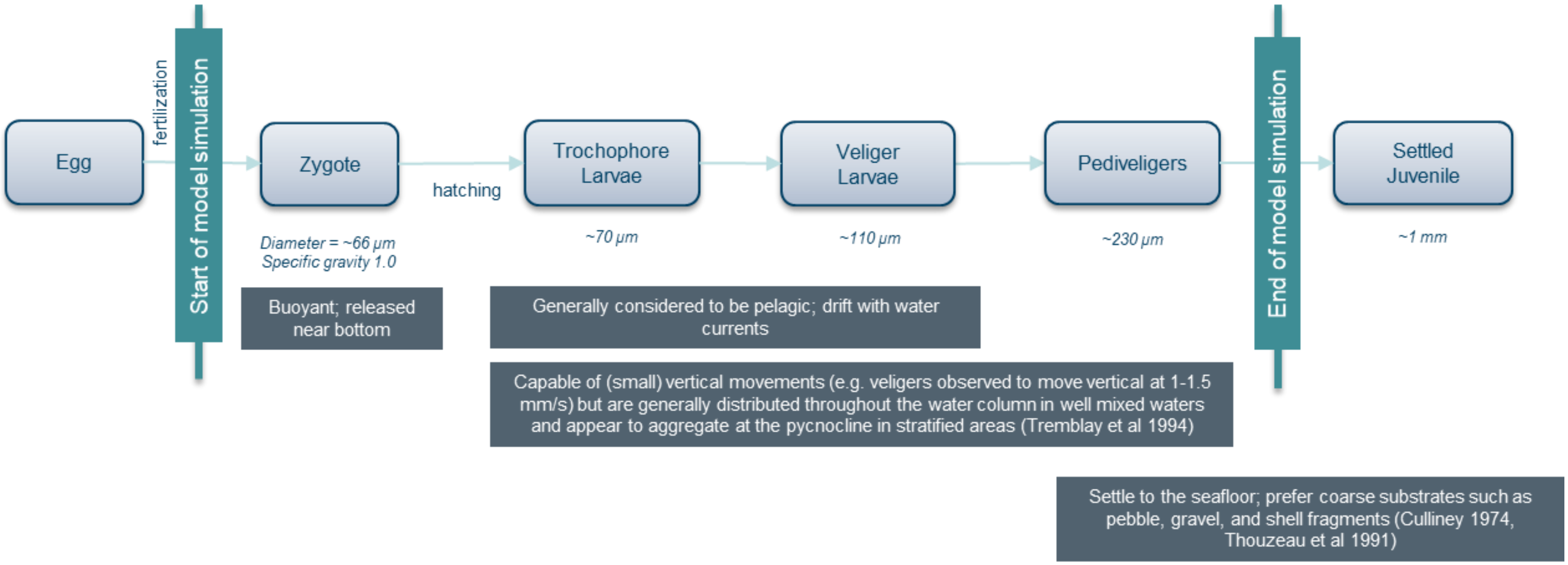

Figure 86. Early life stages of sea scallop as simulated in the ABM
A sea scallop agent is simulated to undergo life stage transformation from a zygote (fertilized egg) to a pediveliger; at this point it is ready to settle to the seafloor and begin its development to become a juvenile. Life stages beyond pediveliger stage are not included in the model.

Table 11. Sea scallop life cycle (growth and mortality) model parameters

Parameter	Literature Information/Value	Parameterized Value
Life Cycle Parameters		
Duration of egg stage *Incubation time from egg to larvae*	Hatch in 30-40 h at 12°C (Culliney et al. 1974)	Minimum zygote duration sampled from normal distribution: Mean: 30 hours Variance: 2 hours Maximum zygote duration sampled from normal distribution: • Mean: 40 hours • Variance: 2 hours All durations are from the time of release of super-agent.
Duration of larval stage *Time spent as a larva before settling/changing state*	Overall range of 28-82 days across four studies: • 40-60 days (Hart and Chute 2004) • 28-50 days in total – veliger (4-23 days), trochophore (13-28 days), prediveliger (28-35 days) (Culliney et al. 1974) • 4-6 weeks egg to settled juvenile (McGarvey et al., 1992) • 32-82 days (Pearce et al. 2004)	Minimum larval duration sampled from normal distribution: • Mean: 32 days • Variance: 1 day All durations are from the time of release of super-agent.
Number of stages between egg and adult *Total number of stages between egg and adult*	4 stages: egg, trochophore, veliger, prediveliger (Culliney et al. 1974)	3 stages modeled: Zygotes, pre-competent larvae, and competent larvae. Trochophore and veliger larvae are broadly categorized under the 'pre-competent larvae' group and pediveliger larvae under the 'competent larvae' group.
Growth Parameters		
Incubation rate of zygotes *Probability that a zygote will hatch and become a larva*	Not available	Age-dependent sigmoidal curve for incubation probability. Values are assumed and calibrated through an iterative process: • Maximum incubation probability: 0.7/day

Parameter	Literature Information/Value	Parameterized Value
Competency gain rate of larvae *Probability that a pre-competent larva will gain competency*	Not available	Age-dependent sigmoidal curve for competency gain probability. Values are assumed and calibrated through an iterative process: • Maximum competency gain probability: 0.8/day
Competency loss rate of larvae *Probability that competent larva will lose competency*	Not available	Age-dependent sigmoidal curve for competency loss probability. Values are assumed and calibrated through an iterative process: • Maximum competency loss probability: 1/day
Mortality Parameters		
Mortality parameters *Parameters related to the selected mortality*	Daily constant mortality of 0.25/day (Hart and Chute 2004)	Age-dependent Type III survivorship curve for mortality rate. Values are assumed and calibrated through an iterative process: • Minimum daily instantaneous mortality rate: 0.01/day • Maximum daily instantaneous mortality rate: 0.3/day

6.2.4.1.5 Movement

Trochophores, veligers, and pediveligers are capable of some vertical movement, but are generally distributed throughout the water column in well mixed waters and appear to aggregate at the pycnocline in stratified areas (Tremblay et al. 1994). At each time step, depending on the dominant life stage of agents contained in the super-agent, the super-agent exhibits different vertical movement behaviors. Additionally, it has been observed that sea scallop larvae can maintain position of their vertical location in the water column to stay near the thermocline. This was implemented in the model by placing a vertical control factor where the sea scallop agent would swim down if the agent's ambient temperature rises to 16.5°C and swim up if the temperature falls to 1°C (Munroe et al. 2018).

An overview of the sea scallop super-agent vertical movement behavior as simulated in the model is presented in **Figure 87** and a summary of parameters related to sea scallop movement is presented in Table **12**. The sea scallop super-agent is considered to be a passive drifter along the transverse plane, and thus its horizontal movement is purely a function of hydrodynamic forcings (i.e. horizontal current speed and direction).

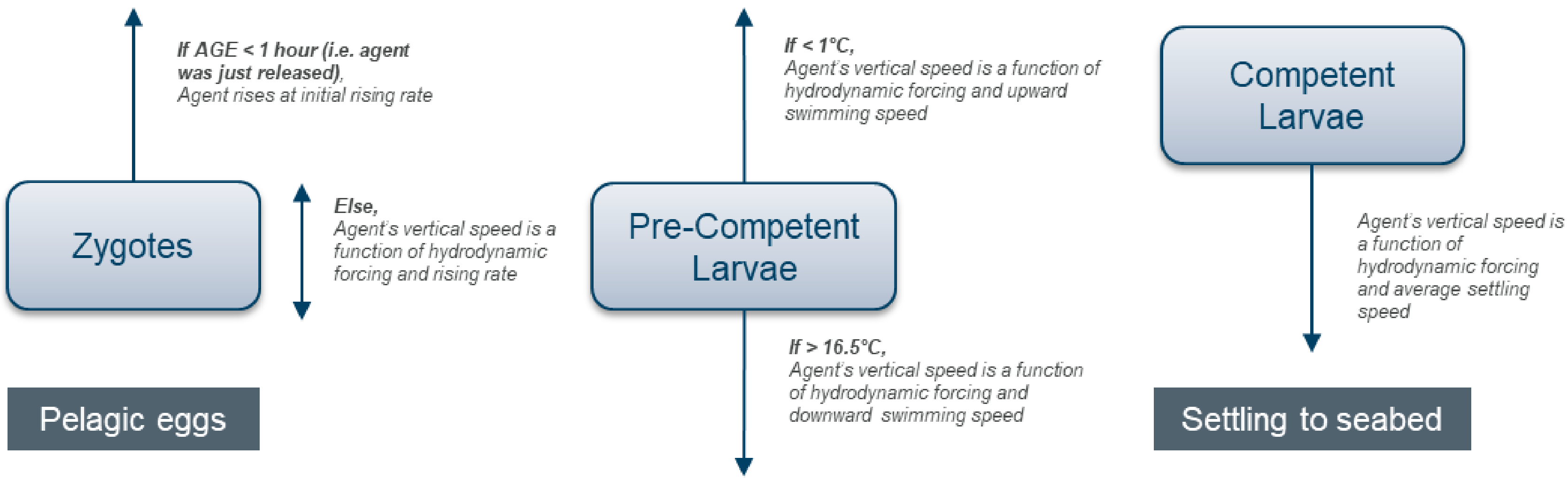

Figure 87. Parameterization of sea scallop zygotes and larval vertical movement characteristics
Sea scallop zygotes are pelagic and rise towards the water surface during their first hour of release from the seabed, after which it drifts passively along the vertical axis. Pre-competent larvae migrate vertically to stay within the thermocline (1-16.5°C). Settle-ready (competent) larvae sink and eventually settle on the seabed.

Table 12. Sea scallop movement model parameters

Parameter	Literature Information/Value	Parameterized Value
Buoyancy of egg *Maximum buoyancy (positive or negative) speed for fertilized zygotes*	Buoyant eggs (~0.66 mm diameter, 1.0 specific gravity) (Tremblay et al. 1994)	Maximum upward speed of 0.0014 m/s
Vertical swim speeds *Maximum vertical swim speed for larvae, independent of current speeds (m/s)*	0.003 m/s	Average vertical swim speed sampled from normal distribution: Mean: 0.003 m/s Standard deviation: 0.0005 m/s
Horizontal swim speeds *Maximum horizontal swim speed for larvae, independent of current speeds (m/s), if present*	0.20 mm/s for a 250 μm veliger	Horizontal swim speed is insignificant relative to hydrodynamic forcings – super-agent assumed to drift passively in horizontal plane.
Temporal changes in vertical distribution *Distribution of larvae in the water column dependent on time of day*	Daily migrations to water surface	Super-agent migrates to water surface at night for feeding. Vertical swim speed is a function of hydrodynamic forcing and upward swimming speed, which is sampled by normal distribution: Mean: 0.003 m/s Standard deviation 0.0005 m/s

6.2.4.1.6 Settlement Suitability

At settlement, pediveligers (spat) prefer coarse substrates such as pebble, gravel, and shell fragments over fine substrates like clay and fine sand (Culliney 1974, Thouzeau et al. 1991). At broad scales (100 m to kms) settlement occurs in areas inhabited by adults (Stokesbury et al. 2016).

Settlement suitability index map for sea scallop (**Figure 88**) is based on the preferred substrate of young sea scallops, which is coarse substrate i.e. pebbles, shells, gravel etc. Each 2D grid cell of the model mesh is assigned a settlement suitability index value between 0 to 1, with higher values indicating higher suitability.

Settling is described as a two-step process, where specific conditions must be met in order for the larvae to settle: the super-agent must contain competent larvae and be located in a grid cell where variables are within the user-determined threshold at the time step of settlement; in this case, water depths must be between 15 to 60 m and temperatures must be between 0 to 21°C for settlement to take place (**Table 13**).

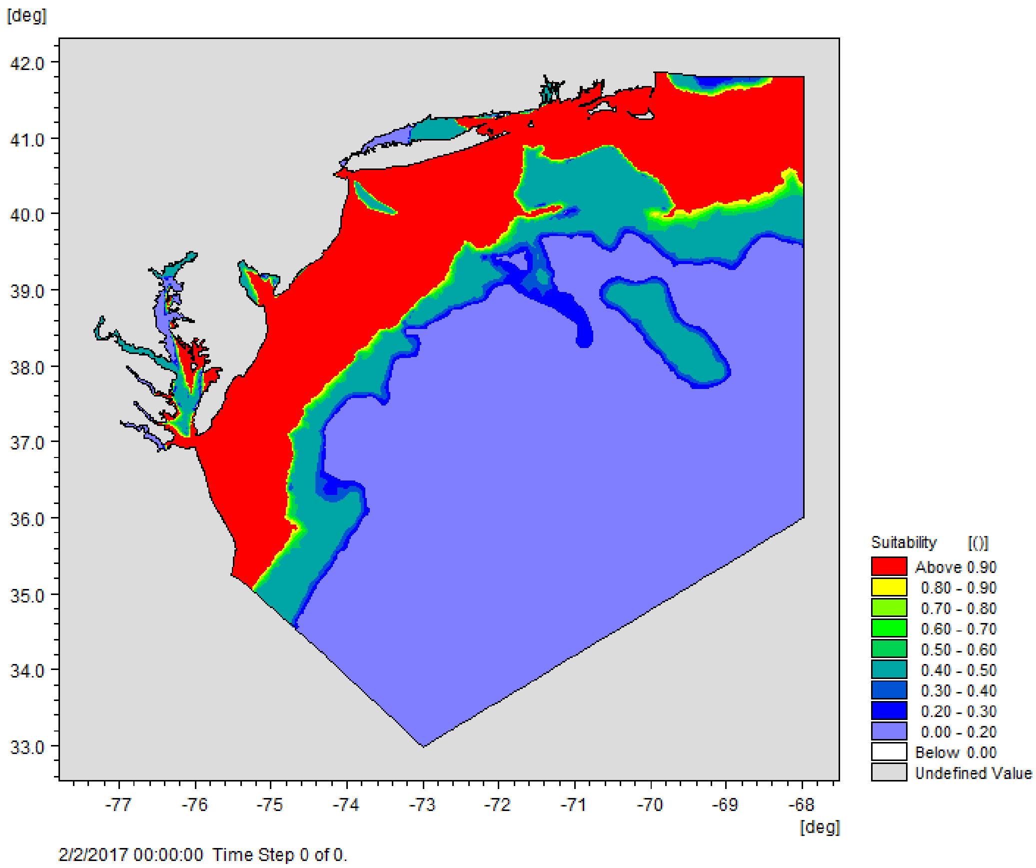

Figure 88. Sea scallop settlement suitability map
Suitability indices are derived using benthic substrate data (USGS 2005), with higher values assigned to areas with substrate types preferred by sea scallop larvae.

Table 13. Sea scallop substrate suitability and settlement conditions

Parameter	Literature Information/Value	Parameterized Value
Settling indicators *Conditions required for larvae to settle/incubate to juvenile*	Substrate type: • Presence of suitable substrate (gravelly sand, shell fragments) • Coarse sediment, gravel, glacial morain • Gravel substrate (>80%); hydroids and filamentous algae (Culliney 1974, Thouzeau et al. 1991) Water depth: • < 100 m	The index values used for the various benthic substrate types are: • Sand/gravel: 0.9 • Clay-sand/silt: 0.5 • Sand-clay/silt: 0.5 • Sand-silt/clay: 0.2 • Sand/silt/clay: 0.1 Water depth thresholds for settlement: • Minimum: 15 m • Maximum: 60 m
Temperature effects *Potential effects from changing temperatures*	Mass larval mortality at >21°C Larvae aggregate above the thermocline (> 5°C) (Stewart and Arnold 1994)	Temperature thresholds for larval survival: • Minimum: 0°C • Maximum: 21°C

6.2.4.2 Silver Hake

6.2.4.2.1 General Overview

The silver hake (*Merluccius bilinearis*) is a cod-like (Gadiformes) species from the family Merlucciidae. Adults reach 47 cm in length and live for at least 12 years (Helser et al.1995). Fishery managers recognize at least two geographically distinct stocks (northern and southern) divided by ~ 41° 30’ N latitude (Helser et al. 1995) within the area of interest. The northern stock occurs in the Gulf of Maine and the southern portion of Georges Bank whereas southern stock includes southern portion of Georges Bank and the shelf and slope off Cape Cod and southern New England (**Figure 89**). Silver hake contribute to commercial and recreational fisheries of the region and are managed by the NEFMC as part of the “small mesh multispecies” complex (NEFMC 2018). The present project is generally located within the area encompassed by the southern stock.

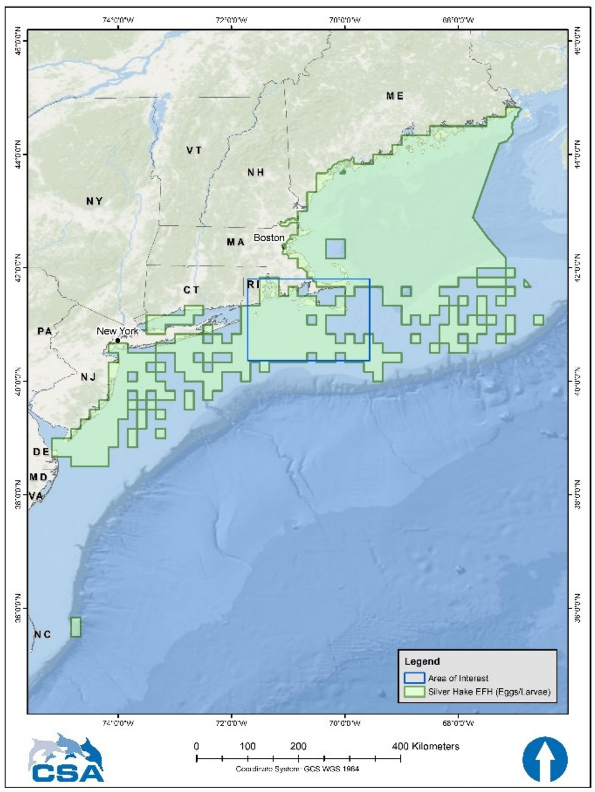

Figure 89. Silver hake habitat map
Silver hake EFH in the Northwest Atlantic Ocean, extending from the Gulf of Maine to Cape Hatteras, North Carolina (NOAA 2018).

Off southern New England silver hake adults inhabit outer shelf waters (54 to 127 m) during winter and spring then migrate inshore to the coast in summer and fall as water temperatures rise (Nye et al. 2011). Juveniles follow a similar seasonal pattern as adults but tend to occur in shallower water (50 to 90 m).

6.2.4.2.2 Super-Agent Class Parameterization

The simulation period for the silver hake model (May 1, 2017 to December 31, 2017) was selected to capture zygotes and larval activity during critical spawning seasons and larval migration periods. The parameterization of silver hake spawning life cycle, mortality, movement, and settlement suitability characteristics are detailed in the subsections below.

6.2.4.2.3 Spawning

Spawning behavior has not been documented, but likely involves pair spawning off bottom (e.g. Erlich et al. 2013). Measurements of daily otolith increments from newly settled juveniles indicate silver hake may spawn during full moon phases (Steves and Cowen 2000). Silver hake super-agent release areas (**Figure 90**) were derived from observed distribution of silver hake eggs – planktonic egg collections made over broad areas reveal spawning occurs from May to November with peak activity in June and July (Fahay 1974). Eggs were collected in a wide range of water temperatures (13.0 to 21.7°C). Most eggs in the project area likely originated from a spawning area on the shelf between Nantucket Shoals and Montauk Point at the eastern end of Long Island, New York. Some eggs entering the project area may come from the spawning ground along the southern shelf edge of Georges Bank.

A total of 173,664 silver hake super-agents were released over the entire simulation period in the model domain. As with sea scallops, each super-agent is initialized with a random number of zygotes sampled from a normal distribution (mean = 25,000 zygotes, standard deviation = 5,000 zygotes). The normal distribution is based on literature review; silver hake are batch (serial) spawners with females releasing up to three egg batches per season (Sherstyukov 1991). Batch fecundity has not been calculated, but Marl and Ramos (1979) have estimated total fecundity from females collected off Georges Bank. From their fecundity-length equations, a 25 cm Total Length (TL) female would produce an average of 25,844 eggs. Sherstyukov (1991) suggested that if three batches were spawned, the first batch released would contain about 50% of the total eggs produced and the remaining batches would contribute about 25% each. Additionally, peak spawning is linked to the lunar cycle and occur during a full moon (Steves and Cowan 2000). A summary of parameters related to silver hake spawning is presented in **Table 15**.

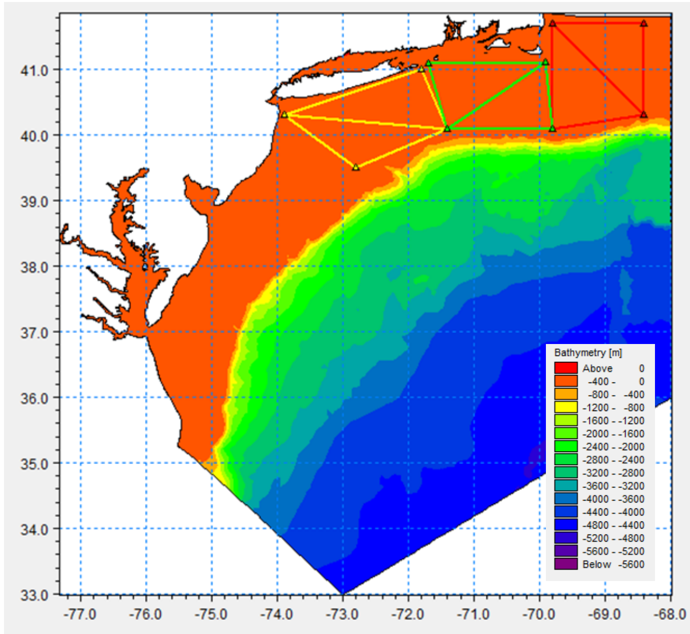

Figure 90. Silver hake model spawning areas
Release areas in the silver hake model are derived from observed silver hake egg spatial data (NOAA 2018).

Table 14. Silver hake release period and volume

Area(s)	Release Period	Time Series
All polygons in **Figure 90**	May 15, 2017 to October 31, 2017 Three peaks in June, July, and August 2017; highest peak in June 2017	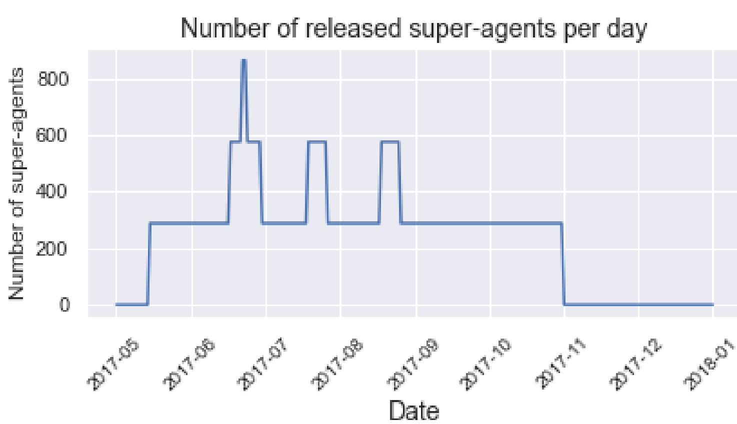

Table 15. Silver hake spawning model parameters

Parameter	Literature Information/Value	Parameterized Value
Timing *Time of year when spawning is initiated*	Spawning period differs across locations. Peak spawning: May to June in the southern stock and July to August in the northern stock (Brodziak et al. 2001). Numbers increase through August and decline during September and October (Berrien and Sibunka, 1999)	Release of super-agents occurs from mid-May (May 15, 2017) to end October (October 31, 2017). Three peaks in June, July, and August 2017; highest peak in June 2017. The peaks follow the lunar cycle for those June, July, and August 2017.
Duration *Spawning period*	Asynchronous spawners that produce and release several batches of eggs during the spawning season (Lock and Packer 2004)	See above
Quantities *Particle release during spawning*	Average of 25,844 eggs per female (Mari and Ramos 1979) 3 batches per season (Lock and Packer 2004) Sherstyukov, (1991) suggested that if three batches were spawned, the first batch released would contain about 50% of the total eggs produced and the remaining batches would contribute about 25% each.	Initial number of zygotes sampled from a normal distribution: Mean: 25,000 zygotes Standard deviation: 5,000 Three peaks were incorporated in the release time series to represent three spawning batches, with the largest number of super-agents released during the first peak.

6.2.4.2.4 Life Cycle

Silver hake eggs are pelagic and drift with prevailing currents, hatching after approximately 2 days. Newly hatched larvae are also pelagic and are about 2.6 to 3.5 mm long. Larval duration in the New York Bight is estimated to be around 34.5 days and reach lengths of 17 to 20mm when the larvae begin to settle to the bottom becoming juveniles. Silver hake juveniles settle on the outer shelf of the New York Bight during summer and fall (Lock and Packer 2005).

An overview of the early life stages of silver hake that are simulated in the model is presented in **Figure 91** and a summary of parameters related to silver hake life cycle (growth and mortality) is presented in **Table 16**.

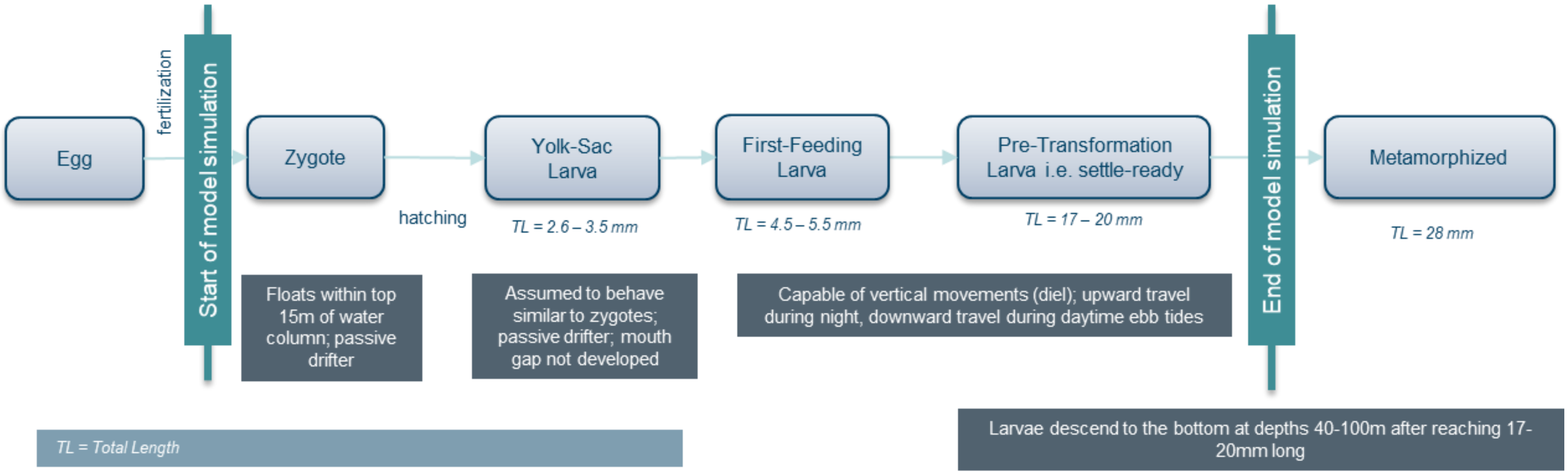

Figure 91. Early life stages of silver hake as simulated in the ABM
A silver hake agent is initialized as a zygote and undergoes transformation to become a pre-transformation larva. At this point, it descends to the bottom of the ocean and begins its metamorphosis process. Life stages beyond the pre-transformation larva stage are not included in the model.

Table 16. Silver hake life cycle (growth and mortality) model parameters

Parameter	Literature Information/Value	Parameterized Value
Life Cycle Parameters		
Duration of egg stage *Incubation time from egg to larvae*	Hatch in 2 days (Lock and Packer 2004)	Minimum zygote duration sampled from normal distribution: • Mean: 30 hours • Variance: 2 hours Maximum zygote duration sampled from normal distribution: • Mean: 40 hours • Variance: 2 hours All durations are from the time of release of super-agent.
Duration of larval stage *Time spent as a larva before settling/changing state*	Ranges from 1-5 months (Steves and Cowen 2000): • New York Bight: 34.5 days • Scotian Shelf: 3 to 5 months	Minimum larval duration sampled from normal distribution: • Mean: 35 days • Variance: 2 days All durations are from the time of release of super-agent.
Number of stages between egg and adult *Total number of stages between egg and adult*	2 stages: larval and juvenile (Steves and Cowen. 2000)	3 stages modeled: Zygotes, pre-competent larvae, and competent larvae.
Growth Parameters		
Incubation rate of zygotes *Probability that a zygote will hatch and become a larva*	Not available	Age-dependent sigmoidal curve for incubation probability. Values are assumed and calibrated against observation data: • Maximum incubation probability: 0.7/day
Competency gain rate of larvae *Probability that a pre-competent larva will gain competency*	Not available	Age-dependent sigmoidal curve for competency gain probability. Values are assumed and calibrated against observation data: • Maximum competency gain probability: 0.8/day

Parameter	Literature Information/Value	Parameterized Value
Competency loss rate of larvae *Probability that competent larva will lose competency*	Not available	Age-dependent sigmoidal curve for competency loss probability. Values are assumed and calibrated against observation data: • Maximum competency loss probability: 0.8/day
Mortality Parameters		
Mortality parameters *Parameters related to the selected mortality*	Overall range of 0.0916 to 0.1626/day for 2001 and 2002, respectively for European hake larvae (Alvarez and Cotano 2005) Daily mortality percentage of 23.67 and 11.3 for January and February, respectively for Argentinian hake (Brown et al. 2004)	Age-dependent Type III survivorship curve for mortality rate. Values are assumed and calibrated against observation data: • Minimum daily instantaneous mortality rate: 0.01/day • Maximum daily instantaneous mortality rate: 0.3/day

6.2.4.2.5 Movement

An overview of the silver hake super-agent vertical movement behavior as simulated in the model is presented in **Figure 92** and a summary of parameters related to silver hake movement is presented in **Table 17**. There is no substantial evidence to conclude that silver hake has the capability to maintain its vertical position to stay near the thermocline. Thus, it was assumed that silver hake would travel up at night and down during the day for protection from predators and to stay near food sources i.e. plankton. The silver hake super-agent is considered to be a passive drifter along the transverse plane, and thus its horizontal movement is purely a function of hydrodynamic forcings (i.e. horizontal current speed and direction).

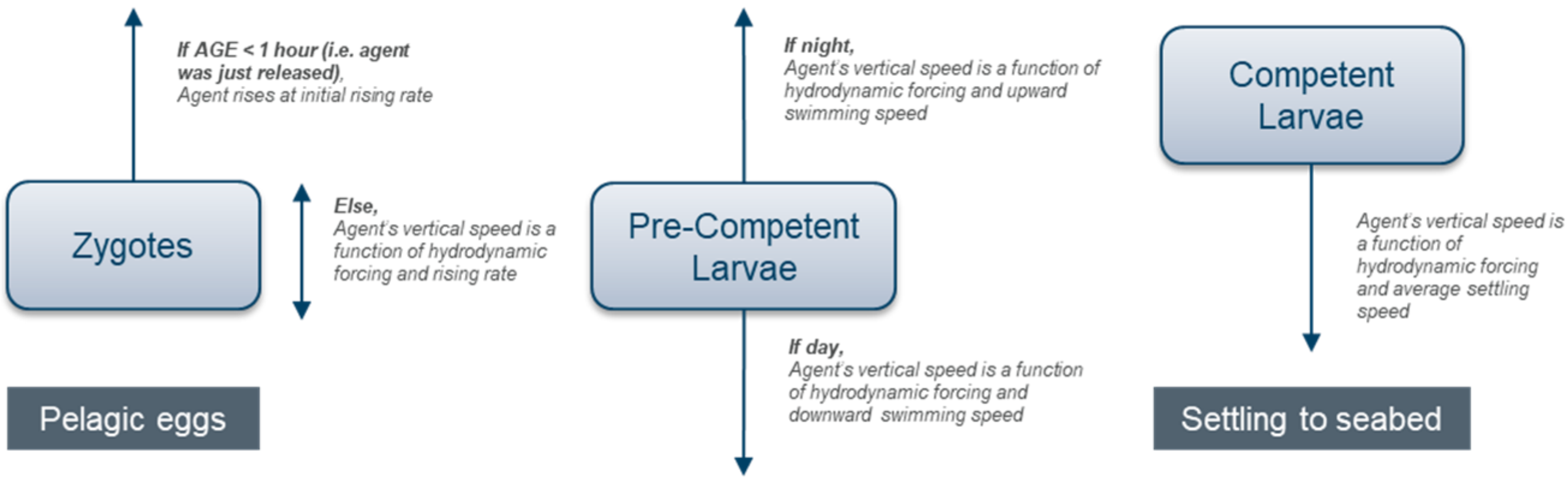

Figure 92. Parameterization of silver hake zygotes and larval vertical movement characteristics
Silver hake zygotes are pelagic and rise towards the water surface during their first hour of release from the seabed, after which it drifts passively along the vertical axis. Pre-competent larvae migrate vertically through the water column depending on daylight, rising towards the surface at night and sinking to the bottom during the day. Settle-ready (competent) larvae sink and eventually settle on the seabed.

Table 17. Silver hake movement model parameters

Parameter	Literature Information/Value	Parameterized Value
Buoyancy of egg *Maximum buoyancy (positive or negative) speed for fertilized zygotes*	Eggs are buoyant with a single yellowish or brownish oil globule of 0.19 to 0.25 mm (Sauskan and Serebryakow 1968)	Super-agents are released 5 m under the water surface and stay in the range of this depth during the initial stages of their lives.
Vertical swim speeds *Maximum vertical swim speed for larvae, independent of current speeds (m/s)*	Not available	Average vertical swim speed sampled from normal distribution: • Mean: 0.001 m/s • Standard deviation: 0.0005 m/s
Horizontal swim speeds *Maximum horizontal swim speed for larvae, independent of current speeds (m/s), if present*	Not available	Horizontal swim speed is insignificant relative to hydrodynamic forcings – super-agent assumed to drift passively in horizontal plane.

6.2.4.2.6 Settlement Suitability

Silver hake settle from June to October in water temperatures ranging from 8 to 11 °C and depths of 40 to 100 m (Auster et al. 1997, Steves et al. 2000). Newly settled individuals have an affinity for amphipod tube mats and sand waves (Auster et al. 1997). Newly settled fish may continue to migrate vertically to feed at night. Adults associate with sand waves, shell fragments, boulders, and other debris on the seafloor (Lock and Packer 2004).

Settlement suitability index map for silver hake (**Figure 93**) is based on abundance of silver hake juveniles (NOAA 2018) and the preferred settlement depth of silver hake larvae, which is between 40 to 100 m. Each 2D grid cell of the model mesh is assigned a suitability index value between 0 to 1, with higher values indicating higher suitability for settlement.

Silver hake settling probability is a function of the settlement suitability map, a spatially varying model constant. As with sea scallops, silver hake settling is described as a two-step process, where specific conditions of water depth and temperature (**Table 18**) must be met in order for the larvae to settle.

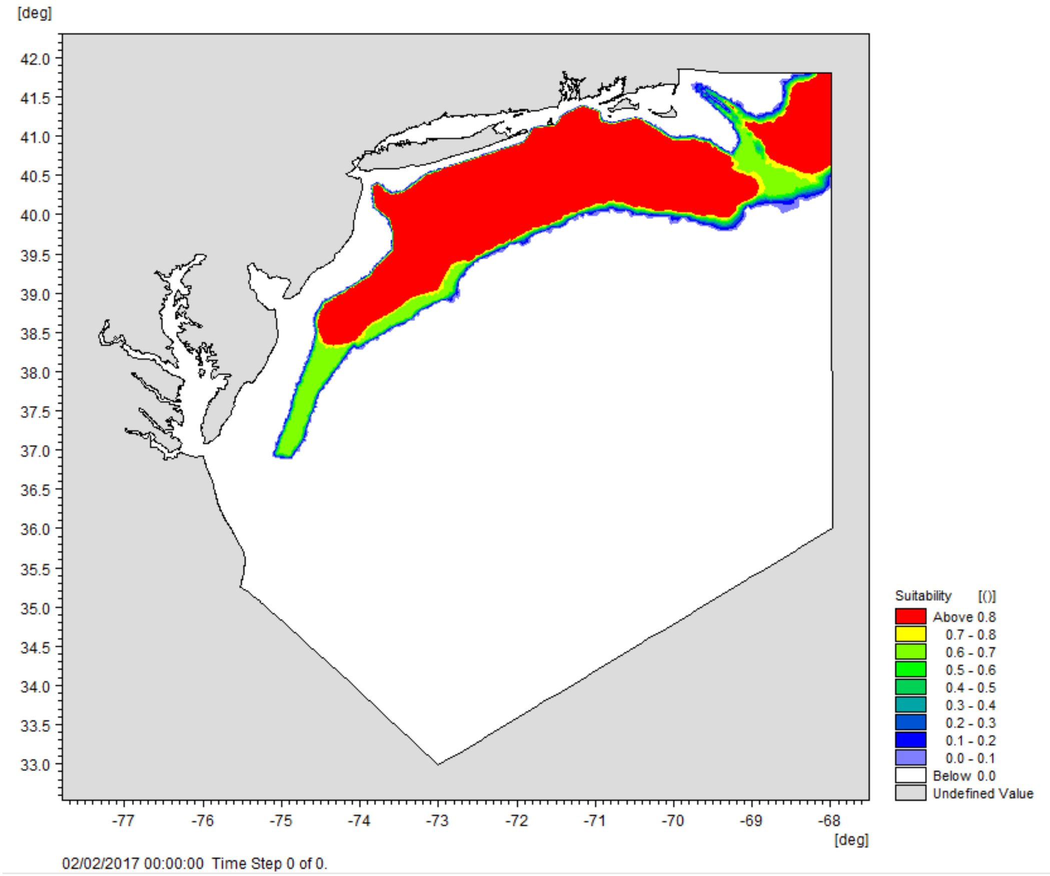

Figure 93. Silver hake settlement suitability map
Suitability indices are derived from water depths and observed abundance pattern in the model domain, with higher values assigned to areas between 40 to 100 m in depth.

Table 18. Silver hake substrate suitability and settlement conditions

Parameter	Literature Information/Value	Parameterized Value
Settling indicators *Conditions required for larvae to settle/incubate to juvenile*	Settle during fall (Steves et al. 2000) Settle on outer shelf (65 to 90 m water depths) (Steves et al. 2000) Once on the bottom, age-0 silver hake may be associated with the presence of amphipod tube mats (Auster et al. 1997)	The index values used in the substrate suitability map is based on water depth: • 40 to 100m + abundance: 0.9 • 40 to 100m + no abundance: 0.7 • <40m or >100m: 0 Water depth thresholds for settlement: • Minimum: 40 m • Maximum: 100 m
Temperature effects	8–11°C at 90 m when settling. Peak abundance of larvae occurred from July to October – during which most	Temperature thresholds for larval survival: • Minimum: 5°C • Maximum: 20°C

Parameter	Literature Information/Value	Parameterized Value
Potential effects from changing temperatures	larvae were found in temperatures of 11 to 16°C. February and March: larvae were found in the coldest water of the year (5 to 12°C) As the water warmed in the spring, the occurrences of larvae shifted to warmer waters Summer: found mostly between 10 to 16°C Autumn: Larvae remained in warmer waters 10 to 16°C (Lock and Packer 2004)	

6.2.4.3 Summer Flounder

6.2.4.3.1 General Overview

Summer flounder (*Paralichthys dentatus*) is a member of the large-toothed flounder family (*Paralichthyidae*) and is distributed from central Florida to the Gulf of Maine. Summer flounder is economically valuable as a recreational and commercial fisheries species across its range and is managed jointly by the Atlantic States Marine Fisheries Commission and the Mid Atlantic Fishery Management Council (Terciero 2018). Fisheries managers historically recognized one stock for the northwest Atlantic Ocean region; however, others have presented evidence supporting the existence of two (or more) geographically segregated stocks: a northern stock in the MAB extending from Cape Cod southward to Delaware Bay and a southern stock in the South Atlantic Bight centered off Cape Hatteras, North Carolina (**Figure 94**).

Stock definition is not fully resolved but for modeling purposes individuals that reside and spawn and within the area of interest are from the northern stock (Kraus and Musick 2001). Recent genetic studies indicate a lack of distinct stocks or geographically segregated subpopulations which supports continued management of a single population (Hoey and Pinksy 2018). In addition, genetic and otolith microchemistry signatures from archived larvae sampled over 24-year period indicated that spawning offshore Cape Hatteras contributes 7 to 50% of the summer flounder larvae dispersing into the MAB (Hoey et al. 2020), the offshore region from Massachusetts to North Carolina.

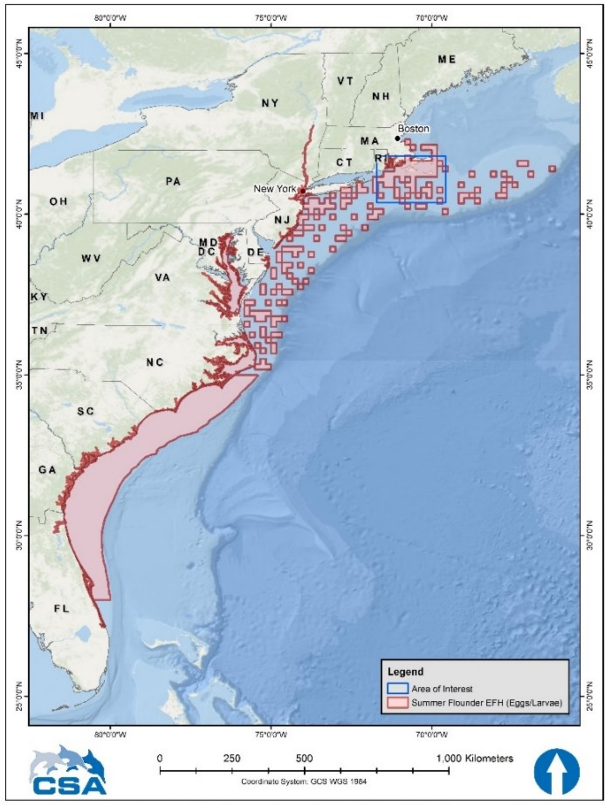

Figure 94. Summer Flounder habitat map
Summer flounder EFH in the Northwest U.S., covering the shallow estuarine waters and outer continental shelf from Florida to George's Bank (NOAA 2018).

6.2.4.3.2 Super-Agent Class Parameterization Data

The simulation period for the summer flounder model (September 1, 2017 to March 31, 2018) is selected to capture zygotes and larval activity during critical spawning seasons and larval migration periods. The parameterization of summer flounder spawning, life cycle, mortality, movement, and settlement suitability characteristics are detailed in the subsections below.

6.2.4.3.3 Spawning

Adults mature at about 30 cm Total Length (TL) reaching a maximum size of 83 cm TL and spend summer months in inner shelf and estuarine waters (Gilbert 1986). During late summer and fall, in response to falling water temperatures, adults migrate offshore to spawn. Relative to the area of interest, fish would be migrating from inner shelf and estuarine waters of southern New England and New York Bight to the outer shelf. Summer flounder super-agent release areas (**Figure 95**) were derived from information from hydrodynamic conditions and bathymetry; spawning takes place in water depths from 60 to 100 m where temperatures range from 12 to 19 °C.

Based on spatial egg distributions from plankton samples (Smith 1973), spawning occurs in the area of interest between eastern Long Island and Nantucket shoals out to the shelf edge (e.g. Smith 1973, Able et al 2010). Egg densities in this area were highest during October and November but spawning can extend from September to February (Morse 1981). Spawning behavior is not well known but likely involves pair spawning with eggs being shed into the water column above the seafloor (< 10 m). Adults are serial spawners with female producing at least six batches of eggs per season (Morse 1981).

A total of 167,040 summer flounder super-agents were released over the entire simulation period in the model domain. As with the other two modeled species, each super-agent is initialized with a random number of zygotes sampled from a normal distribution (mean = 1,700,000 zygotes, standard deviation = 200,000 zygotes). Estimated number of eggs produced per batch can range 27,080 to 251,280 for females measuring 37 and 68 cm TL, respectively, with fecundity positively correlated with both length and weight. The mean egg production per female ranged from 1,077 to 1,265 eggs per gram of body weight (Morse 1981). A summary of parameters related to summer flounder spawning is presented in **Table 19**.

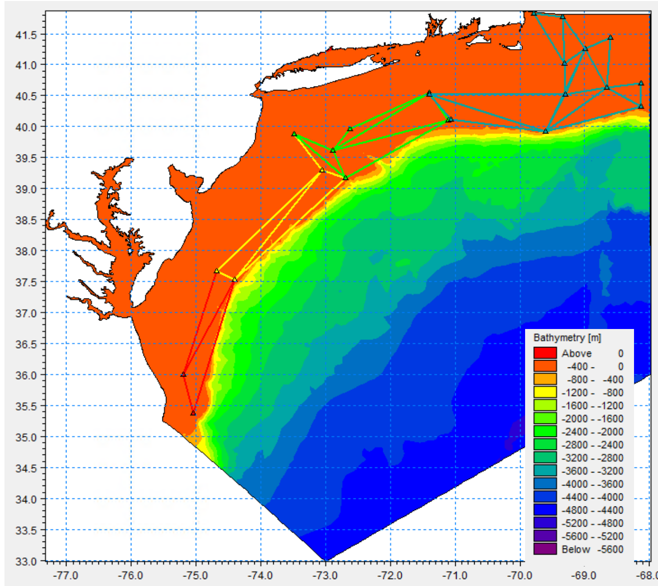

Figure 95. Summer flounder model spawning areas
Release areas in the summer flounder model are derived from bathymetric information and temperature conditions at which spawning activity was observed.

Table 19. Summer Flounder release period and volume

Area(s)	Release Period	Time Series
Red, yellow, and blue polygons in **Figure 95**	September 1, 2017 to November 30, 2017 Peak from October 1, 2017 to October 31 2017	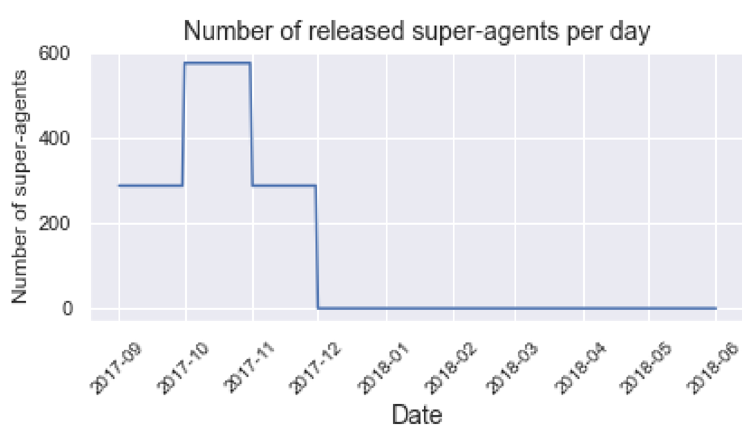

Area(s)	Release Period	Time Series
Green polygon in **Figure 95**	September 1, 2017 to December 31, 2017 Largest peak from October 1, 2017 to October 30 2017	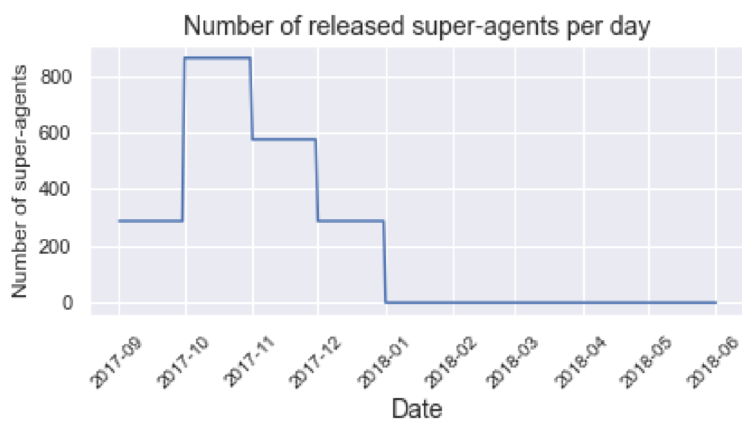

Table 20. Summer flounder spawning model parameters

Parameter	Literature Information/Value	Parameterized Value
Timing *Time of year when spawning is initiated*	September to December, peak in October to November. One study cites July to February with peaks from September to November in water temperatures ranging 12 to 19°C (Smith 1973)	Release of super-agents occurs from September to December or September to November, depending on region.
Duration *Spawning period*	September to December (120 days), peak in October to November (60 days) (Morse 1981)	See above.
Quantities *Particle release during spawning*	Estimate of 0.46 to 4.18 million ova per female (Morse 1981)	Initial number of zygotes sampled from a normal distribution: • Mean: 1,7000,000 zygotes • Standard deviation: 200,000 Peak release patterns are based on monthly abundance of eggs by region from NEFSC MARMAP offshore ichthyoplankton surveys during 1979-1981, 1984 and 1985 (Packer et al. 1999)

6.2.4.3.4 Life Cycle

Newly hatched larvae have eyes on either side of the body and orient their body axis perpendicular to the seafloor (Keefe and Able 1993). These larvae have yolk sacs which may be completely absorbed in four days or less, depending on water temperature (Miller et al. 1991). Developing larvae undergo a complex metamorphosis involving multiple stages and migration of the eyes from bilaterally symmetrical positions on either side of the head to the left side of the body. The entire metamorphosis can take between 25 and 93 days to complete depending on water temperatures (Able and Kaiser 1994). Miller et al. (1991) reported that metamorphosing larvae between 12 to 14 mm long and 30 to 70 days old enter estuaries, coastal rivers, and sounds of the MAB from October to April.

An overview of the early life stages of summer flounder that are simulated in the model is presented in **Figure 96** and a summary of parameters related to summer flounder life cycle (growth and mortality) is presented in **Table 21**.

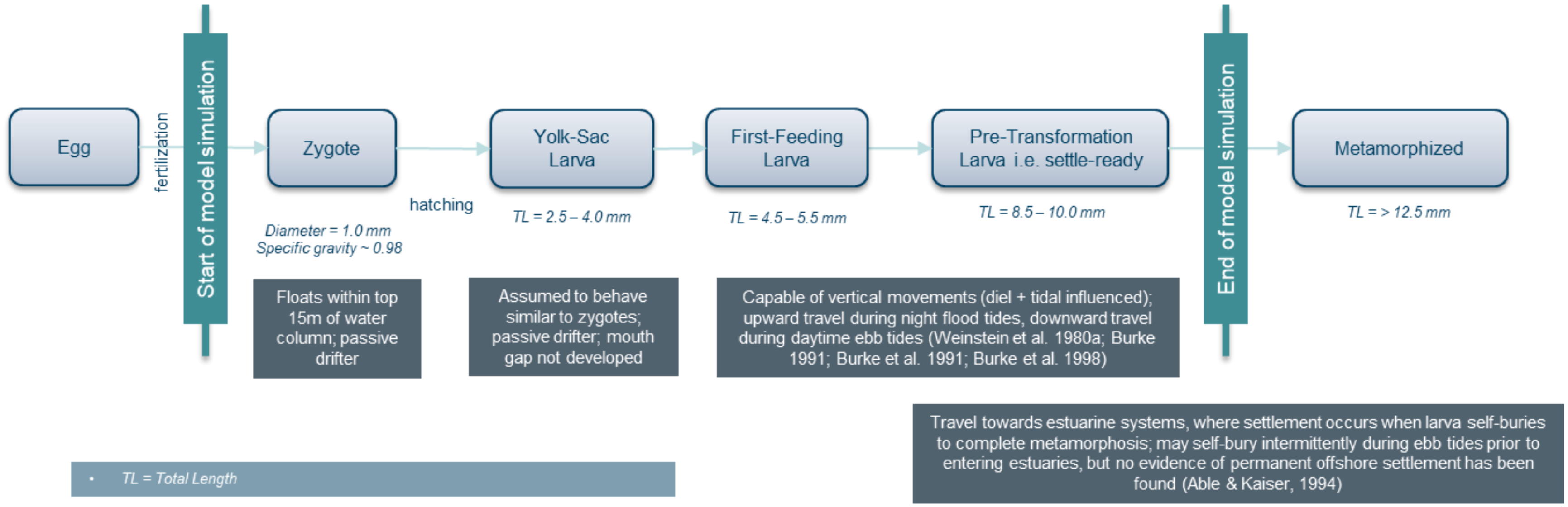

Figure 96. Early life stages of summer flounder as simulated in the ABM
A summer flounder agent is initialized as a zygote and undergoes transformation to become a pre-transformation larva. At this point it is ready to settle in estuarine systems to begin its metamorphosis process.

Table 21. Summer flounder life cycle (growth and mortality) model parameters

Parameter	Literature Information/Value	Parameterized Value
Life Cycle Parameters		
Duration of egg stage *Incubation time from egg to larvae*	Hatch in 2 to 6 days, depending on ambient water temperature: • 142 h at 9°C • 85 h at 12.5°C • 72 to 75 h at 18°C • 60 h at 21°C • 56 h at 23°C (Bisbal and Bengtson 1995, Johns and Howell 1980, Packer et al. 1999)	Minimum zygote duration sampled from normal distribution: • Mean: 48 hours • Variance: 2.4 hours Maximum zygote duration sampled from normal distribution: • Mean: 96 hours • Variance: 2.4 hours All durations are from the time of release of super-agent.
Duration of larval stage *Time spent as a larva before settling/changing state*	Ranges from 20 to 99 days, depending on ambient water temperature: • 67 to 99 days at 6.6°C • 31 to 62 days at 14.5°C • 20 to 32 days at 16.6°C (Houde 1989, Burke et al. 1991, Keefe and Able 1993, van Maaren and Daniels 2000)	Minimum larval duration sampled from normal distribution: • Mean: 25 days • Variance: 3 days All durations are from the time of release of super-agent.
Number of stages between egg and adult *Total number of stages between egg and adult*	8 stages from hatching to metamorphosis (Martinez and Bolker 2003)	4 stages modeled: Zygotes, yolk-sac larvae, post-feeding pre-competent larvae, and competent larvae.
Growth Parameters		
Incubation rate of zygotes *Probability that a zygote will hatch and become a larva*	Not available	Age-dependent sigmoidal curve for incubation probability. Values are assumed and calibrated against observation data: • Maximum incubation probability: 0.7/day
Competency gain rate of larvae *Probability that a pre-competent larva will gain competency*	Not available	Age-dependent sigmoidal curve for competency gain probability. Values are assumed and calibrated against observation data: • Maximum competency gain probability: 0.5/day

Parameter	Literature Information/Value	Parameterized Value
Competency loss rate of larvae *Probability that competent larva will lose competency*	Not available	Age-dependent sigmoidal curve for competency loss probability. Values are assumed and calibrated against observation data: • Maximum competency loss probability: 0.1/day
Mortality Parameters		
Mortality parameters *Parameters related to the selected mortality*	Overall range of 0.05 to 0.33/day (Houde 1989): 0.05 to 0.33 for Pseudopleuronectes americanus (winter flounder) 0.05 to 0.24 for *Paralichthys dentatus* (summer flounder)	Age-dependent Type III survivorship curve for mortality rate. Values are assumed and calibrated against observation data: • Minimum daily instantaneous mortality rate: 0.01/day • Maximum daily instantaneous mortality rate: 0.3/day

6.2.4.3.5 Movement

Hydrated eggs average 1.0 mm in diameter and are positively buoyant (specific gravity = 1.0). These eggs will float up into near-surface waters, drift passively from the spawning sites, and remain in the upper water column until yolk reserves are fully metabolized. The egg will transform into a larva at this time and will continue as a passive particle but will sink lower in the water column. During this metamorphosis, larvae move toward shore but clear behavioral mechanisms for facilitating the shoreward movement are unknown (Able and Kaiser 1994). Once near the mouths of estuaries or coastal rivers where tidal forces are prevalent, transforming larvae use selective tidal stream transport to ride the tide upstream (Miller et al. 1991; Forward et al. 1999). Juveniles will ultimately reside within physiologically favorable segments of salinity and temperature gradients (Howson and Targett 2019).

An overview of the summer flounder super-agent vertical and horizontal movement behaviors as simulated in the model are presented in **Figure 97** and **Figure 98,** and a summary of parameters related to summer flounder movement is presented in **Table 22**.

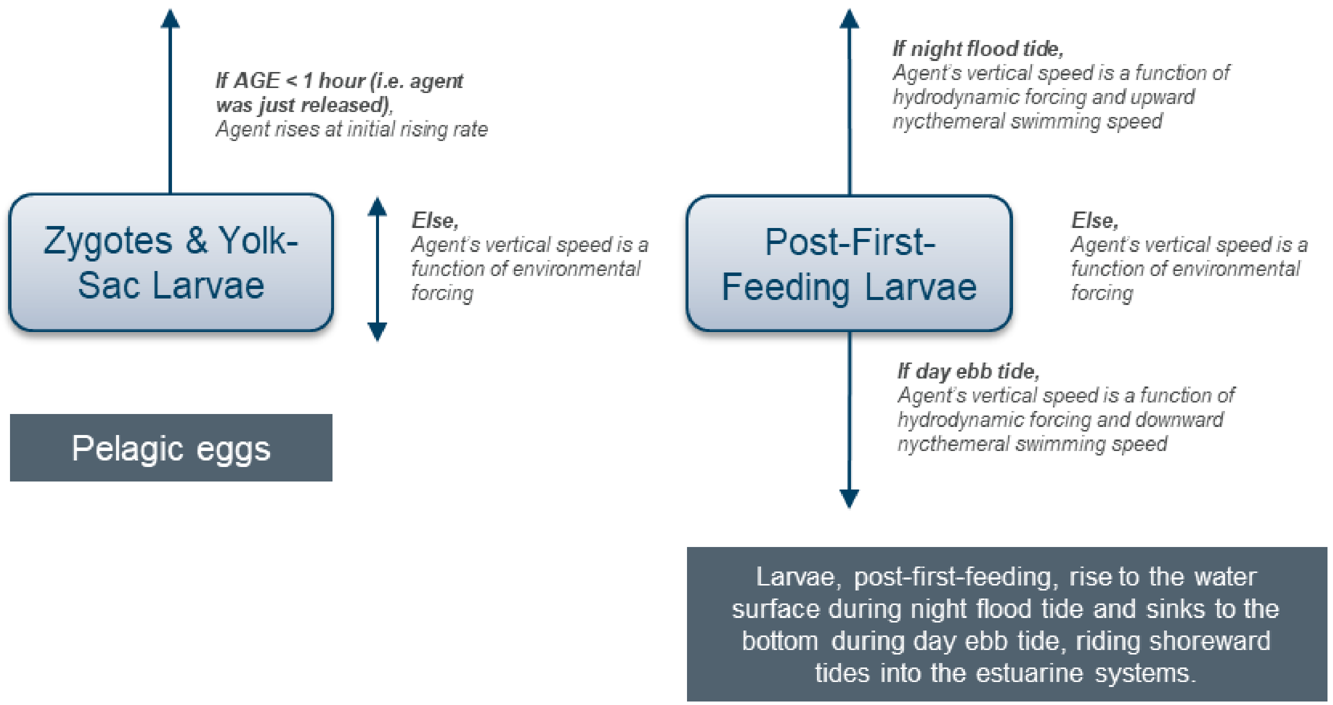

Figure 97. Parameterization of summer flounder zygotes and larval vertical movement
Summer flounder zygotes are pelagic and remain buoyant up until they become yolk-sac larvae. Once they start to feed, larvae are capable to vertical swimming, rising to the water surface during night flood tides and sinking to the bottom during day ebb tides.

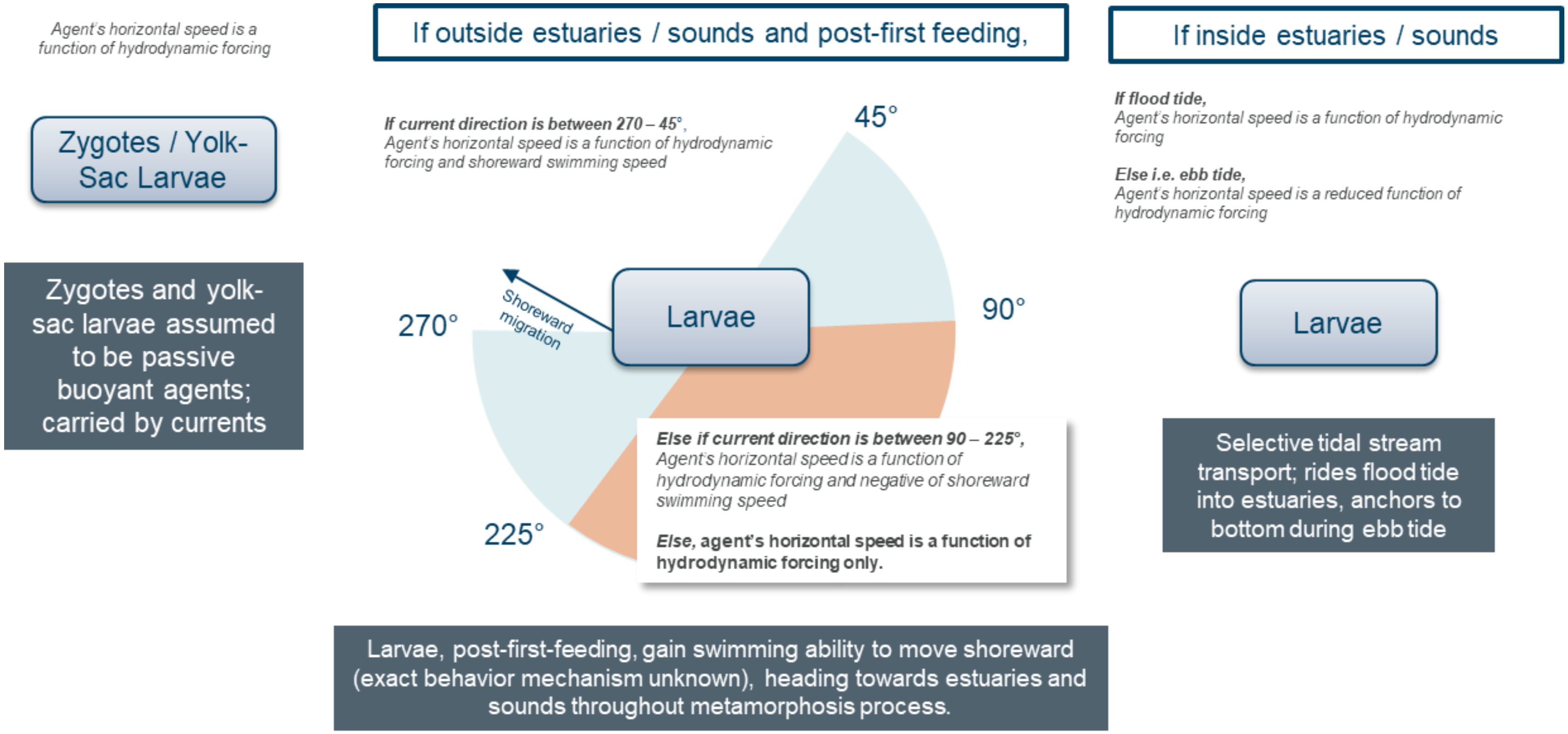

Figure 98. Parameterization of summer flounder zygotes and larval horizontal movement
Agents are passive agents along the transverse plane during the early life stages (i.e. zygotes and yolk-sac larvae). Post-first-feeding, larvae gain swimming ability, migrating shoreward towards the northeastern U.S. coastline. Larvae that have entered the estuarine systems make use of selective tidal stream transport to ride flood tides upstream of the estuaries.

Table 22. Summer flounder movement model parameters

Parameter	Literature Information/Value	Parameterized Value
Buoyancy of egg *Maximum buoyancy (positive or negative) speed for fertilized zygotes*	Specific gravity of 1.0 – buoyant (Packer et al. 1999)	Maximum upward speed of 0.0012 m/s
Vertical swim speeds *Maximum vertical swim speed for larvae, independent of current speeds (m/s)*	Nychthemeral speeds (Barbut et al. 2019): • Upward speed of 0.003 m/s during night flood tides • Downward speed of 0.001 m/s during day ebb tides	Vertical swim speed is function of hydrodynamic forcings and nychthemeral speeds as detailed in Barbut et al. (2019), depending on daylight and tidal conditions at given timestep.
Horizontal swim speeds *Maximum horizontal swim speed for larvae, independent of current speeds (m/s), if present*	Shoreward swimming speeds of larvae is estimated to be within the range of 6 cm/s for species with small larvae (i.e. 9 to 11 mm) to 10 cm/s for species with large larvae (i.e. 14 to 16 mm) (Faillettaz et al. 2018)	Shoreward swimming speed of 0.007 m/s. Shoreward direction is taken to be between 270° to 360° and between 0° to 45° degree, where North is 0°.
Temporal changes in vertical distribution *Distribution of larvae in the water column dependent on time of day*	Movement of late-stage larvae into estuaries October to April. Larvae present in Narragansett Bay from Sept to December (Able and Kaiser, 1994) Late-stage larvae (11 to 15 mm SL) are on bottom at ebb and slack tides but move vertically into the water column on flood tide to facilitate upstream transport (Forward et al. 1999, Hare et al. 2006) Selective tidal stream transport into estuaries (Miller et al. 1991, Forward et al. 1999, Hare et al. 2006)	See above on vertical swim speeds for vertical migration to facilitate upstream transport of larvae. When larvae are in estuaries, selective tidal stream transport is modeled by varying the super-agent's horizontal speed based on tidal conditions; during flood tide, the horizontal speed is a function of hydrodynamic forcing, while during ebb tide, the horizontal speed is a reduced function of hydrodynamic forcing (to simulate anchoring to estuary/riverbed during ebb tide conditions)

6.2.4.3.6 Settlement Suitability

When larvae enter the mouths and estuaries and rivers, the individuals settle to the bottom or near-bottom waters during ebb tide then migrate upward during flood tides. Individuals will ultimately settle where sediments are fine, and salinity is between 10 and 30 psu. Taylor et al. (2016) verified that newly settled juvenile summer flounder occur in the estuaries of Narragansett Bay and Block Island sound just inshore of the area of interest. Larvae seem to prefer (or survive best) in water temperatures ranging from 9 to 18°C.

Settlement suitability index map for summer flounder (**Figure 99**) is based on the preferred substrate of young summer flounder, which is typically sandy material. The summer flounder settling process is similar to that of sea scallop and silver hake, except that the super-agent must be located in a grid cell of water depth, temperature, and salinity values within the user-determined thresholds at the time step of settlement. A summary of parameters related to summer flounder settlement suitability is presented in **Table 23**.

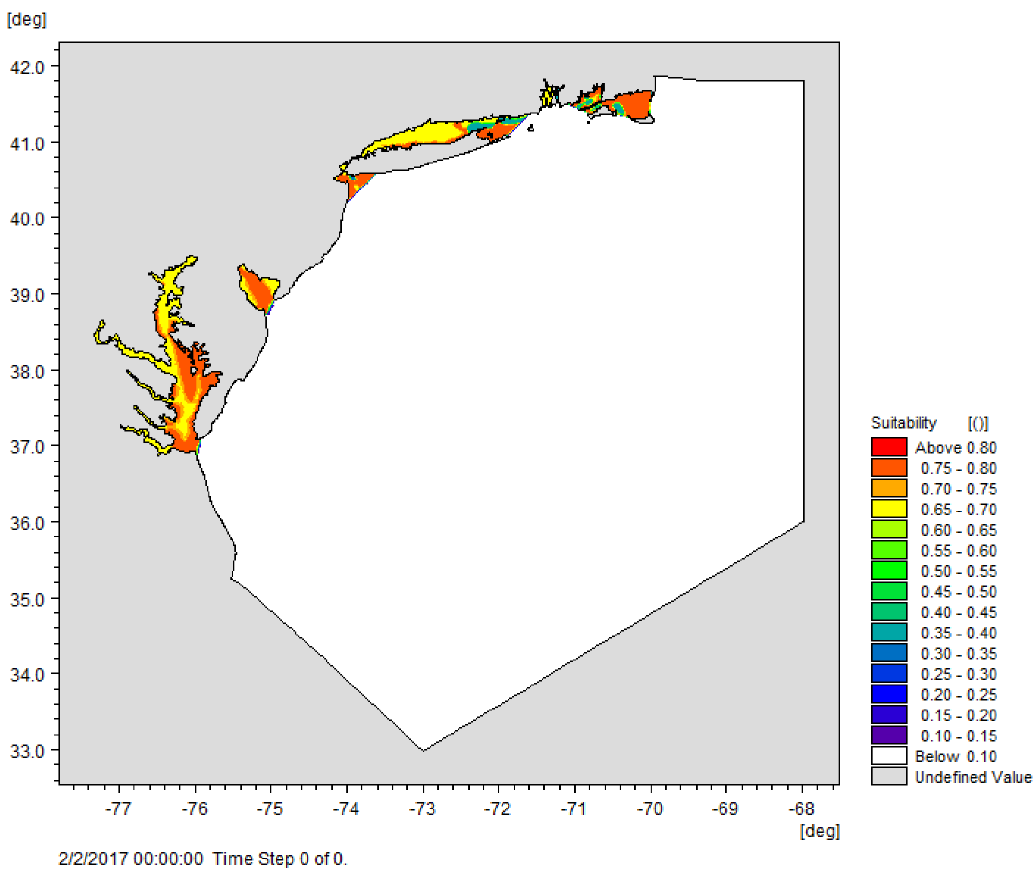

Figure 99. Summer flounder settlement suitability map
Suitability indices are derived from the benthic substrate data (USGS 2005), with higher values assigned to areas with substrate types preferred by summer flounder larvae.

Table 23. Summer flounder substrate suitability and settlement conditions

Parameter	Literature Information/Value	Parameterized Value
Settling indicators *Conditions required for larvae to settle/incubate to juvenile*	Metamorphic larvae (stages G to H-) prefer sand over mud substrates (Keefe and Able 1993)	The index values used for the various benthic substrate types are: • Sand: 0.8 (preferred) • Sand-clay/silt: 0.7 (above average) • Sand-silt/clay: 0.7 (above average) • Sand-clay/silt: 0.7 (above average) • Clay: 0.4 (below average) • Gravel-sand: 0.4 (below average) • Gravel: 0.3 (low) • Bedrock: 0.01 (very low) • Outside estuaries: 0.001 x of the values above, depending on substrate type Water depth thresholds for settlement: • Minimum: 1 m • Maximum: 35 m
Temperature effects *Potential effects from changing temperatures*	High mortality in water temperatures < 4.4°C (Keefe and Able 1993) Larvae survival at 4 to 25°C (Taylor et al. 2016)	Temperature thresholds for larval settlement: • Minimum: 4°C • Maximum: 25°C
Salinity effects *Potential effects from changing salinity*	Larvae collected from 0 to 33 psu (Able and Kaiser 1994) Larvae found in estuarine salinities 0.1 to 5 psu; 16 to 19 psu (Taylor et al. 2016)	Salinity thresholds for larvae settlement: • Minimum: 0 psu • Maximum: 35 psu

6.3 Agent-Based Modeling Validation Method

The ABM results was validated using Pattern Oriented Modeling (POM), a bottom-up approach to complex systems analysis developed to model complex ecological and agent-based systems (Grimm and Railsback 2005). According to Grimm et al. (2005) traditional ecosystem models attempt to approximate the real system as closely as possible. Whereas POM works under the assumption that an ecosystem is so information-rich that the respective model will inevitably either leave out relevant information or become over-parameterized and lose predictive power. By focusing on only the relevant patterns in the real system, POM offers a meaningful alternative to the traditional approach.

As stated in Grimm et al. (1996), POM is an attempt to mimic the scientific method, as it requires the researcher to begin with a pattern found in the real system, posit hypotheses to explain the pattern, and then develop predictions that can be tested. Through this focus on the pattern, the model can be constructed to include only information relevant to the question at hand. POM also supports modeling by better enabling the identification of the appropriate temporal and spatial scale at which to study a pattern, thereby avoiding the assumption that a single process might explain a pattern at multiple temporal or spatial scales (Grimm et al. 2005). It does, however, offer the opportunity to look explicitly at how processes at multiple scales might be driving a particular pattern.

The baseline results from all species were validated using POM through a comparison of model outputs with ecological patterns for the target species apparent from applied survey datasets (see **Section 6.2.2.2**) or values from peer-reviewed literature. Three overall pattern structures selected for the current analysis were spatial distribution, temporal development, and vertical distribution of agents. Each structure was analyzed using different approaches but were, to the extent possible, kept similar across species.

6.3.1 Pattern 1: Spatial Distribution

The spatial distribution of modeled larvae was compared to available information on the observed spatial distribution. This was done by correlating the observed distributions with model distributions of either suspended or settled larvae. The correlation was conducted using a Gamma Rank correlation, which measures the ordinal association between two vectors. The Gamma Rank correlation was selected as it compares values based on an ordinal scale rather than on absolute values. Initially, a spatial grid with a pre-set resolution was superimposed on the model data and the associated observation data. Abundance within each grid cell was summarized into a grid-cell value. Subsequently, the Gamma Rank correlation was conducted pairwise between corresponding spatial-grid cells. Furthermore, to analyses the effect of resolution on the validation results, the analysis was conducted several times, using a varying grid-cell resolution between 1,000 m and 10,000 m cell size, with 1,000 m increments. Comparisons were also conducted visually, by plotting the model and survey distributions in the most suitable resolution, estimated from the Gamma Rank correlation.

6.3.2 Pattern 2: Temporal Development

The transformation from zygote to settled organism was coded in the ABM as a stochastic process, with incubation times governed by probability functions. The transition between phases was adjusted through a series of probabilities, which estimated the chance of an agent within the super-agent to transition into the next phase, to stay in current phase or to die. This pattern of transition into phases was used as a secondary validation pattern. As no raw data was available for direct comparison between model output and empirical survey data, referenced literature was applied at it does provide an indicate phase durations. These values were compared with average phase durations in the model data.

6.3.3 Pattern 3: Vertical Distribution

The vertical distribution of suspended zygotes and larvae was used as a third pattern, to ensure that the vertical position of agents coincided with observed vertical distributions of the species. While most of the vertical transport was governed by the vertical currents in the HDM, some of the selected species did have independent vertical movement abilities.

The initial analysis was based on the vertical depth distribution of the particles. This was analyzed by estimating the average depth of the suspended particles across the domain at every time step, along with the estimate of the standard deviation. This distribution was compared to literature information on depth distribution of the species. Additionally, for the species that could control their vertical movement the diurnal vertical movement of the particles was estimated by calculating the average vertical movement at each half hour during a diurnal cycle, including the standard deviation in vertical movement. This was also compared to literature values.

6.4 Agent-Based Model Results

6.4.1 Baseline Results

The baseline model simulations were conducted for all three species with the setup specified in **Section 3** and baseline hydrodynamic conditions without effects of the OSW buildout. This resulted in three distinct settlement patterns across the model range (**Figure 100**, **Figure 101**, **Figure 102**). It should also be recalled that water temperature and stratification are included in all scenario results as they are integral to the ABM modeling with respect to parameterization of larvae behavior and mortality. For sea scallop the baseline ABM predicts distribution of the larval settlement to occur along the continental shelf, extending in various densities from waters off North Carolina to the western edge of the Georges Bank in the northeast boundary of the model domain. Likewise, the baseline distribution of larval silver hake largely remains on the continental shelf and extend from the Hudson Shelf Valley to Georges Bank in the northeast boundary of the model domain. In contrast, the settlement of the summer flounder larvae, i.e. pre-transformation larvae, ranges throughout the model domain, remaining on the continental shelf, with higher settlement concentrations closer to shore and in various bays and estuaries.

For all three species, the cumulative distribution of settled larvae density from model results i.e. for each of the three larvae species, was plotted along with EFH demarcations for an initial verification of the model results (NOAA 2018). The EFH areas represent, for sea scallop, the spatial extent of habitat across all life stages for sea scallop; for silver hake, the habitat extent of juveniles; and for summer flounder, the habitat extent of suspended larvae and juveniles. It is apparent that the general distribution of the settled larvae occurs within the EFH relevant for the species.

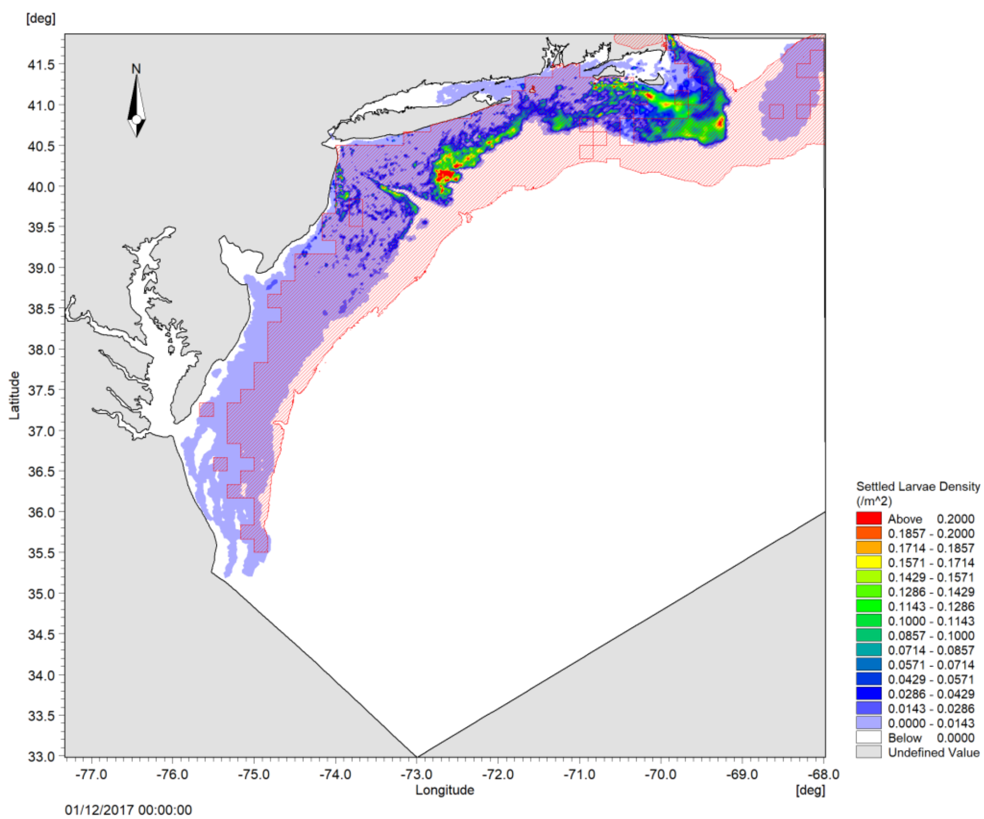

Figure 100. Settled larval sea scallop density and sea scallop EFH

Modeled settled larval sea scallop density (larvae/m^2) in the full model domain. Sea scallop EFH (NOAA 2018) is displayed in red hatches for comparison.

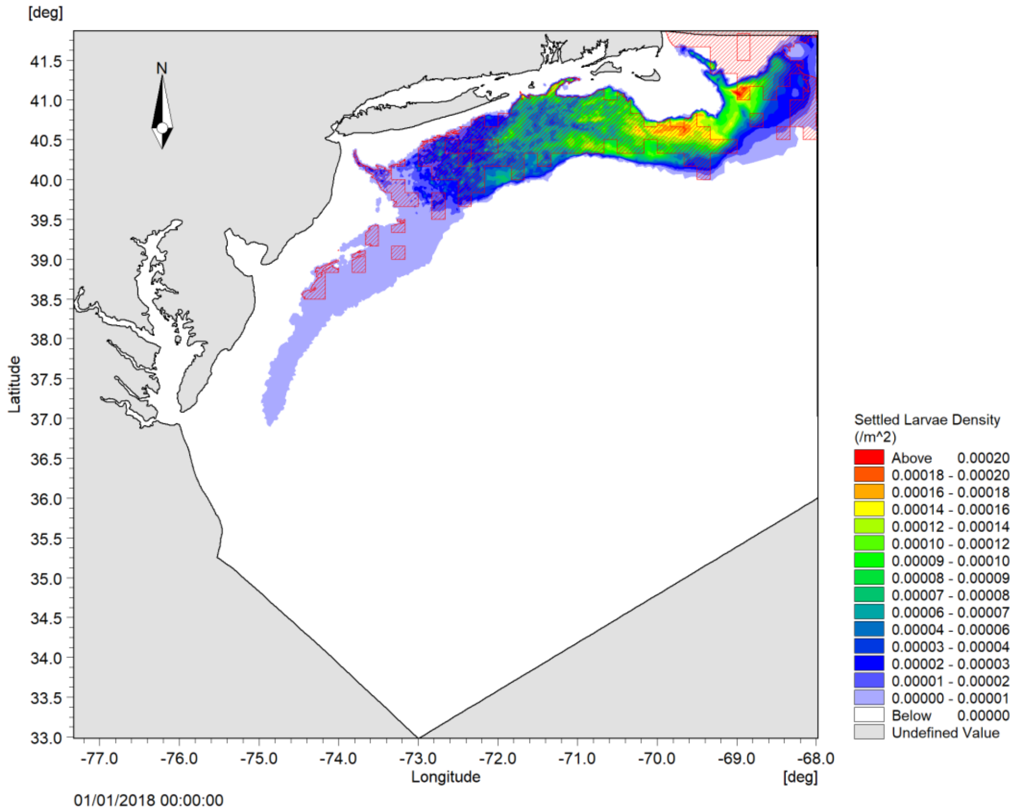

Figure 101. Settled larval silver hake density and silver hake juvenile fish EFH

Modeled settled larval silver hake density (larvae/m^2) in the full model domain. Silver hake juvenile fish EFH (NOAA 2018) is displayed in red hatches for comparison.

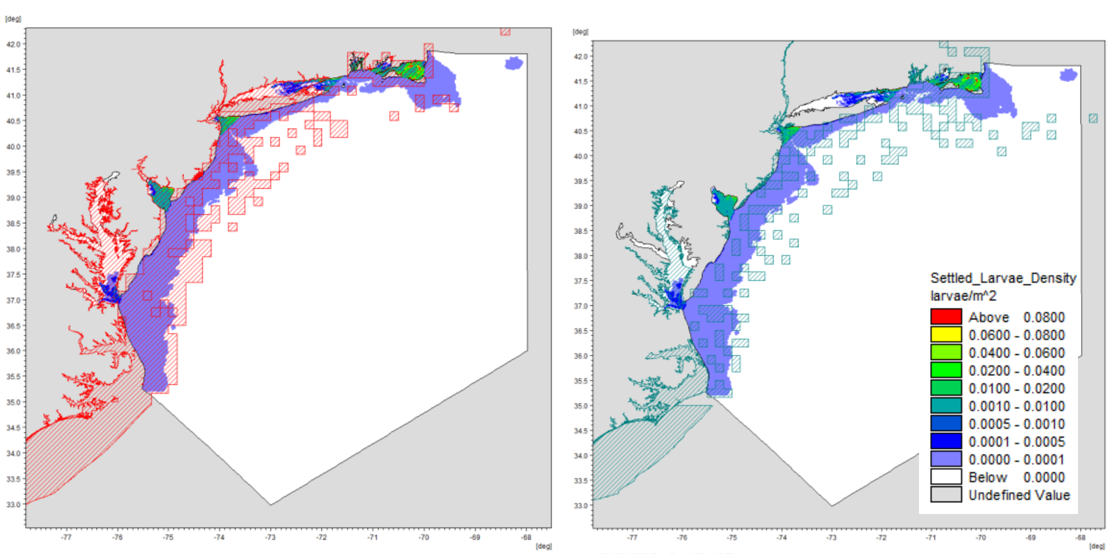

Figure 102. Settled larval summer flounder density and summer flounder juvenile fish EFH

Modeled settled larval summer flounder density (larvae/m^2) in the full model domain. (Left) Summer flounder juvenile fish EFH (NOAA 2018) is displayed in red hatches. (Right) Summer flounder larval fish EFH (NOAA 2018) is displayed in green hatches for comparison.

Focusing on the general OSW build-out area, a continuous area of higher sea scallop larval settlement density is predicted to occur in, and to the south of, the Nantucket Shoals (**Figure 103**). For geographic place reference, please refer to **Figure 14.** Massachusetts-Rhode Island Offshore Wind Farm study focus area. Whereas patches of higher density sea scallop larval settlement are also evident along Great South Channel (incl. eastern slope of the Davis Bank), to the south and southwest of Martha's Vineyard and in waters to the east of Long Island. More significant densities of silver hake larval settlement are predicted to occur to the south - southeast of Martha's Vineyard and Nantucket (**Figure 104**), with the highest of these densities near or beyond the Phelps Bank. Higher densities of silver hake larval settlement are also generally evident in the area of the Georges Bank. For the summer flounder, settlement occurs primarily in Nantucket and Block Island Sound, as well as upstream in Buzzards Bay and Narragansett Bay **(Figure 105**).

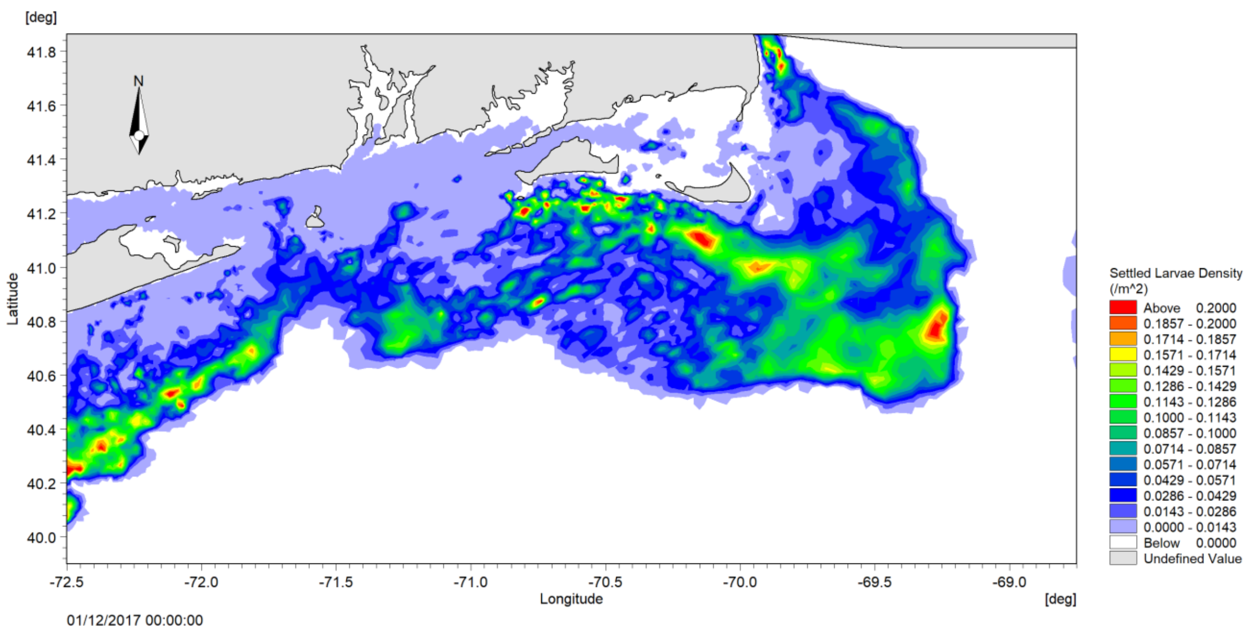

Figure 103. Settled larval sea scallop density
Modeled settled larval sea scallop density (larvae/m^2) in the study area.

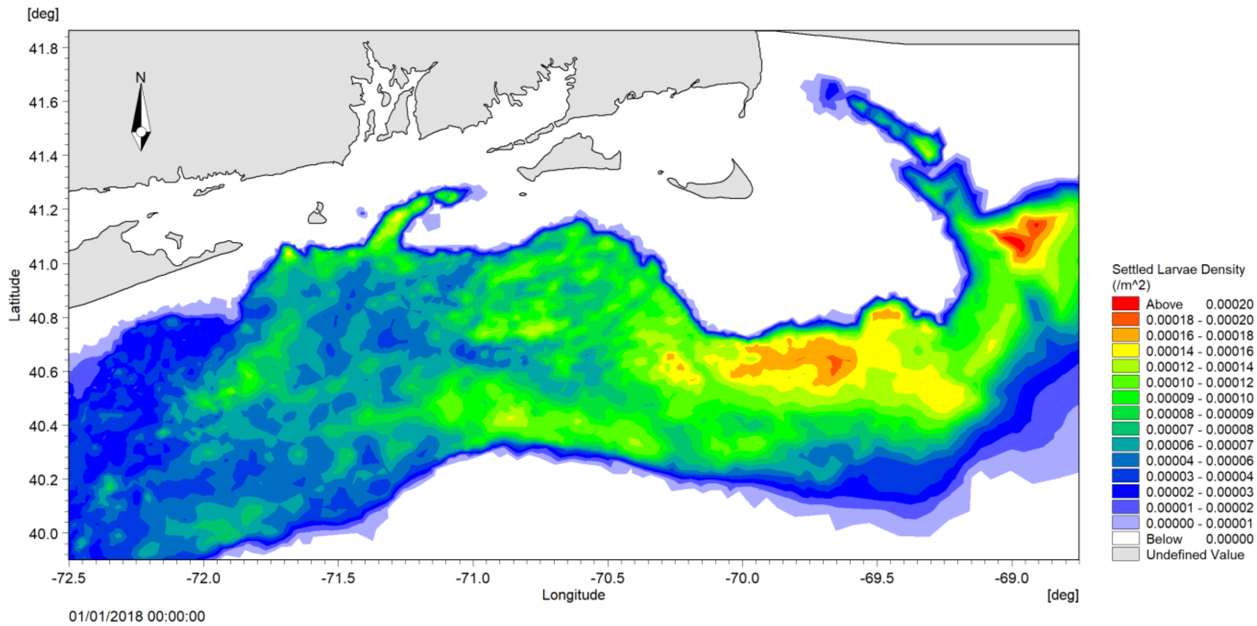

Figure 104. Settled larval silver hake density
Modeled settled larval silver hake density (larvae/m^2) in the study area.

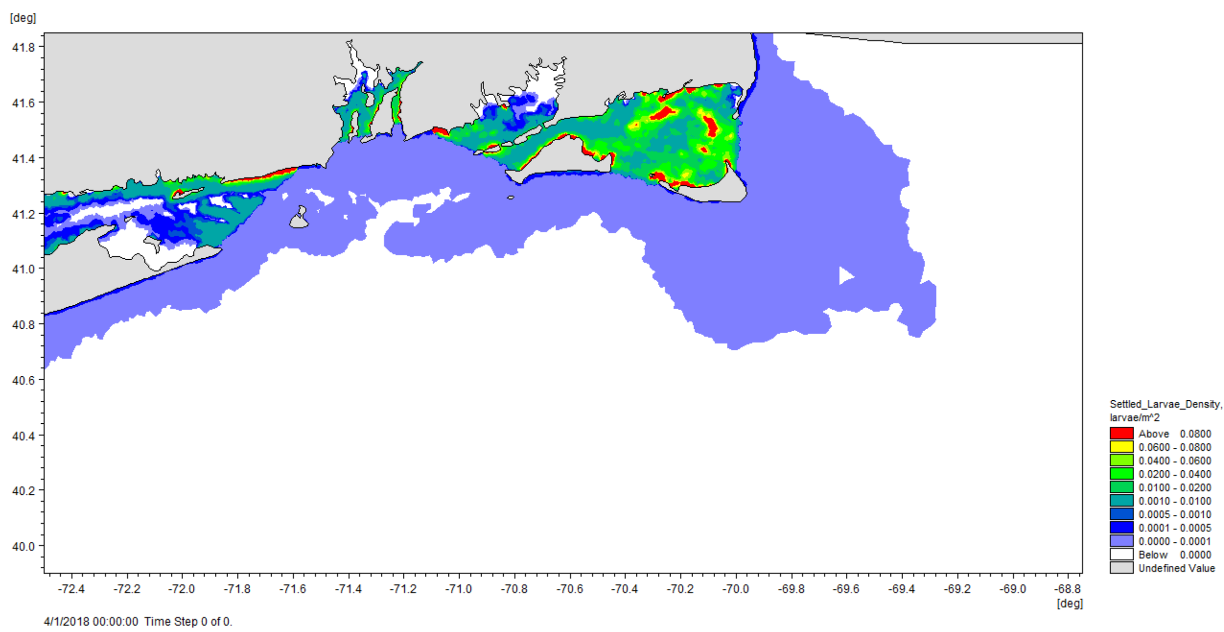

Figure 105. Settled larval summer flounder density
Modeled settled larval summer flounder density (larvae/m^2) in the study area.

6.4.2 Validation of Baseline Scenario

6.4.2.1 Pattern 1: Spatial distribution

As the spatial component is a key element in the ABMs applied in this project, the modeled spatial distribution of larvae of the three species was validated with survey data (see **Section 6.2.2.2**). For sea scallop, the distribution of settled larvae was compared to the distribution of adults, obtained from the SMAST survey (SMAST 2016), while the average monthly abundance of suspended larvae for silver hake and summer flounder was compared to the average monthly abundance of suspended larvae observed in the EcoMon dataset.

As spatial correlation can vary depending on the resolution of the compared distributions, the comparisons was conducted on resolutions from 10 to 100 km^2, using a Gamma Rank correlation. Overall, the correlation increased with resolution for all species (**Figure 106, Figure 107, Figure 108**), with an optimum around 60 to 80 km^2. In summary, correlation for sea scallop was good (Gamma Rank correlation max = 0.33); it was excellent for silver hake (Gamma Rank correlation max = 0.71) and acceptable for summer flounder (Gamma Rank correlation max = 0.21).

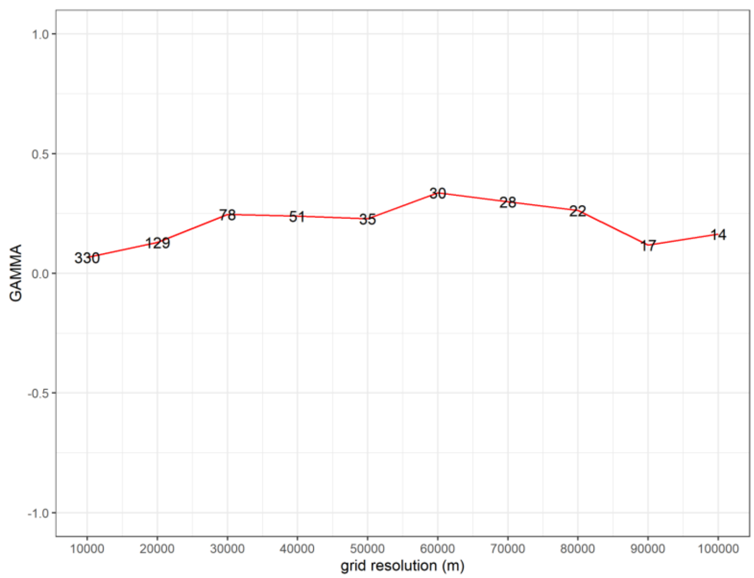

Figure 106. Gamma Rank correlation results for sea scallop
Correlation between modeled sea scallop larval settlement patterns and observed abundances of adult sea scallop (SMAST survey 1966 – 2015). The correlation coefficients range from -1 to 1 on the y-axis. The spatial scale shown on the X-axis ranges from 10 to 100 km. Sample sizes are indicated at each point.

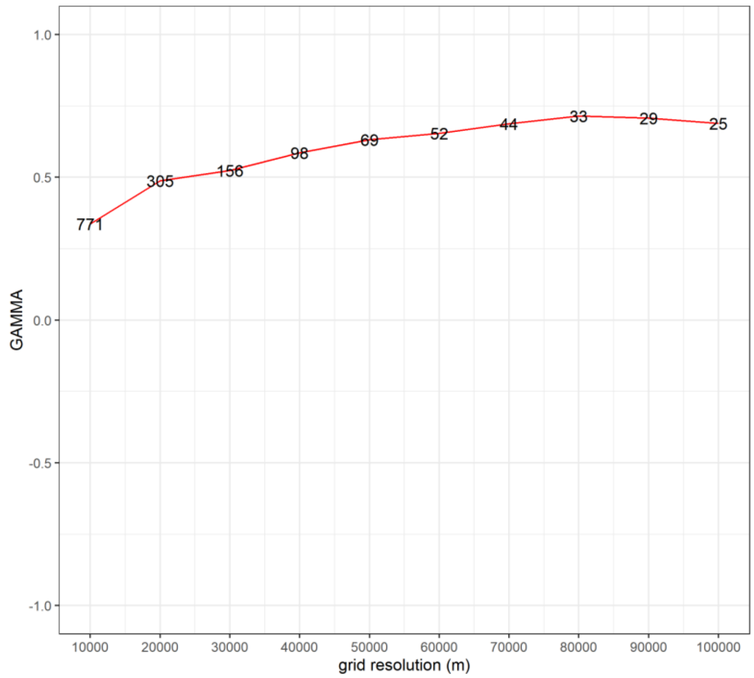

Figure 107. Gamma Rank correlation results for silver hake
Correlation between modeled spatial distribution of average suspended silver hake larvae and observed average abundances of suspended silver hake larvae (EcoMon survey 1966 – 2015). The correlation coefficients range from -1 to 1 on the y-axis. The spatial scale shown on the X-axis ranges from 10 to 100 km. Sample sizes are indicated at each point.

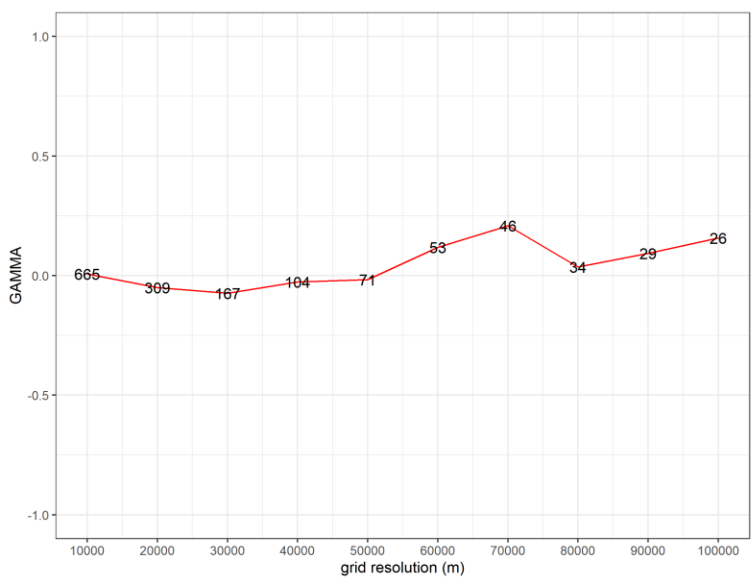

Figure 108. Gamma Rank correlation results for summer flounder
Correlation between the spatial distribution of modeled average suspended larvae for summer flounder and observed average abundances of suspended summer flounder larvae from the EcoMon survey (Sep – Dec). The correlation coefficients range from -1 to 1 on the y-axis. Spatial scale shown on the X-axis ranges from 10 to 100 km. Sample sizes are indicated at each point.

To verify the analyzed Gamma Rank correlations for the three species, the modeled spatial distributions were further compared visually to the observed spatial distribution in their optimal resolution (**Figure 109**). The overall patterns of the model output to a large degree reflected the observed spatial distribution of each species. Only summer flounder, which also had the lowest correlation index had a slight displacement of distribution further from shore than the observed distribution, which also explains the relatively low correlations scores for the summer flounder in the finer resolutions. Yet, despite these small deviations, the results from the spatial analysis showed an overall good correlation between the model output and the observed spatial distribution for each of the three species.

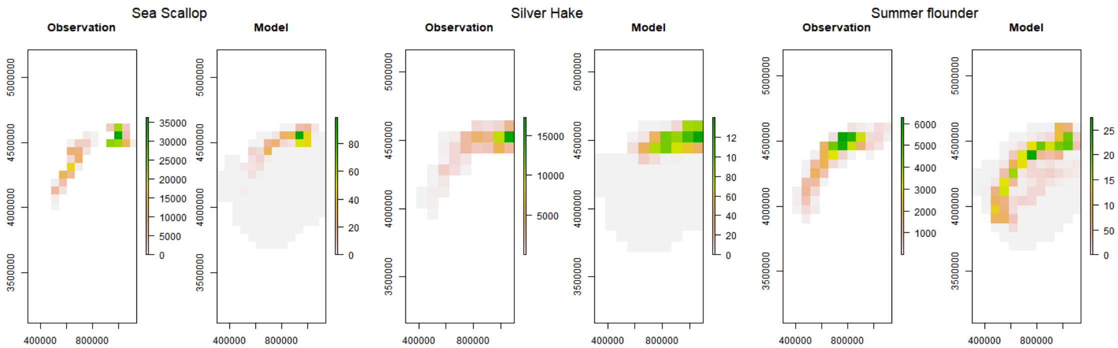

Figure 109. Comparison of modeled spatial distribution and observed distribution
Comparison was performed for all three species in their optimal resolution (sea scallop 60 km^2, silver hake 80 km^2 and summer flounder 70 km^2).

6.4.2.2 Pattern 2: Temporal Development

While there were no survey data available for comparison between model incubation times and real-world incubation of the three species, there was an overall good agreement between model results and literature. Both modeled sea scallop and silver hake zygotes hatched between 1 – 2 days after spawning (mean = 1.46 days, max = 1.9, min = 1.0). For sea scallop, this corresponded with the incubation time assessed by Culliney et al. (1974), which found the development time from zygote to a swimming gastrula to be between 30 to 40 hours at 12°C. For silver hake, model results matched the findings of Lock and Packer (2004), which found the mean incubation time to be 2 days. The emergent incubation time for summer flounder was on average 3 days (max = 5.29, min = 1.28), which corresponded with the expected incubation time between 72 and 75 hours estimated by Packer et al. (1999).

The transition from planktonic larvae to settled individual corresponded well with literature data for all three species. Sea scallops had, on average, the shortest transition time of 34.28 days (max = 40.0, min = 29.3), followed by silver hake (mean = 36.54 days, max = 45.07, min = 25.64) and summer flounder (39.9 days, max = 59.4, min = 19.9). In comparison, McGarvey et al. (1992) found that sea scallops transitioned from egg to settled juveniles in 4 to 6 weeks, Hart and Chute (2004) estimated that it took 40 to 60 days before sea scallops reached the juvenile stage, and Culliney et al. (1974) found that the pediveliger stage occurred after 28 to 35 days. Steves and Cowen (2000) estimated that silver hake larvae settled on average after 34.5 days in the New York Bight and Keefe and Able (1993) estimated that summer flounder transitioned to juveniles after 20 to 62 days in water temperatures between 14.5 to 16.6°C. Modeled summer flounder larvae were suspended at temperatures between 12 to 18°C, which corresponds with the development temperatures applied by Keefe and Able (1993).

6.4.2.3 Pattern 3: Vertical distribution

The vertical distribution of the planktonic larvae for all three species was mainly governed by the vertical currents and buoyancy of the larvae, as little vertical movement could affect the distribution. Thus, for both sea scallop and silver hake, the larvae were distributed across most of the water column, which was supported by Tremblay and Sinclair (1988), who found that sea scallop larvae in well-mixed waters would be evenly distributed along the water column. Reiss et al. (2002) found similar distributions for silver hake larvae, with an even distribution across their sampling range (3 to 44 m). The emergent average depth range for summer flounder was found to be between 0 to 25 m (see Figure 110, for example), likely due to their vertical swimming capabilities, corresponding well with the findings of Burke et al. (1998) which found that the highest abundances occurs at mid-depth between 0 to 20 m.

For both silver hake and summer flounder, there was a distinct diurnal vertical movement pattern (see **Figure 111** for example) which was absent in sea scallop. For silver hake, the pattern resembled the nightly upward migration of the larvae and daily downward migration, which was identified by Alvarez-Colombo et al. (2011). The same pattern was seen for the summer flounder which experiences upward migration during night-time flood tides and downward migration during daytime ebb tides, which was identified by Henderson and Fabrizio (2014). The sea scallop was parameterized to stay within temperature ranges of 1 to 16.5°C as suggested by Munroe et al. (2018). However, this vertical movement did not result in any specific diurnal pattern, which again corresponded with the findings by Tremblay and Sinclair (1988). Thus, the emergent diurnal vertical distribution of the larvae corresponded well with literature and the parameterized swimming patterns were sufficient to enable the diurnal patterns to emerge in concert with the occupied vertical currents.

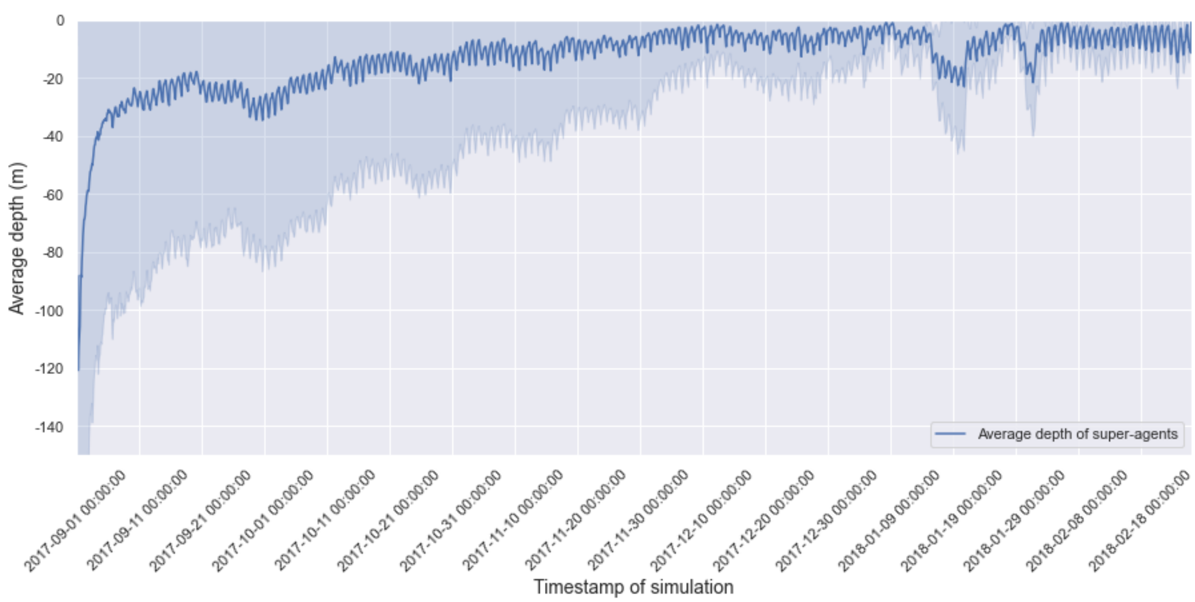

Figure 110. Average vertical distribution of all summer flounder super-agents in each timestep. The blue line indicates average values across super-agents, while the shaded area indicates standard deviation of the average.

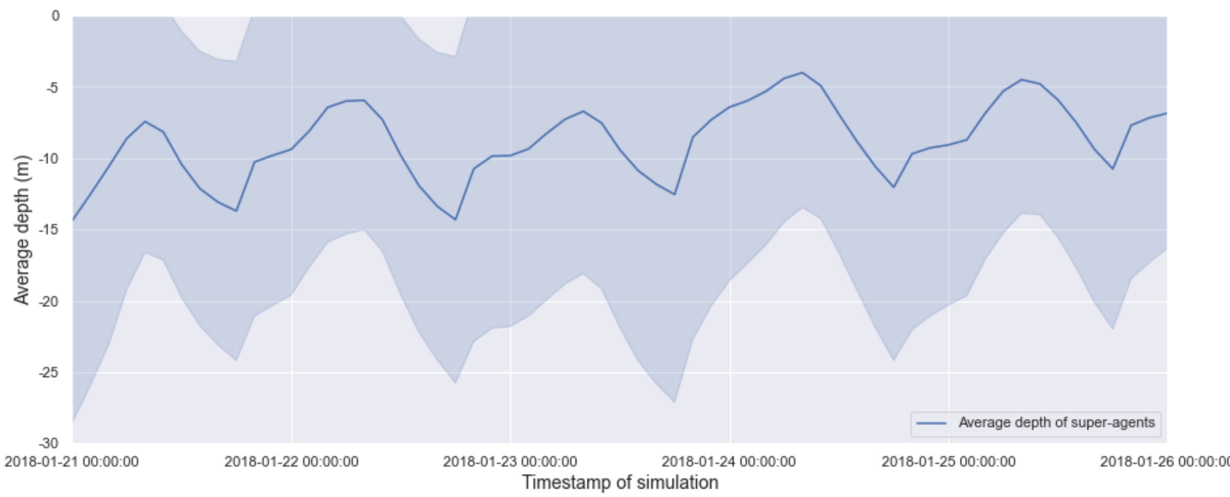

Figure 111. Average vertical distribution of summer flounder super-agents over five 24-hour periods.
The blue line indicates the average depth of super-agents at each time step of the model simulation, while shaded area indicates the standard deviation in depth.

6.4.3 Sensitivity Analyses

Sensitivity analyses were conducted on key parameters in each ABM setup, which were done to enable the assessment of model robustness and parameter fitness. Additionally, the sensitivity analysis can support an understanding of linear or non-linear effects of parameters on model output. The approach was to select three key parameters for each species, which were thought to have a key impact on the larval settlement. Subsequently, each parameter was incremented or decremented by 25% and a new simulation was run while keeping all other parameters constant (this approach is also known as 'one factor at a time', or OFAT). The effect of the parameter change was then assessed by examining the difference in settlement between each sensitivity run and the baseline run (see **Appendix C**).

The same parameters were selected for each species, to enable consistency of comparison. These were maximum daily zygote and larval mortality rate, maximum competency gain probability and settling coefficient. Overall, this exercise revealed that each species model was sufficiently robust, with no individual parameters having a profound effect on the model output. However, each species exhibited different responses to changes in the three selected parameters.

For sea scallop, changes in zygote and larval mortality did not show any unidirectional effect. A redistribution of settlement was rather apparent, which is more likely due to stochasticity in the model rather than a parameter effect. It is likely that direct mortality of individuals does not have a significant effect on the number of settled larvae, where indirect mortality such as unsuitable substrate or other development parameters exert a larger effect. Changes in maximum competency gain on the other hand showed a linear response to change, evident in the reductions in competency gain and reduced settlement, and vice versa. This is expected as larvae cannot settle until they reach competency. Thus, competency gain had a more profound effect than mortality. Likewise, there was a linear effect of the settling coefficient, with a larger effect than competency gain.

The sensitivity adjustment effect on silver hake zygote and larval mortality demonstrates, in contrast to the sea scallop, a non-linear response. Here, reduction in mortality resulted in an overall small increase in settlement, while an increase does not significantly alter larval settlement. The remaining two parameters exhibit the same linear response as that of the sea scallop larvae. For summer flounder, the effects of sensitivity adjustments of all three selected parameters show little overall effect, with no apparent directionality. This is likely due to the summer flounder larval settlement being governed by their ability to swim to estuaries.

In summary, the influence of sensitivity analysis adjustments varied for the three species. This is likely due to emergent settlement of the larvae being governed by different elements of the model. However, none of the selected parameters cause model outputs to significantly vary, suggesting a suitable robustness in the model setup. Results from previous model setups also suggest that agent release areas and release abundances had a larger impact on larval settlement, which is also likely, as hydrodynamic conditions are a primary influence on the distribution of the larvae.

7 Agent-Based Model Results of Larval Transport and Settlement

7.1 Overview

The subsequent sections provide the results of two analyses associated with the execution of the ABM of OSW build-out scenarios for sea scallops, silver hake, and summer flounder. Namely, a descriptive analysis of the change of each species' larval distribution in relation to the four OSW build-out scenarios, and an overall concluding analysis of the effect of OSW induced changes to oceanic responses and the corresponding distribution impact to selected larvae. This broader closing analysis draws on the totality of results from the oceanic response modeling and ABM to summarize the impacts and provide a general synopsis of their relevance.

To provide the reader a reminder when reviewing the modeled results in subsequent subsections, the analyzed OSW build-out scenarios are noted below:

- Scenario 2: Full build-out OSW lease offshore MA-RI area, 12 MW turbines (1,063 towers)
- Scenario 3: OCS-A 0501, 12 MW turbines (197 towers)
- Scenario 4: Full build-out OSW lease offshore MA-RI area, 15 MW turbines (1,063 towers)
- Scenario 5: Mid-level, 12 MW turbines (766 towers).

Similarly, as a reminder, the ABM hindcast run periods are noted below:

- ***Sea scallop*** model runs were performed with a spawning release period from August 8, 2017 to October 13, 2017. The final timestep investigated for full settlement was December 1, 2017.
- ***Silver hake*** model runs were performed with a spawning release period from May 15, 2017 to October 31, 2017. The final timestep investigated for full settlement was January 1, 2018.
- ***Summer flounder*** model runs were performed with a spawning release period from September 01, 2017 to December 31, 2017. The final timestep investigated for full settlement was April 1, 2018.

Finally, for geographic place reference, please refer to **Figure 14.** Massachusetts-Rhode Island Offshore Wind Farm study focus area.

Larval settlement difference plots were determined to be the best technique to demonstrate OSW oceanic response changes to larval transport. These plots simply illustrate the cumulative change (i.e. over the duration of the model period) in settled larval density (expressed as larvae/m^2) due to the influence of the OSW scenarios.

7.2 Sea Scallop Model Results

7.2.1 Scenario 2

Scenario 2 model results for sea scallops (see **Figure 112**) predicts larger areas of settled larval density increases in the western portion of the OSW build-out area, and to its west and south west. Whereas larger areas of substantial settled larval density decreases are evident to the east of Long Island and south of Martha's Vineyard. There are also noticeable patches of increases and decreases south of Nantucket and in the Davis Bank area, along with an area of larval density increase towards the south of Cape Cod.

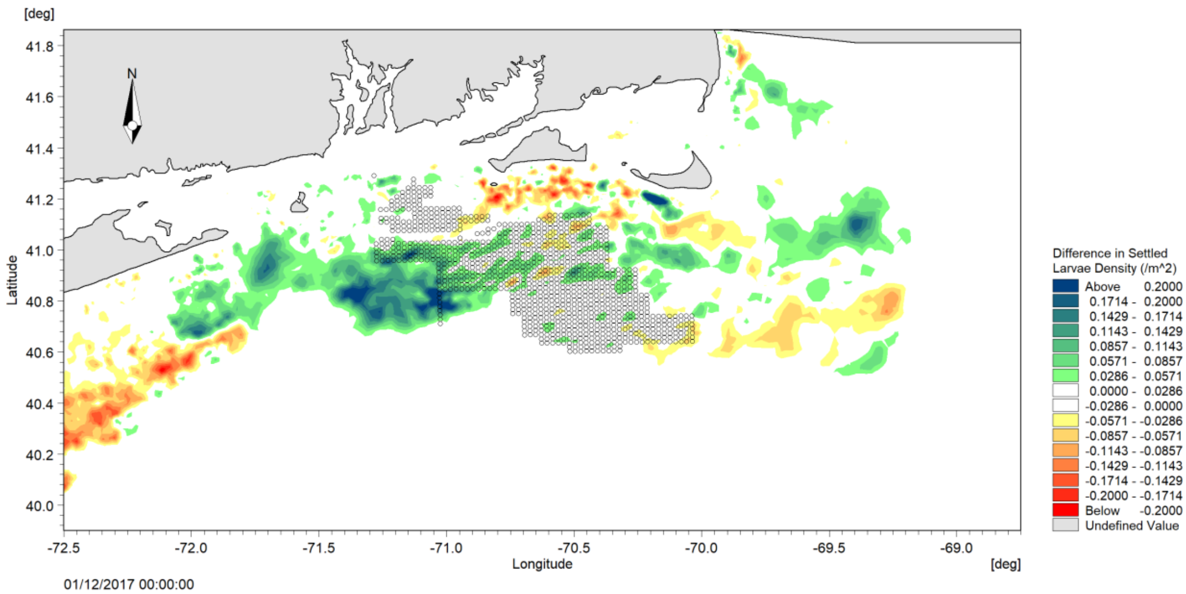

Figure 112. Predicted Scenario 2 differences in settled larval sea scallop density (larvae/m^2)
Change in settled sea scallop larval density (larvae/m^2), in relation to modeled baseline levels, due to the influence of Scenario 2 (i.e. shaded greens = increases in density, and shades of yellow/red = decrease in density).

7.2.2 Scenario 3

An evaluation of larval sea scallop settlement patterns in a Scenario 3 OSW build-out scenario (**Figure 113**) demonstrates a more scattered pattern of change than that for Scenario 2. There are, nevertheless, observable areas of more coherent patches of larval settlement density changes from baseline to Scenario 3. In terms of density increases, these entail a larger patch off Long Island, and to the southwest of the study area, inside and north of the Scenario 3 build-out area. With regards to density decreases, the area to the south of Martha's Vineyard is noticeable as well as an area of lesser consolidated patches in vicinity of the Nantucket Shoals.

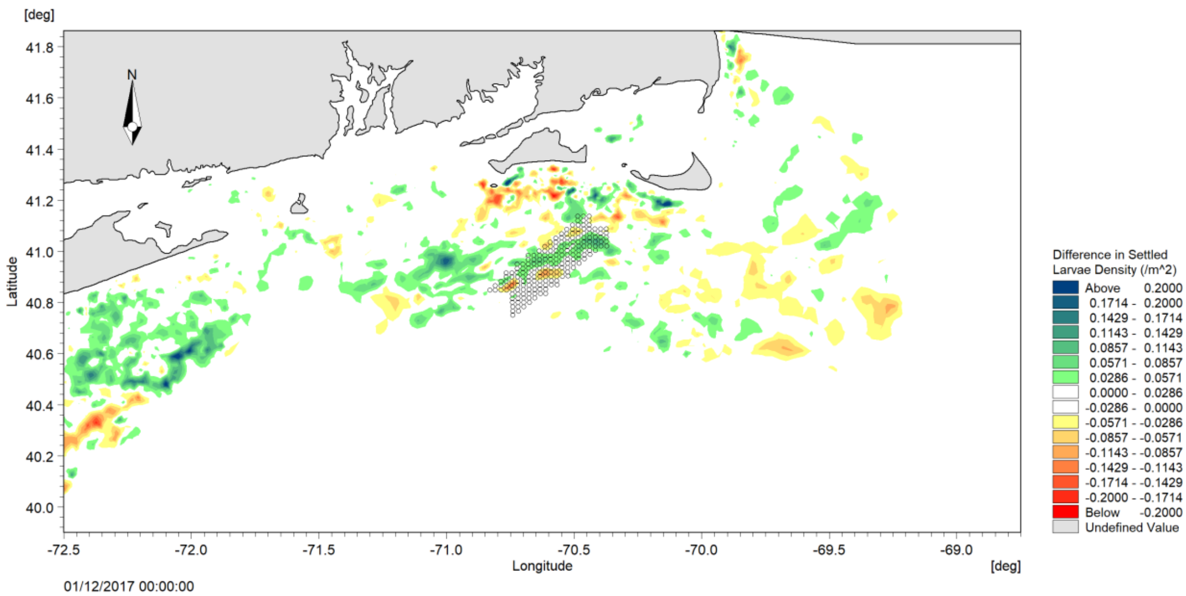

Figure 113. Predicted Scenario 3 differences in settled larval sea scallop density (larvae/m^2)
Change in settled sea scallop larval density (larvae/m^2), in relation to modeled baseline levels, due to the influence of Scenario 3 (i.e. shaded greens = increases in density, and shades of yellow/red = decrease in density).

7.2.3 Scenario 4

With larger turbines and the same layout as Scenario 2, Scenario 4 model results (**Figure 114**) demonstrate a similar general pattern of larval sea scallop settlement changes as in the transition from baseline to Scenario 2. Namely, increases in deposition to the west – southwest of the OSW build-out area and reductions to the north and in the waters south of Martha's Vineyard. Of these changes, a contiguous area of higher increases in sea scallop larval settlement densities south of Block Island is the most obvious (i.e. with a notable change in density greater than 0.2 larvae/m^2), along with less consolidated patchy increases running adjacent to Long Island. Other areas of larval sea scallop settlement increases are visible in the OSW build-out area, to the south – southwest of Nantucket, and scattered in areas of the Nantucket Shoal and Davis Bank. Notable areas of decreases in settlement between baseline and this particular OSW layout entail the aforementioned area south of Martha's Vineyard and an elongated patch running along the noted area of increased larval settlement adjacent to Long Island.

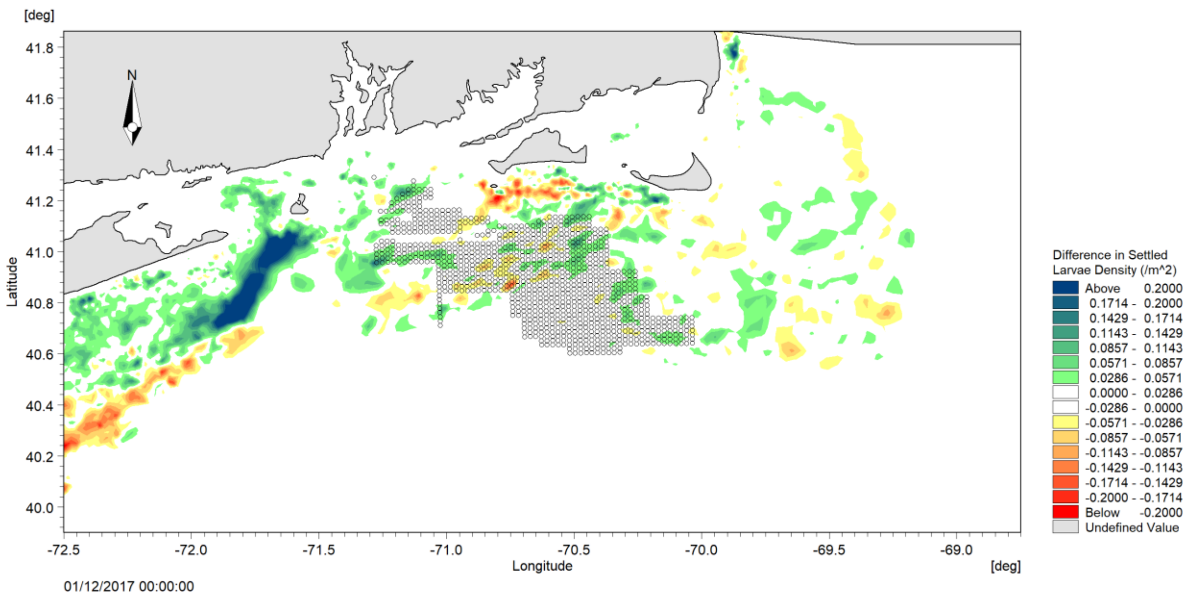

Figure 114. Predicted Scenario 4 differences in settled larval sea scallop density (larvae/m^2)
Change in settled sea scallop larval density (larvae/m^2), in relation to modeled baseline levels, due to the influence of Scenario 4 (i.e. shaded greens = increases in density, and shades of yellow/red = decrease in density).

7.2.4 Scenario 5

Scenario 5 model results (**Figure 115**) demonstrate a change in larval sea scallop settlement distribution between baseline and OSW situation similar to that of Scenario 4. Higher increases in larval settlement again appear in the area south of Block Island (i.e. with densities differences ranging between 0.08 larvae/m^2 to greater than 0.2 larvae/m^2) with patchy increases running further south to the east of Long Island. Other areas of patchy sea scallop larval density increases are situated primarily within the northern portions of the OSW and south -southwest of Nantucket. Discernable areas of decrease in larval settlement density are south of Martha's Vineyard, and in the Nantucket Shoals.

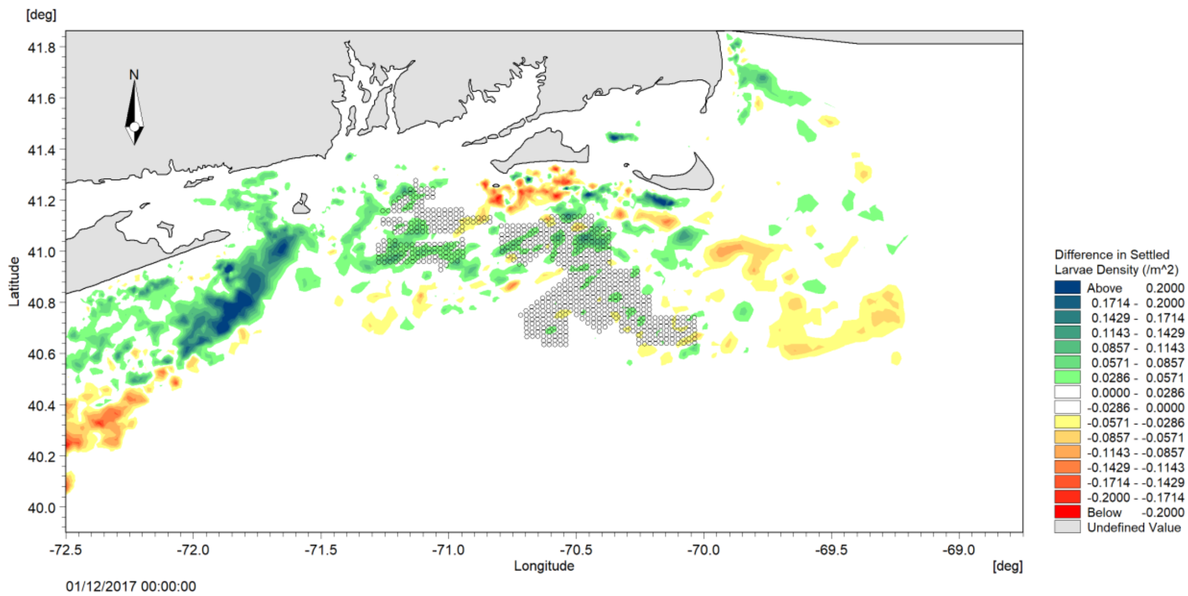

Figure 115. Predicted Scenario 5 differences in settled larval sea scallop density (larvae/m^2)
Change in settled sea scallop larval density (larvae/m^2), in relation to modeled baseline levels, due to the influence of Scenario 5 (i.e. shaded greens = increases in density, and shades of yellow/red = decrease in density).

7.2.5 Determinant Oceanic Responses

When reviewing the overall results (including animations of scenario runs) in relation to hydrodynamics and ABM characterization of larval sea scallop transport, it is generally apparent that changes in current speed are the main OSW-related oceanic responses behind the altered settlement distribution of larval sea scallop. For Scenario 2, for example, increases in current speed are predicted to the north and to the south of the OSW build-out area, with discernable decreases in current speeds (e.g. in relation to 75th percentile depth averages) evident in, and to the southwest. These observed changes broadly indicate that prevailing larval sea scallop transport from the Georges Bank enter areas of altered currents direction and/or increased current speed and, via influence of areas of decreased current speed, settle in greater densities to the southwest of the Scenario 2 OSW build-out area.

These same factors are also determined to be the cause of Scenario 4 and 5 larval settlement density shifts, as sea scallop larval transport from the east encounter areas of altered currents and settle in greater densities in areas of reduced current speeds. This general pattern becomes more evident in plots illustrating baseline and Scenario 4 suspended competent larvae counts per super-agent (see Figure 116). The suspended competent larvae represent the state of the larvae at a final stage before settlement.

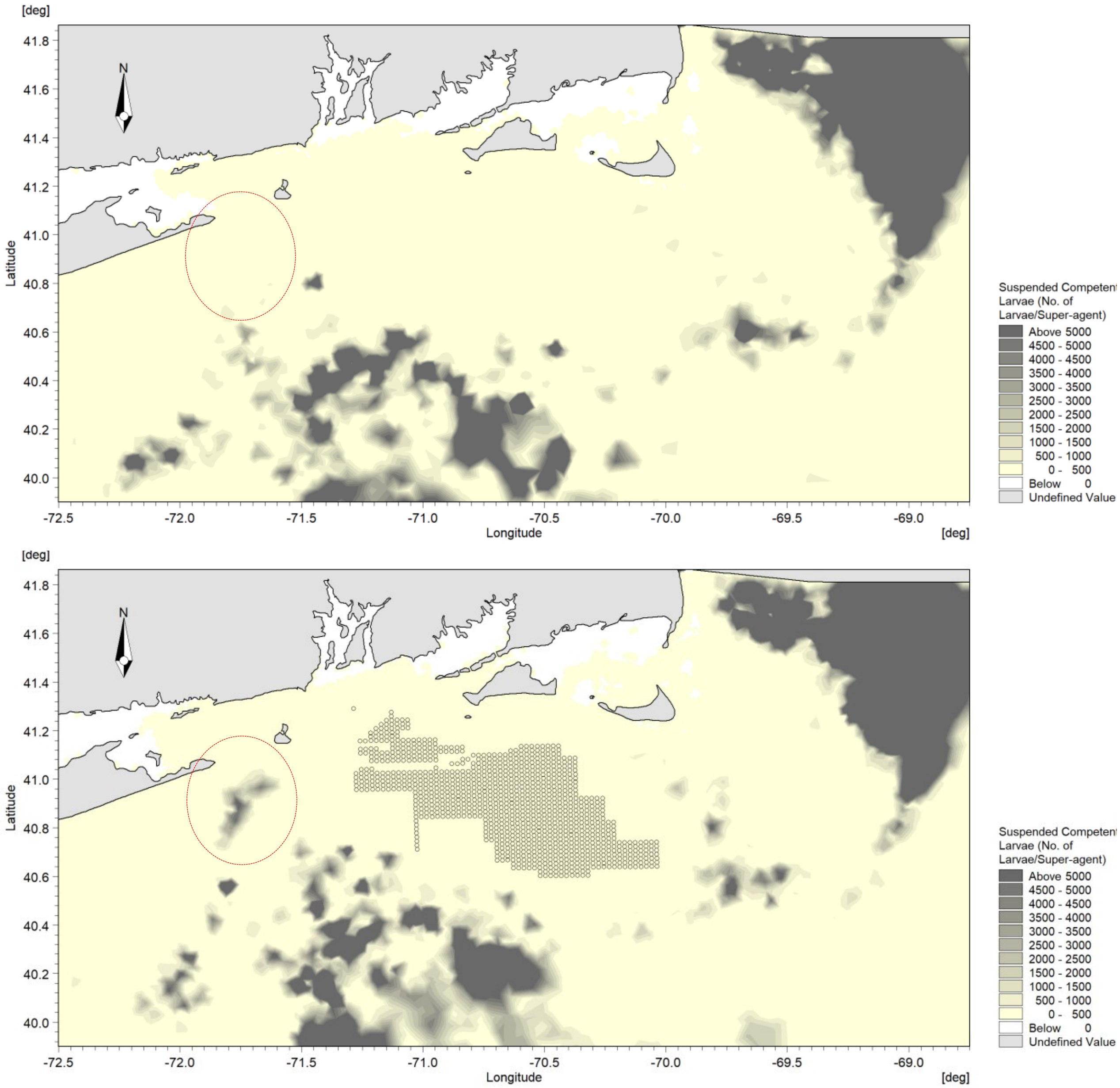

Figure 116. 95th percentile suspended competent larval sea scallop concentrations (larval count per super-agent) - baseline (above) and Scenario 4 (below)
Post final release suspended competent sea scallop larvae (super agents) - 95th percentile. The red circle indicates (i.e. through comparison with the same circle in the baseline plot) a key area where suspended larval counts per super-agent align with increases in settled larvae.

Figure 117 also shows that Scenario 4 reduced current speeds to the south limit larval transport in a southwest direction (via a slight accumulation of suspended larvae south of the OSW build up area) and push it slightly northwest. While currents to north of the OSW shift the larvae to the same area over the course of the model run. This convergence of suspended larval sea scallop transport to the area south of Block Island mimics the general pattern of settled larval densities evident in **Figure 114**.

In Scenario 3, less pronounced increases in current speeds north of the Scenario 3 OSW build-out area also appear to move larvae away from the area south of Martha's Vineyard and shift settlement patterns to the southwest of the OSW build-out area and to the area adjacent to Long Island. It is not clear, however, if the small area of reduced current speeds (75th percentile depth average) in the southern part of the OSW build-out area also plays a role in the change in larval settlement.

7.3 Silver Hake Model Results

7.3.1 Scenario 2

Model results (**Figure 117**) illustrate silver hake baseline and Scenario 2 larval settlement density differences in various areas east of Long Island, to south of the Nantucket Shoals and into the general Georges Bank area. While the pattern of settlement density change appears sporadic, patches of increases of larvae are apparent within the OSW, with more discernable, unified, and pronounced increases evident south of the Nantucket Shoals, and along the Great Southern Channel. In terms of decreases in larval density, patches are apparent southwest of, and within the Scenario 2 OSW build-out area; with a more distinct area of change directly to the south. This area also has higher levels of density decreases.

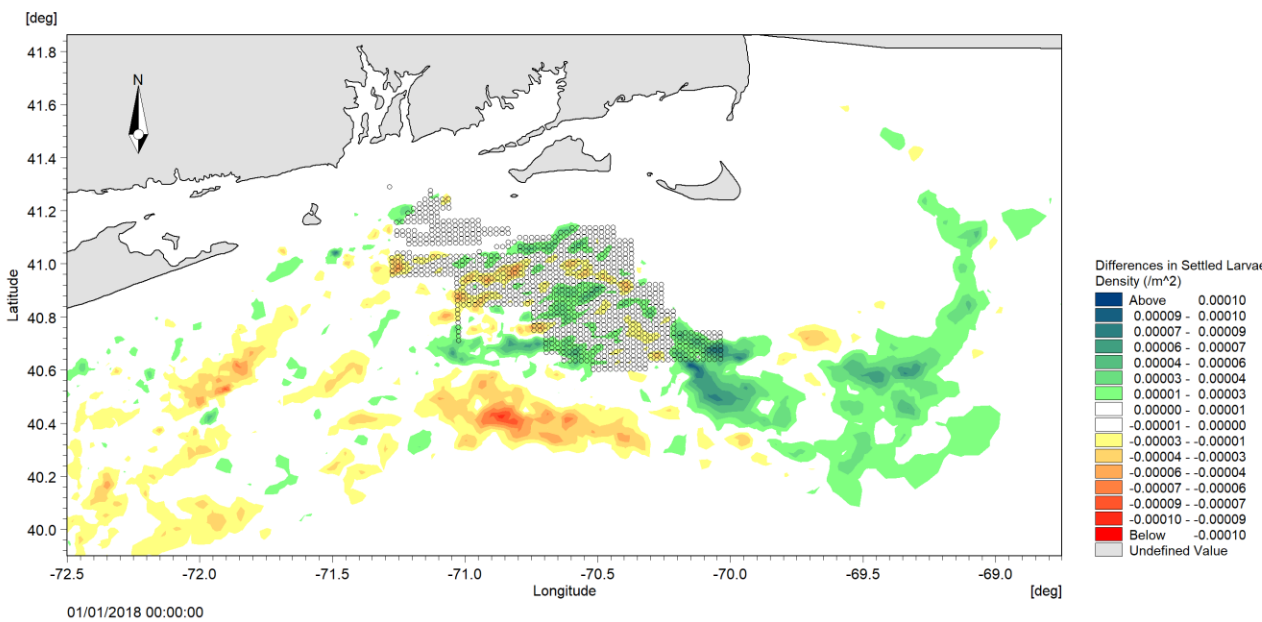

Figure 117. Predicted Scenario 2 differences in settled larval silver hake density (larvae/m^2)
Change in settled silver hake larval density (larvae/m^2), in relation to modeled baseline levels, due to the influence of Scenario 2 (i.e. shaded greens = increases in density, and shades of yellow/red = decrease in density).

7.3.2 Scenario 3

A review of the Scenario 3 model results (**Figure 118**) demonstrates a somewhat more irregular change in larval silver hake settlement distribution than that for Scenario 2 in the same general area. However, areas of more consistent patches of settlement density change are evident southeast of the Scenario 3 OSW build-out area, in the area south of the Nantucket Shoals, and to the east along the Great Southern Channel. Decreases in larval silver hake density are more variable, appearing mainly to the southwest and south of the Scenario 3 OSW build-out area.

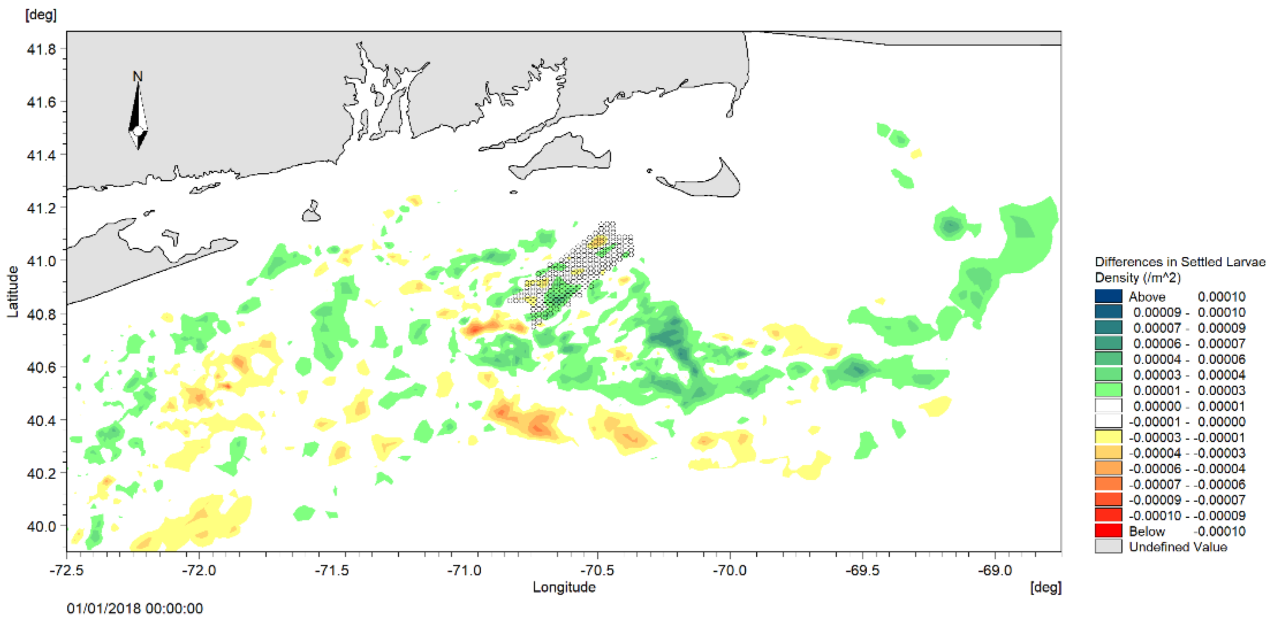

Figure 118. Predicted Scenario 3 differences in settled larval silver hake density (larvae/m^2)
Change in settled silver hake larval density (larvae/m^2), in relation to modeled baseline levels, due to the influence of Scenario 3 (i.e. shaded greens = increases in density, and shades of yellow/red = decrease in density).

7.3.3 Scenario 4

Following the general approach, the influence of Scenario 4 i.e. a fully built-out OSW MA-RI area with 15 MW turbines and 1,063 towers, on larval silver hake settlement distribution was modeled (**Figure 119**). With some similarities to Scenario 2, Scenario 4 model results illustrate that larval silver hake settlement changes occur in various areas east of Long Island, to south of the Nantucket Shoals and into the general Georges Bank area. The pattern of changes in settlement density are, however, more pronounced directly south of the Scenario 4 OSW build-out area and less evident south of the Nantucket Shoals and along the Great Southern Channel. Areas of increases in larval silver hake settlement are apparent within the OSW, with a more distinct and cohesive area of higher density increases directly south of the build-out area and south of the Nantucket Shoals. The most apparent area of decrease in larval density lies directly below the above-mentioned southern area of increased larval settlement.

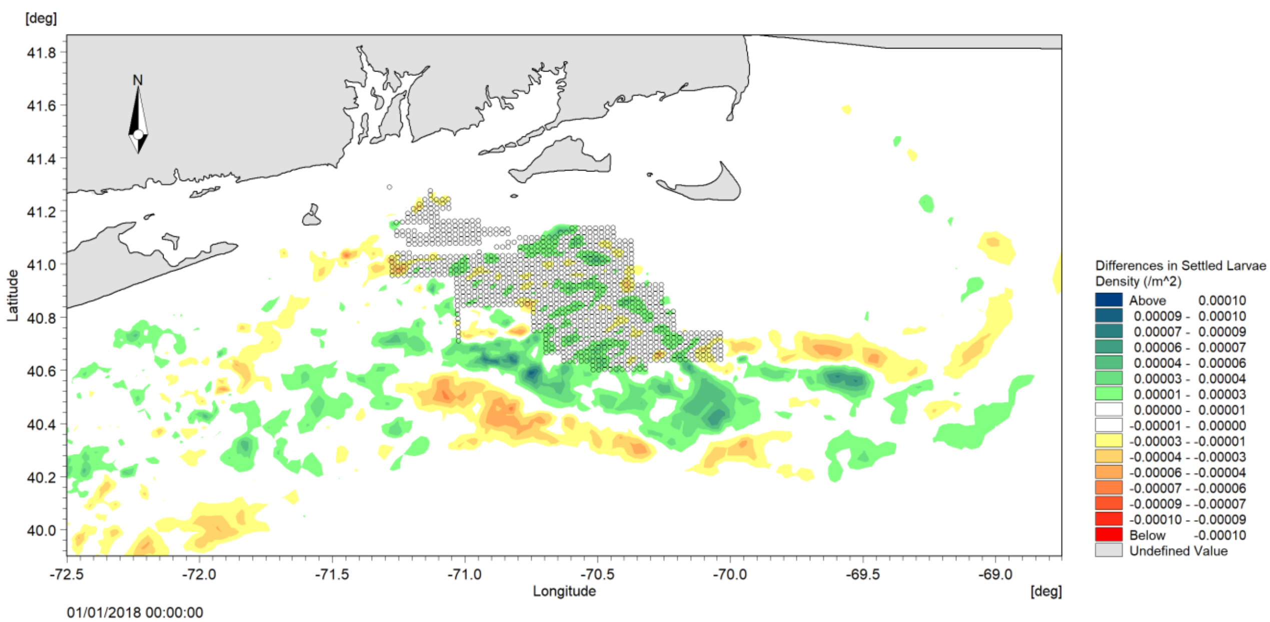

Figure 119. Predicted Scenario 4 differences in settled larval silver hake density (larvae/m^2)
Change in settled silver hake larval density (larvae/m^2), in relation to modeled baseline levels, due to the influence of Scenario 4 (i.e. shaded greens = increases in density, and shades of yellow/red = decrease in density).

7.3.4 Scenario 5

A review of the Scenario 5 model results (**Figure 120**) illustrates a general change in larval silver hake settlement distribution not dissimilar to that for Scenario 4. Patches of change are apparent in areas east of Long Island to south of the Nantucket Shoals and into the general Georges Bank area; with a prominent area of increase in larval settlement density predicted south of the OSW build-out area. The patchy areas of density increase, however, extend slightly further to the southwest, into areas south of the Nantucket Shoals and along the Georges Bank. An apparent area of decrease in larval density lies directly below the above-mentioned southern area of increased larval settlement, with patches again extending to the southwest and northeast of this area.

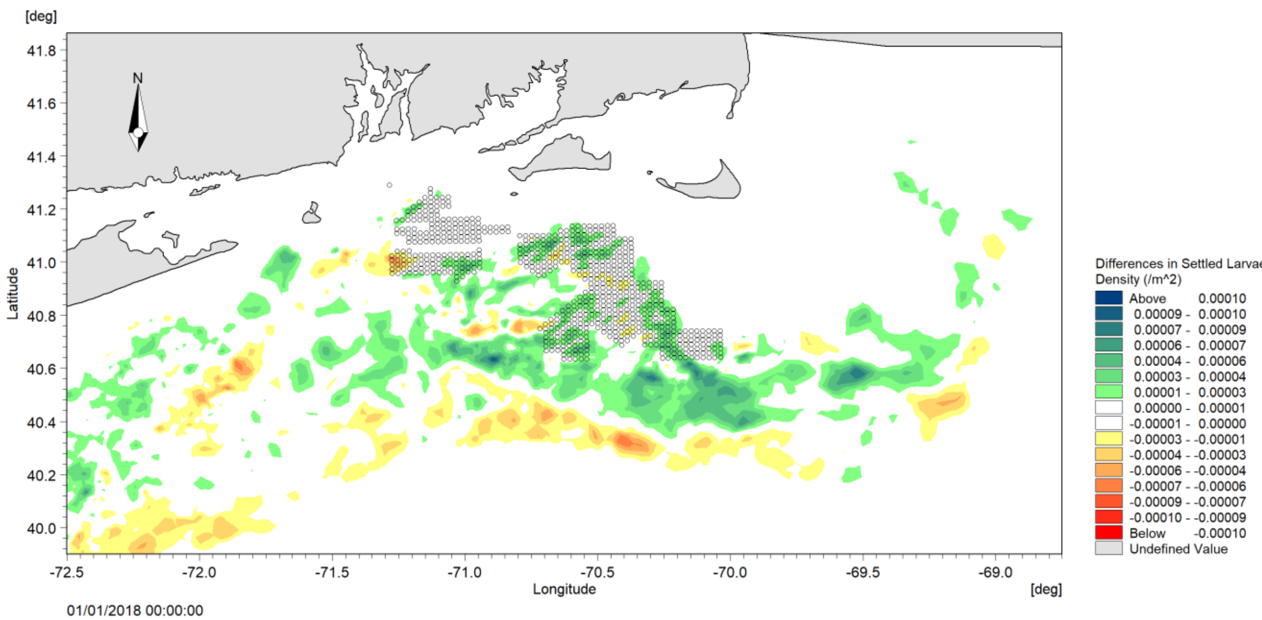

Figure 120. Predicted Scenario 5 differences in settled larval silver hake density (larvae/m^2)
Change in settled silver hake larval density (larvae/m^2), in relation to modeled baseline levels, due to the influence of Scenario 5 (i.e. shaded greens = increases in density, and shades of yellow/red = decrease in density).

7.3.5 Determinant Oceanic Responses

When reviewing results for Scenarios 2 to 5 (including animations of scenario runs) in relation to hydrodynamic results (e.g. depth average current speeds) and parameterized features of larval silver hake transport, indications are that changes in current speeds again play a determinant role in altered larval transport. For Scenario 2, it is generally evident that slight decreases of current speed within the OSW build-out areas, and slight increases in current speed south and north of the Scenario 2 OSW are influential in the aforementioned shift in settlement. Here, larval silver hake transport i.e. moving in circulating pattern over the study area with no prevailing directional source of larvae, appear to settle in greater densities when they encounter areas of slightly decreased currents speeds south of the Nantucket Shoals, and along the Great Southern Channel. This conclusion is further supported by plots of baseline and Scenario 4 suspended competent larval counts per super-agent (see **Figure 123**) with similar distribution over the study area. Here, the lack of evident patterns, in relation to larval settlement, show that slower current speeds cause the increase settlement rather than a clear change in the transport of suspended larvae.

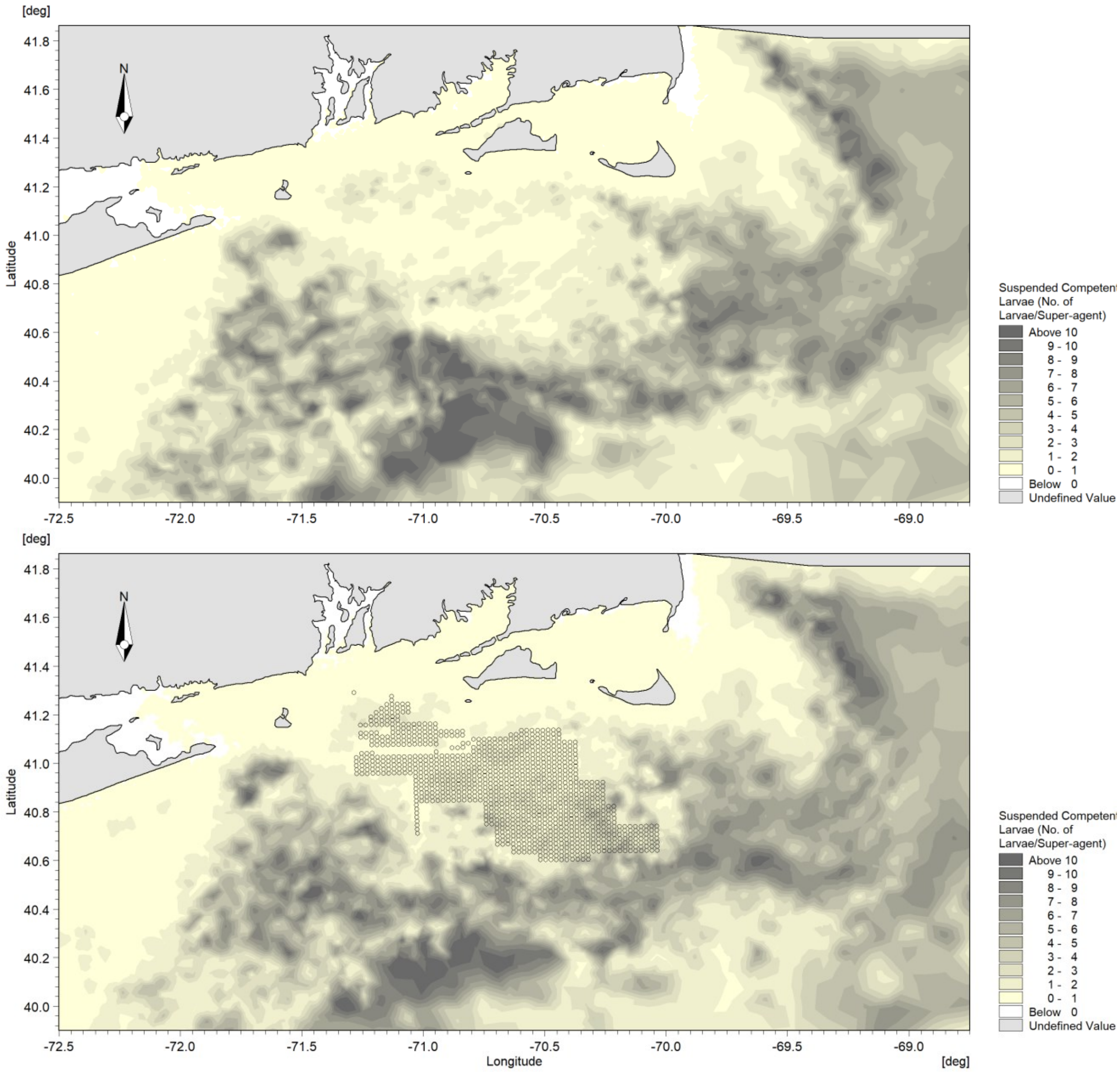

Figure 121. 95th percentile suspended competent larval silver hake concentrations (larval count per super-agent) - baseline (above) and Scenario 4 (below)
Post final release suspended competent silver hake counts per super-agent - 95th percentile

Scenario 4 and Scenario 5 reductions in current speeds play a similar role in the spatial shift in silver hake densities evident for these scenarios. Both scenarios show increases in current speed along northern portions of the OSW build-out areas and to the north, with differing areas of decreases in current speed to south and along the Georges Bank. This again suggests that larval silver hake circulating over the study area tend to settle in higher densities when they encounter slightly lower current speeds. For Scenario 3, a less defined but fairly prominent area of decreased current speed south of the Nantucket Shoals and along the Great Southern Channel is also seen as the determinant oceanic response causing consistent patches of larval silver hake settlement density increases in this area.

7.4 Summer Flounder Model Results

7.4.1 Scenario 2

Figure 122 shows that Scenario 2 would lead to varied larval summer flounder settlement density change in relation to the baseline scenario. No observable differences in larval settlement are evident in the direct vicinity of the Scenario 2 OSW build-out, east of Long Island or towards the Georges Bank. The primary discernable change is evident in the Nantucket Sound, with an overall reduction and small patches of increases north of Nantucket. Other changes are apparent mainly in shoreline areas of Vineyard Sound, Block Island Sound, Buzzards Bay and Narragansett Bay. Here, slight overall areas of increase are observable in Narragansett Bay, with variations in areas of increase and decrease in Block Island Sound and Buzzards Bay.

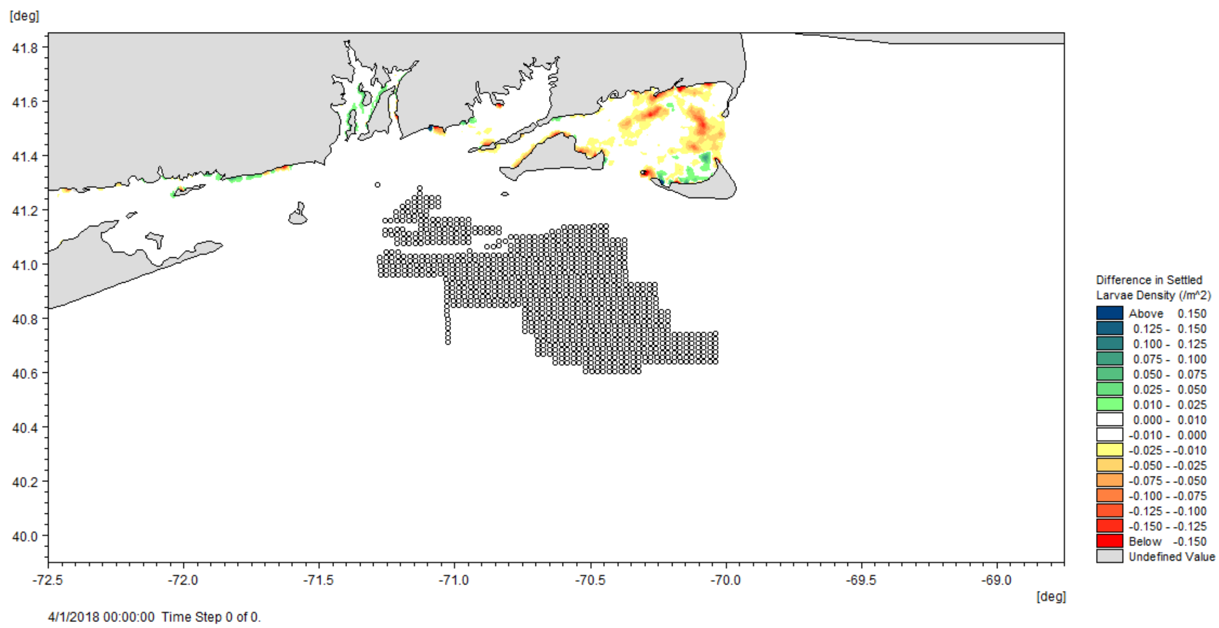

Figure 122. Predicted Scenario 2 differences in settled larval summer flounder density (larvae/m^2)
Change in settled summer flounder larval density (larvae/m^2), in relation to modeled baseline levels, due to the influence of Scenario 2 (i.e. shaded greens = increases in density, and shades of yellow/red = decrease in density).

7.4.2 Scenario 3

The influence of Scenario 3 on larval summer flounder settlement distribution is shown in **Figure 123**. As with Scenario 2, varied change in settlement density distribution is evident, with no observable differences in the direct vicinity of the Scenario 3 OSW build-out area, east of Long Island or towards the Georges Bank. Change in settlement again primarily occurs in Nantucket Sound, with mainly small patches of slight increases in shoreline areas of the Vineyard Sound, Block Island Sound, Buzzards Bay and Narragansett Bay. Settled larval density changes within the Nantucket Sound vary, with some localized areas of higher densities and some with lower densities than the baseline case.

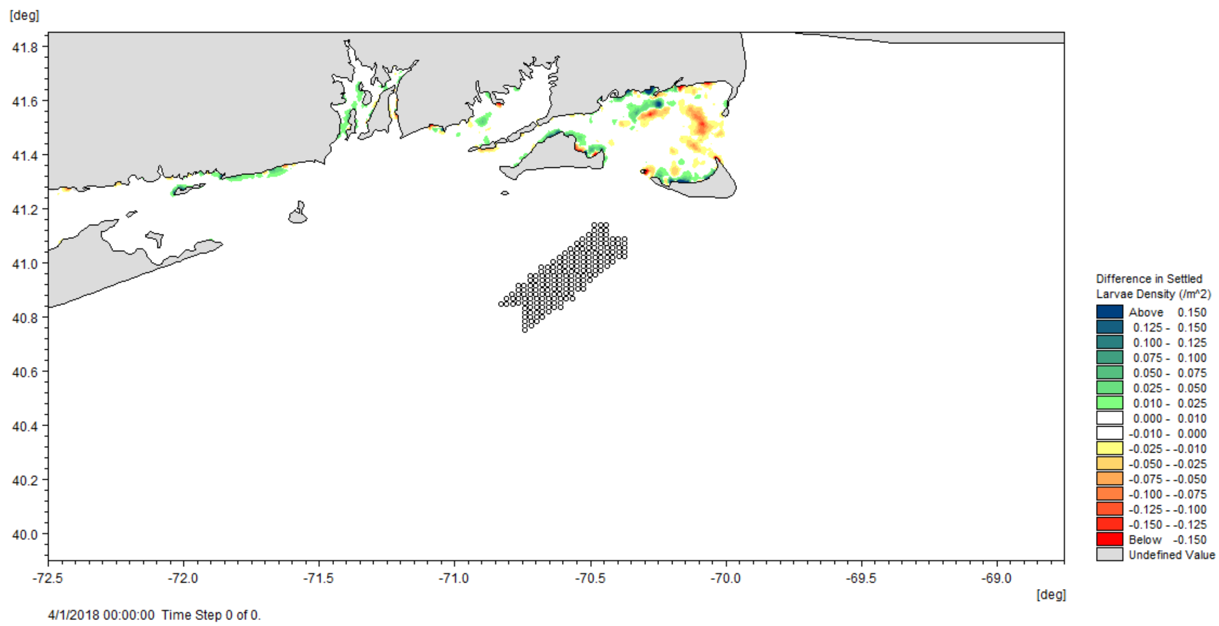

Figure 123. Predicted Scenario 3 differences in settled larval summer flounder density (larvae/m^2)
Change in settled summer flounder larval density (larvae/m^2), in relation to modeled baseline levels, due to the influence of Scenario 3 (i.e. shaded greens = increases in density, and shades of yellow/red = decrease in density).

7.4.3 Scenario 4

The influence of a fully built-out 15 MW turbines MA-RI OSW with 1,063 towers on larval summer flounder settlement density distribution is shown in **Figure 124**. This scenario, only different to Scenario 2 in terms of turbine size, again shows no noticeable differences in baseline larval density settlement in the direct vicinity of the Scenarios 4 OSW build-out area, east of Long Island or towards the Georges Bank. The main area of change in larval settlement is again the Nantucket Sound. However, contrary to Scenario 2, this seems to entail mainly slight increases in shoreline areas in the Block Island Sound, Buzzards Bay and Narragansett Bay.

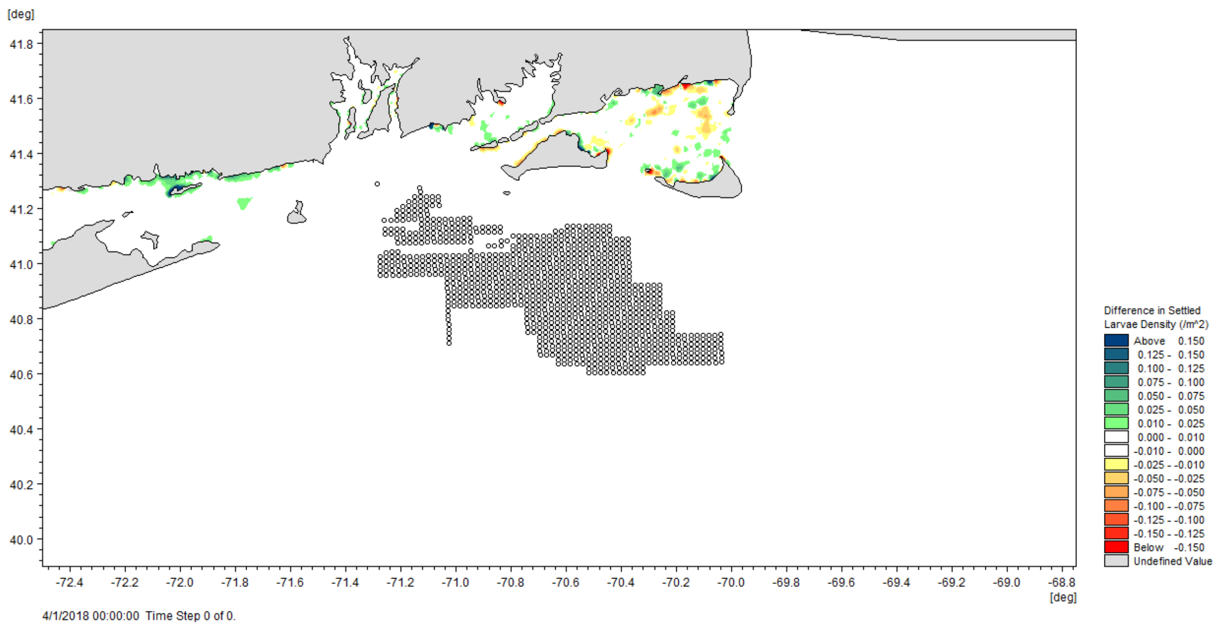

Figure 124. Predicted Scenario 4 differences in settled larval summer flounder density (larvae/m^2)
Change in settled summer flounder larval density (larvae/m^2), in relation to modeled baseline levels, due to the influence of Scenario 4 (i.e. shaded greens = increases in density, and shades of yellow/red = decrease in density).

7.4.4 Scenario 5

As with the other scenarios, Scenario 5 results (**Figure 125**) mainly exhibit discernable change in larval summer flounder settlement in the Nantucket Sound and no notable differences in larval settlement in / near the Scenario 5 OSW build-out area, offshore areas east of Long Island or towards the Georges Bank. Other areas of change are apparent mainly in shoreline areas of the Vineyard Sound, Block Island Sound, Buzzards Bay and Narragansett Bay. Here, slight overall areas of increase are observable in Narragansett Bay, with variations in areas of increase and decrease of settled larvae in the other areas.

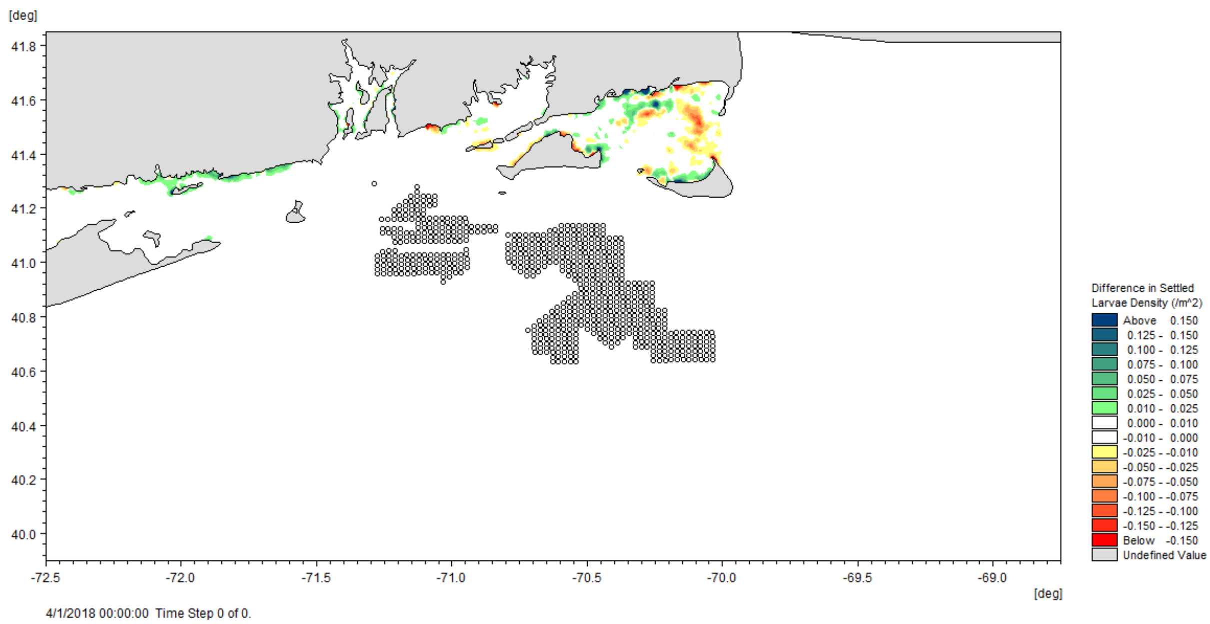

Figure 125. Predicted Scenario 5 differences in settled larval summer flounder density (larvae/m^2)
Change in settled summer flounder larval density (larvae/m^2), in relation to modeled baseline levels, due to the influence of Scenario 5 (i.e. shaded greens = increases in density, and shades of yellow/red = decrease in density).

7.4.5 Determinant Oceanic Responses

Oceanic responses influencing Scenarios 2 to 5 results become evident when reviewing animations of scenario runs and changes in hydrodynamics, and when considering the parameterized features of the summer flounder, namely, its parameterized swimming speed and swimming direction. It is hypothesized that some of the summer flounder larvae enter an area of lower current speeds to the southeast of the OSW build-out area. In these waters, their horizontal swimming and directional preferences cannot overcome the reduction in current speed and changes in current direction, thereby preventing some from entering Nantucket Sound. It is also evident that this influences the larval settlement density changes apparent to the north and northwest of the OSW build-out area. It is noted that summer flounder transport behavior within Nantucket Sound (and other estuarine systems in the area) is defined as tidally influenced in the ABM (see **Section 6.2.4.3.5**) and is, as such, governed by a separate set of transport parameters based on selective tidal stream transport behavior of pre-settlement larvae (Hare et al. 2006).

The general altered summer flounder transport pattern described above is further evident in plots illustrating baseline and Scenario 4 suspended competent larval counts per super-agent (see **Figure 126**).

The plotted suspended competent summer flounder larvae represent the beginning of the stage at which they swim shoreward toward estuarine systems.

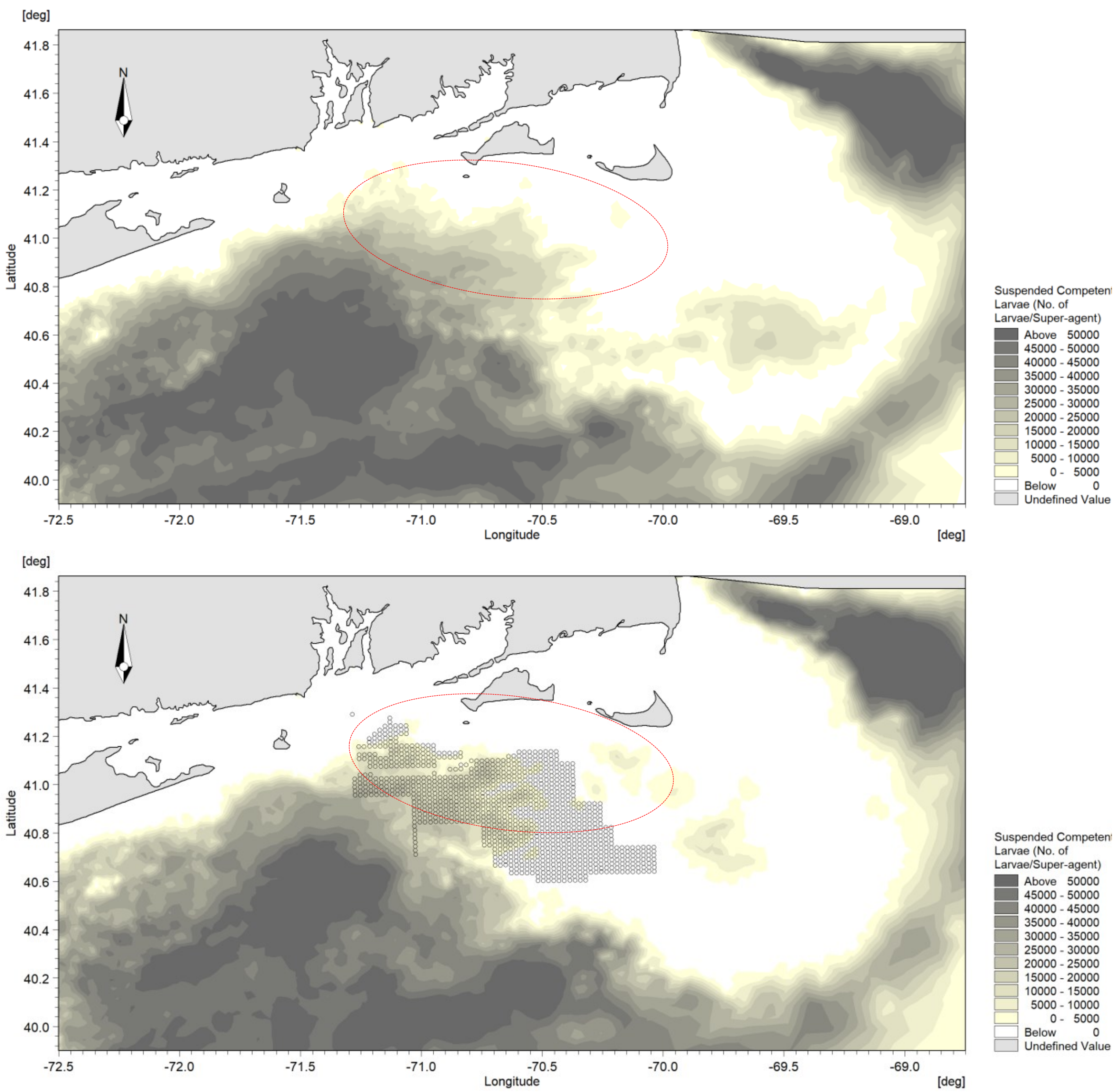

Figure 126. 95th percentile suspended competent larval sea scallop concentrations (larval count) - baseline (above) and Scenario 4 (below)
Post final release suspended competent summer flounder Larvae (super agents) - 95th percentile. The red circle indicates (i.e. through comparison with the same circle in the baseline plot) an area of reduced suspended larval counts caused by Scenario 4.

Figure 126 illustrates that Scenario 4 induced current speed reductions to the southwest of the OSW area hinder competent larval summer flounder transport in a northeast direction over the OSW build up area leading to a reduced competent larva count directly south of Nantucket (see circled area) in relation to the baseline. As previously mentioned, it is this change in suspended larval transport that prevents some larval summer flounder from reaching, and settling in, the Nantucket Sound. Conversely, a slight localized accumulation of competent larvae towards the south of Block Island and lower current speeds in the area appear to allow marginal increases of competent larvae to swim in a shoreward direction and settle in the shoreline areas of Block Island Sound, Buzzards Bay and Narragansett Bay (see **Figure 122, Figure 123, Figure 124, Figure 125**).

7.5 Conclusions Drawn from Agent-Based Modeling

Through a review of the overall baseline and OSW build-out ABM result for sea scallops, silver hake, and summer flounder in the study area, a number of conclusions can be drawn regarding the influence of the analyzed OSW build-out scenarios on their effect on the distribution of larval settlement. The following section provides summarized explanations of these conclusions as they relate to baseline and OSW build-out scenarios, with a focus on the key findings and related determinant oceanic responses and larval transport and settlement characteristics. The section is further concluded with a discussion on the general relevance of the change in larval transport and settlement.

7.5.1 Baseline Larval Distribution Validation

POM analyses applied defined datasets (e.g. EcoMon, SMAST) and progressively targeted validation comparisons aimed at spatial distribution. The results showed an overall good (and partly excellent) agreement between model and survey results, which is particularly positive when considering the spatial dimensions of the study area and the different spatial effort between surveys and model runs. POM validation of vertical and temporal model results also illustrated a good match with cited literature values for all three species. Given this, it can be concluded that baseline spatial distribution, temporal development and vertical distribution of larvae were well represented in the executed baseline modeling results. As such, the results were considered very relevant starting points on which to carry out an analysis of larval transport impacts caused by the OSW scenarios and the related oceanic responses.

7.5.2 OSW Scenario Build-out Impacts

The general observable consequence of considered OSW developments for larval sea scallop transport, particularly for Scenarios 2, 4 and 5, is a shift in settlement to the southwest of the OSW buildup areas with discernable and notable increases in settled larval density in an area south of Block Island and south to the east of Long Island. Distinct areas of decrease in larval sea scallop settlement density are evident to the south of Martha's Vineyard in all build-out scenarios and, to some degree, in the Nantucket Shoals. The oceanic response attributed to these changes is an increase in current speeds north of the OSW build-out areas that shifts Georges Bank larval sea scallop transport from the area north of the OSW area. For several scenarios there is a shift from the Nantucket Shoals in a southwesterly direction, where they either simply settle in normal current speeds or encounter areas of reduced current speeds and settle in greater densities.

When reviewing the overall build-out modeling results for larval silver hake settlement, it is evident that reduced current speeds are the prominent OSW related oceanic response behind a general shift in settled larvae to the south of the Nantucket Shoals and into the general Georges Bank area. While increases in current speed are generally apparent to the west and north of all OSW build-out scenario areas, a broad pattern of reduced current speeds is apparent within the OSW build-out scenarios and/or to their southwest, south, and east. This suggests that observed larval silver hake density shifts in each OSW build-out scenario are caused by suspended larvae that encounter slightly lower current speeds and as a result settle in higher densities.

An analysis of the cumulative summer flounder OSW development scenario modeling results illustrates the combined influence of parameterized swimming speed and direction and altered currents; where it is again evident that a reduction in current speeds is a determinant OSW related oceanic response. The main discernable change in summer flounder density across all analyzed OSW build-out scenarios is a general decrease in larval settlement density in the Nantucket Sound. The postulated reason for this is that predominant larval transport from the south enters into, at varying degrees but generally evident, areas of lower current speeds (e.g. 50 percentile or 75 percentile depth averaged) to the southwest of each OSW build-out scenario area. In these waters, the larvae's horizontal swimming and directional attributes cannot overcome the reduction in current speed, thereby preventing some from entering the Nantucket Sound.

7.5.3 Relevance of Shifts in Larval Transport and Settlement

The modeled changes in larval transport and settlement described above can affect adult populations as well as the fisheries they support in several ways. Populations of marine organisms with complex life cycles (characterized by pelagic larvae and demersal adults) generally consist of spatially distinct subpopulations connected by planktonic larval dispersal (Kritzer and Sale 2006). Mature adults spawn, releasing planktonic propagules into the water column to be dispersed away from, or retained within natal areas (Sinclair 1988). Larvae carried by currents or tides will settle to the seafloor following the maturation process and when suitable habitat or environmental conditions are found. Changing pathways of dispersal in such a system can disrupt the processes of connectivity, settlement, and recruitment. Effects to oceanographic conditions such as those described in this report may potentially create "sinks" or subpopulations that no longer contribute propagules to the overall regional population network. Alternatively, the loss of viable and productive subpopulations ("sources") is also a possible consequence of these effects. Depending on the species and spatial scale of the population network, changes in larval distribution and settlement density can affect regional or local abundances. Dispersal pathways, settlement habitat, spawning, and recruitment vary greatly in time across the MAB and Georges Bank region (Steves et al. 1999; Carey and Stokesbury 2011; Perretti and Thorson 2019). Risks of disrupting life cycle processes include fragmentation of subpopulations, loss of connectivity, reduced settlement, and failed recruitment. The relative importance of these processes and potential risks of disrupting them ultimately depends on life history characteristics of species in question. The focal species examined in this report, specific to complexities of their life histories are discussed below.

Sea scallop adults, essentially sessile organisms, release abundant planktonic larvae that are transported over broad areas from Georges Bank to the MAB (Stokesbury et al. 2007). Mesoscale (1 to 100s km) hydrodynamics play an important role in completing the sea scallop's life cycle (Munroe et al. 2018; Tian et al. 2009; Davies et al. 2014). Larval settlement density can vary widely in the region and cause crowding within small areas (Bethoney and Stokesbury 2019). Sea scallops are managed through permanent and rotational areal closures to prevent harvest of undersized individuals and protect spawning adults (Stokesbury et al. 2007). Adult spawning in closed areas contributes pelagic eggs and larvae to adjacent open areas spanning considerable distances (Davies et al. 2014). These populations are not closed at small scales throughout the region and changes in modeled settlement near the OSW are not likely to affect larger Georges Bank or MAB stocks as managed by NEFMC. Modeled changes in larval distributions may, however, affect distribution and survival of settlers adjacent to the OSW areas. In addition, if changes alter spatial distribution of settlement areas currently fished by scallop draggers, undersized individuals may be susceptible to harvest.

Silver hake adults are distributed widely in the region and move from mid shelf to offshore waters to spawn. Pelagic larvae are transported inshore with settlement generally occurring over shelf waters and survival is best among scattered, emergent biota or in the troughs of sand waves. Based on wide distribution of settlement over the adjacent continental shelf (Steves et al. 1999), shifts in settlement density of this species are not likely to affect regionally managed fishery stocks or changes in subpopulations near the OSW.

The summer flounder life cycle involves offshore spawning, shoreward migration by larvae, which undergo metamorphosis in the process, and entry into coastal estuaries where they spend their first year. Evidence indicates that although there is a subpopulation structure, a high proportion of larval settling in the project area can be from as far away as Cape Hatteras, North Carolina (Hoey et al. 2020). Thus, regionally managed fishery stocks are not likely to be affected by changes caused by the OSW. Risks to summer flounder subpopulations due to the presence of the OSW will primarily be related to transport of settlers to local estuaries such as Narragansett Bay and Buzzards Bay.

8 Analysis Explanations and Follow-up Research

To provide further context to the results of this study, it was deemed appropriate to provide concluding explanation of the level (e.g. in terms of resolution and accuracy) and appropriate application of the various generated modeling results. In addition, recommendations for follow-up research are offered. These were specifically developed to provide supplementary insight into the herein uncovered OSW-induced potential oceanic response impact risks to fisheries resources and aid in related OSW approval decision-making processes and post-development monitoring.

8.1 Analysis Explanations

8.1.1 Hydrodynamic Model

The HDM, i.e. modeling of oceanic responses, developed for the study meets common standards of calibration and validation for regional impact assessment tools and thereby provides sufficiently robust descriptions of the current and wave variations throughout the area for use in the assessment changes in oceanic responses as a result of the OSW's. It should also be noted that hydrodynamic modeling of this nature is most suited to the review of the differences between one scenario and another, as per the present application, with the relative accuracy between scenarios generally being considered higher than the absolute accuracy for individual scenarios.

There are three aspects that should be kept in mind when judging a HDM current model: 1) absolute currents speed and direction, 2) residual current speed and direction and 3) difference between one scenario and another.

When the results from two observation stations (Orsted-F180 and MVCO) in close proximity to the planned OSW are recalled, the currents were seen to be tidally influenced, reversing in direction, but also influenced by local and regional oceanic currents. The mean current speeds through the year at 5 m depth were on the order of +/- 20 cm/s (see **Section 3.3.1** and **Appendix A.2.1**). With the typical absolute accuracy of a well calibrated and validated HDM being in the order of +/-10% it is clear that resolution of small absolute changes (below for example 1 cm/s) will be at the limit of accuracy of the model.

The second aspect of the hydrodynamics that arguably most affects the distribution of settled particles/agents is the net current flow or residual. This is the difference between the reversing current flows driven by the tide and is influenced by wind and local and regional currents such as the Gulf Stream, Gulf Stream eddies and the southward flowing cool current. While longer term residuals may be constant, short (weeks to months) and medium terms (months to years) flows are highly variable. The present study looks at only one instance (year) of residual currents and has focused on the simulation of a typical year, with no significant extremes.

Finally, the third aspect that this study relies upon is the ability to introduce the effect of the OSW structures on the absolute and residual currents. This requires parameterization of the effect of the structures and thus is a further source of uncertainty. For HDMs it is customary to benchmark the results of such parameterization on the current fields against actual observations. However, it is recognized that the OSW scenarios are not built, as yet, so this is not possible. Furthermore, changes of the magnitudes seen in the HDM are very difficult to measure directly in an variable open ocean environment. Consequently, in the absence of site-specific benchmarking data, while it is normally accepted that the relative accuracy between HDM scenarios (i.e. the difference plots between the build-out scenarios and the baseline model results (see **Sections 5.2.2** to **Section 5.2.5**)) is higher than the absolute accuracy, in the present case - where the change is dependent on a parameterization - it would be precautionary to not expect such a higher level of relative compared to absolute accuracy. Consequently, when reviewing these results, the accuracy of the build-out Scenarios 2 through 5 differences with baseline results should be considered to have the same sort of accuracy as the absolute accuracy, i.e. in the order of +/-2 cm/s.

8.1.2 Agent-Based Model

While the ABM results show good agreement with survey data, the validation and sensitivity analyses (as well as the standard particle tracking modeling results) reveal that ABM output are sensitive to the characteristics of larval releases. Thus, different timing, locations, and volumes (proportions) of released super-agents do affect resulting baseline and OSW build-out larval transport and settlement patterns. This is of particular note as the various survey datasets show differing degrees of variability in these characteristics for each modeled species.

It is also of note, that these datasets entail different survey techniques and levels of effort coverage. In this regard, it needs to be pointed out that the ABM analyses focus on a typical year (this study included one spawning season), where variations in larval releases had to be normalized to allow for a representative modeling. Given this, statistical processing of the results is not recommended, and – similar to the HDM - interpolation should be carried out with the expectation of a higher level of relative accuracy as compared to absolute accuracy.

It should nevertheless be emphasized that, as a whole, the modeling study sets itself apart through its technically comprehensive integrated modeling of the combined effects of wind field modification and in-situ structure friction, and target larval responses to oceanic predictors relevant to their key habitats and modeled life-cycle stages, as recommended by van Berkel et al. (2020). It also goes to great lengths to validate and test model results to ensure that natural variables at play are realistically reflected. Given this, the generated results can be considered to be a highly advanced and reliable interpretation of oceanic responses to OSW developments and the related impacts to target species larval transport and settlement.

8.2 Follow-up Research

In light of the above discussion, there are a number of important ways in which the oceanic modeling (HDM) and ABM, and related analyses, can be further developed to provide more insight. Related recommendations in this regard are classified in terms of their application in further cumulative analyses, Construction and Operations Plans (COPs) and Environmental Impact Statement (EIS) analyses, and post-development monitoring.

8.2.1 Cumulative Analyses

The main area for potential improvement for the HDM and ABM of larval transport and settlement is to simulate additional years. From a HDM perspective, this is recommended as it is not possible to assess the year-to-year variability in the residual currents with a single year of model simulations. For the larval ABM, modeling more than the requested single spawning season will allow experts to better understand the long-term structural shift in larval settlement patterns and the possible corresponding secondary impacts.

In addition, with the established integrated HDM and ABM's, relatively small modeling steps can be taken to expand on the cumulative analyses carried out in the present study, such as the following:

- Including more species of commercial fish or shellfish, especially those exhibiting less passive transport characteristics, to allow for a broader understanding of all potential patterns of larval settlement shifts.

- Execution of modeling analyses that include additional OSW development scenarios (e.g. lease areas off of New York, New Jersey, Delaware and Virginia), thereby allowing for additional coverage of cumulative oceanic responses and related larval settlement shifts.
- Inclusion of juvenile and adult stages of development in ABM, especially where patterns of larval settlement change is more prominent and deemed to entail a level of impact risk.
- Inclusion of the artificial reef effect (Mineur et al. 2012, Degraer et al. 2020, Glarou et al. 2020) in ABM analyses, with specific focus on the 'Spillover Effect' (van Berkel et al. 2020). This would allow experts to better understand the extent at which proposed OSW developments have the potential to be become new habitat for fisheries relevant species and gain more insight into the relevance of oceanic response induced larval settlement changes in light of these other known OSW influences.

8.2.2 Construction/Operation Plans and Environmental Impact Statements

An important factor arising from the present study is the recognition that larval settlement responds to the oceanic responses arising from the cumulative effect of OSW development. This places a challenge on the typical COP processes that tend to be focused on individual rather than cumulative effects of development. Emphasis will need to be placed on proper inclusion of cumulative effects in COPs/EISs and tools such as that developed for the present study will need to be updated to maintain a balance of the cumulative effects. Thereby ensuring that tipping points are not reached.

In relation to the above, additional research insight related to this study can also be gained through individual COP and impact assessment stages of the OSW development cycle. For example, as shown and discussed in this study, additional OSW developments can alter larvae "sinks" and "sources", with varying scales of possible risk to fisheries species sub-populations. Given this, each EIS, and associated EFH assessment, could delve specifically into the related sensitivity of the effected sub-populations in terms of local baseline characteristics (e.g. spawning, settlement and nursery habitat, etc.) and related relevance to localized fisheries activities. This can provide assurances that no unacceptable impact occurs.

8.2.3 Post-Development Monitoring

In brief, and generally following best practice for post-construction monitoring, the following operational monitoring is recommended to provide validation of this study's results and, ultimately, allow for improvement of on-going modeling and impact analyses:

- In relation to oceanic responses (HDM), collect current, temperature and salinity measurements in strategic locations within an OSW build-out area to allow for improved calibration of the effect of the structures.
- In relation to this study and/or potential project specific COP/EIS analyses of the shift in fisheries species larval settlement, existing or new post-development monitoring should align or realign efforts to cover suspended competent larval levels (abundance) and OSW-impacted settlement densities to observed change hotspots. Dedicated surveys should follow a before-after-control-impact or before-after-gradient-design (e.g. Methratta 2020).

9 References

9.1 References: Hydrodynamics

Andersen OB, Knudsen P. 2009. DNSC08 mean sea surface and mean dynamic topography models, J. Geophys. Res., 114, C11001, doi:10.1029/2008JC005179.

Chen C, Beardsley RC, Qi J, Lin H. 2016. Use of Finite-Volume Modeling and the Northeast Coastal Ocean Forecast System in Offshore Wind Energy Resource Planning. Final Report to the U.S. Department of the Interior, Bureau of Ocean Energy Management, Office of Renewable Energy Programs. BOEM 2016-050. 131pp

[DHI] DHI Water & Environment. 2017. (unpublished industry report) MetOcean Hindcast Study - Vineyard Offshore Wind Farm MA, USA, DHI, Copenhagen.

[FEHY] FEhmarnbelt HYdrography. 2010a. (unpublished industry report) "Initial study of mixing and parameterisation refined flow (CFD). Analyses of the mixing of density stratified currents". Report 11802650-14-E1TR0035.

FEHY. 2010b. (unpublished industry report) "Initial study of sixing and parameterisation - physical model experiments", Vol. I – III. Report 11802650-14-E1TR0015.

FEHY (Petersen OS, Burchard H. 2011). (unpublished industry report) Parameterisation of bridge piers and ferry mixing. Report 11802650-14-E1TR0041

Fernando HJ. 1991. Turbulent Mixing in Stratified Fluids. Annu. Rev. Fluid Mech. 23:455–493.

Floeter J, van Beusekom JEE, Auch D, Callies U, Carpenter J, Dudeck T, Eberle S, Eckhardt A, Gloe D, Hänselmann K, et al. 2017. Pelagic effects of offshore wind farm foundations in the stratified North Sea. Prog. Oceanogr. 156:154–173.

Frandsen S. 1992. On the wind speed reduction in the center of large clusters of wind turbines. J. Wind. Eng. Ind. Aerodyn. 39:251–265.

Fredsoe J. 1984. Turbulent boundary layers in combined wave current motion. J. Hydraul. Eng. ASCE, Vol. 110, No. HY8, pp. 1103-1120

Grubert JP. 1989. Interfacial Mixing in Stratified Channel Flows. J. Hydraul. Eng. 115:887–905.

Helber RW, Townsend TL, Barron CN, Dastugue JM, Carnes MR. 2013. Validation Test Report for the Improved Synthetic Ocean Profile (ISOP) System, Part I: Synthetic Profile Methods and Algorithm. NRL Memo. Report, NRL/MR/7320—13-9364.

Holmboe J. 1962. On the behavior of symmetric waves in stratified shear layers. Deep-Sea Res. Oceanogr. Abstr. 9:395–396.

Ivey GN, Imberger J. 1991. On the Nature of Turbulence in a Stratified Fluid. Part I: The Energetics of Mixing. J. Phys. Oceanogr. 21:650–658.

Iqbal M. 1983. An Introduction to Solar Radiation, Academic Press, Toronto

Jakobsen F, Hansen IS, Ottesen Hansen N-E, Østrup-Rasmussen F. 2010. Flow resistance in the Great Belt, the biggest strait between the North Sea and the Baltic Sea. Estuar. Coast. Shelf Sci. 87:325–332.

Jensen B, Carstensen S, Christensen ED. 2018. Mixing of Stratified Flow around Bridge Piers in Steady Current. J. Hydraul. Eng. 144(8):04018041. doi:10.1061/(asce)hy.1943-7900.0001481

Jones O, Zyserman JA, Wu Y. 2014. Influence of apparent roughness on pipeline design conditions under combined waves and current. Proceedings of the ASME 2014 33rd International Conference on Ocean, Offshore and Arctic Engineering.

Lentz SJ. 2017. Seasonal warming of the Middle Atlantic Bight Cold Pool. J. Geophys. Res. Oceans. 122:941–954.

Lind G, Falkenmark M. 1972, Hydrology en inledring till vattenressurslaran, Studenlitteratur (in Swedish)

O'Reilly J, Zetlin C. 1998. Seasonal horizontal and vertical distribution of phytoplankton chlorophyll northeast us continental shelf ecosystem. NOAA Technical report NMFS 139. Fish. Bull.

Ørsted .2020. Metadata for current measurements at the US East Coast. Report Rev. no.: 06354878_A, 13 July 2020

Peltier WR, Caulfield CP. 2003. Mixing efficiency in stratified shear flow. Annu. Rev. Fluid Mech. 35:135–167.

Peña A, Rathmann O. 2013. Atmospheric stability-dependent infinite wind-farm models and the wake-decay coefficient. Wind. Energy. 17:1269–1285.

Roarty H, Glenn S, Brodie J, Nazzaro L, Smith M, Handel E, Kohut J, Updyke T, Atkinson L, Boicourt W, et al. 2020. Annual and Seasonal Surface Circulation Over the Mid-Atlantic Bight Continental Shelf Derived From a Decade of High Frequency Radar Observations. J. Geophys. Res. Oceans. 125(11). doi:10.1029/2020jc016368

Rouse H, Dodu J. 1955. Turbulent diffusion across a density discontinuity. La Houille Blanche:522–532.

Sahlberg J. 1984. A hydrodynamic model for heat contents calculations on lakes at the ice formation date. Document D4: 1984, Swedish council for Building Research

Smyth WD, Winters KB. 2003. Turbulence and Mixing in Holmboe Waves. J. Phys. Oceanogr. 33:694–711.

Strang EJ, Fernando HJ. 2001. Entrainment and mixing in stratified shear flows. J. Fluid Mech. 428:349–386.

Stevenson D, Chiarella L, Stephan D, Reid R, Wilhelm K, McCarthy J, Pentony M. 2004. Characterization of the fishing practices and marine benthic ecosystems of the northeast US shelf, and an evaluation of the potential effects of fishing on essential habitat. NOAA Tech Memo NMFS NE 181; 179 p.

Turner JS. 1973 Buoyancy effects in fluids Cambridge [Eng.]: University Press. pp. 367

Rodi W. 1980. Turbulence Models and Their Application in Hydraulics – A State of the Art Review, Special IAHR Publication.

Soulsby RL, Clark S. 2005. Bed shear-stress under combined waves and currents on smooth and rough beds. Report TR 137. Hydraulics Research Wallingford.

9.2 References: Agent-Based Models

Allain G, Petigas P, Lazure P, Grellier P. 2007. Biophysical modelling of larval drift, growth and survival for the prediction of anchovy (Engraulis encrasicolus) recruitment in the Bay of Biscay (NE Atlantic). Fish. Oceanogr. 16:489–505.

Benson T, de Bie J, Gaskell J, Vezza P, Kerr JR, Lumbroso D, Owen MR, Kemp PS. 2021. Agent-based modelling of juvenile eel migration via selective tidal stream transport. Ecol. Model. 443:109448.

Bethoney ND, Stokesbury KD. 2018. Methods for Image-based Surveys of Benthic Macroinvertebrates and Their Habitat Exemplified by the Drop Camera Survey for the Atlantic Sea Scallop. J. Vis. Exp. 137. doi:10.3791/57493

Davies KTA, Gentleman WC, DiBacco C, Johnson CL. 2014. Semi-annual spawning in marine scallops strengthens larval recruitment and connectivity on Georges Bank: a model study. Mar. Ecol. Prog. Ser. 516:209-227.

De Roos AM, Persson L. 2005. Unstructured Population Models: Do Population-Level Assumptions Yield General Theory? Ecological Paradigms Lost:31–62.

Degraer S, Carey D, Coolen J, Hutchison Z, Kerckhof F, Rumes B, Vanaverbeke J. 2020. Offshore Wind Farm Artificial Reefs Affect Ecosystem Structure and Functioning: A Synthesis. Oceanogr. 33(4):48–57. doi:10.5670/oceanog.2020.405

Faillettaz R, Paris CB, Irisson J-O. 2018. Larval Fish Swimming Behavior Alters Dispersal Patterns From Marine Protected Areas in the North-Western Mediterranean Sea. Front. Mar. Sci. 5.

[GEBCO] GEBCO Bathymetric Compilation Group 2020. 2020. The GEBCO_2020 Grid - a continuous terrain model of the global oceans and land. British Oceanographic Data Centre, National Oceanography Centre, NERC, UK. [accessed 2020 May 10]. doi:10.5285/a29c5465-b138-234d-e053-6c86abc040b9.

Glarou M, Zrust M, Svendsen JC. 2020. Using Artificial-Reef Knowledge to Enhance the Ecological Function of Offshore Wind Turbine Foundations: Implications for Fish Abundance and Diversity. J. Mar. Sci. Eng. 8(5):332. doi:10.3390/jmse8050332

Grimm V, Frank K, Jeltsch F, Brandl R, Uchmański J, Wissel C. 1996. Pattern-oriented modelling in population ecology. Sci. Total Environ.183(1-2):151–166. doi:10.1016/0048-9697(95)04966-5

Grimm V, Railsback SF. 2005. Individual-based Modeling and Ecology, Princeton University Press.

Grimm V. 2005. Pattern-Oriented Modeling of Agent-Based Complex Systems: Lessons from Ecology. Science. 310(5750):987–991. doi:10.1126/science.1116681

Grimm V, Railsback SF, Vincenot CE, Berger U, Gallagher C, DeAngelis DL, Edmonds B, Ge J, Giske J, Groeneveld J, et al. 2020. The ODD Protocol for Describing Agent-Based and Other Simulation Models: A Second Update to Improve Clarity, Replication, and Structural Realism. J. Artif. Soc. Soc. Simul. 23.

Hare J. 2015. Abundance and proportion of ichthyoplankton of the Northeast U.S. Shelf from surveys conducted during the MARMAP (1977-1987) and EcoMon (1999-2008) programs. Biological and Chemical Oceanography Data Management Office (BCO-DMO). (Version 1) Version Date 2015-06-16. doi:10.1575/1912/bco-dmo.560448.1

Heinänen S, Chudzinska ME, Brandi Mortensen J, Teo TZ, Rong Utne K, Doksæter Sivle L, Thomsen F. 2018. Integrated modelling of Atlantic mackerel distribution patterns and movements: A template for dynamic impact assessments. Ecol. Model. 387:118–133.

Houde ED. 2002. Chapter 3. Mortality. In: Fuiman, L. A. and R. G. Werner (eds.), Fishery science: The unique contribution of early life stages. Blackwell Scientific Publishing, Oxford.

Jenkins GP, Welsford DC, Keough MJ, Hamer PA. 1998. Diurnal and tidal vertical migration of pre-settlement King George whiting Sillaginodes punctata in relation to feeding and vertical distribution of prey in a temperate bay. Mar. Ecol. Prog. Ser. 170:239–248.

Kritzer JP, Sale PF. 2006. Marine Metapopulations. Academic Press. Amsterdam. 544 pp.

Methratta ET. 2020. Monitoring fisheries resources at offshore wind farms: BACI vs. BAG designs. ICES J. Mar. Sci. 77(3):890–900. doi:10.1093/icesjms/fsaa026

Mineur F, Cook E, Minchin D, Bohn K, Macleod A, Maggs C. 2012. Changing coasts: marine aliens and artificial structures. Oceanogr. Mar. Biol. 50:189-234, https://doi.org/10.1201/b12157-5.

Mortensen LO, Chudzinska ME, Slabbekoorn H, Thomsen F. 2021. Agent-based models to investigate sound impact on marine animals: Bridging the gap between effects on individual behaviour and population level consequences. Oikos (in press). DOI: 10.1111/oik.08078.

Parry HR, Bithell M. 2012. Large Scale Agent-Based Modelling: A Review and Guidelines for Model Scaling. In: Heppenstall A, Crooks A, See L, Batty M. (eds) Agent-Based Models of Geographical Systems. Springer, Dordrecht. https://doi.org/10.1007/978-90-481-8927-4_14

Parry HR, Evans AJ. 2008. A comparative analysis of parallel processing and super-individual methods for improving the computational performance of a large individual-based model. Ecol. Model. 214:141-152.

[NEFSC] Northeast Fisheries Science Center. 2021: Sea Scallop Survey. NOAA National Centers for Environmental Information. [updated 2020 May 14; accessed 2020 Jun 18]. https://www.fisheries.noaa.gov/inport/item/22564.

[NOAA] National Oceanic and Atmospheric Administration. 2018. Essential Fish Habitat – Data Inventory. [accessed 2020 Sep 07]. https://www.habitat.noaa.gov/application/efhinventory/index.html.

NOAA. 2007. Magnuson-Stevens Fishery Conservation and Management Act. Second Printing - As Amended Through January 12, 2007.

NOAA. 2004. NCEI Multibeam Bathymetry Database (MBBDB). [accessed 2020 May 10]. https://doi.org/doi:10.7289/V56T0JNC.

[NROC] Northeast Regional Ocean Council. 2009. Northeast Ocean Data Portal. [accessed 2020 Mar 02]. www.northeastoceandata.org.

Scheffer M, Baveco JM, DeAngelis DL, Rose KA, van Nes EH. 1995. Super-individuals a simple solution for modelling large populations on an individual basis. Ecol. Model. 80:161–170.

Sinclair M. 1988. Marine populations: an essay on population regulation and speciation. University of Washington Press, Seattle.

[SMAST] School of Marine Science and Technology, University of Massachusetts Dartmouth. 2016. Average (2003-2012) Presence/Abundance from SMAST Survey Northeast United States. [accessed 2020 Sep 07].

Steves BP, Cowen RK, Malchoff MA. 1999. Settlement and nursery habitats for demersal fishes on the continental shelf of the New York Bight. Fish. Bull. 98: 167-188.

Tian T, Fiksen Ø, Folkvord A. 2007. Estimating larval fish growth under size-dependent mortality: a numerical analysis of bias. Can. J. Fish. Aquat. 64:554–562.

Thomsen F, Mortensen LO, van Berkel JJ. 2019. Agent-Based Modeling: Dynamic Mapping of the Movements of Marine Life. Environment Coastal and Offshore (ECO), Special Issue Ocean Sound, 31-33.

[USGS] United States Geological Survey. 2000. CONMAP Sediment Maps. https://pubs.usgs.gov/of/2000/of00-358/mapping/conmap/conmapsg.htm

USGS. 2005. CONMAPSG: Continental Margin Mapping (CONMAP) sediments grain size distribution for the United States East Coast Continental Margin. Open File Report 2005-1001, US Geological Survey, Coastal and Marine Geology Program, Woods Hole Science Center, Woods Hole, MA. [accessed 2020 Jun 15].

van Berkel JJ, Burchard H, Christensen A, Mortensen LO, Svenstrup Petersen O, Thomsen F. 2020. The effects of offshore wind farms on hydrodynamics and implications for fishes. Oceanogr. 33(4):108–117, https://doi.org/10.5670/oceanog.2020.410.

9.3 References: Atlantic Sea Scallops

Bethoney ND, Asci S, Stokesbury KDE. 2016. Implications of extremely high recruitment events into the US sea scallop fishery. Mar. Ecol. Prog. Ser. 547: 137-147.

Carey JD, Stokesbury KDE. 2011. An assessment of juvenile and adult sea scallop, *Placopecten magellanicus*, distribution in the northwest Atlantic using high-resolution still imagery. J. Shellfish Res. 30 (3): 569–582.

Culliney JL. 1974. Larval development of the giant scallop Placopecten magellanicus (Gmelin). Biol. Bull. 147:321–332.

Hart DR, Chute AS. 2004. Essential fish habitat source document: sea scallop, Placopecten magellanicus, life history and habitat characteristics. NOAA Tech Memo NMFS NE-189, Woods Hole, MA. 21p.

Langton RW, Robinson WE, Schick D. 1987. Fecundity and reproductive effort of sea scallops Placopecten magellanicus from the Gulf of Maine. Mar. Ecol. Prog. Ser. 37: 19-25.

McGarvey R, Serchuk FM, McLaren IA. 1992. Statistics of Reproduction and Early Life History Survival of the Georges Bank Sea Scallop (Placopecten magellanicus) Population. J. Northwest Atl. Fish. Sci. 13:83–99.

Munroe DM, Haidvogel D, Caracappa JC, Klinck JM, Powell EN, Hofmann EE, Shank BV, Hart DR. 2018. Modeling larval dispersal and connectivity for Atlantic sea scallop (Placopecten magellanicus) in the Middle Atlantic Bight. Fish. Res. 208:7–15.

[NEFMC] New England Fishery Management Council. 2014. Framework 25 to the Scallop Including a Final Environmental Assessment (EA), an Initial Regulatory Flexibility Analysis and Stock Assessment and Fishery Evaluation (SAFE Report), Newburyport, MA.

Pearce CM, Manuel JL, Gallager SM, Manning DA, O'Dor RK, Bourget E. 2004. Depth and timing of settlement of veligers from different populations of giant scallop, Placopecten magellanicus (Gmelin), in thermally stratified mesocosms. J. Exp. Mar. Biol. Ecol. 312:187–214.

Stewart PL, Arnold SH. 1994. Environmental requirements of the sea scallop (Placopecten magellanicus) in eastern Canada and its response to human impacts. Can. Tech. Rep. Fish. Aquat. Sci. 2005: 1-36

Stokesbury KDE. 2012. Stock Definition and Recruitment: Implications for the U.S. Sea Scallop (Placopecten magellanicus) Fishery from 2003 to 2011. Rev. Fish. Sci. Aquac., 20:3, 154-164.

Stokesbury KDE, Harris BP, Marino MC, Nogueira JI. 2007. Sea scallop mass mortality in a Marine Protected Area. Mar. Ecol. Prog. Ser. 349:151–158.

Stokesbury KDE, O'Keefe, CE, Harris, BP. 2016. Fisheries Sea Scallop, Placopecten magellanicus. Pp.719-736, in: Shumway, S.E. and Parsons, G.J. (eds), Scallops: Biology, Ecology, Aquaculture, and Fisheries. Elsevier.

Thouzeau G, Robert G, Smith SJ. 1991. Spatial variability in distribution and growth of juvenile and adult sea scallops Placopecten magellanicus (Gmelin) on eastern Georges Bank (Northwest Atlantic). Mar. Ecol. Prog. Ser. 74:205–218.

Tian RC, Chen C, Stokesbury KDE, Rothschild B, Cowles GW, Xu Q, Hu S, Harris BP, Marino MC II. 2009. Modeling the connectivity between sea scallop populations in the Middle Atlantic Bight and over Georges Bank. Mar. Ecol. Prog. Ser. 380:147–160.

Torre MP, Tanaka KR, Chen Y. 2018. A spatiotemporal Evaluation of Atlantic Sea Scallop Placopecten magellanicus Habitat in the Gulf of Maine Using a Bioclimate Envelope Model. Mar. Coast. Fish. 10:224–235.

Tremblay JM, Loder J, Werner F, Naimie C, Page F, Sinclair M. 1994. Drift of sea scallop larvae Placopecten magellanicus on Georges Bank: a model study of the roles of mean advection, larval behavior and larval origin. Deep Sea Res. Part II Top. Stud. Oceanogr. 41:7–49.

Tremblay AM, Sinclair MM. 1988. The Vertical and Horizontal Distribution of Sea Scallop (Placopecten magellanicus) Larvae in the Bay of Fundy in 1984 and 1985. J. Northwest Atl. Fish. Sci. 8:43–53.

9.4 References: Silver Hake

Alvarez-Colombo GL. 2011. Distribution and behavior of Argentine hake larvae: Evidence of a biophysical mechanism for self-recruitment in northern Patagonian shelf waters. Ciencias Marinas 37:633–657.

Alvarez P, Cotano U. 2005. Growth, mortality and hatch-date distributions of European hake larvae, Merluccius (L.), in the Bay of Biscay. Fish. Res. 76:379–391.

Auster PJ, Malatesta RJ, Donaldson CL. 1997. Distributional responses to small-scale habitat variability by early juvenile silver hake, Merluccius bilinearis. Environ. Biol. Fishes 50:195–200.

Berrien P, Sibunka J. 1999. Distribution patterns of fish eggs in the United States northeast continental shelf ecosystem, 1977-1987. NOAA Tech. Rep. NMFS 145: 310.

Brodziak JKT, Holmes EM, Sosebee KA, Mayo RK. 2001. Assessment of the Silver Hake Resource in the Northwest Atlantic in 2000. Northeast Fish. Sci. Cent. Ref. Doc. 01-03.

Brown DR, Leonarduzzi E, Machinandiarena L. 2004. Age, growth and mortality of Hake larvae (Merluccius hubbsi) in the north Patagonian shelf. Sci. Mar. 68:273–283.

Ehrlich M, Macchi G, Madriolas A, Machinandiarena L. 2013. Vertical distribution of hake Merluccius hubbsi in spawning aggregations in North Patagonian waters of the Southwest Atlantic. Fish. Res. 138: 89-98.

Fahay MP. 1974. Occurrence of silver hake, Merluccius bilinearis, eggs and larvae along the Middle Atlantic continental shelf during the 1966 period. U.S. Fish. Bull. 72: 813-834.

Helser TE, Almeida FP, Waldron DE. 1995. Biology and fisheries of North-west Atlantic hake (silver hake: M. bilinearis). Hake:203–237.

Lock MC, Packer DB. 2004. Essential Fish Habitat Source Document: Silver Hake, Merluccius bilinearis, Life History and Habitat Characteristics Second Edition, NOAA Technical Memorandum NMFS-NE-186, Northeast Fisheries Science Center, Woods Hole, Massachusetts. pp 78.

Marl A, Ramos I. 1979. Fecundity of silver hake on the Scottian Shelf. ICNAF. Res. Doc. 79/VI/66.

[NEFMC] New England Fishery Management Council. 2018. Small-mesh multispecies fishing year 2018-2020 specifications, environmental assessment, regulatory impact review, and initial regulatory flexibility analysis. 211 pp.

Nye JA, Joyce TM, Kwon Y-O, Link JS. 2011. Silver hake tracks changes in Northwest Atlantic circulation. Nat. Commun. 2.

Reiss C, Anis A, Taggart CT, Dower JF, Ruddick B. 2002. Relationships among vertically structured in situ measures of turbulence, larval fish abundance and feeding success and copepods on Western Bank, Scotian Shelf. Fish. Oceanogr. 11(3), 156–174. https://doi.org/10.1046/j.1365-2419.2002.00194.x

Sauskan VI, Serebryakov VP. 1968. Reproduction and development of the silver hake, Merluccius bilinearis (Mitchell). Vopr, Ikhtiol. 8(3): 398-414.

Sherstyukov AI. 1991. On reproduction and formation of silver hake (Merluccius bilinearis Mitchill) Year-class strengths at early ontogenesis on the Scotian Shelf, Northwest Atlantic Fisheries Organization, Serial no. N1893, NFO SCR Doc 91/19.

Steves BP, Cowen RK. 2000. Settlement, growth, and movement of silver hake Merluccius bilinearis in nursery habitat on the New York Bight continental shelf. Mar. Ecol. Prog. Ser. 196:279–290.

Steves BP, Cowen RK, Malchoff MH. 2000. Settlement and nursery habitats for demersal fishes on the continental shelf of the New York Bight. Fish. Bull. 98(1), 167–188.

9.5 References: Summer Flounder

Able KW, Kaiser SC. 1994. Synthesis of summer flounder habitat parameters. 68 p. NOAA Coastal Ocean Program Decision Analysis Series No. 1.

Able KW, Sullivan MC, Hare JA, Bath-Martin G, Taylor JC, Hagan R. 2010. Larval abundance of summer flounder (Paralichthys dentatus) as a measure of recruitment and stock status. Fish. Bull. 109: 68-78.

Barbut L, Groot CC, Delerue-Ricard S, Vandamme S, Volckaert FA, Lacroix G. 2019. How larval traits of six flatfish species impact connectivity. Limnol. Oceanogr. 64:1150–1171.

Benson T, de Bie J, Gaskell J, Vezza P, Kerr JR, Lumbroso D, Owen MR, Kemp PS. 2021. Agent-based modelling of juvenile eel migration via selective tidal stream transport. Ecol. Model. 443:109448.

Bisbal GA, Bengtson DA. 1995. Effects of delayed feeding on survival and growth of summer flounder Paralichthys dentatus larvae. Mar. Ecol. Prog. Ser. 121:301–306.

Burke JS, Miller JS, Hoss DE. 1991. Immigration and settlement pattern of Paralichthys dentatus and P. lethostigma in an estuarine nursery ground, North Carolina, USA. Neth. J. Sea Res. 27: 393–405.

Faillettaz R, Paris CB, Irisson J-O. 2018. Larval Fish Swimming Behavior Alters Dispersal Patterns From Marine Protected Areas in the North-Western Mediterranean Sea. Front. Mar. Sci. 5.

Forward RB, Reinsel KA, Peters DS, Tankersley RA, Churchill JH, Crowder LB, Hettler WF, Warlen SM, Green MD. 1999. Transport of fish larvae through a tidal inlet. Fish. Oceanogr. 8:153–172.

Gilbert CR. 1986. Species profiles: life histories and environmental requirements of coastal fishes and invertebrates (south Florida): southern, gulf, and summer flounders. U.S. Fish Wildl. Serv. Biol. Rep. 82 (11.54): 24.

Hare, JA, Walsh, HJ, Wuenschel, MJ. 2006. Sinking rates of late-stage fish larvae: Implications for larval ingress into estuarine nursery habitats. J. Exp. Mar. Biol. Ecol. 330(2), 493-504.

Henderson MJ, Fabrizio MC. 2014. Small-Scale Vertical Movements of Summer Flounder Relative to Diurnal, Tidal, and Temperature Changes. Mar. Coast. Fish. 6(1):108–118. doi:10.1080/19425120.2014.893468

Hoey JA, Pinksy ML. 2018 Genomic signatures of environmental selection despite near-panmixia in summer flounder. Evol. Appl. 11:1732–1747.

Hoey JA, Fodrie FJ, Walker QA, Hilton EJ, Kellison GT, Targett TE, Taylor JC, Able KW, Pinsky ML. 2020. Using multiple natural tags provides evidence for extensive larval dispersal across space and through time in summer flounder. Mol. Ecol. 29:1421–1435.

Houde ED. 1989. Comparative Growth, Mortality, and Energetics of Marine Fish Larvae: Temperature and Implied Latitudinal Effects. Fish. Bull. U.S. 87:471-495.

Howson UA, Targett TE. 2019. Comparison of thermohaline optima for juveniles of two sympatric paralichthyid flounders: ecophysiological evaluation of estuarine nursery quality. Estuaries Coast. 43: 135–150.

Johns DM, Howell WH. 1980. Yolk Utilization in Summer Flounder (Paralichthys dentatus) Embryos and Larvae Reared at Two Temperatures. Mar. Ecol. Prog. Ser. 2:1-8.

Keefe M, Able KW. 1993. Patterns of metamorphosis in summer flounder, Paralichthys dentatus. J. Fish Biol. 42:713–728.

Kraus RT, Musick JA. 2001. A brief interpretation of summer flounder, Paralichthys dentatus, movements and stock structure with new tagging data on juveniles. Mar. Fish. Rev. 63(3): 1-6.

Martinez GM, Bolker JA. 2003. Embryonic and Larval Staging of Summer Flounder (Paralichthys dentatus). J. Morphol. 255:162-176.

Miller JM, Burke JS, Fitzhugh GR. 1991. Early life history patterns of Atlantic North American flatfish: Likely (and unlikely) factors controlling recruitment. Neth. J. Sea Res. 27:261–275.

Morse WW. 1981. Reproduction of the summer flounder, Paralichthys dentatus (L.). J. Fish Biol. 19:189–203.

Packer DB, Griesbach SJ, Berrien PL, Zetlin CA, Johnson DL, Morse WW. 1999. Essential fish habitat source document: Summer flounder, Paralichthys dentatus, life history and habitat characteristics. NOAA Tech Memo NMFS NE 151: 88.

Perretti CT, Thorson JT. 2019. Spatio-temporal dynamics of summer flounder (Paralichthys dentatus) on the Northeast US shelf. Fish. Res. 215: 62-68.

Smith WG. 1973. The distribution of summer flounder, Paralichthys dentatus, eggs and larvae on the continental shelf between Cape Cod and Cape Lookout, 1965-66 Fish. Bull.71 (2):527- 548.

Taylor DL, McNamee J, Lake J, Gervasi CL, Palance DG. 2016. Juvenile winter flounder (Pseudopleuronectes americanus) and summer flounder (Paralichthys dentatus) utilization of Southern New England nurseries: comparisons among estuarine, tidal river, and coastal lagoon shallow-water habitats. Estuaries Coast 39 (5): 1505–1525.

Terciero M. 2018. The summer flounder chronicles III: struggling with success, 2011–2016. Rev. Fish Biol. Fish. 28:381–404.

van Maaren CC, Daniels HV. 2000. Temperature Tolerance and Oxygen Consumption Rates for Juvenile Southern Flounder Acclimated to Five Different Temperatures. In Spawning and Maturation of Aquaculture Species. Tamaru, C.C., Tamaru, C.S., McVey, J.P., and Ikuta, K. (eds) Proceedings of the United States-Japan Natural Resources meeting. UJNR Technical Report No. 28: 135-140.

A Supplementary Hydrodynamic Modeling Results

A.1 Model Quality Indices

To obtain an objective and quantitative measure of how well the model data compared to the observed data, several statistical parameters so-called quality indices (QI's) are calculated.

Prior to the comparisons, the model data are synchronized to the time stamps of the observations so that both time series had equal length and overlapping time stamps. For each valid observation, measured at time t, the corresponding model value is found using linear interpolation between the model time steps before and after t. Only observed values that had model values within ± the representative sampling or averaging period of the observations are included (e.g. for 10-min observed wind speeds measured every 10 min compared to modeled values every hour, only the observed value every hour is included in the comparison).

The comparisons of the synchronized observed and modeled data are illustrated in (some of) the following figures:

- Time series plot including general statistics
- Scatter plot including quantiles, QQ-fit and QI's (dots colored according to the density)
- Histogram of occurrence vs. magnitude or direction
- Histogram of bias vs. magnitude
- Histogram of bias vs. direction
- Dual rose plot (overlapping roses)
- Peak event plot including joint (coinciding) individual peaks

The quality indices are described below. Their definitions are listed in **Table 24**. Most of the quality indices are based on the entire data set, and hence the quality indices should be considered averaged measures and may not be representative of the accuracy during rare conditions.

The MEAN represents the mean of modeled data, while the BIAS is the mean difference between the modeled and observed data. AME is the mean of the absolute difference, and RMSE is the root mean square of the difference. The MEAN, BIAS, AME and RMSE are given as absolute values and relative to the average of the observed data in percent in the scatter plot.

The scatter index (SI) is a non-dimensional measure of the difference calculated as the unbiased root-mean-square difference relative to the mean absolute value of the observations. In open water, an SI below 0.2 is usually considered a small difference (excellent agreement) for significant wave heights. In confined areas or during calm conditions, where mean significant wave heights are generally lower, a slightly higher SI may be acceptable (the definition of SI implies that it is negatively biased (lower) for time series with high mean values compared to time series with lower mean values (and same scatter/spreading), although it is normalized).

EV is the explained variation and measures the proportion [0 - 1] to which the model accounts for the variation (dispersion) of the observations.

The correlation coefficient (CC) is a non-dimensional measure reflecting the degree to which the variation of the first variable is reflected linearly in the variation of the second variable. A value close to 0 indicates very limited or no (linear) correlation between the two data sets, while a value close to 1 indicates a very high or perfect correlation. Typically, a CC above 0.9 is considered a high correlation (good agreement) for wave heights. It is noted that CC is 1 (or -1) for any two fully linearly correlated variables, even if they are not 1:1. However, the slope and intercept of the linear relation may be different from 1 and 0, respectively, despite CC of 1 (or -1).

The Q-Q line slope and intercept are found from a linear fit to the data quantiles in a least- square sense. The lower and uppermost quantiles are not included on the fit. A regression line slope different from 1 may indicate a trend in the difference.

The peak ratio (PR) is the average of the N_{peak} highest model values divided by the average of the N_{peak} highest observations. The peaks are found individually for each data set through the Peak-Over-Threshold (POT) method applying an average annual number of exceedances of 4 and an inter-event time of 36 hours. A general underestimation of the modeled peak events results in PR below 1, while an overestimation results in a PR above 1.

An example of a peak plot is shown in **Figure 127**. 'X' represents the observed peaks (x-axis), while 'Y' represents the modeled peaks (y-axis), based on the POT methodology, both represented by circles ('o') in the plot. The joint (coinciding) peaks, defined as any X and Y peaks within ±36 hours1 of each other (i.e. less than or equal to the number of individual peaks), are represented by crosses ('x'). Hence, the joint peaks ('x') overlap with the individual peaks ('o') only if they occur at the same time exactly. Otherwise, the joint peaks ('x') represent an additional point in the plot, which may be associated with the observed and modeled individual peaks ('o') by searching in the respective X and Y-axis directions, see example with red lines in **Figure 127**. It is seen that the 'X' peaks are often underneath the 1:1 line, while the 'Y' peaks are often above the 1:1 line.

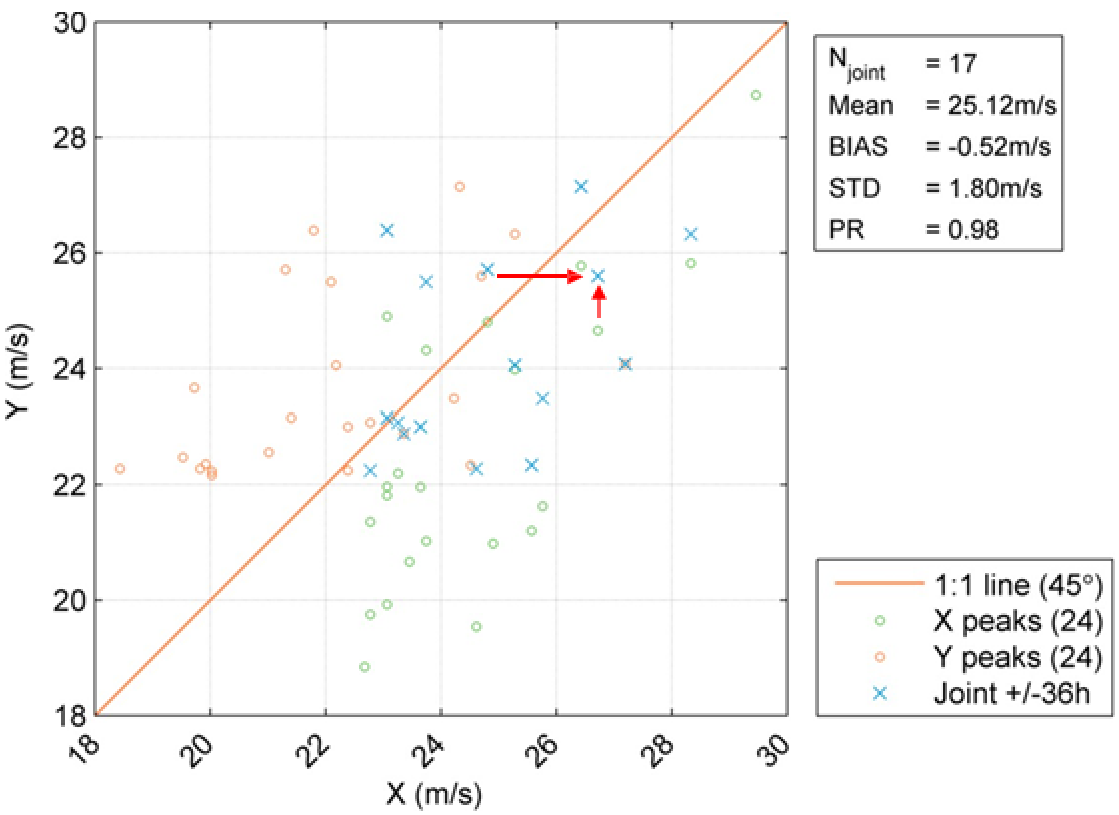

Figure 127. Example of peak event plot (wind speed)

Table 24. Definition of model quality indices (X = Observation, Y = Model)

Abbreviation	Description	Definition
N	Number of data (synchronized)	–
MEAN	Mean of Y data,Mean of X data	$\frac{1}{N}\sum_{i=1}^{N} Y_i \equiv \bar{Y}$, $\frac{1}{N}\sum_{i=1}^{N} X_i \equiv \bar{X}$
STD	Standard deviation of Y dataStandard deviation of X data	$\sqrt{\frac{1}{N-1}\sum_{i=1}^{N}(Y-\bar{Y})_i^2}$, $\sqrt{\frac{1}{N-1}\sum_{i=1}^{N}(X-\bar{X})_i^2}$
BIAS	Mean difference	$\frac{1}{N}\sum_{i=1}^{N}(Y-X)_i = \bar{Y}-\bar{X}$
AME	Absolute mean difference	$\frac{1}{N}\sum_{i=1}^{N}(\lvert Y-X\rvert)_i$
RMSE	Root mean square difference	$\sqrt{\frac{1}{N}\sum_{i=1}^{N}(Y-X)_i^2}$
SI	Scatter index (unbiased)	$\frac{\sqrt{\frac{1}{N}\sum_{i=1}^{N}(Y-X-\mathrm{BIAS})_i^2}}{\frac{1}{N}\sum_{i=1}^{N}\lvert X_i\rvert}$
EV	Explained variance	$\frac{\sum_{i=1}^{N}(X_i-\bar{X})^2-\sum_{i=1}^{N}[(X_i-\bar{X})-(Y_i-\bar{Y})]^2}{\sum_{i=1}^{N}(X_i-\bar{X})^2}$
CC	Correlation coefficient	$\frac{\sum_{i=1}^{N}(X_i-\bar{X})(Y_i-\bar{Y})}{\sqrt{\sum_{i=1}^{N}(X-\bar{X})_i^2\sum_{i=1}^{N}(Y-\bar{Y})_i^2}}$
QQ	Quantile-Quantile (line slope and intercept)	Linear least square fit to quantiles
PR	Peak ratio (of N_{peak} highest events)	$PR = \frac{\sum_{i=1}^{N_{peak}} Y_i}{\sum_{i=1}^{N_{peak}} X_i}$

A.2 Additional Hydrodynamic Model Baseline Validation Plots

A.2.1 Hydrodynamic Model Baseline Current Validation Plots

The following current measurement stations were compared against model results. The plots for each station include time series, current rose, scatter, and frequency of exceedance plots.

- Martha's Vineyard Coastal Observatory (MVCO) maintained by Woods Hole Oceanographic Institution (WHOI) has an Acoustic Doppler Current Profiler (ADCP) approximately 1.5 km south of Martha's Vineyard (41.33 N, 70.55 W) with observations in ~12m water depth.
- Wind farm developer Orsted provided data from several ADCP locations:
    - Orsted OR F180 ADCP (40.92 N, 70.92972 W) in ~55.6m water depth – *Included in the body of the report above.*
    - Orsted OR F190 ADCP (41.11917 N, 70.60056 W) in ~42.2m water depth
    - WBU Triaxys ADCP (41.11333 N, 70.59111W) in ~42.8m water depth
    - Orsted OR F240 ADCP (41.08806 N, 71.22194 W) in ~35.4m water depth
    - Orsted Acoustic Wave and Current profiler (AWAC) (71.51675 W, 41.10964 N) in ~26.5m water depth
    - Orsted OR F230 ADCP (39.07028 N, 74.4472 W) in ~18.6m water depth
- Coastal Pioneer Array maintained by Ocean Observation Initiative has several ADCPs approximately 120 km south of Martha's Vineyard (39.6 N, 70.6 W) at the shelf edge. The two locations that were used were:
    - Central Offshore Profiler Mooring (CP02PMCO) (40.10108 N, 70.88765 W) in ~148m water depth

It should be noted that the model results at the Coastal Pioneer Array did not demonstrate the same behavior as the observations. The measurements show a dominant westward current while the model appears to be tidally dominated at this location. This leads the authors to believe that the Coastal Pioneer Array may be inside the Mid-Atlantic region of southward-flowing cool current or the array is inside a recirculation eddy derived from the Gulf Stream, as shown in the oceanographic process section of the report. The results in the model were reviewed to locate the westward flowing currents that are seen in the measurements. The model results and the measurements line up more closely ~100 km South of the array location in the model. The model results at the array location and 100 km South are presented for information in this Appendix.

The time series, current rose, frequency of occurrence and scatter plots follow.

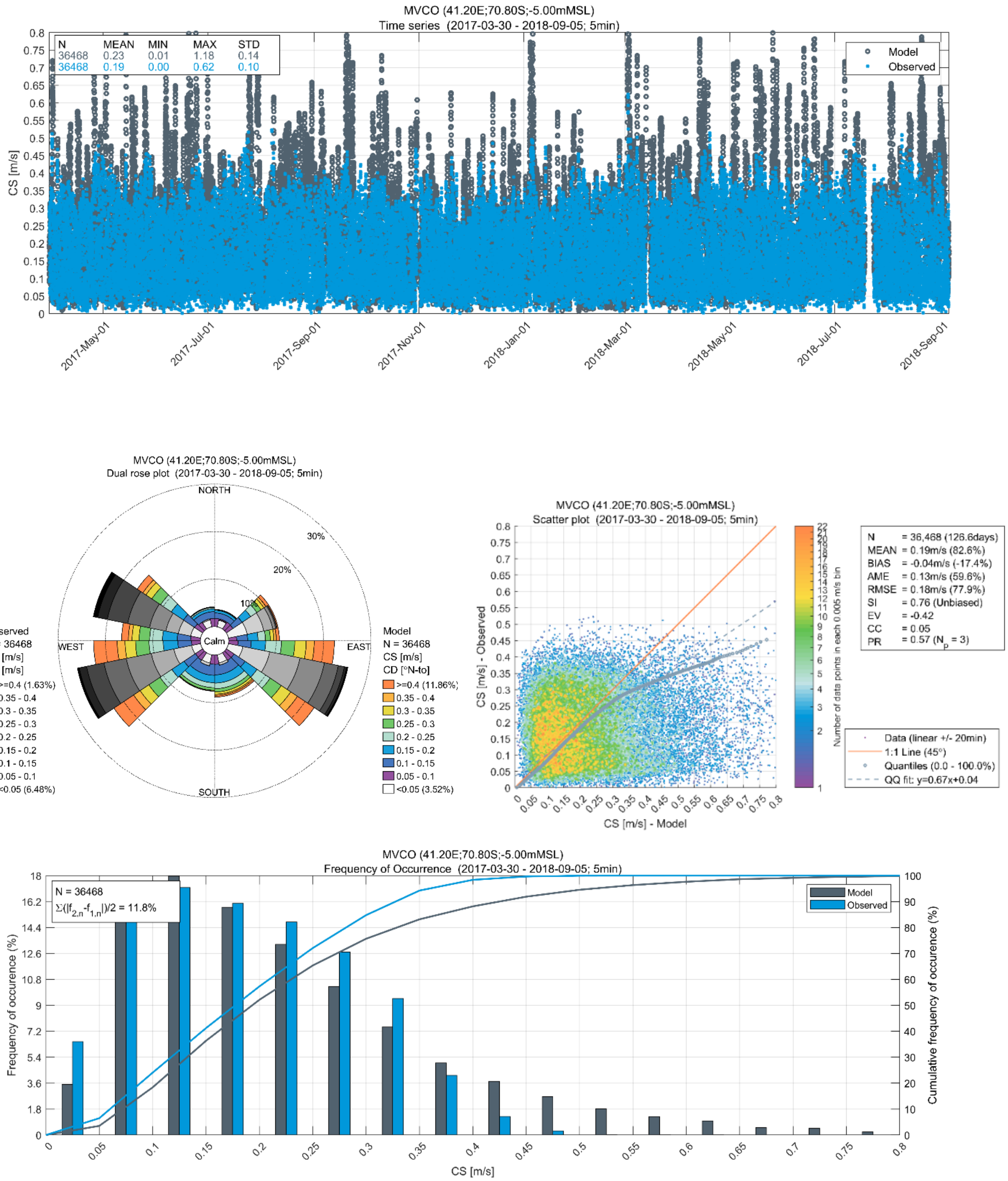

Figure 128. MVCO current measurements at 5 m depth vs. model results

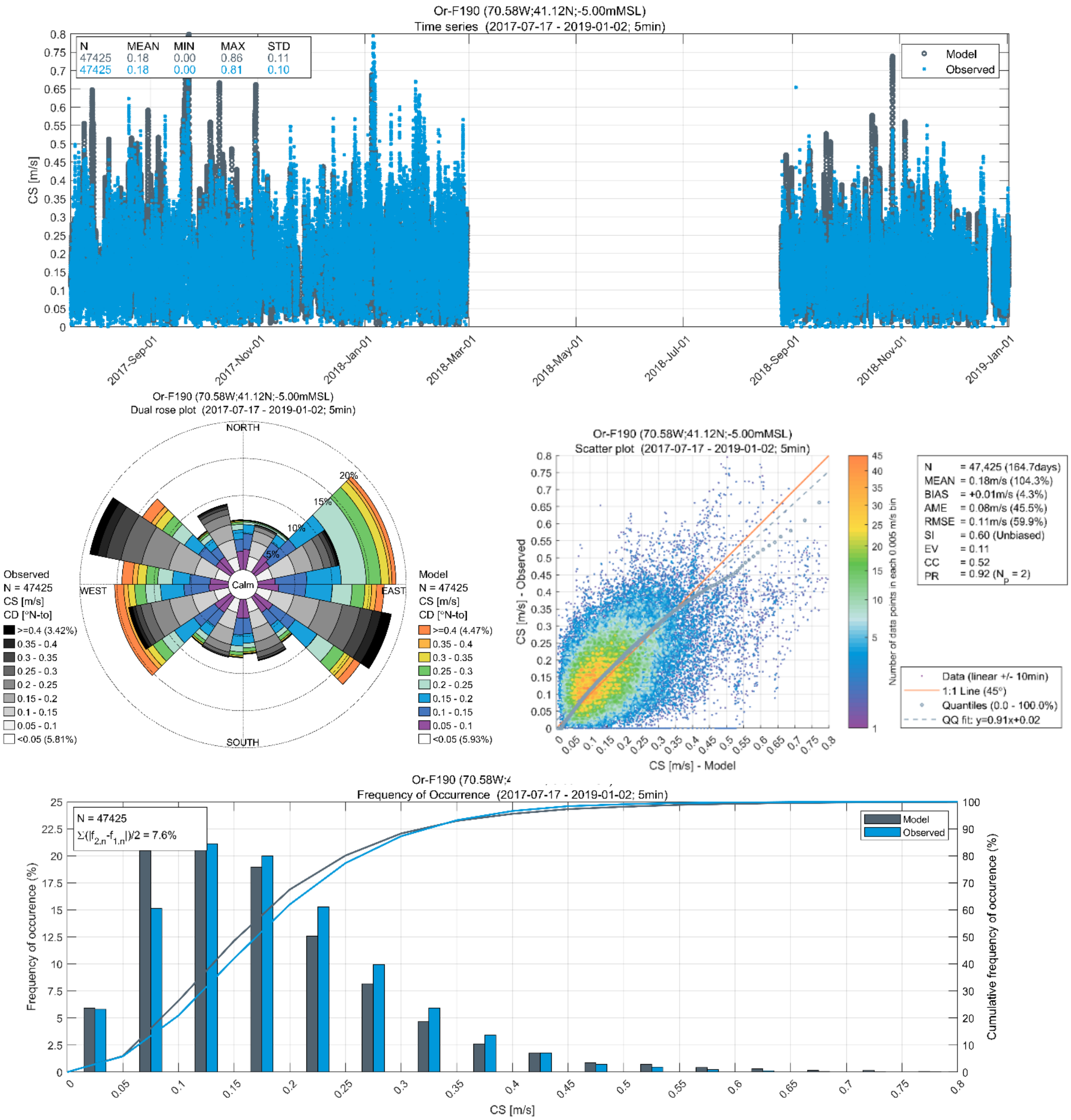

Figure 129. Orsted OR F190 current measurements at 5 m depth vs. model results

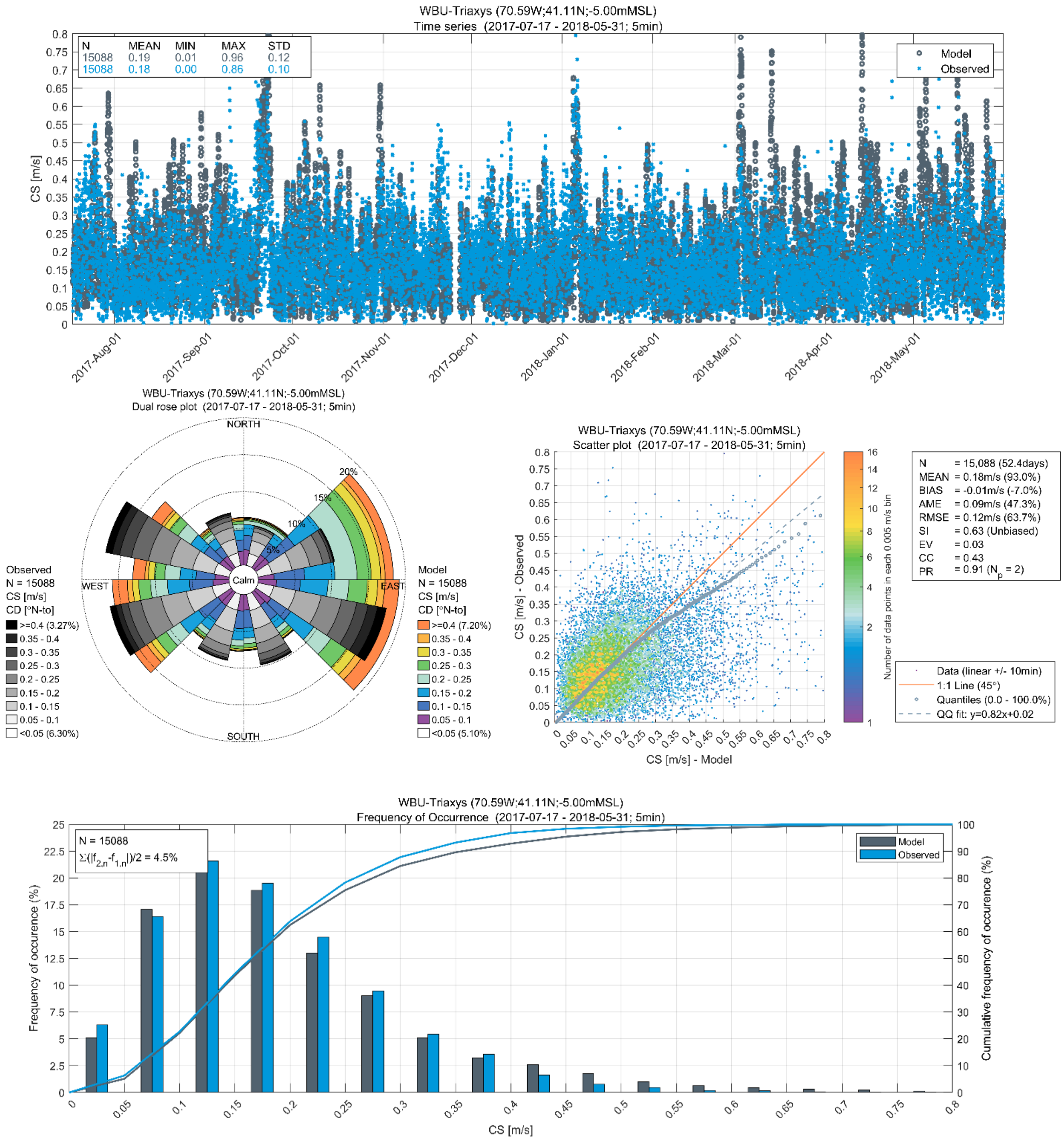

Figure 130. WBU Triaxys current measurements at 5 m depth vs. model results

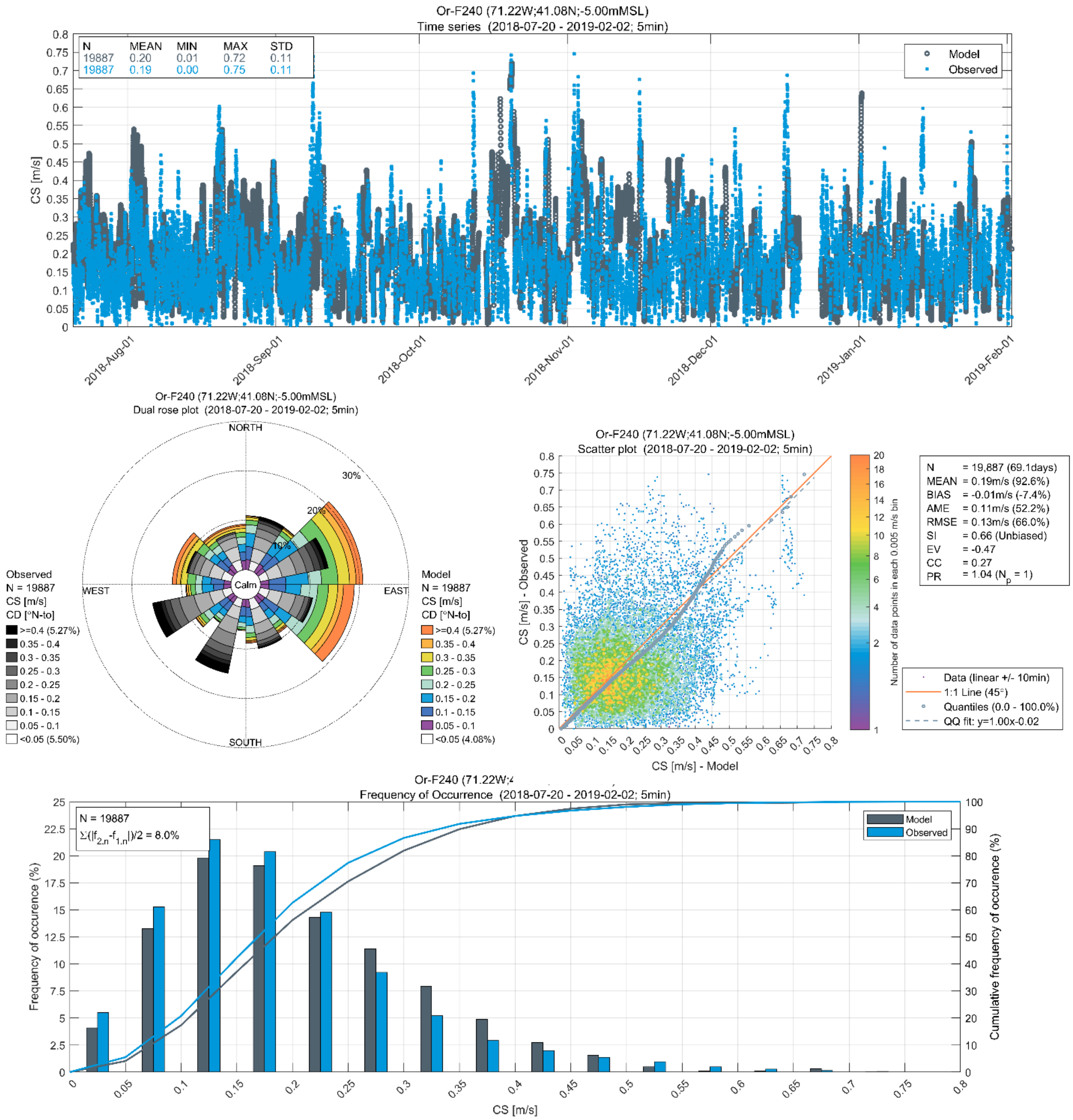

Figure 131. Orsted OR F240 current measurements at 5 m depth vs. model results

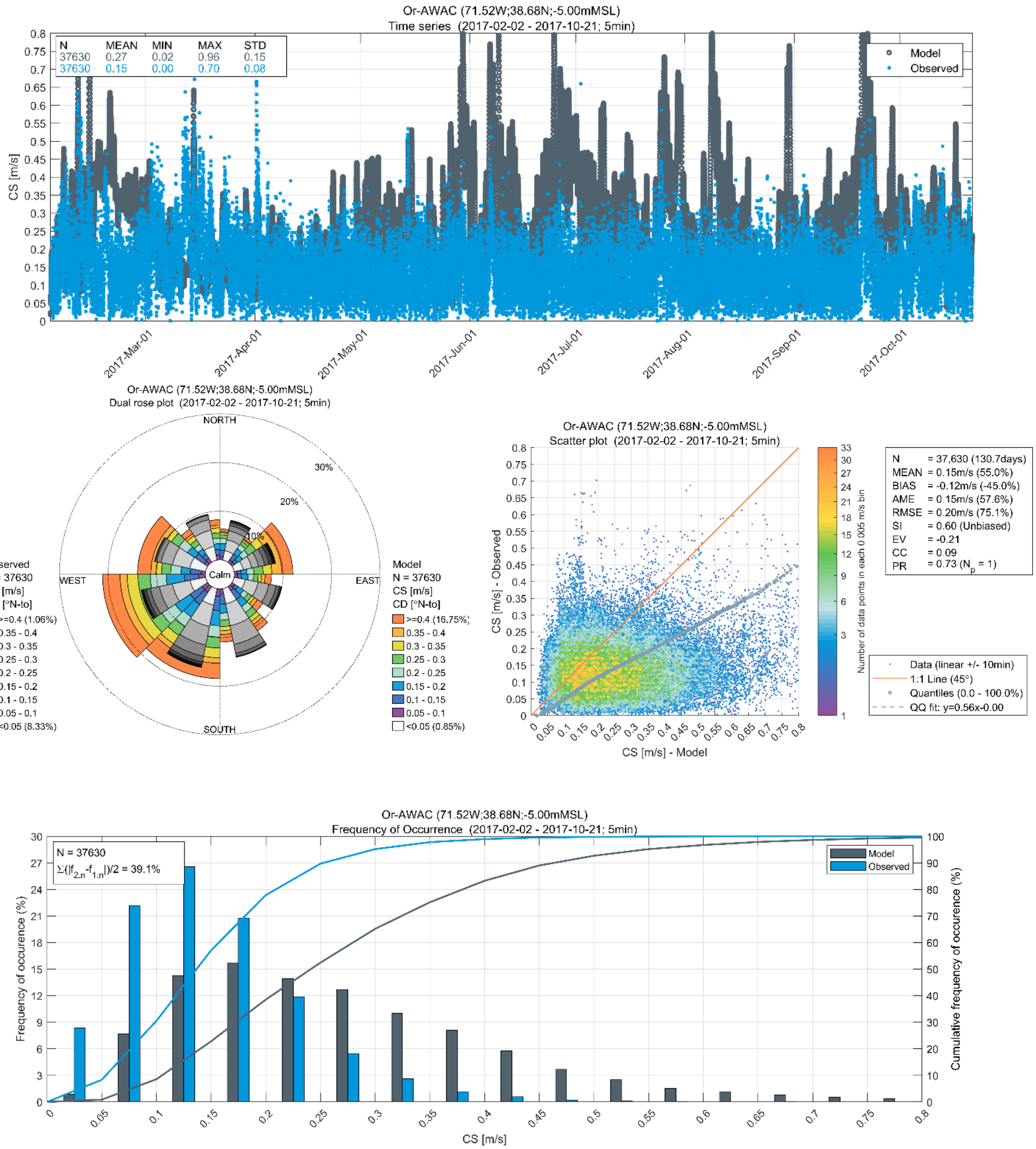

Figure 132. Orsted AWAC current measurements at 5 m depth vs. model results

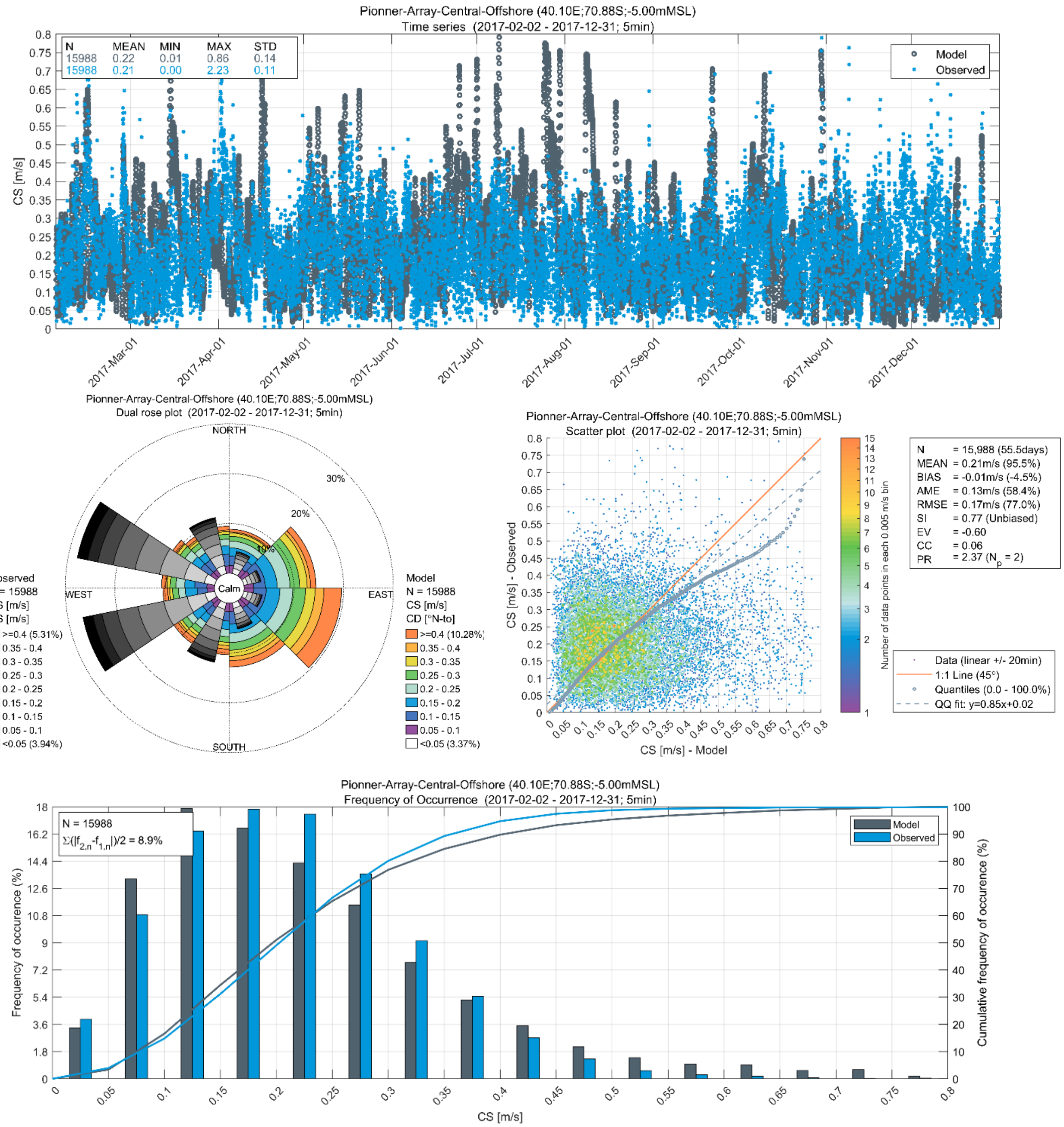

Figure 133. Coastal Pioneer Array Central Offshore Profiler current measurements vs. model results at 5 to 13 m depth (model results at the array location in the model)

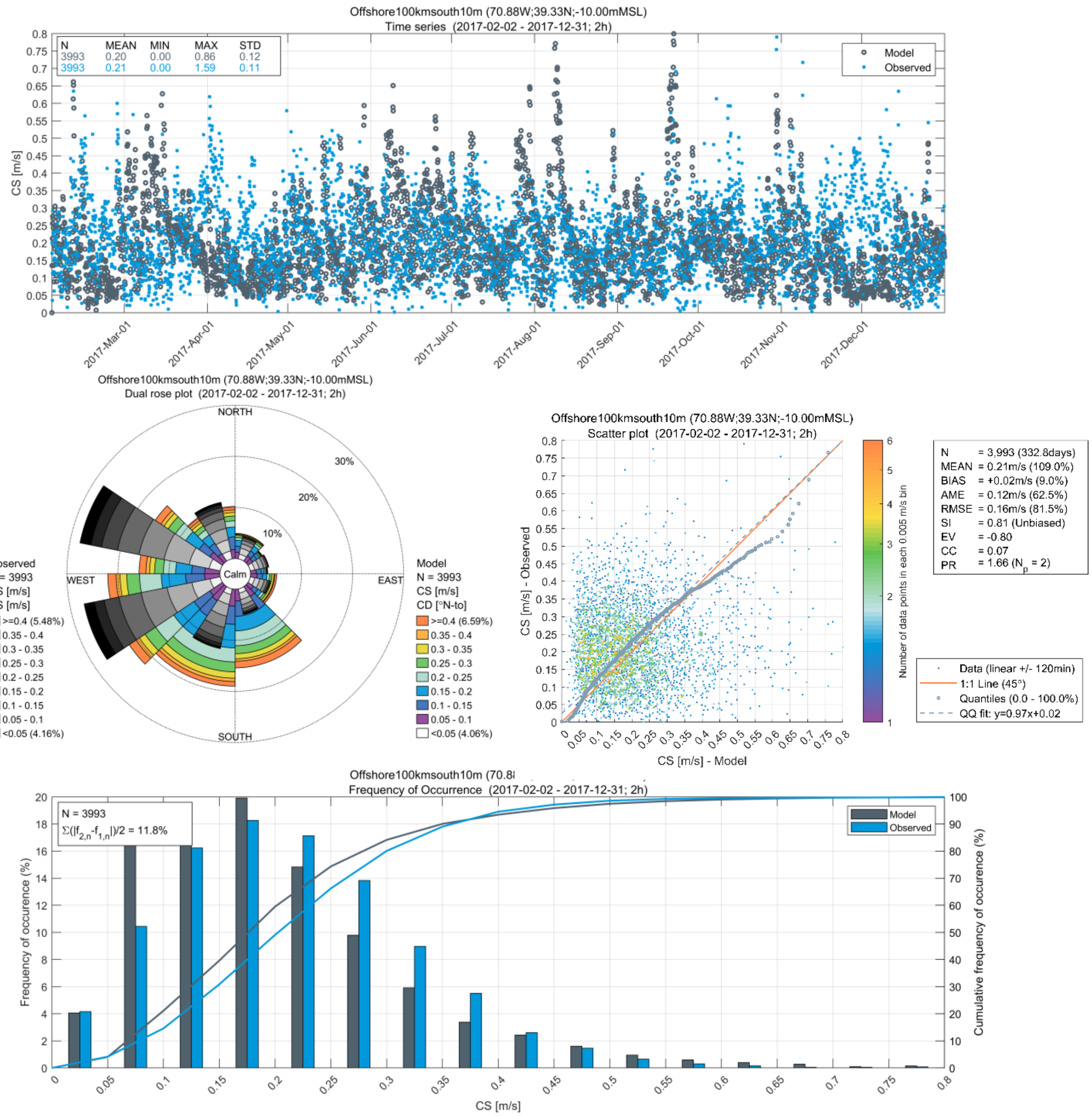

Figure 134. Coastal Pioneer Array Central Offshore Profiler current measurements at ~13 m depth vs. model results at 10 m depth (model results 100 km South of the array location)

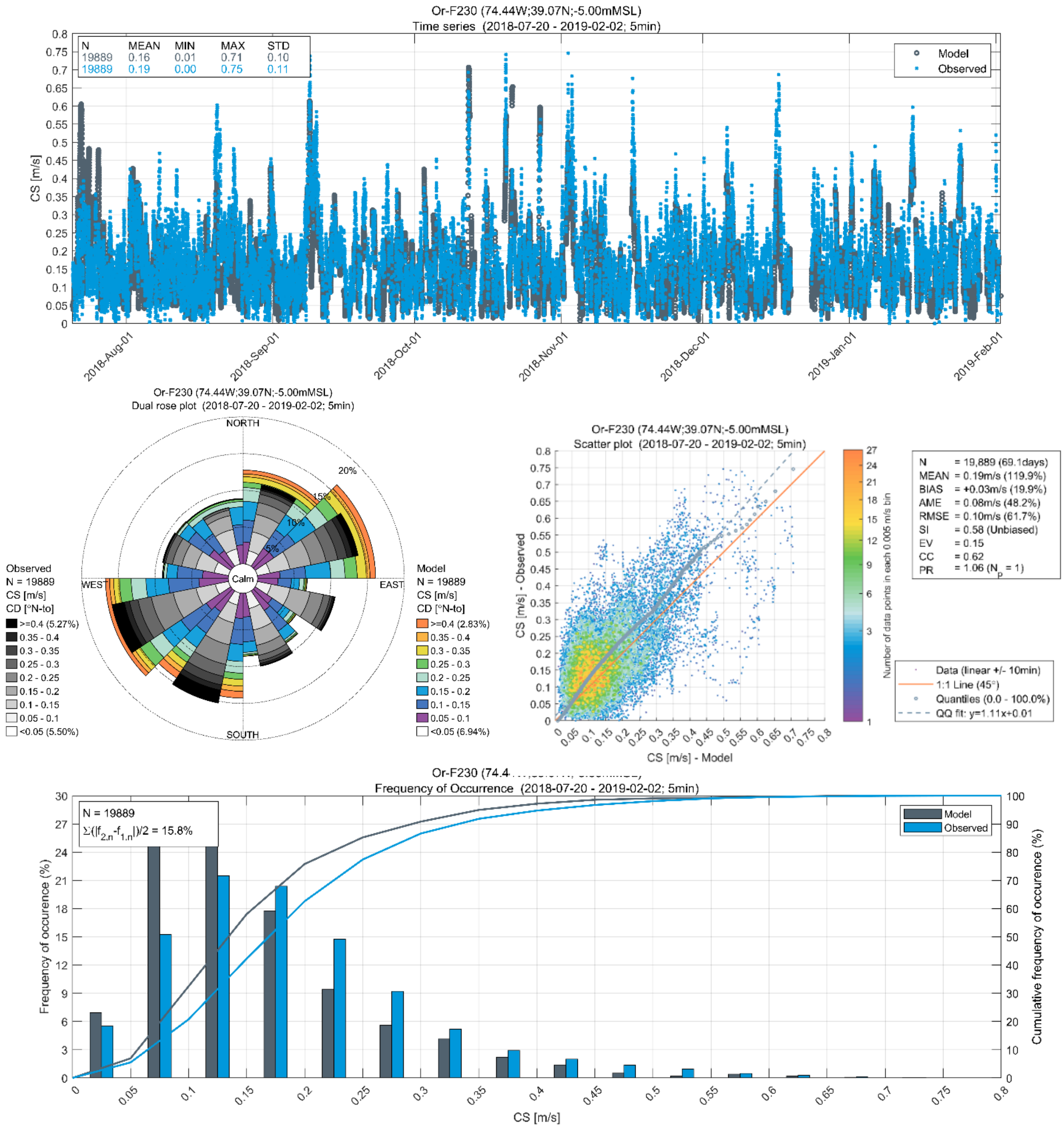

Figure 135. Orsted OR F230 current measurements at 5 m depth vs. model results

A.2.2 Hydrodynamic Model Baseline Wave Validation Plots

The Block Island (NDBC 44097 station) wave H_{m0} time series, wave H_{m0} wave rose, wave H_{m0} frequency of occurrence and wave H_{m0} scatter, wave peak period time series and wave peak period frequency of occurrence plots follow.

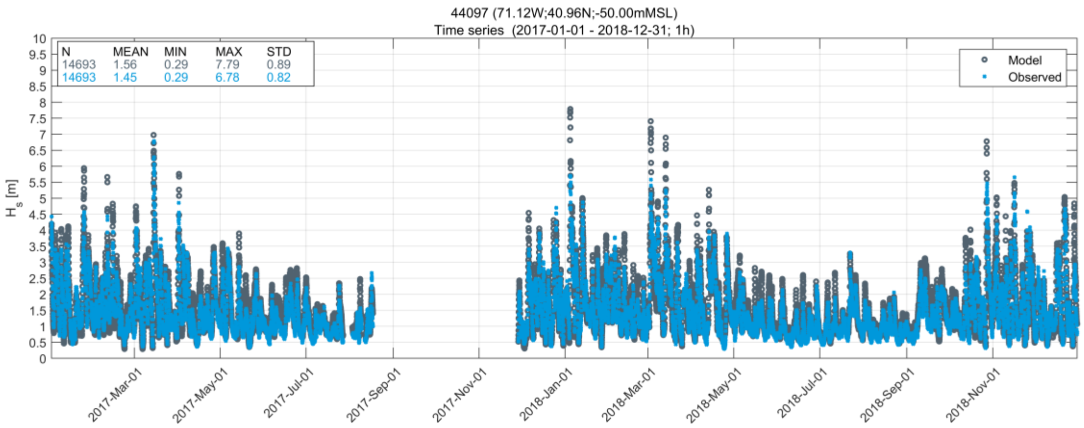

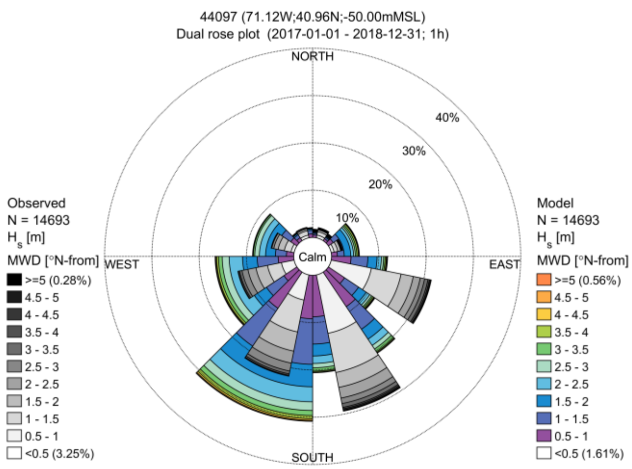

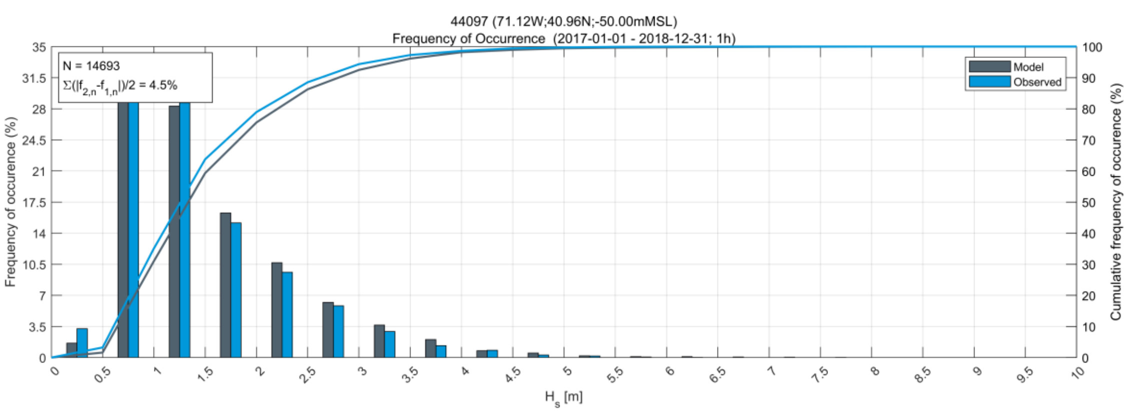

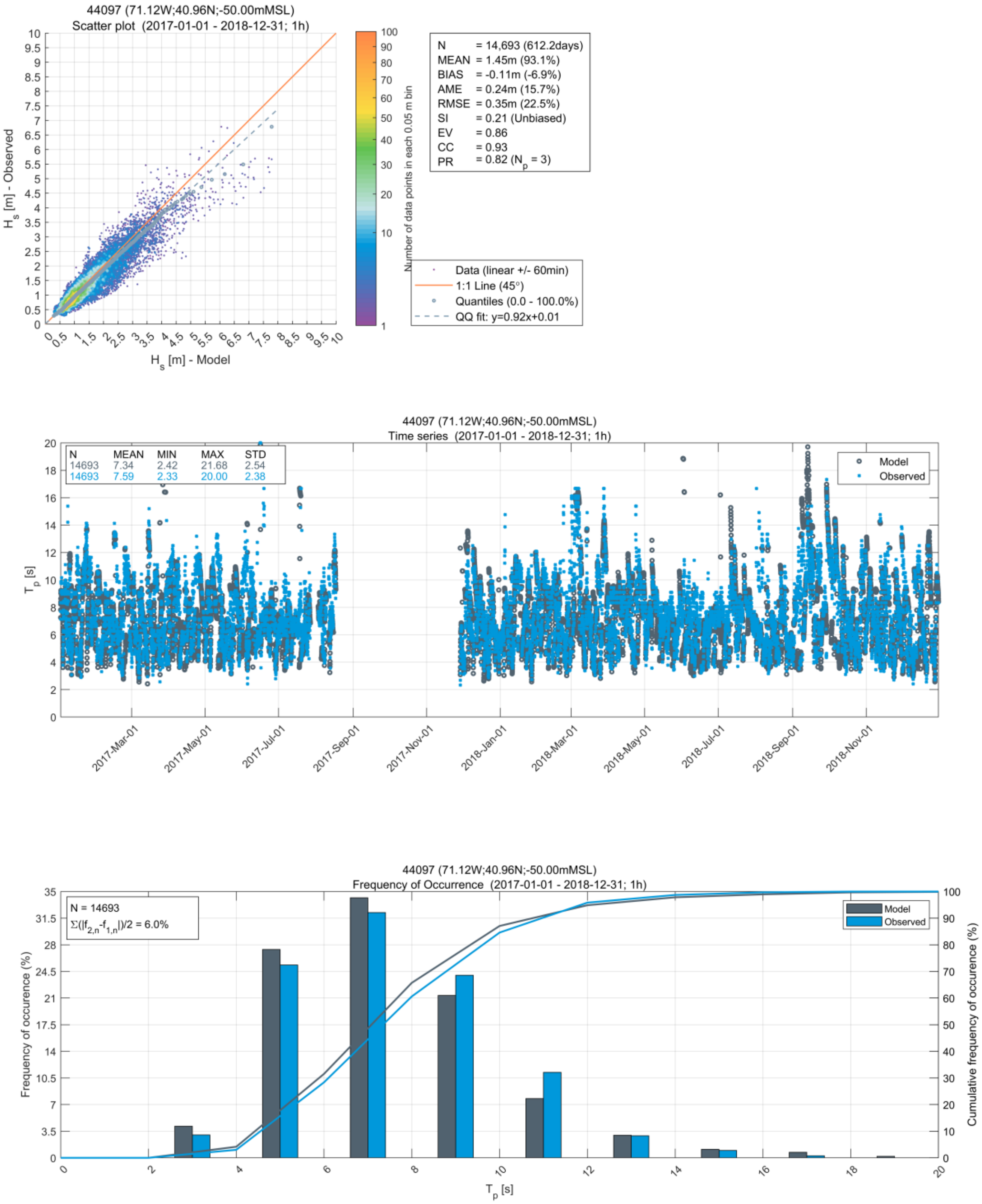

Figure 136. Block Island wave measurement vs. model results

A.2.3 Hydrodynamic Model Baseline Water Level Validation Plots

Relevant water level measurement data collected and used included:

- Station NTKM3 - 8449130 - Nantucket Island, MA (41.285 N 70.096 W) – *Included in the body of the report*
- Station NWPR1 - 8452660 - Newport, RI (41.504 N 71.326 W)
- Station QPTR1 - 8454049 - Quonset Point, RI (41.586 N 71.407 W)
- Station ACYN4 - 8534720 - Atlantic City, NJ (39.357 N 74.418 W)
- Station BRND1 - 8555889 - Brandywine Shoal Light, DE (38.987 N 75.113 W)

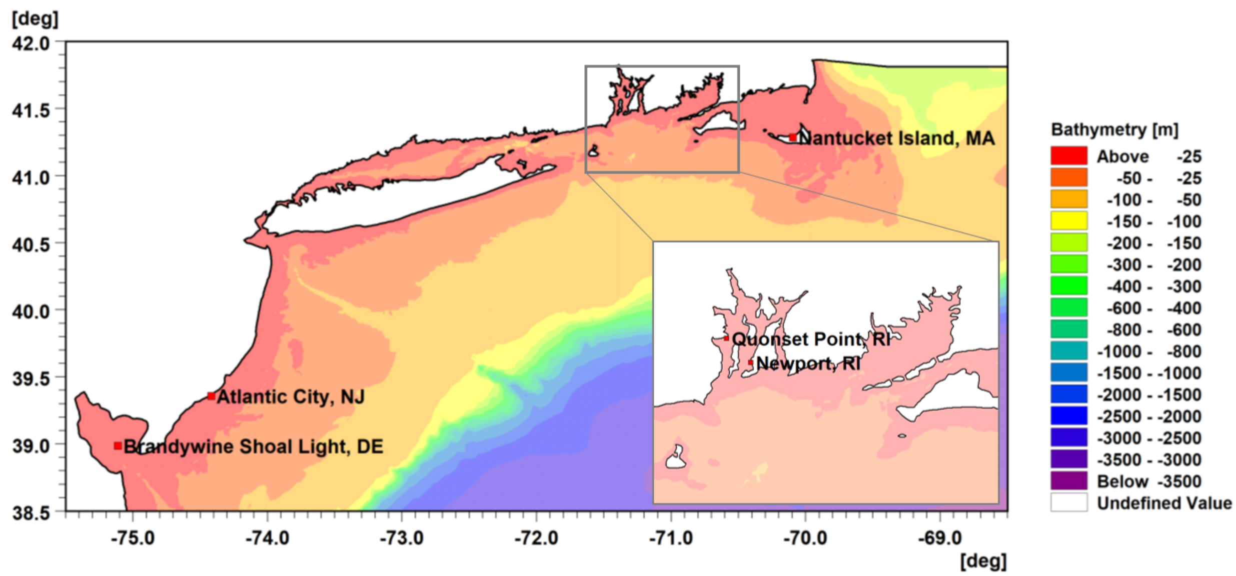

Figure 137. Water level measurement locations

The time series, scatter and frequency of occurrence plots follow.

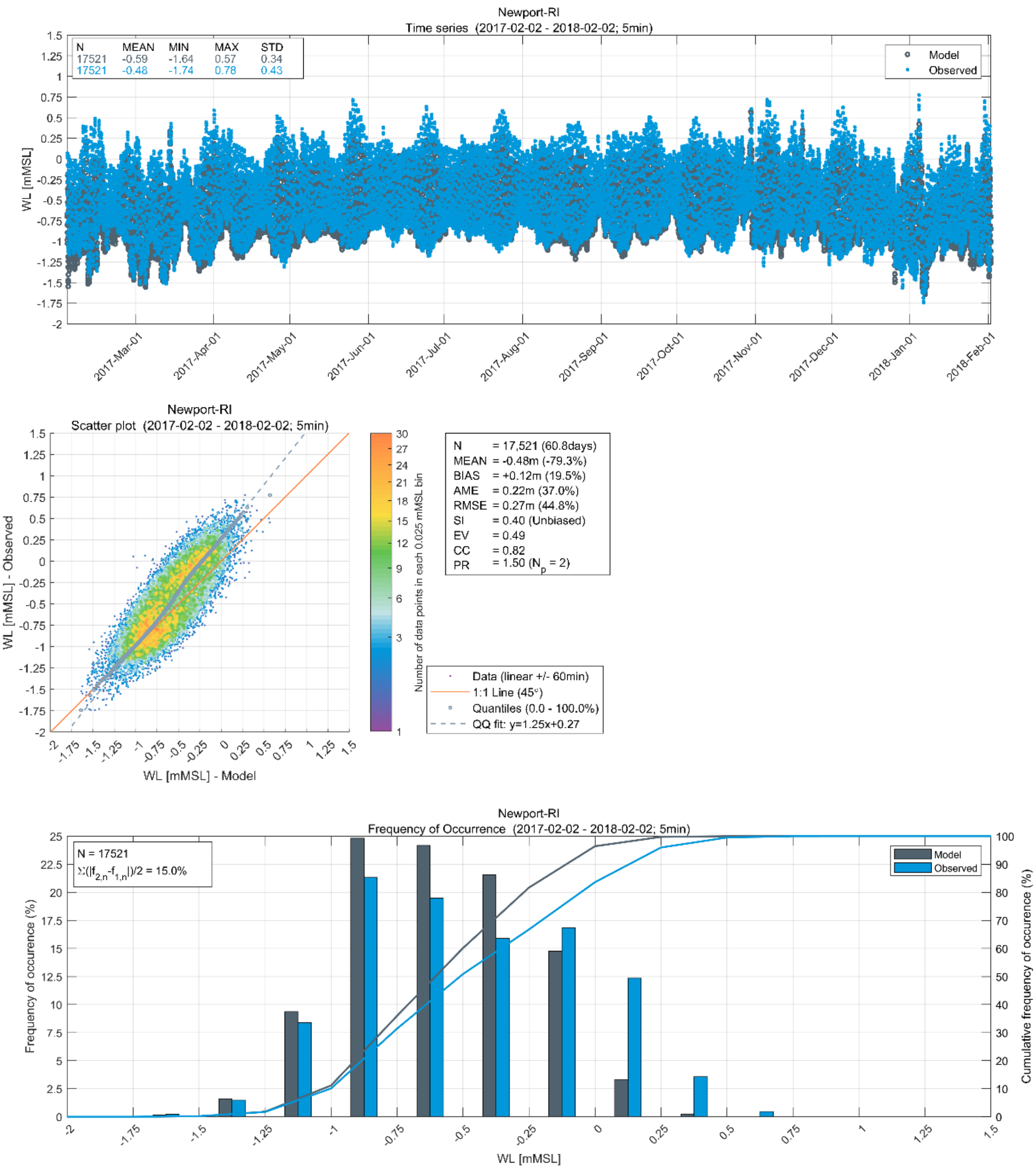

Figure 138. Newport, Rhode Island station water level measurements vs. model results

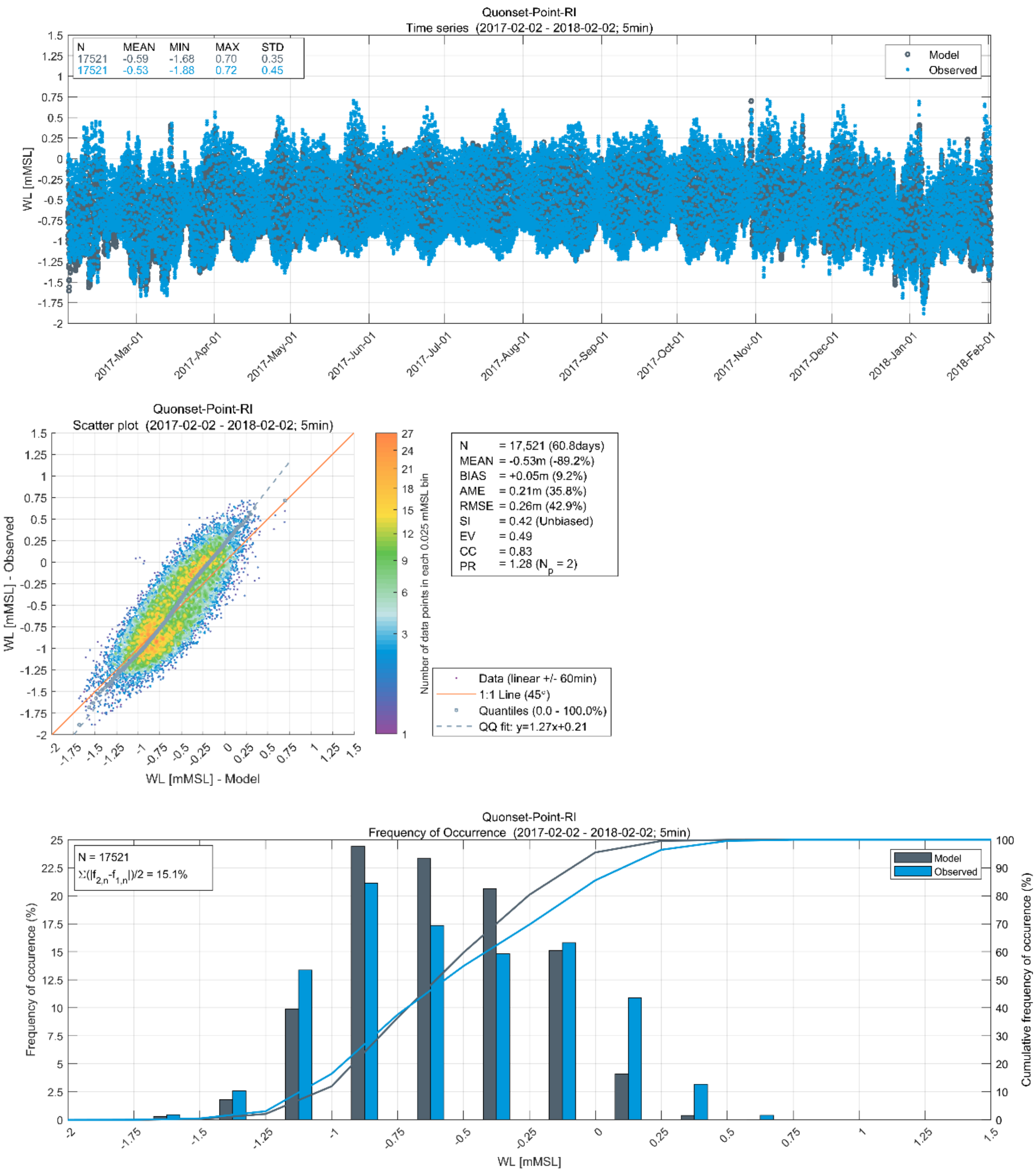

Figure 139. Quonset Point, Rhode Island station water level measurements vs. model results

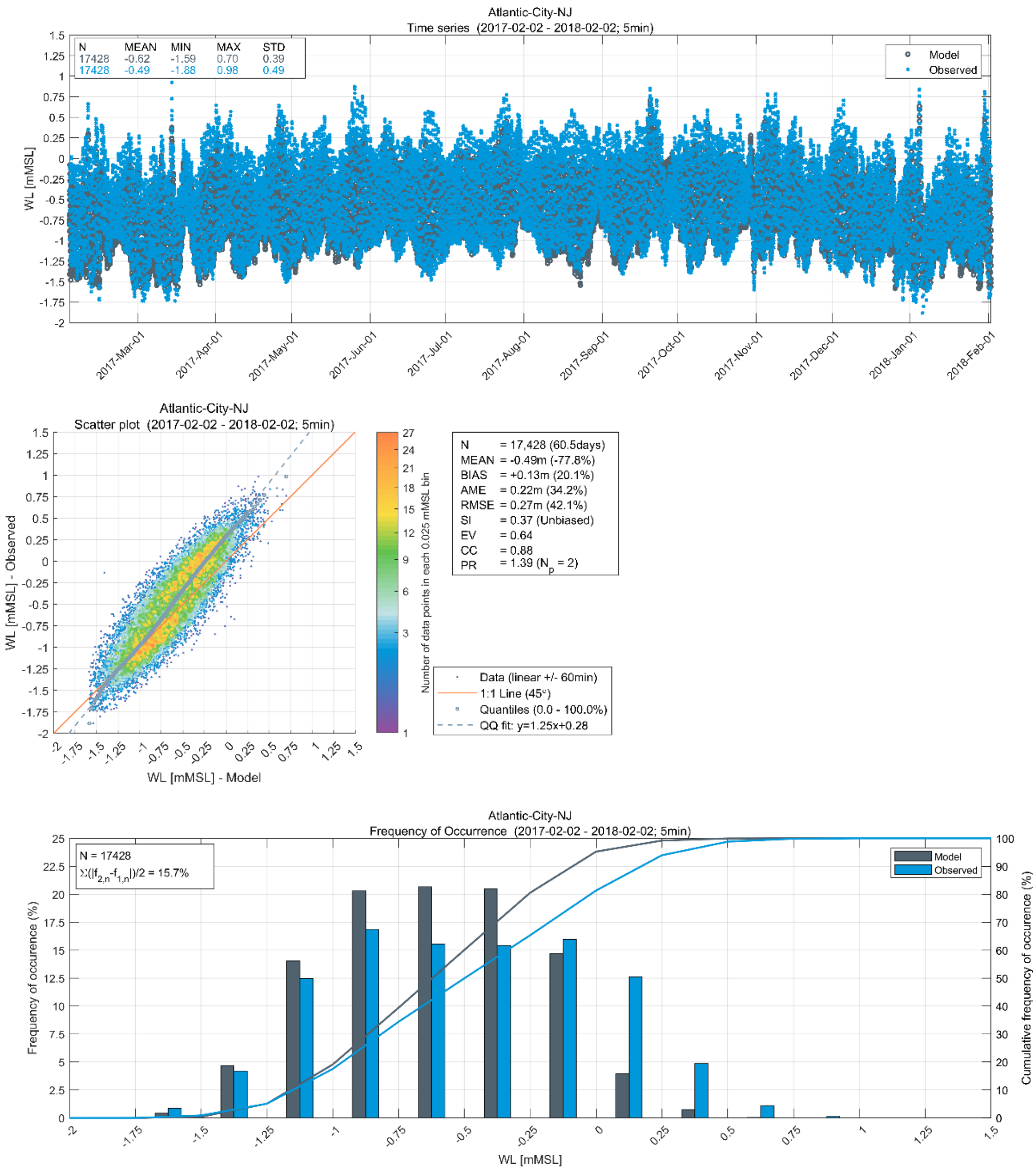

Figure 140. Atlantic City, New Jersey station water level measurements vs. model results

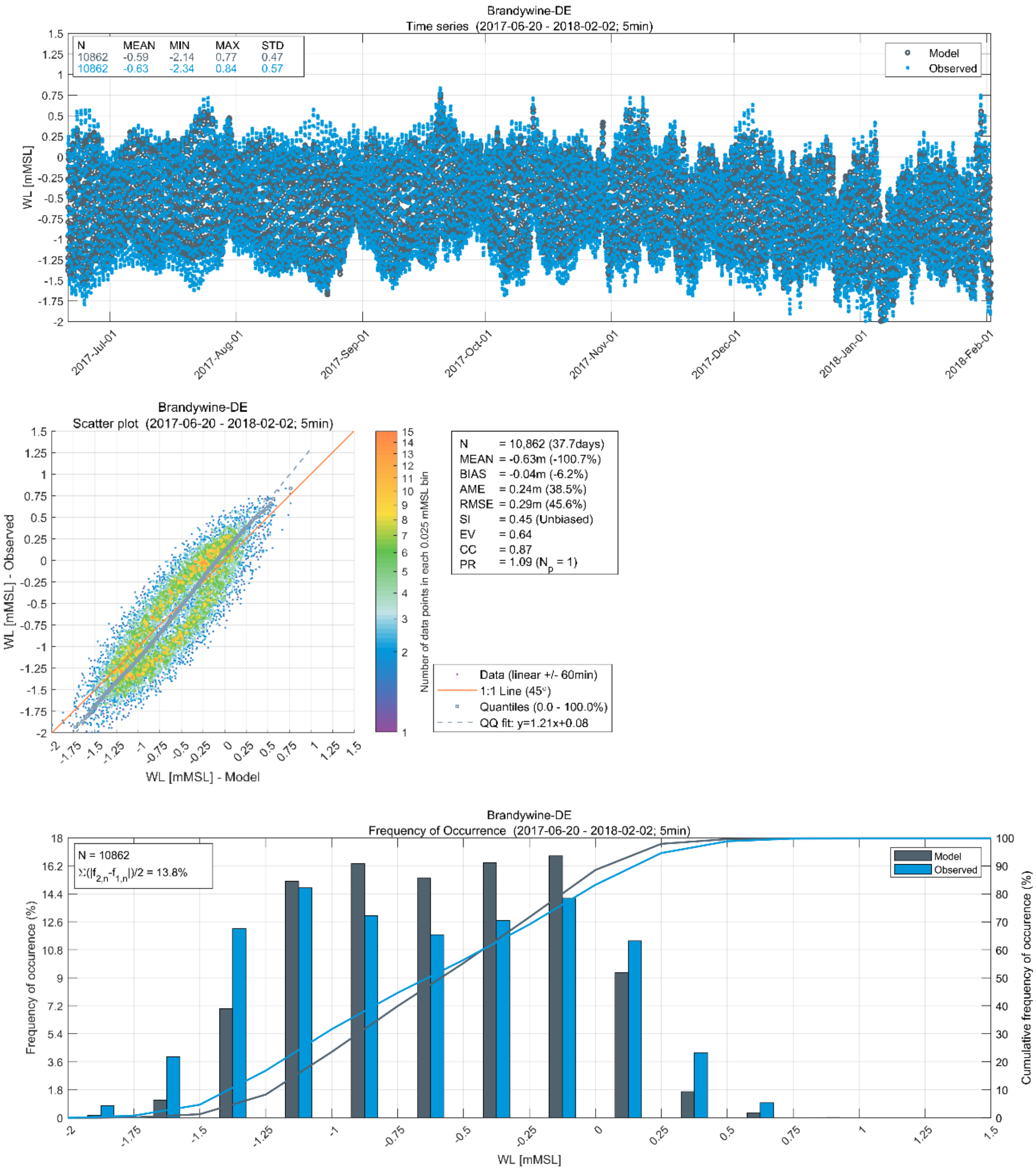

Figure 141. Brandywine Shoal Light, Delaware station water level measurements vs. model results

A.2.4 Hydrodynamic Model Baseline Sea Temperature Validation Plots

Relevant sea temperature measurement data collected and used from NDBC buoys included:

- Station 44008 (offshore) - Nantucket 54 NM Southeast of Nantucket. 40.504 N 69.248 W). Sea temp depth: 1.5 m below water line. Water depth: 74.7 m
- Station 44097 - Block Island, RI. (40.967 N 71.126 W). Sea temp depth: 0.46 m below water line. Water depth: 51 m – *Included in the body of the report above.*
- Station 44017 - Montauk Point - 23 NM SSW of Montauk Point, NY (40.693 N 72.049 W). Sea temp depth: 1.5 m below water line. Water depth: 48 m
- Station 44025 - Long Island - 30 NM South of Islip, (NY40.251 N 73.164 W). Sea temp depth: 1.5 m below water line. Water depth: 36.3 m
- Station 44065 - New York Harbor Entrance - 15 NM SE of Breezy Point, NY (40.369 N 73.703 W). Sea temp depth: 1.5 m below water line. Water depth: 25 m

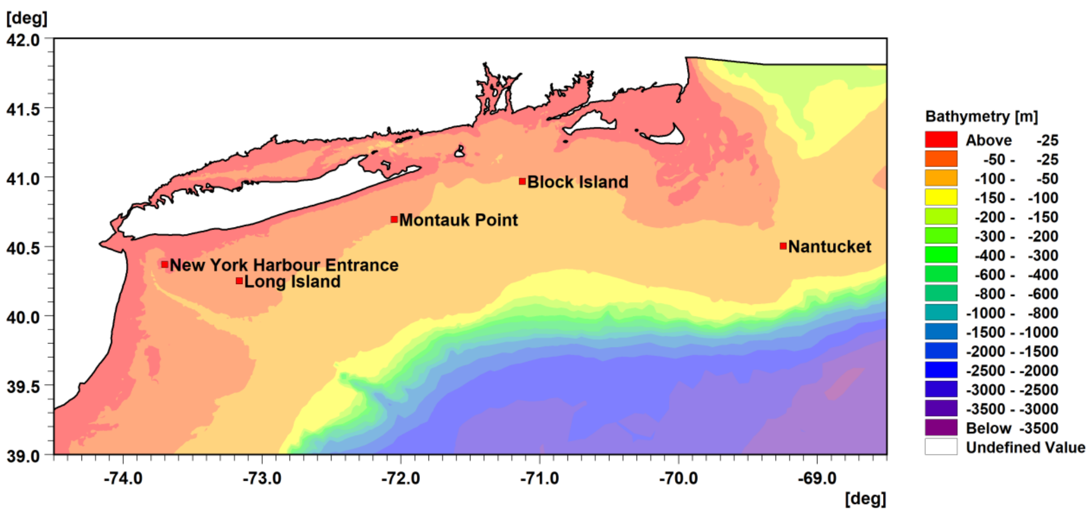

Figure 142. Sea temperature measurement locations

The time series, scatter plots frequency of occurrence plots follow for the NDBC buoy stations.

Regional sea surface temperature OSTIA satellite measurements side-by-side model results are also included below. The October 1, 2017 OSTIA satellite and model result plots are included in the body of the document above.

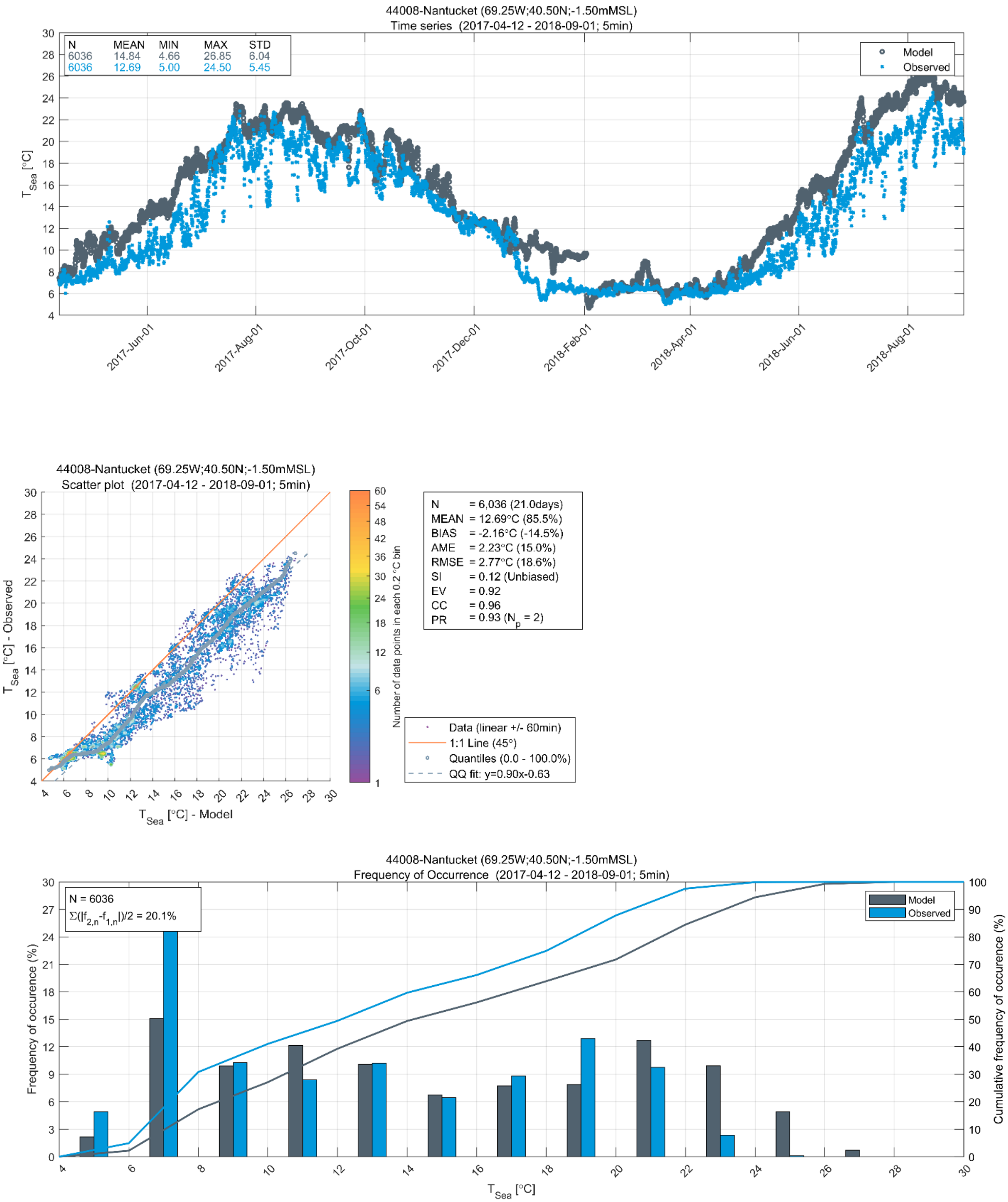

Figure 143. Nantucket sea temperature measurements at 1.5 m depth vs. model results

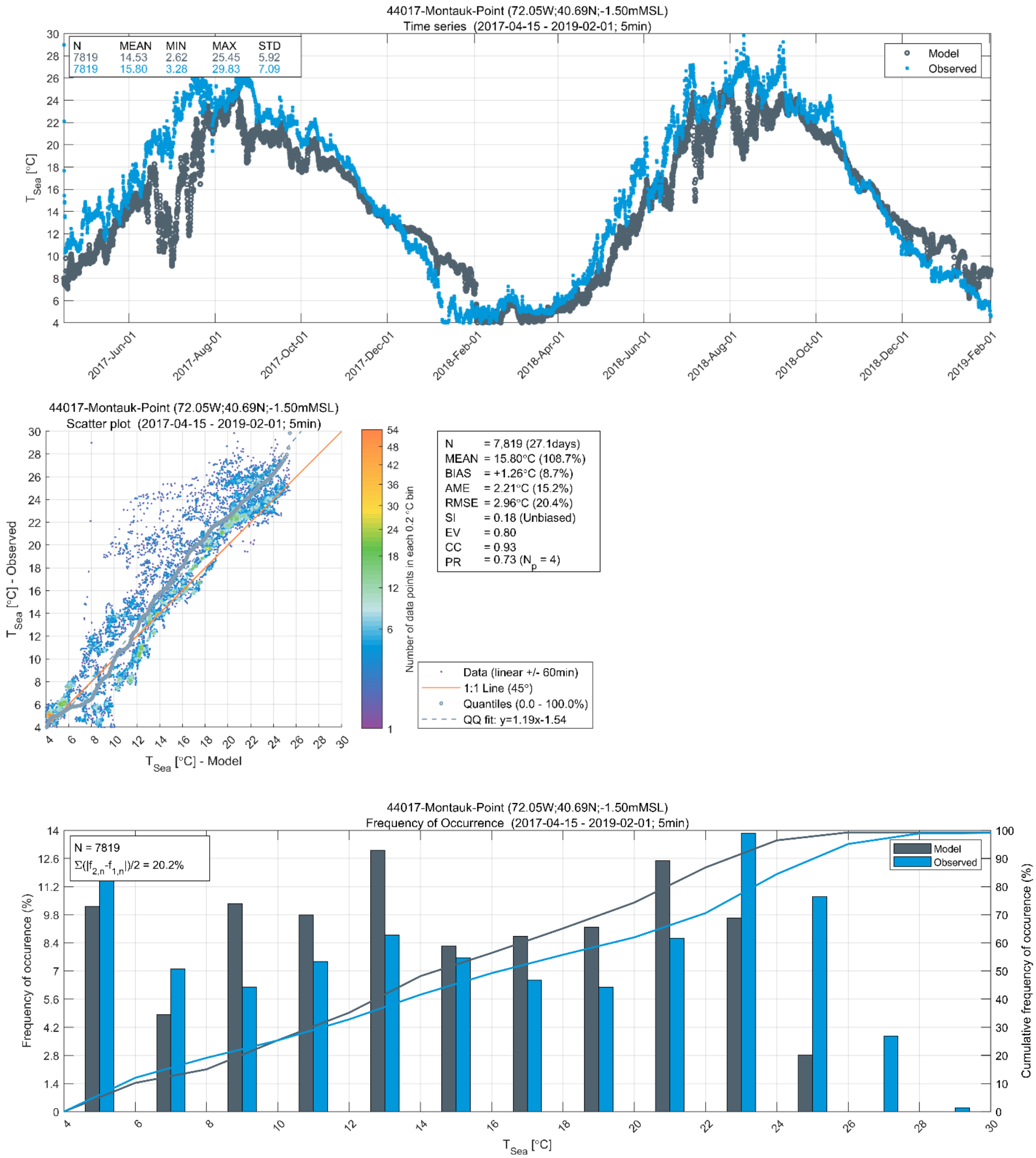

Figure 144. Montauk Point sea temperature measurements at 1.5 m depth vs. model results

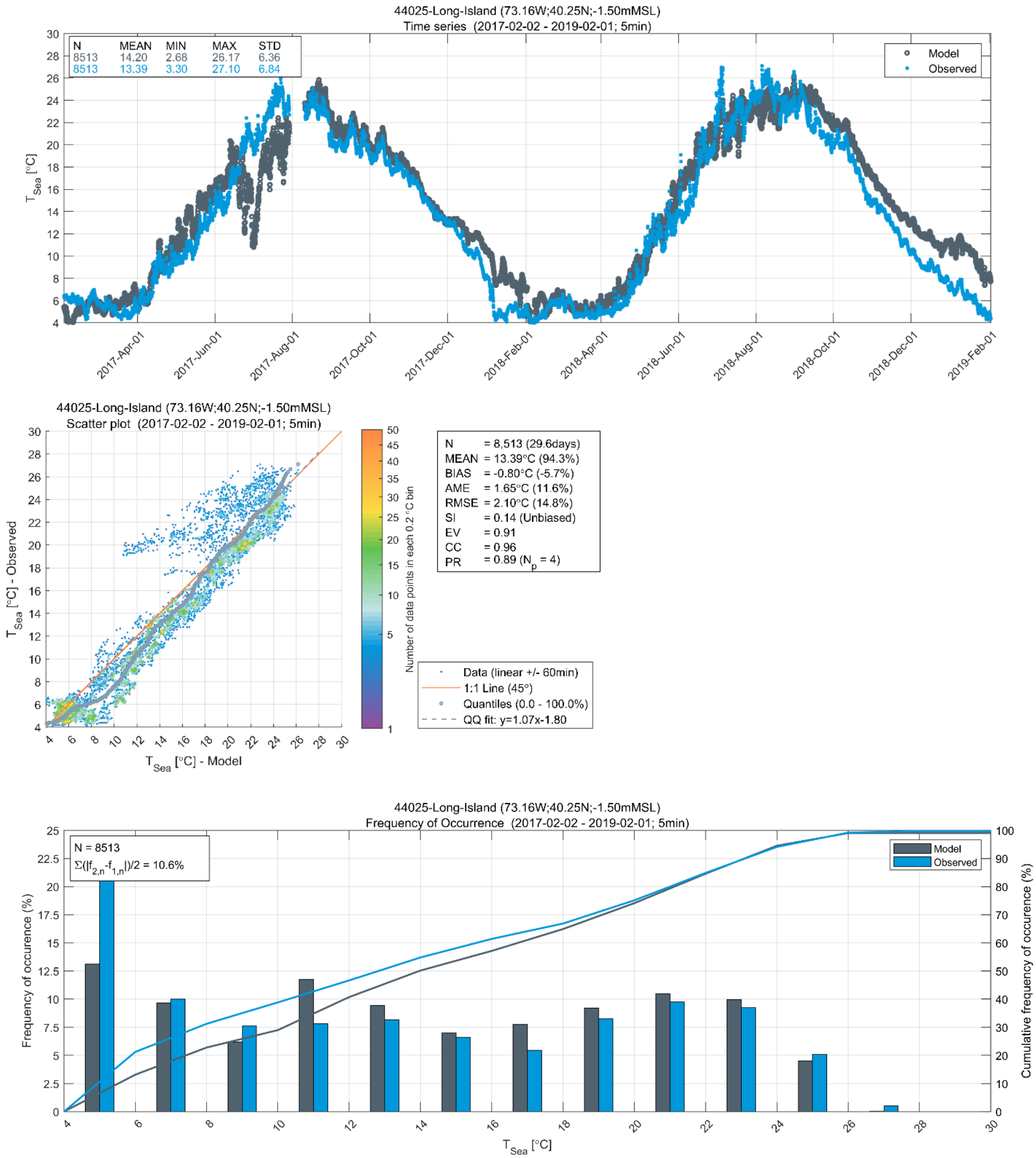

Figure 145. Long Island sea temperature measurements at 1.5 m depth vs. model results

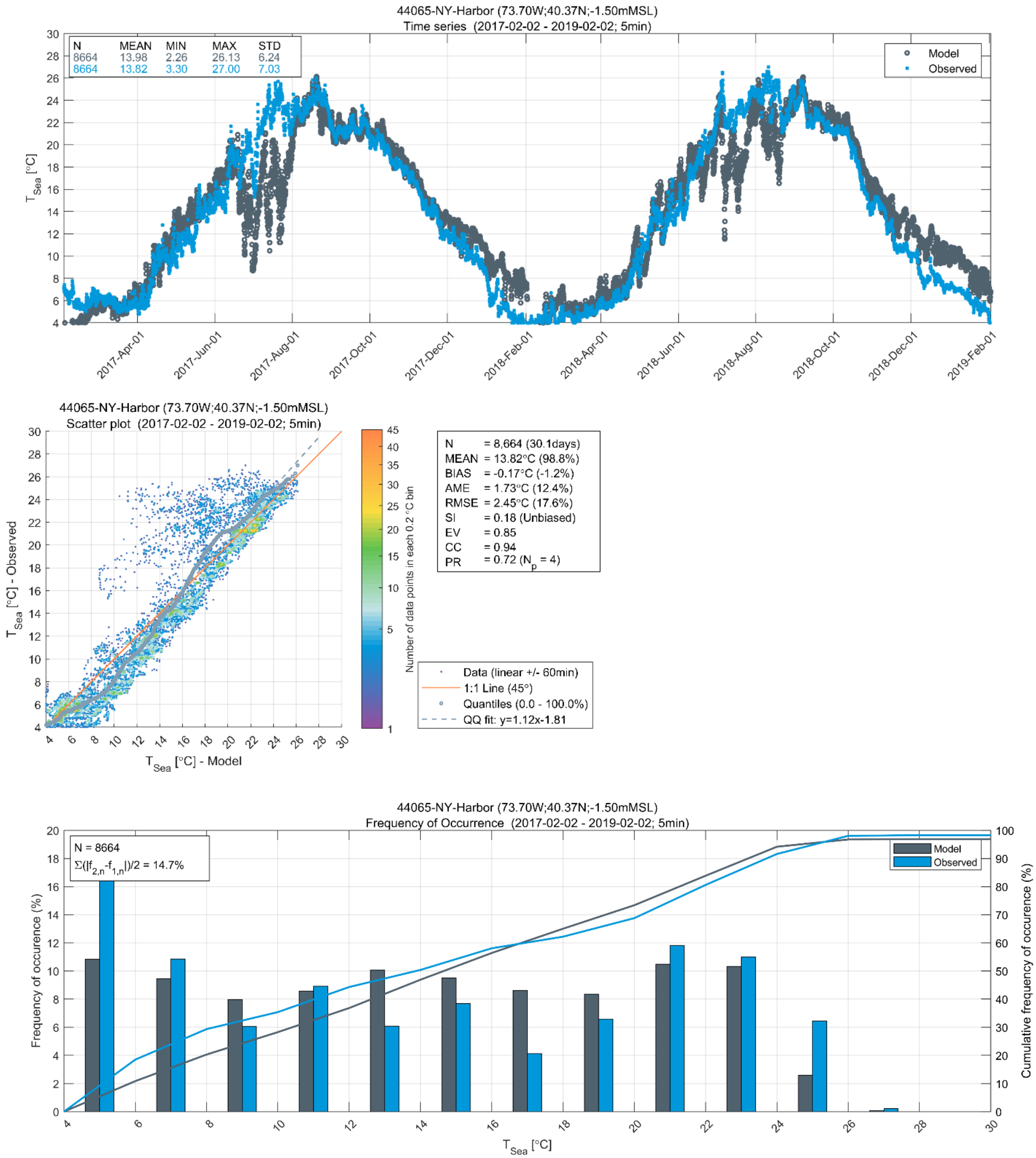

Figure 146. New York Harbor Entrance sea temperature measurements at 1.5 m depth vs. model results

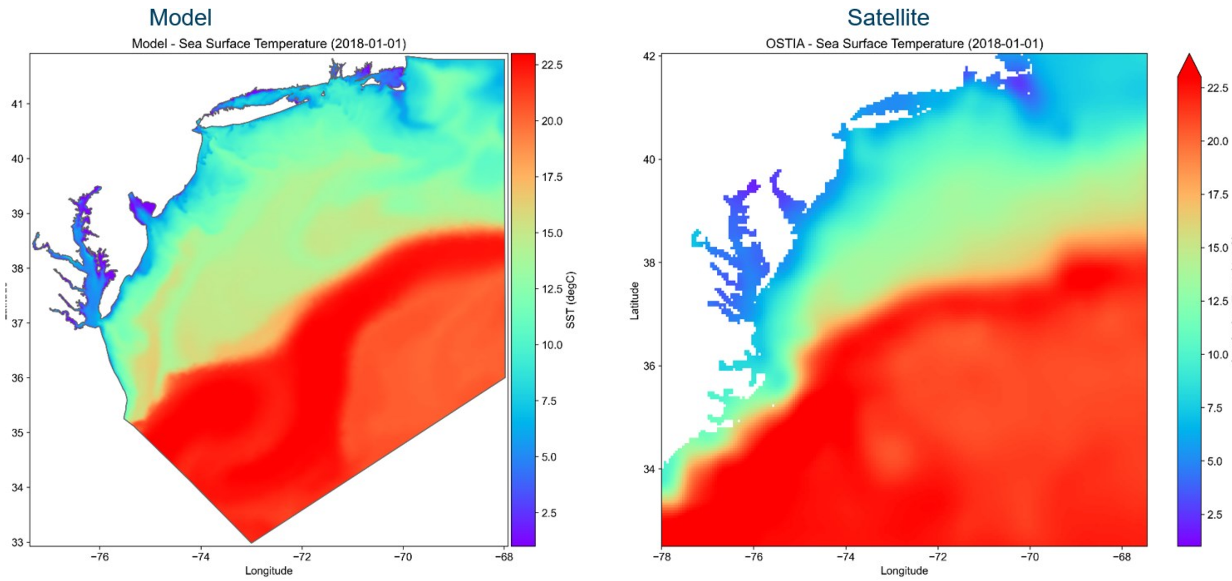

Figure 147. Regional sea surface temperature OSTIA satellite measurements side-by-side model results (January 1, 2017)

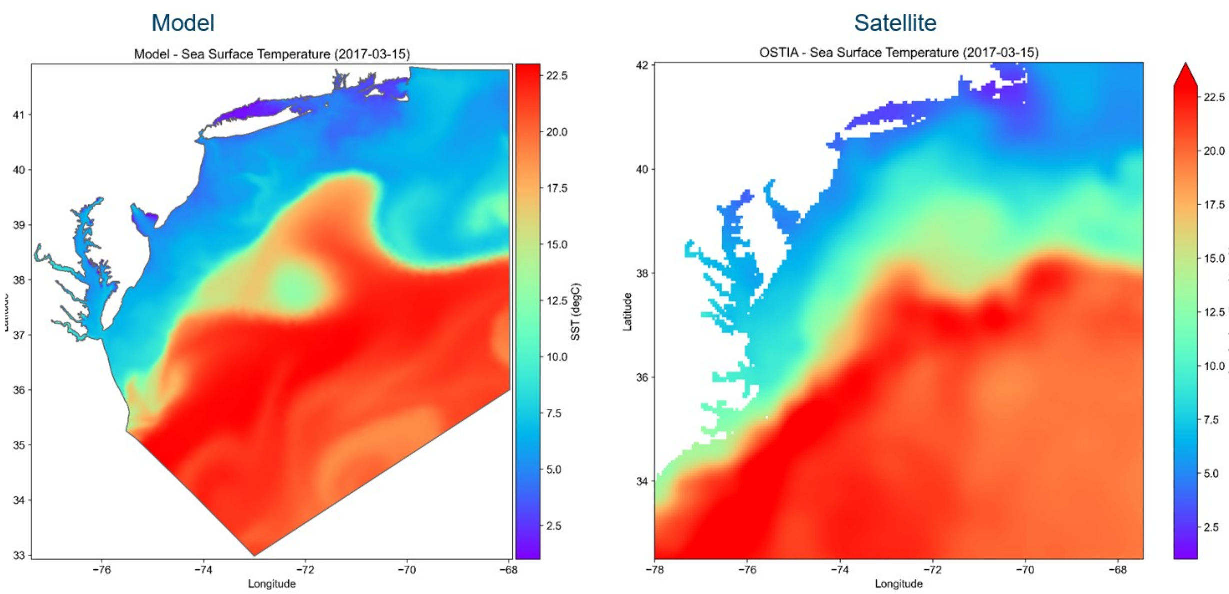

Figure 148. Regional sea surface temperature OSTIA satellite measurements side-by-side model results (March 15, 2017)

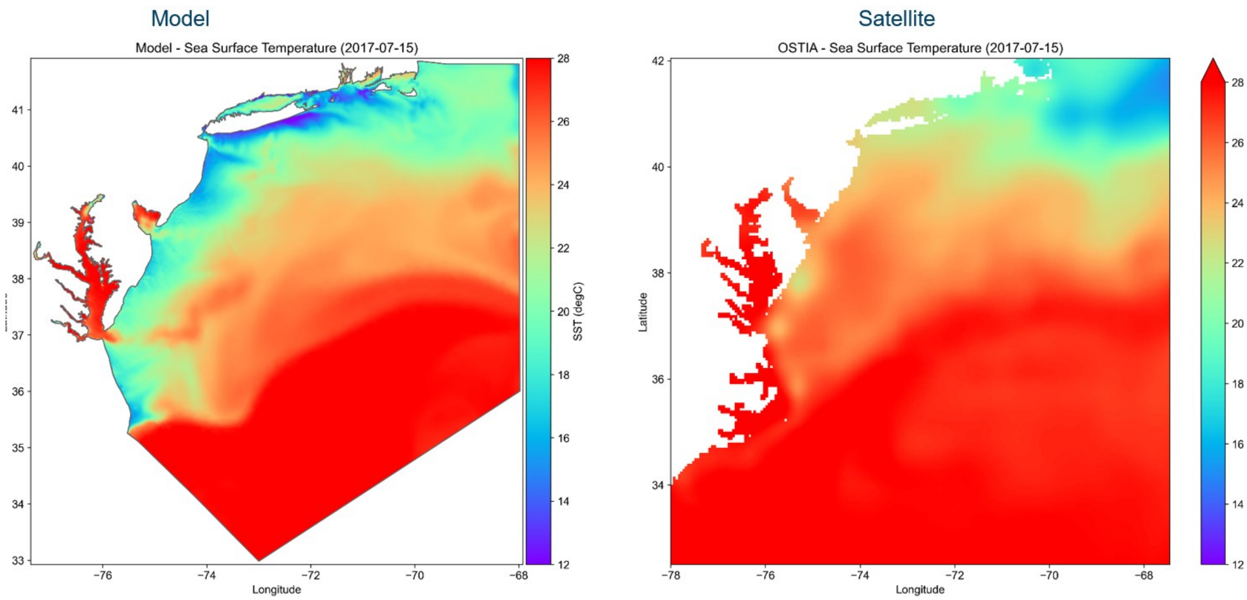

Figure 149. Regional sea surface temperature OSTIA satellite measurements side-by-side model results (July 15, 2017)

B Agent-Based Model Overview, Design Concepts and Details (ODD) Protocol

The descriptions of the silver hake, sea scallop and summer flounder ABMs follow the updated "Overview, Design concepts, Details" protocol, which is a standard format for describing and disseminating individual based models (Grimm et al. 2020). Some sections in this ODD have been previously described in the main body of the report (**Section 6**) and are repeated in the following sections for completeness of the ODD.

B.1 Purpose

The purpose of the models is to simulate the larval transport of selected key species, namely the ***sea scallop*** (*Placopecten magellanicus*), ***silver hake*** (*Merluccius bilinearis*), and ***summer flounder*** (*Paralichthys dentatus*), and changes in transport patterns, if any, arising from the alteration of oceanographic transport patterns in the indicated study area because of offshore wind construction projects. The results of this study will be used to assess impact to larval transport and settlement from wind turbine placement in certain geographic regions and will be used to evaluate the need for and the formation of mitigation measures, if deemed necessary.

The models are evaluated by their ability to reproduce larval dispersal and settlement patterns. The following evaluations may only be performed after satisfactory calibration and validation of the hydrodynamic forcings that are inputs to the ABM (as detailed in **Section 3** of the present report).

1. **Larval dispersal pattern**. This pattern reflects the horizontal and vertical migration of larvae across the simulated life stages, as the larvae develop from an initial state of passive drifter whereby their movements are predominantly dependent on hydrodynamic forcings, to later stages of development when the larvae develop limited capability for horizontal and/or vertical swimming, thereby exerting control over their migration patterns to a certain extent. These dispersal patterns, if sufficiently replicated, provide indication that parameterized movement processes of agents within the model are representative of real-life larval movement processes.

2. **Settlement location of larvae**. This pattern reflects how pre-transformation larvae select locations suitable for settlement, depending on environmental factors including temperature, salinity, water depth and riverbed/seabed substrate type. Larval settlement occurs when a super-agent carries within it some competent larvae (i.e. larvae that are ready to settle), of which the numbers are determined by growth processes that are built into the model. Depending on the species being modeled, settlement characteristics may vary substantially (e.g. summer flounder larvae migrate to settle in estuaries and river systems, while sea scallop and silver hake larvae settle in the open ocean waters). These settlement patterns, if sufficiently replicated, provide indication that the parameterized zygote/larval growth, mortality and settlement processes are adequately descriptive of real-life larval growth, mortality, and settlement processes.

B.2 Entities, State Variables and Scales

B.2.1 Entities

The following entities are included in the models: super-agents representing a group of simulated species at post-fertilization, pre-transformation life stages (i.e. zygotes and larvae of the three species), grid cells, (i.e. virtual geographical location) representing the oceanic and estuarine conditions, such as salinity, temperature, and hydrodynamic conditions including horizontal and vertical current speeds and direction, and the global environment which primarily provide temporal information.

B.2.2 State Variables

The model comprises **global** variables that change only across time. In the models, the global variables are related to the time of the instance being simulated. The global variables are presented in **Table 25** below.

Table 25. Global state variables

Variable name	Variable type and units	Meaning
Timestamp	Datetime, yyyy-mm-dd hh:mm:ss	Datetime of simulated instance
Is_daytime	Binary	Indicates if the current timestep is during daytime (TRUE) or nighttime (FALSE).

Grid cells are the smallest computational two-dimensional area in the model; each grid cell represents a polygon in the transverse plane, which in turn represents the entire water column within the spatial footprint of the cell. The model comprises grid cell state variables that change over the time of the model simulation, computed for each cell in the model mesh. The grid cell state variables are related to numbers and densities of settled larvae, as well as the cumulative numbers and densities of transported agents within the model domain. The grid cell state variables are presented in **Table 26** below.

Table 26. Grid cell state variables

Variable name	Variable type and units	Meaning
Settled_Larvae_Density	Real number, larvae/m^2	Number of settled larvae per square meter
Settled_Larvae_Absolute	Real number, larvae	Number of settled larvae (in the grid) in absolute numbers
Cumulative_All	Real number, agents/m^2	Cumulative density of live agents passing through the area, indicating transport rate in the area
Cumulative_Competent	Real number, agents/m^2	Cumulative density of live competent (i.e. ready to settle) agents passing through the area, indicating transport rate in the area

Super-agents are objects containing a group of individual agents (i.e. zygotes and larvae) of each modeled species. The zygotes and larvae are mobile and dynamic organisms that grow or decay (die) over the simulation period. During their growth, the individual agents undergo three main development stages – first, they are initialized as zygotes, which are then incubated and hatch as larvae. After a stipulated larval development time period, the larvae grow to be competent and can settle. During the growth process, a proportion of individuals contained in the super-agents die due to natural mortality. The super-agents are predominantly driven, spatially, by hydrodynamic forcings and by the larvae's swimming ability which is developed at later stages of growth.

The super-agent state variables are presented in **Table 27** below. These comprise dynamic variables that change over time, such the number of zygotes and larvae contained within the super-agent and the cumulative distance traveled by the super-agent, and static variables that stay constant through the super-agent's lifetime, such as the growth parameters which are randomly sampled for each super-agent (e.g. minimum incubation time required for competency acquisition), as well as the coordinates at which the particular super-agent was spawned or released at.

Table 27. Super-agent state variables

Variable name	Variable type and units	Meaning
sv_n_live_agents	Real number; agent	Number of zygotes/larvae alive in super-agent
sv_n_zygotes	Real number; zygote	Number of live zygotes in the agent
sv_n_larvae	Real number; larvae	Number of live pre-competent larvae in the agent
sv_n_competent_larvae	Real number; larvae	Number of live settle-ready larvae in the agent
sv_n_settled	Real number; larvae	Number of settled larvae in the agent
sv_n_dead_individuals	Real number; agent	Number of dead larvae in the agent
sv_zygote_incubation_min	Real number; days	Minimum incubation time required for competency acquisition, from time of hatching, sampled from a normal distribution
sv_zygote_incubation_max	Real number; days	Maximum incubation time before a zygote will die due failing to develop, from time of hatching, sampled from a normal distribution
sv_larvae_development_minimum	Real number; days	Minimum time to pass before larvae can start settling, from time of hatching, sampled from a normal distribution
sv_larvae_development_maximum	Real number; days	Maximum time to pass before larvae can start settling, from time of hatching, sampled from a normal distribution
sv_feeding_age	Real number; days	First-feeding age of larvae, sampled from normal distribution. Only active in Summer Flounder (*Paralichthys dentatus*) ABM.
sv_Home_X	Real number	X-coordinate of zygote release point
sv_Home_Y	Real number	Y-coordinate of zygote release point
sv_Home_Z	Real number	Z-coordinate of zygote release point
XPOS	Real number	X-coordinate of super-agent at current timestep

Variable name	Variable type and units	Meaning
YPOS	Real number	Y-coordinate of super-agent at current timestep
ZPOS	Real number	Z-coordinate of super-agent at current timestep
AGE	Real number, seconds	Age of super-agent in seconds

B.2.3 Scales

The model's spatial extent for the ABM is identical to the spatial extent of the regional hydrodynamic model, as described in **Section 2.1** and **Section 3.2** of the main report. For ease of reference, an excerpt of the description is replicated in this section. The geographic extent of the regional hydrodynamic model was approximately from offshore Massachusetts (Cape Cod) to offshore North Carolina (Cape Hatteras). The model was established in hindcast mode, using MIKE 3 FM HD. Data is included for the years 2017 and 2018, with targeted localized resolution in the project area (i.e. the Offshore Wind Farm leases located off of Massachusetts and Rhode Island). The model's space is represented as bounded and not toroidal, therefore super-agents leaving the boundary of an edge of the domain will not reappear in grid cells along the opposite edge.

The model was bounded on the south near Cape Hatteras at 35° North Latitude with the boundary angled to the Southeast to a point at 33° North and 73° degrees East. From there the model boundary proceeds Northeast to a point 36° North and 68° degrees East. The boundary from there goes north to Cape Cod at 41.75° North Latitude.

The flexible mesh of the model allows for efficient focusing of computer resources around the areas of interest, while avoiding unnecessary resolution and computational demands in areas where high resolution is not essential to the problem at hand. Therefore, the grid cells are smaller in area within the study area (i.e. higher resolution), and resolution is coarser at areas further from the study area. The water body within the model extent is stratified into layers, of 20 sigma levels in the top 150 m of the water column and 45 z-levels of 20 m to 200 m resolution below the sigma levels. Super-agents are capable of traversing along the horizontal plane (across grid cells) and vertical plane (across the sigma and z-levels).

The model runs at 300-seconds (or 5-minutes) time step from the start date to the end date of the simulation. Therefore, computations are performed, and state variables and super-agent positions are updated for up to 288 times per day of the simulation.

B.3 Process Overview and Scheduling

B.3.1 Processes

The model is developed to cover the early life stages of the three identified species, from zygote stage to pre-transformation larval stage. It is structured in five processes: one related to movement (vertical and horizontal) of the agents, one related to natural survival and mortality, two concerning development of the agent, namely the hatching of eggs and the development of larvae, and the final one related to settling of the agent.

The super-agents and grid cells update their state variables at every time step over the entire model simulation period. Super-agents perform each of their processes at every time step of the simulation, until there are no live agents left in the super-agent (i.e. all agents have either died or settled). It is also worthy to note that if a super-agent's age exceeds the stochastically determined maximum incubation time period or maximum larval development time period, all remaining zygotes die, and all remaining non-competent larvae die in these respective scenarios.

B.3.2 Schedule

All model calculations of state variable and updates of environmental forcings occur at a discrete time step size of five (5) minutes over the simulation period. At the beginning of each model time step, the following sequential order is applied:

- Release new super-agents into the model domain relative to time-varying normalized agent-release rates.
- Update of Eulerian meteorological and hydrodynamic forcings, e.g. currents and water levels.
- Calculation and evaluation of Lagrangian arithmetic expressions and sub-modules based on updated values obtained from above step and the previous status of the super-agent.
- Update of new super-agent position (x, y, z) and Lagrangian state-variables based on calculations.

B.4 Agent-Based Model: Design Concepts

B.4.1 Basic Principles

The general concept of the model is to account for growth and mortality features, movement patterns and settlement characteristics of larvae, and couple it with high-resolution, high-accuracy 3D current and flow fields in order to attempt to simulate a more realistic dispersal and settlement pattern than what can be achieved with standard passive drift particle-tracking algorithms and/or with 2nd order advection-dispersion transport models. The main mechanisms important for dispersal of larvae which the model attempts to replicate have been identified in the existing literature and are:

- Changes in larval settlement rate and population abundance as a function of mortality and growth parameters (Allain et al. 2007)
- Changes in settlement probability as a function of life stage, substrate material, and environmental variables including temperature, water depth, and salinity
- Changes in fish larval dispersal patterns, and hence recruitment rates at different sink areas, as a result of larval fish swimming speeds (Faillettaz et al. 2018)
- Changes in vertical migration patterns of larvae as a function of daylight and tidal conditions (Jenkins et al. 1998, Benson et al. 2021)

B.4.2 Emergence

The transport patterns that arise between spawn and sink locations can be described as a long intricate series of sequential interactions between predicted oceanographic forcings with the included zygotes/larval properties. While the level of interaction is complex, it is still largely predictable and thus cannot be labelled as a true emergent property of the system components.

B.4.3 Objectives

The objective measures used by the models is the change in settlement density of larvae at sink locations, and changes in larval transport between the sites. The level of impacts brought about by the construction of offshore wind farms in each of the proposed configurations are assessed based on these dynamics.

B.4.4 Stochasticity

Stochasticity is applied in the model at different levels to varying degrees. The following processes are either semi- or fully dependent on stochastic processes:

- Upon the release of each super-agent, a random number is sampled from a normal distribution to determine the number of zygotes to be contained within the super-agent, in order to account for the varying levels of fecundity of each individual mature reproducing adult.
- Upon the release of each super-agent, random numbers are sampled from a normal distribution to determine the following growth parameters: minimum and maximum zygote incubation time and minimum and maximum larval development time, to account for varying pelagic larval duration for each individual super-agent.
- Mortality rates from time-step to time-step are controlled by an age-dependent survivorship Type III curve (Houde 2002), with curve parameters input by the user.
- Zygote incubation and larval development rates from time-step to time-step are controlled by an age-dependent sigmoidal gain/loss curve (Tian et al. 2007), with curve parameters input by the user.
- Horizontal and vertical dispersion of super-agents in order to account for the effects of unresolved turbulence in the hydrodynamic model. The magnitude of dispersion is scaled to the magnitude of the predicted currents.
- Release points of super-agents are randomly determined by the model (within the user-determined release areas) to account for indeterministic nature of mature adult migration.

B.4.5 Observation

In order to identify overall settlement success and periods where high settlement occurs, the model outputs analyzed in post-processing are the dispersal patterns and settlement density of larvae across the model domain at the end of simulation as well as over time.

B.4.6 Other Concepts

The other standard concepts proposed by the ODD protocol, including *adaptation*, *learning*, *prediction*, *sensing*, *interaction*, and collectives are not implemented in the present modeling study.

B.5 Initialization

For each model source setup, a set number of super-agents to be released was randomly scattered within user-determined spawning areas located in the model domain. The spawning areas are selected based on spawning characteristics and preferences of adults for the studied species and verified against observation data (NOAA 2018). The volumes of released super-agents over the simulation period were scaled to the egg abundance observation data collected in the area of study to represent the spawning activity and seasonality in these areas. A total of 82,080 super-agents were released for sea scallop, 173,664 for silver hake, and 167,040 for summer flounder over each model's simulation period. Graphical representations of the release time series can be found in **Section 6** of the main report.

Upon the first time-step, fecundity level (number of zygotes) and growth properties (zygote incubation and larval development time) are sampled from normal distributions defined by means and given standard deviations, which are parameterized with values available from literature of similar studies on the species under study. Sea scallop and summer flounder super-agents are released at 5m above the seabed, while silver hake super-agents are released at 10 m below the water surface. Initially released super-agents are assumed to be passive drifters along the transverse plane, but as the eggs of all three species are known to be buoyant, the super-agents migrate vertically through the water column towards the water surface during the initial stage of their lifetime.

B.6 Input Data

The larvae ABM's are directly coupled to the HDM, thus built-in forcings of horizontal current speed (m/s) and direction (degrees), vertical current speed (m/s), water level (m), temperature (degree C) and Salinity (psu) are directly read by the ABM following the same spatiotemporal definitions of the hydrodynamic model. See **Appendix A** for an in-depth description of these parameters. Substrate suitability maps generated based on benthic substrate maps (USGS 2005) suitable for settlement and are required as input to determined settling probabilities of competent larvae. Detailed descriptions of substrate suitability for each species are given in **Section 6** of the main report. Timeseries data of super-agents release rates were generated based on abundance data and values reported by literature for the modeled species (NOAA 2018).

B.7 Sub-models

B.7.1 Movement

The parameterization of movement characteristics is documented in **Section 6.2.4.1.5** for sea scallop, **Section 6.2.4.2.5** for silver hake and **Section 6.2.4.2.5** for summer flounder.

B.7.2 Mortality and Growth

The parameterization of mortality and growth characteristics is documented in **Section 6.2.4.1.4** for sea scallop, **Section 6.2.4.2.4** for silver hake and **Section 6.2.4.3.4** for summer flounder.

B.7.3 Settlement Property

The parameterization of settlement characteristics is documented in **Section 6.2.4.1.6** for sea scallop, **Section 6.2.4.2.6** for silver hake and **Section 6.2.4.3.6** for summer flounder.

C Agent-Based Model Sensitivity Analysis

For each of the larvae species ABM, sensitivity tests for key parameters were run. The following sections outline the simulations run and what variables were tested.

C.1 Sea Scallop Larval Sensitivity Analysis Scenario 1 (Baseline)

Table 28. Sea scallop baseline model sensitivity tests

Sensitivity Test	Variable tested	Baseline Value	Sensitivity Test Value (Percentage Change)
1a	Maximum daily zygote and larval mortality rate	0.3/day	0.225/day (-25%)
1b			0.375/day (+25%)
2a	Maximum competency gain probability	0.8/day	0.6/day (-25%)
2b			1.0/day (+25%)
3a	Settling Coefficient	0.8/day	0.6/day (-25%)
3b			1.0/day (+25%)

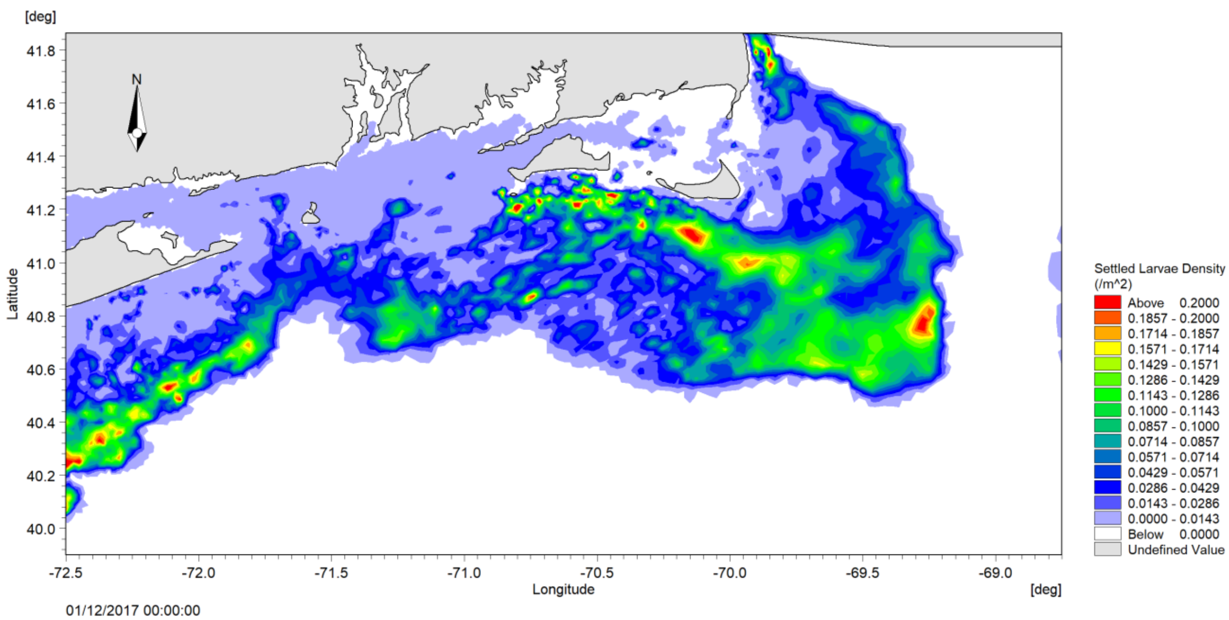

Figure 150. Baseline settled larval sea scallop density
Modeled settled larval sea scallop density (larvae/m^2) in the study area.

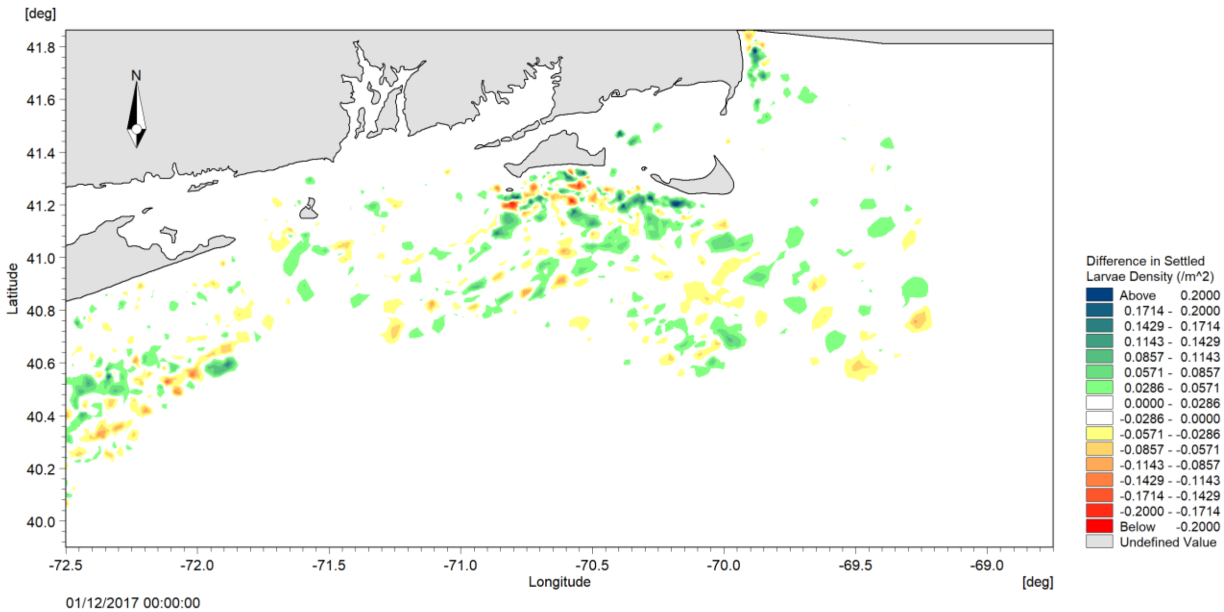

Figure 151. Difference plot of sea scallop settled larval density: Sensitivity Test 1a within the area of study: 25% reduction in maximum daily zygote and larval mortality rate

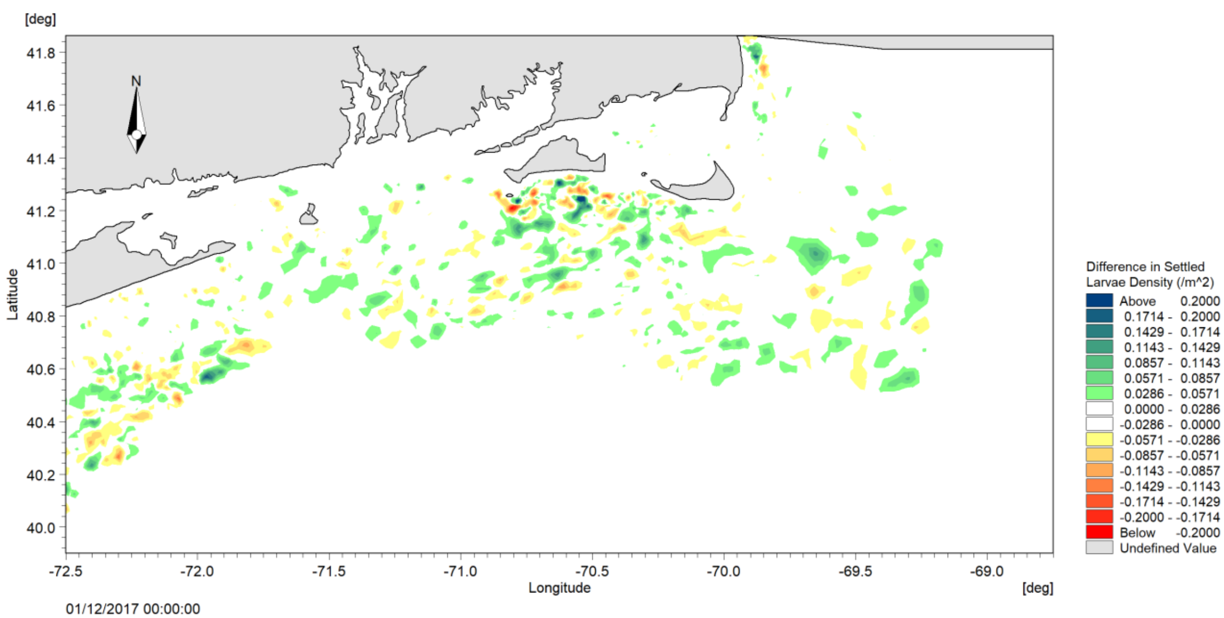

Figure 152. Difference plot of sea scallop settled larval density: Sensitivity Test 1b within the area of study: 25% increase in maximum daily zygote and larval mortality rate

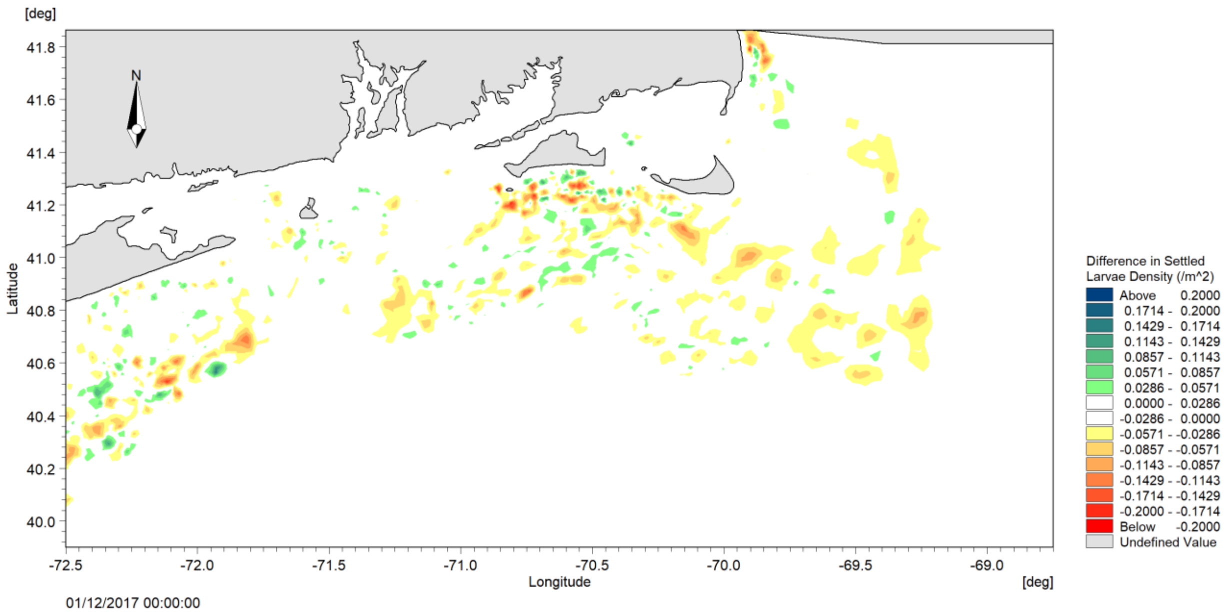

Figure 153. Difference plot of sea scallop settled larval density: Sensitivity Test 2a within the area of study: 25% reduction in maximum competency gain probability

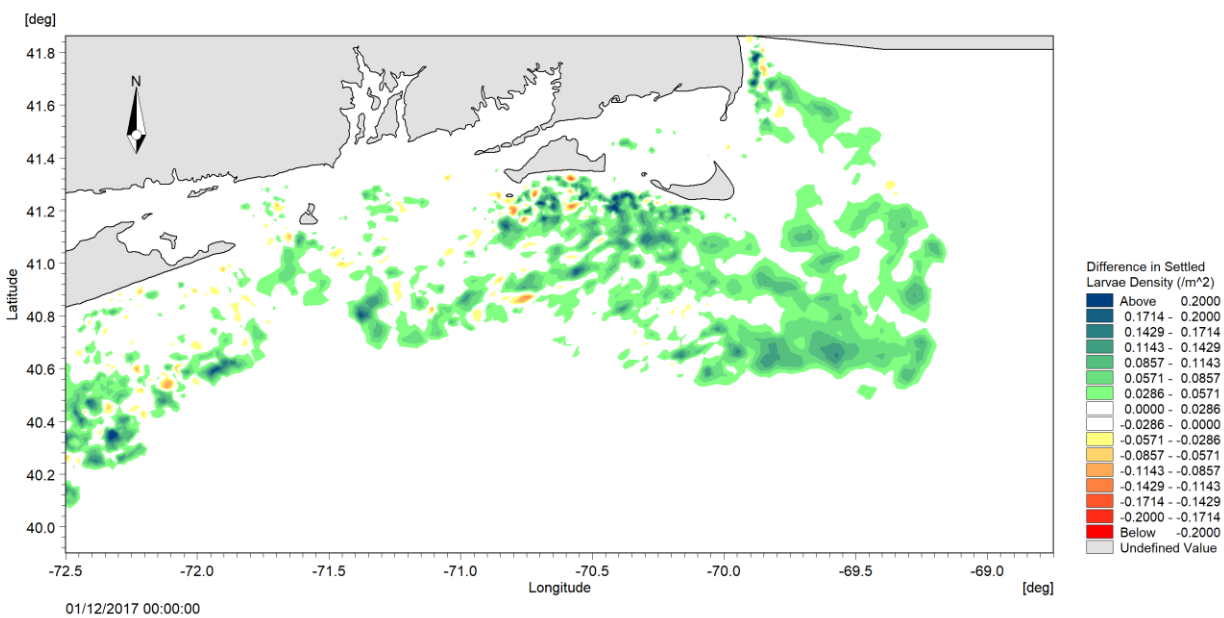

Figure 154. Difference plot of sea scallop settled larval density: Sensitivity Test 2b within the area of study: 25% increase in maximum competency gain probability

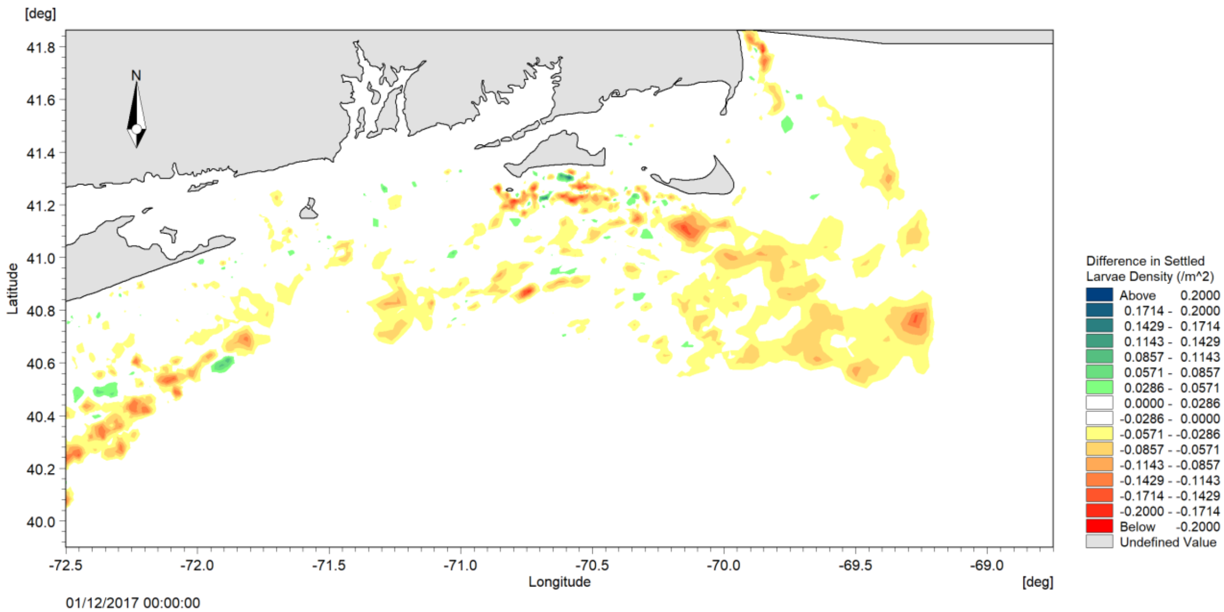

Figure 155. Difference plot of sea scallop settled larval density: Sensitivity Test 3a within the area of study: 25% reduction in settling coefficient

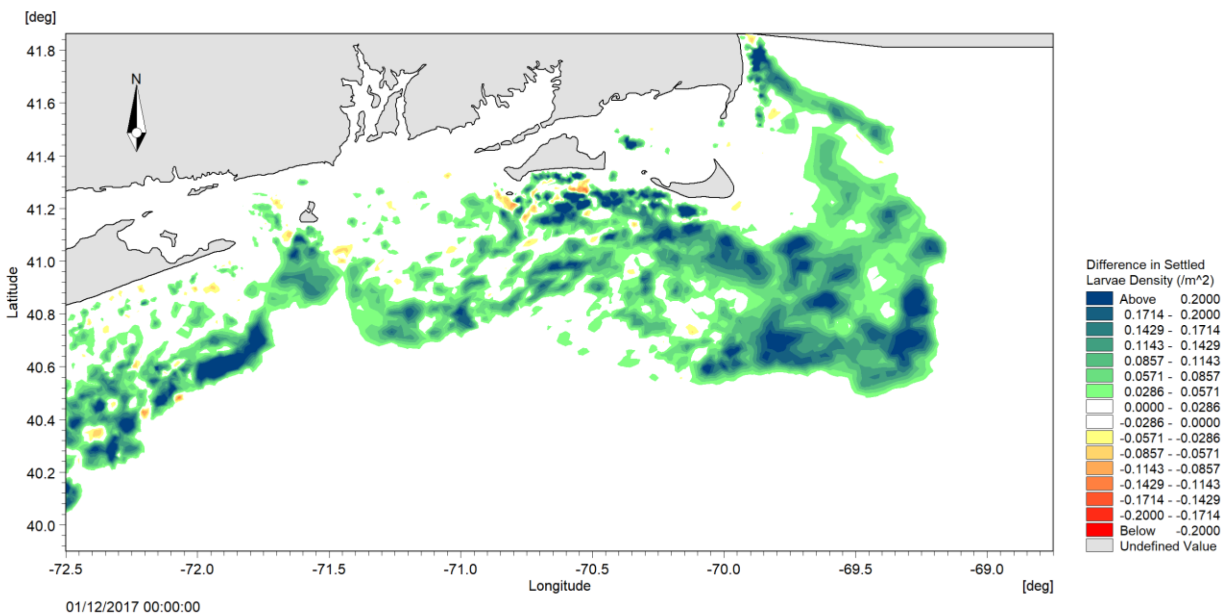

Figure 156. Difference plot of sea scallop settled larval density: Sensitivity Test 3b within the area of study: 25% increase in settling coefficient

C.2 Silver Hake Larval Sensitivity Analysis Scenario 1 (Baseline)

Table 29. Silver hake baseline model sensitivity tests

Sensitivity Test	Variable tested	Baseline Value	Sensitivity Test Value (Percentage Change)
1a	Maximum daily zygote and larval mortality rate	0.24/day	0.18/day (-25%)
1b			0.3/day (+25%)
2a	Maximum daily zygote incubation probability	0.7/day	0.525/day (-25%)
2b			0.875/day (+25%)
3a	Settling Coefficient	0.8/day	0.6/day (-25%)
3b			1.0/day (+25%)

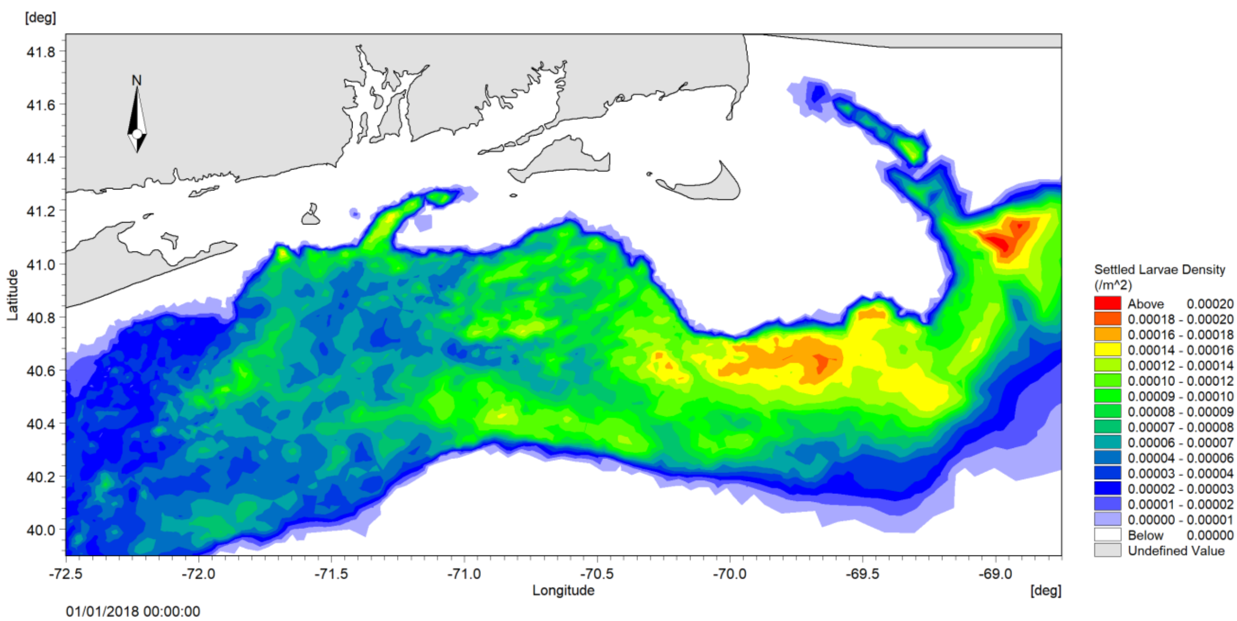

Figure 157. Baseline settled larval silver hake density
Modeled settled larval silver hake density (larvae/m^2) in the study area.

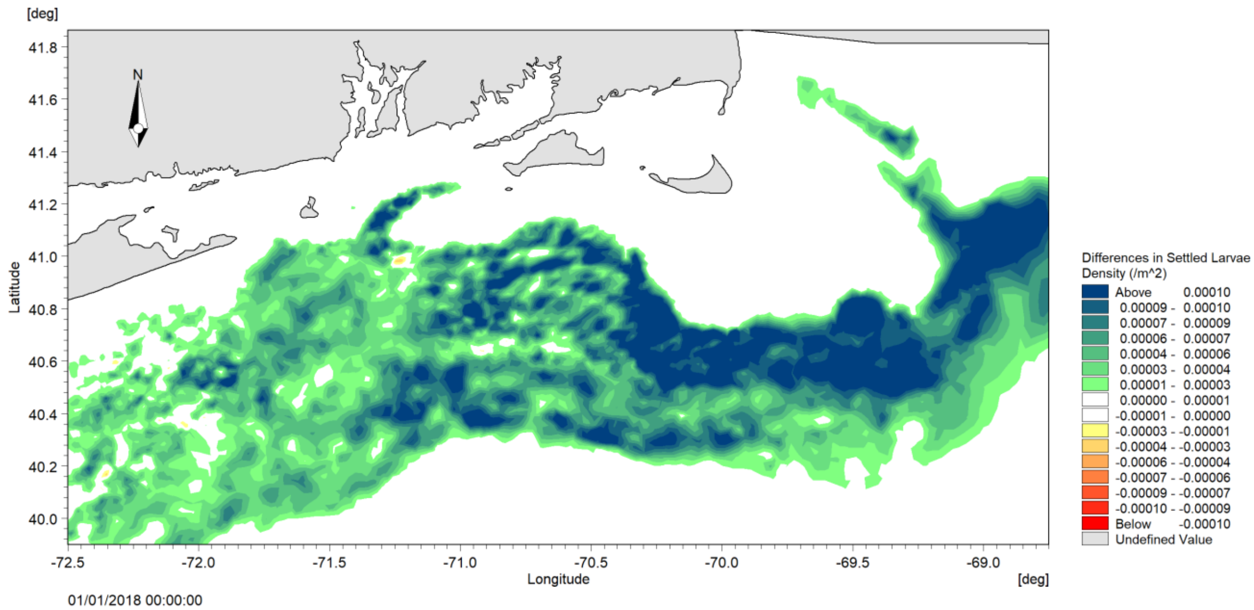

Figure 158. Difference plot of silver hake settled larval density: Sensitivity Test 1a within the area of study: 25% reduction in maximum daily zygote and larval mortality rate

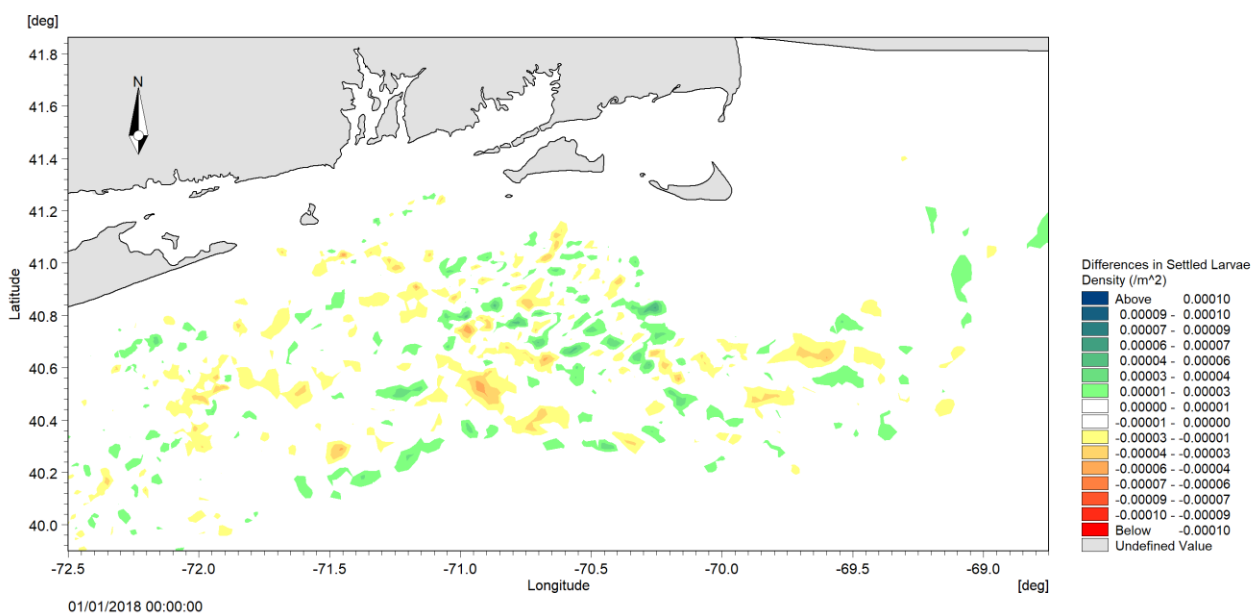

Figure 159. Difference plot of silver hake settled larval density: Sensitivity Test 1b within the area of study: 25% increase in maximum daily zygote and larval mortality rate

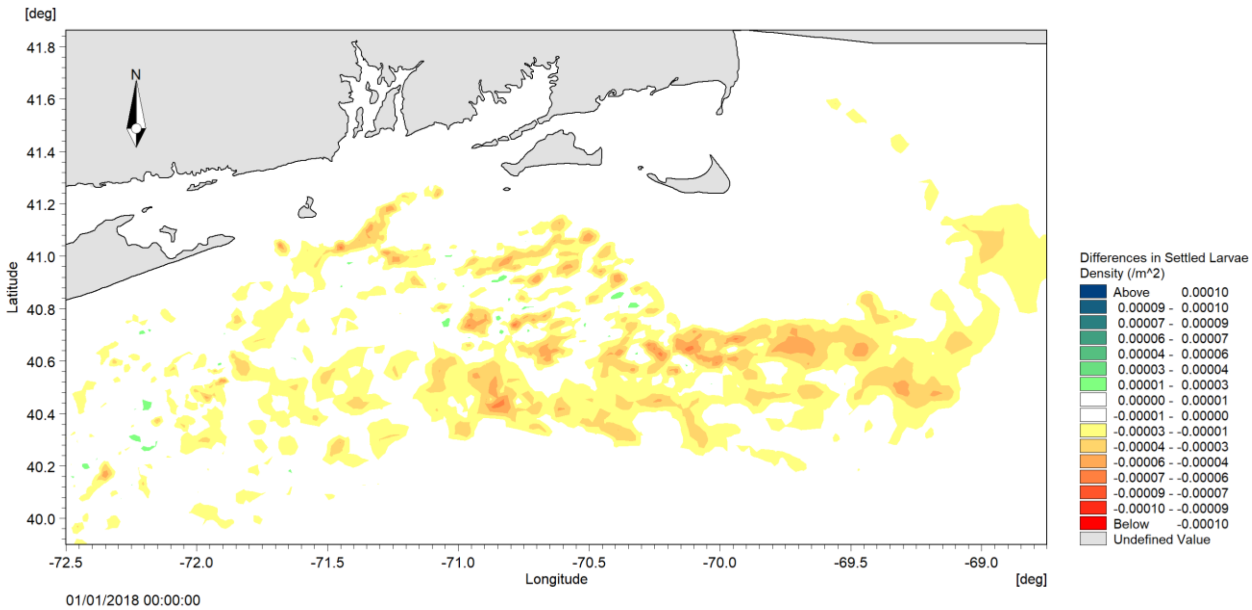

Figure 160. Difference plot of silver hake settled larval density: Sensitivity Test 2a within the area of study: 25% reduction in maximum competency gain probability

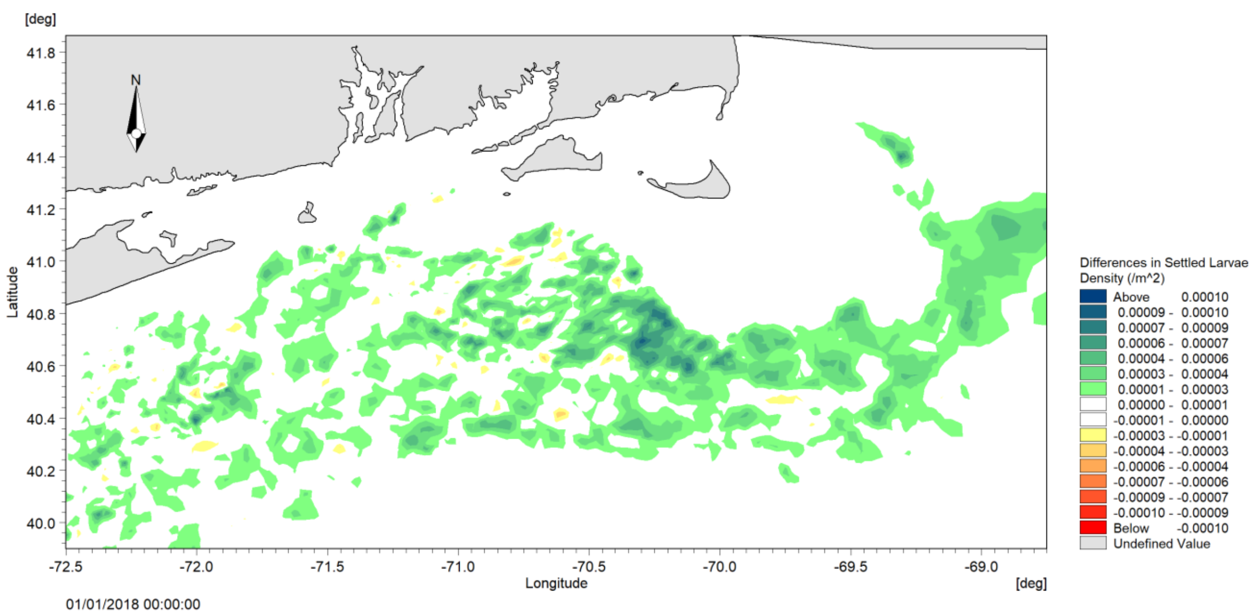

Figure 161. Difference plot of silver hake settled larval density: Sensitivity Test 2b within the area of study: 25% increase in maximum competency gain probability

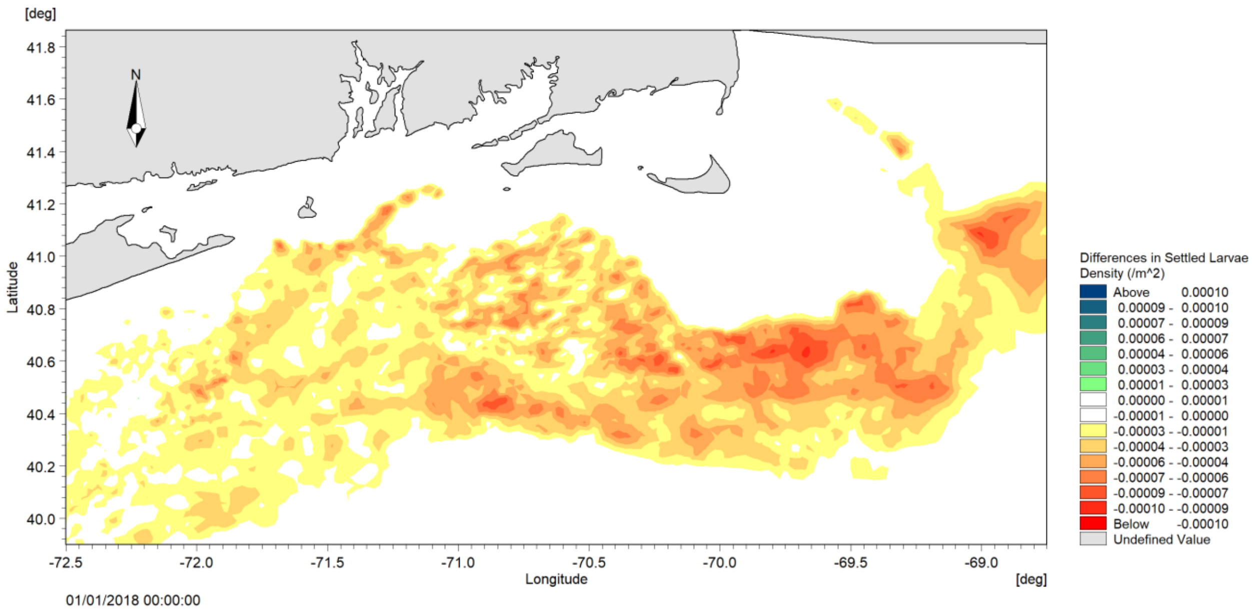

Figure 162. Difference plot of silver hake settled larval density: Sensitivity Test 3a within the area of study: 25% reduction in settling coefficient

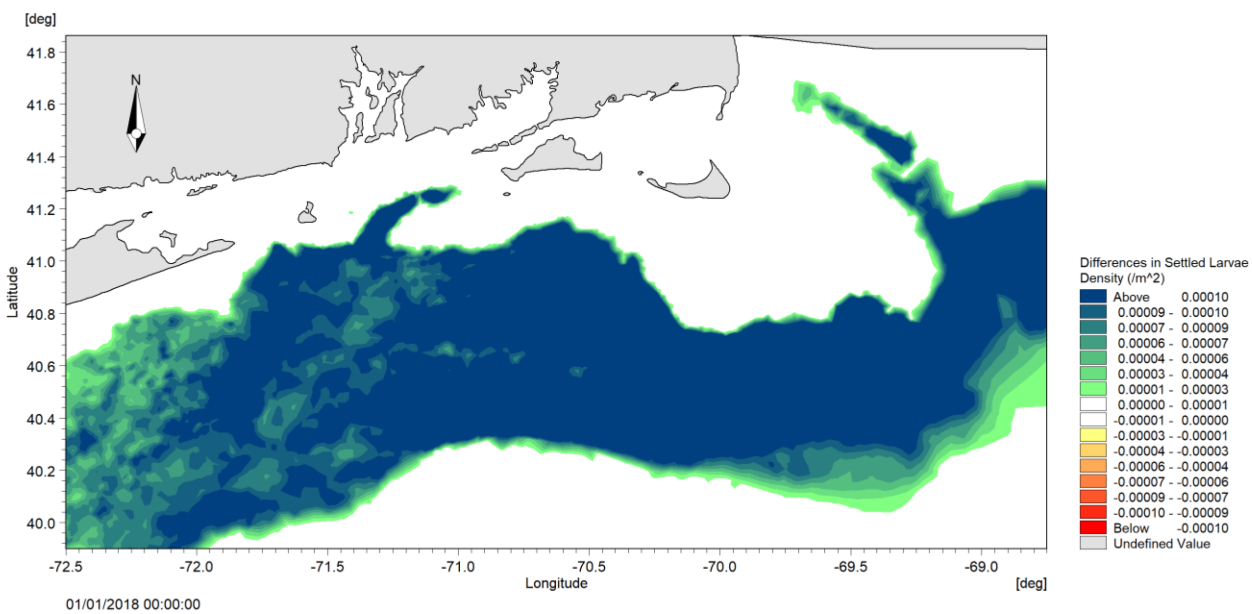

Figure 163. Difference plot of silver hake settled larval density: Sensitivity Test 3b within the area of study: 25% increase in settling coefficient

C.3 Summer Flounder Larval Sensitivity Analysis Scenario 1 (Baseline)

Table 30. Summer flounder baseline model sensitivity tests

Sensitivity Test	Variable tested	Baseline Value	Sensitivity Test Value (Percentage Change)
1a	Maximum daily zygote and larval mortality rate	0.3/day	0.225/day (-25%)
1b			0.375/day (+25%)
2a	Maximum daily zygote incubation probability	0.7/day	0.525/day (-25%)
2b			0.875/day (+25%)
3a	Maximum daily larva competency gain probability	0.4/day	0.3/day (-25%)
3b			0.5/day (+25%)

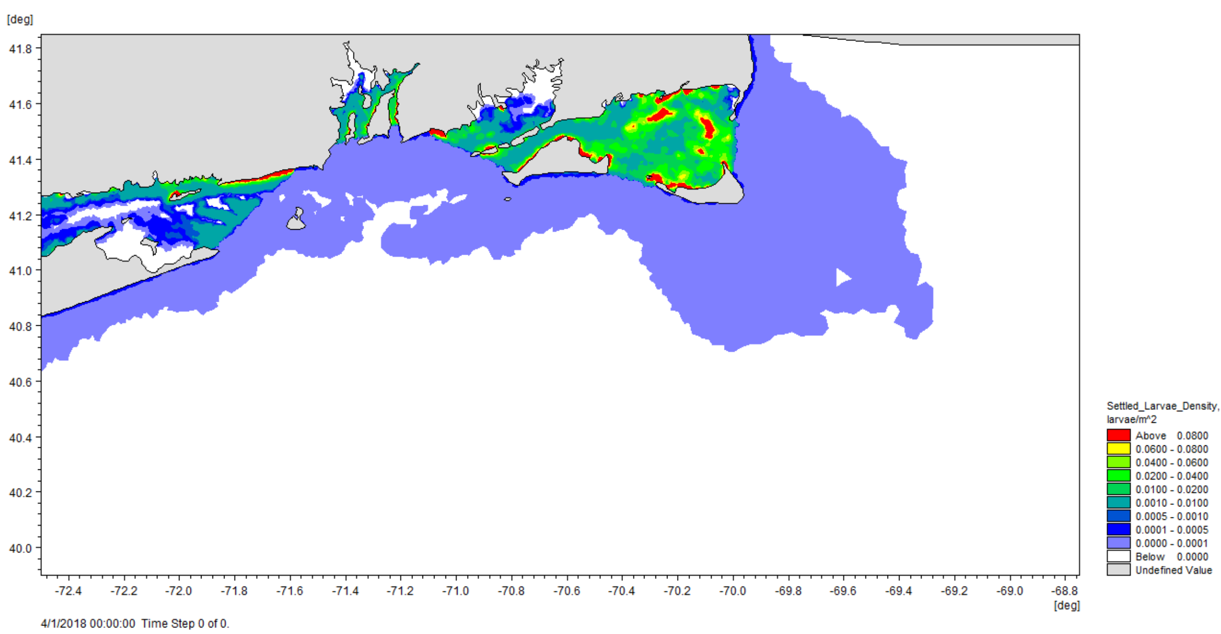

Figure 164. Baseline settled larval summer flounder density
Modeled settled larval summer flounder density (larvae/m^2) in the study area.

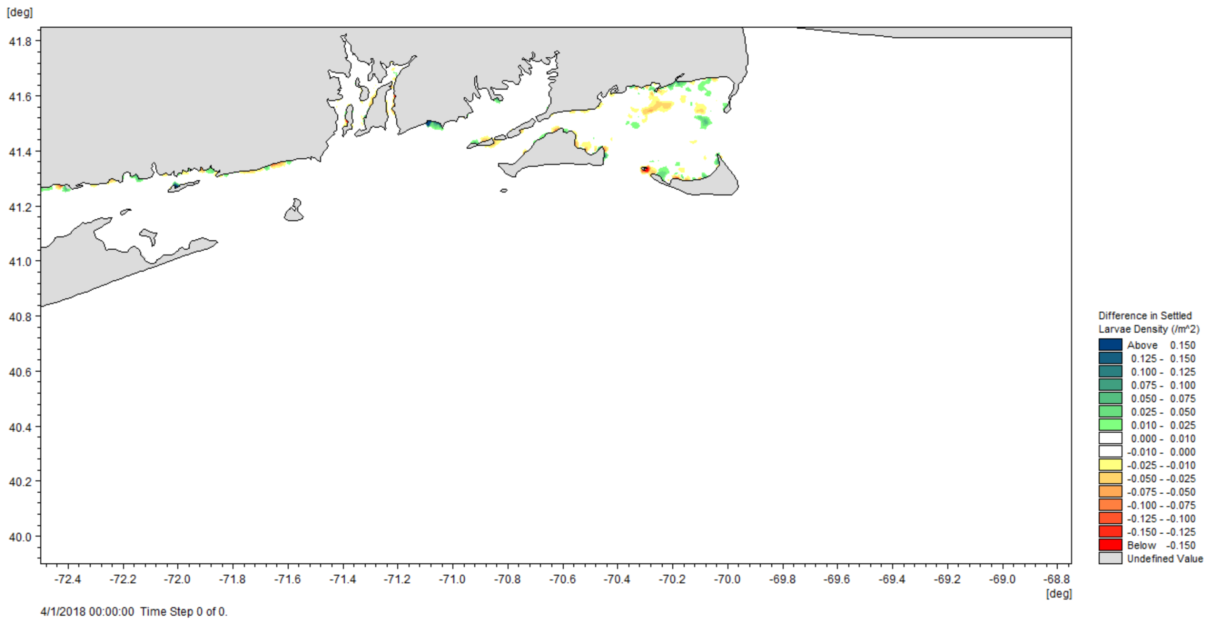

Figure 165. Difference plot of summer flounder settled larval density: Sensitivity Test 1a within the area of study: 25% reduction in maximum daily zygote and larval mortality rate

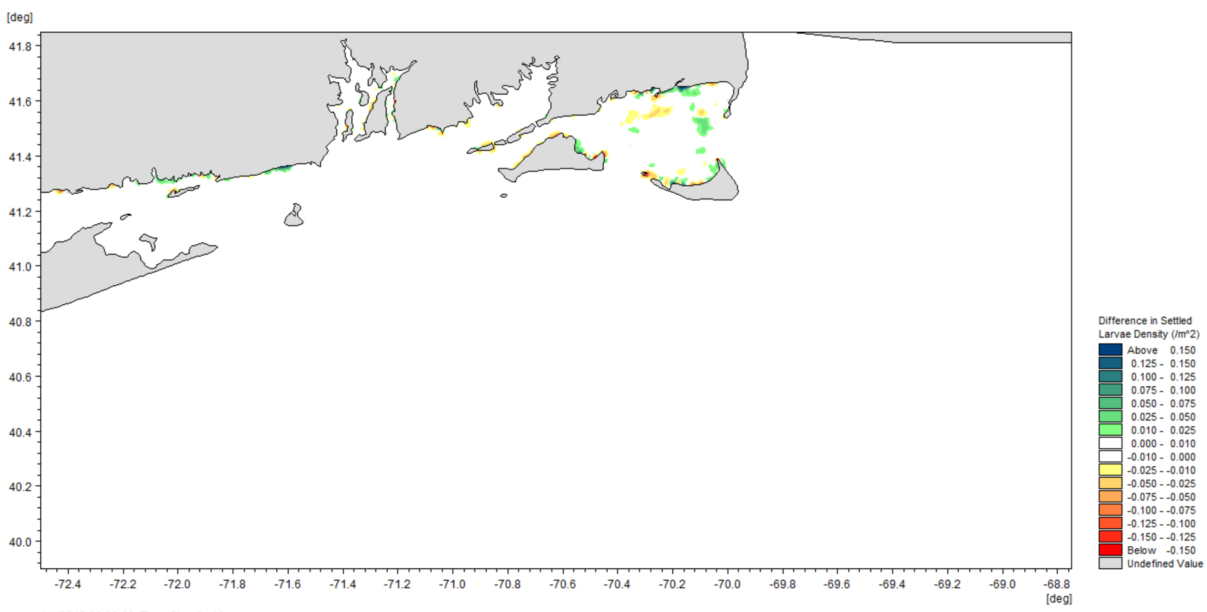

Figure 166. Difference plot of summer flounder settled larval density: Sensitivity Test 1b within the area of study: 25% increase in maximum daily zygote and larval mortality rate

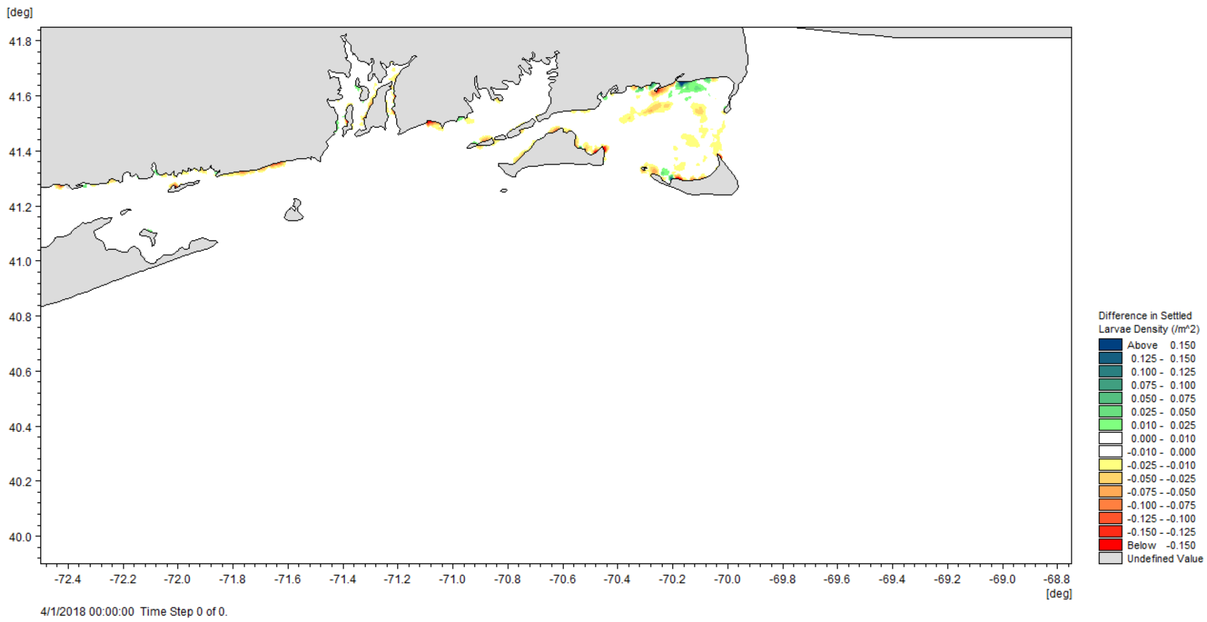

Figure 167. Difference plot of summer flounder settled larval density: Sensitivity Test 2a within the area of study: 25% reduction in maximum daily zygote incubation rate

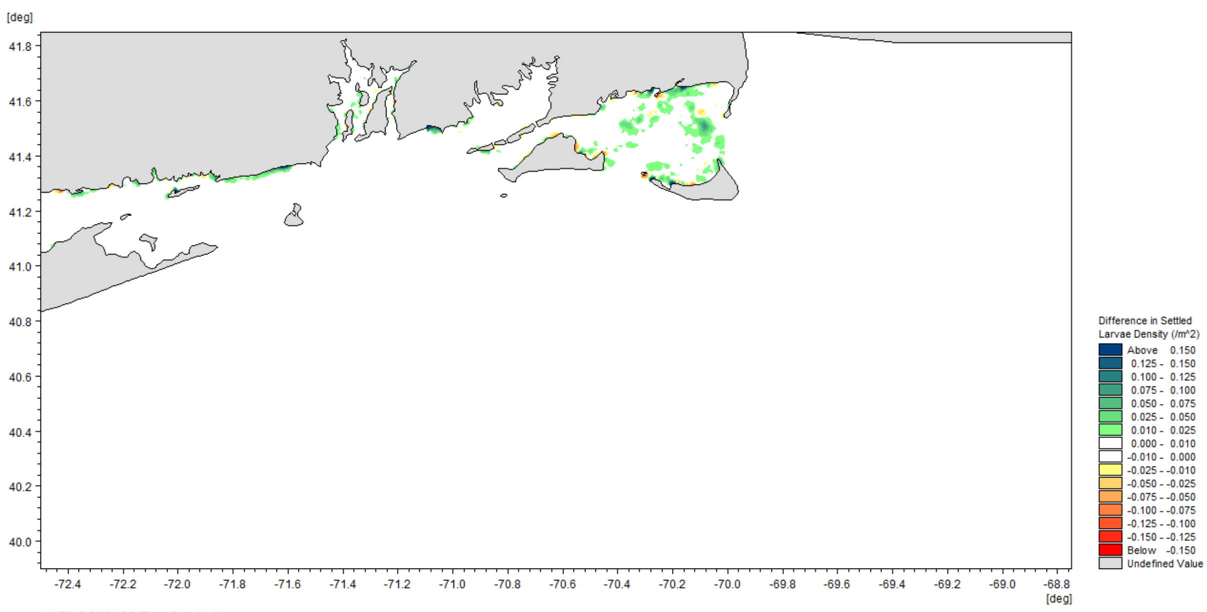

Figure 168. Difference plot of summer flounder settled larval density: Sensitivity Test 2b within the area of study: 25% increase in maximum daily zygote incubation rate

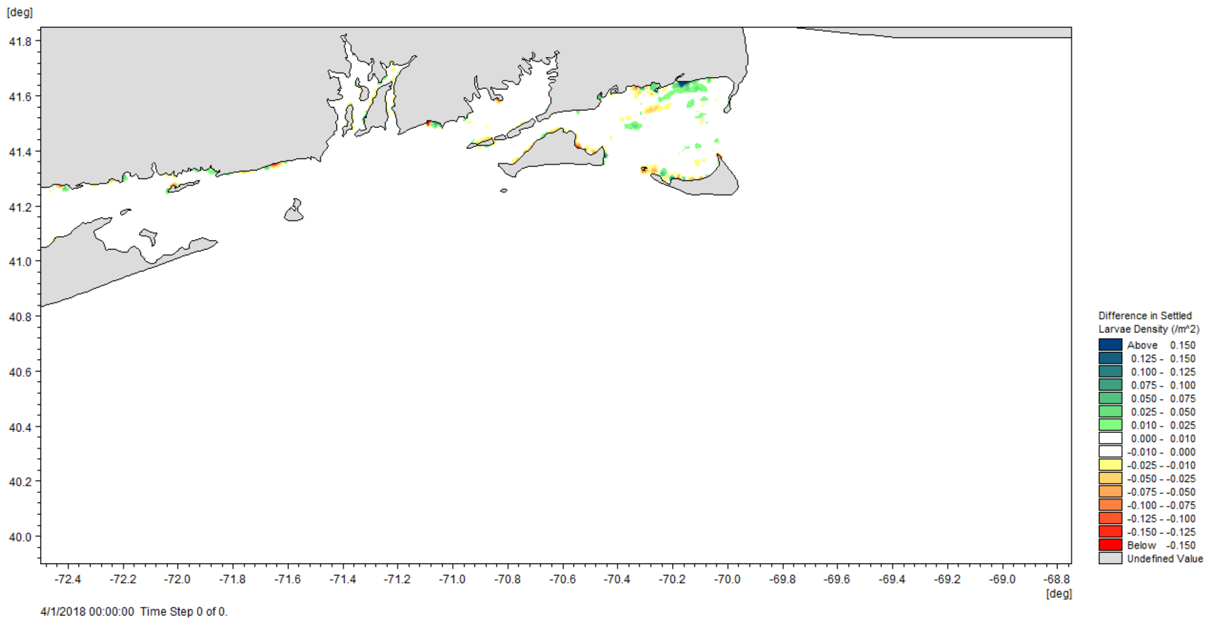

Figure 169. Difference plot of summer flounder settled larval density: Sensitivity Test 3a within the area of study: 25% reduction in maximum daily larva competency gain rate

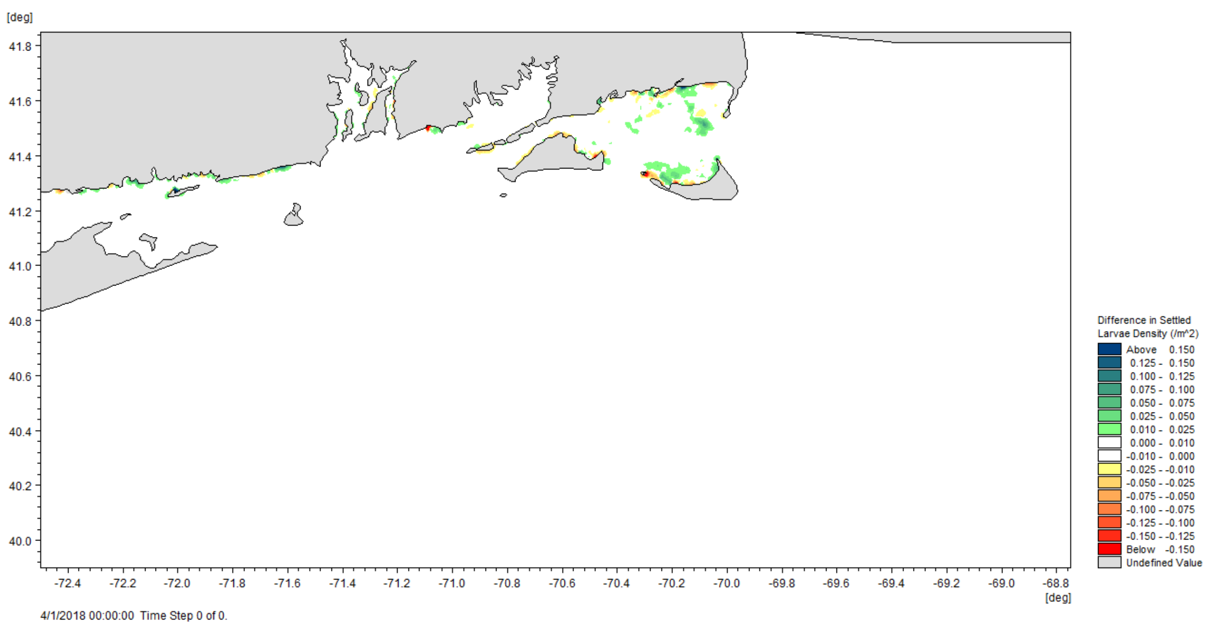

Figure 170. Difference plot of summer flounder settled larval density: Sensitivity Test 3b within the area of study: 25% increase in maximum daily larva competency gain rate

Department of the Interior (DOI)
The Department of the Interior protects and manages the Nation's natural resources and cultural heritage; provides scientific and other information about those resources; and honors the Nation's trust responsibilities or special commitments to American Indians, Alaska Natives, and affiliated island communities.

Bureau of Ocean Energy Management (BOEM)
The mission of the Bureau of Ocean Energy Management is to manage development of U.S. Outer Continental Shelf energy and mineral resources in an environmentally and economically responsible way.

BOEM Environmental Studies Program
The mission of the Environmental Studies Program is to provide the information needed to predict, assess, and manage impacts from offshore energy and marine mineral exploration, development, and production activities on human, marine, and coastal environments. The proposal, selection, research, review, collaboration, production, and dissemination of each of BOEM's Environmental Studies follows the DOI Code of Scientific and Scholarly Conduct, in support of a culture of scientific and professional integrity, as set out in the DOI Departmental Manual (305 DM 3).